THESE

Morphological and Stent Design Risks Factors to prevent Migration Phenomena and Type 1a Endoleak for Thoracic Aneurysm: a numerical analysis

Présentée devant
L'Institut National des Sciences Appliquées de Lyon

Pour obtenir
Le GRADE DE DOCTEUR

Ecole doctorale:
Mécanique, ´Energétique, Génie Civil, Acoustique

Spécialité :
Biomécanique

Par

Sam ALTNJI

Thèse soutenue le 2 Juin 2014 devant la Commission d'examen

Jury

Rapporteur	Valérie DEPLANO	Chargée de Recherche, HDR (IRPHE, Marseille)
Rapporteur	John TICHY	Professeur des Universités (R.P.I, Troy, USA)
Examinateur	Jérôme CHEVALIER	Professeur des Universités (INSA de Lyon)
Examinateur	Philippe VEZIN	Directeur de Recherche (IFSTTAR-Université Lyon 1)
Examinateur	Patrick LERMUSIAUX	Professeur des Universités (Hospices Civils de Lyon)
Directeur de thèse	Benyebka BOU-SAÏD	Maître de Conférences, HDR (INSA de Lyon)
Co-Directrice de thèse	Hélène WALTER-LE-BERRE	Maître de Conférences (INSA de Lyon)
Examinateur	Fouad EL-KHALDI	Ingénieur, Docteur (ESI GROUP de Paris)

LaMCoS - UMR CNRS 5514 - INSA de Lyon
20, avenue Albert Einstein, 69621 Villeurbanne Cedex (FRANCE)

INSA Direction de la Recherche - Ecoles Doctorales – Quinquennal 2011-2015		
SIGLE	**ECOLE DOCTORALE**	**NOM ET COORDONNEES DU RESPONSABLE**
CHIMIE	**CHIMIE DE LYON** **http://www.edchimie-lyon.fr** Insa : R. GOURDON	M. Jean Marc LANCELIN Université de Lyon – Collège Doctoral Bât ESCPE 43 bd du 11 novembre 1918 69622 VILLEURBANNE Cedex Tél : 04.72.43 13 95 directeur@edchimie-lyon.fr
E.E.A.	**ELECTRONIQUE,** **ELECTROTECHNIQUE,** **AUTOMATIQUE** **http://edeea.ec-lyon.fr** Secrétariat : M.C. HAVGOUDOUKIAN eea@ec-lyon.fr	M. Gérard SCORLETTI Ecole Centrale de Lyon 36 avenue Guy de Collongue 69134 ECULLY Tél : 04.72.18 60 97 Fax : 04 78 43 37 17 Gerard.scorletti@ec-lyon.fr
E2M2	**EVOLUTION, ECOSYSTEME,** **MICROBIOLOGIE,** **MODELISATION** **http://e2m2.universite-lyon.fr** Insa : H. CHARLES	Mme Gudrun BORNETTE CNRS UMR 5023 LEHNA Université Claude Bernard Lyon 1 Bât Forel 43 bd du 11 novembre 1918 69622 VILLEURBANNE Cédex Tél : 04.72.43.12.94 e2m2@biomserv.univ-lyon1.fr
EDISS	**INTERDISCIPLINAIRE** **SCIENCES-** **SANTE** **http://ww2.ibcp.fr/ediss** Sec : Safia AIT CHALAL Insa : M. LAGARDE	M. Didier REVEL Hôpital Louis Pradel Bâtiment Central 28 Avenue Doyen Lépine 69677 BRON Tél : 04.72.68 49 09 Fax :04 72 35 49 16 Didier.revel@creatis.uni-lyon1.fr
INFOMATHS	**INFORMATIQUE ET** **MATHEMATIQUES** **http://infomaths.univ-lyon1.fr**	M. Johannes KELLENDONK Université Claude Bernard Lyon 1 INFOMATHS Bâtiment Braconnier 43 bd du 11 novembre 1918 69622 VILLEURBANNE Cedex Tél : 04.72. 44.82.94 Fax 04 72 43 16 87 infomaths@univ-lyon1.fr
Matériaux	**MATERIAUX DE LYON** Secrétariat : M. LABOUNE PM : 71.70 –Fax : 87.12 Bat. Saint Exupéry Ed.materiaux@insa-lyon.fr	M. Jean-Yves BUFFIERE INSA de Lyon MATEIS Bâtiment Saint Exupéry 7 avenue Jean Capelle 69621 VILLEURBANNE Cédex Tél : 04.72.43 83 18 Fax 04 72 43 85 28 Jean-yves.buffiere@insa-lyon.fr
MEGA	**MECANIQUE, ENERGETIQUE,** **GENIE** **CIVIL, ACOUSTIQUE** Secrétariat : M. LABOUNE PM : 71.70 –Fax : 87.12 Bat. Saint Exupéry mega@insa-lyon.fr	M. Philippe BOISSE INSA de Lyon Laboratoire LAMCOS Bâtiment Jacquard 25 bis avenue Jean Capelle 69621 VILLEURBANNE Cedex Tél : 04.72.43.71.70 Fax : 04 72 43 72 37 Philippe.boisse@insa-lyon.fr
ScSo	**ScSo*** **M. OBADIA Lionel** Sec : Viviane POLSINELLI Insa : J.Y. TOUSSAINT	M. OBADIA Lionel Université Lyon 2 86 rue Pasteur 69365 LYON Cedex 07 Tél : 04.78.69.72.76 Fax : 04.37.28.04.48 Lionel.Obadia@univ-lyon2.fr

*ScSo : Histoire, Géographie, Aménagement, Urbanisme, Archéologie, Science politique, Sociologie, Anthropologie

ACKNOWLEDGEMENTS

The list of the people I need to thank will not fit to a single Acknowledgement section. I just mention some people whose contribution is obvious.

First and Foremost, I would like to express my sincere gratitude to my supervisor, *Mr. BOU-SAID Benyebka*, for the continuous support of my Ph.D study and research, for his patience, motivation, enthusiasm, and immense knowledge. His guidance helped me in all the time of research and writing of this thesis. I could not have imagined having a better advisor and mentor for my Ph.D study. One simply could not wish for a better or friendlier supervisor. Furthermore, I would like to thank my co-supervisor *Mrs. WALTER-LE BERRE Hélène* for her useful comments, remarks and good company.

I am grateful for the thoughtful and detailed comments of my examiner.

I would like to acknowledge the, academic and technical support of the national institute of applied sciences (INSA of Lyon). It has provided the support and equipment i have needed to produce and complete my thesis.

I wish to thank my friend (Dr.Montaser AWAL), for helping me get through the difficult times, and for all the emotional support.

Above all, I would like to thank my wife 'RAMA' for her personal support, patience and love during the past few years. She was always there cheering me up and stood by me through the good times and bad. Her support and encouragement was in the end what made this dissertation possible.

I would not have contemplated this road if not for my parents. They receive my deepest gratitude and love for their dedication and the many years of support during my undergraduate studies that provided the foundation for this work. They bore me, raised me, supported me, taught me, and loved me, who gave me a home away from home.

My parents, my wife, my lovely son 'Yazan', to you I dedicate this thesis.

Sam ALTNJI-2014

Résumé

Introduction

Avec plus de 180000 décès par an en France, les maladies cardiovasculaires sont la première cause de mortalité. Elles représentent une cause majeure de décès dans les pays occidentaux ce qui justifie pleinement des recherches constantes sur la compréhension, la prévention, l'amélioration des traitements thérapeutiques.

Un anévrisme est une dilatation localisée et permanente de la paroi d'une artère aboutissant à la formation d'une poche de taille variable, communiquant avec l'artère au moyen d'une zone rétrécie que l'on nomme le collet. Sa forme habituelle est celle d'un sac dont le diamètre peut atteindre plusieurs centimètres. Avec le temps, la taille de l'anévrisme soumis aux impulsions sanguines augmente progressivement. Lorsqu'il se rompt, l'anévrisme provoque une hémorragie interne pouvant rapidement entraîner la mort. La rupture d'anévrisme est un accident redoutable et mortel. En France, plus de 5000 cas de rupture sont recensés par an. La prévention de la rupture est donc un enjeu majeur d'un point de vue médical. Les anévrismes constituent la 3e cause de décès cardiovasculaire.
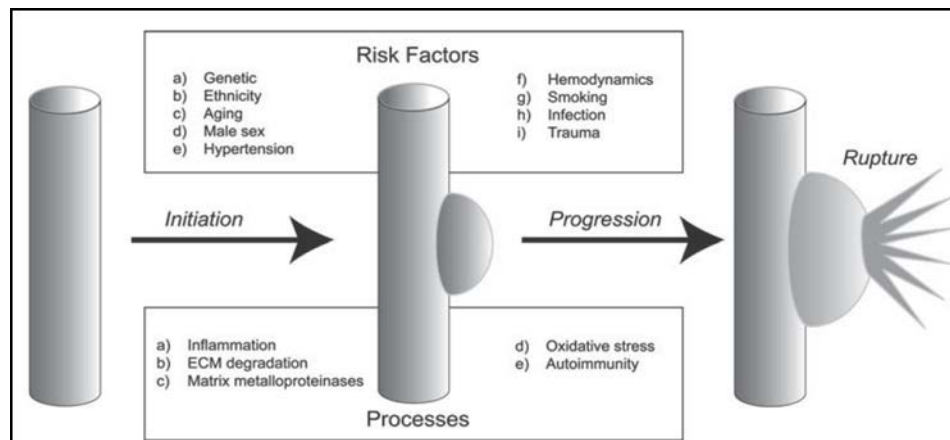
Formation, croissance et rupture d'un Anévrisme de l'Aorte Abdominale (AAA) : facteurs de risque et processus biologique observé lors de la formation de l'AAA

Il existe deux techniques de traitement possibles des anévrismes de l'aorte. (i) La procédure chirurgicale classique, utilisée en urgence dans le cas d'une rupture de l'anévrisme, mais également pour les traitements préventifs, qui consiste à réaliser une grande incision dans l'abdomen du patient puis à implanter une prothèse synthétique à la place de l'anévrisme. Cette technique possède l'avantage d'être efficace et fiable mais reste une intervention lourde avec de nombreux risques et complications cardiaque et respiratoire. (ii) La procédure endovasculaire (Endovascular Aneurysm Repair ou EVAR) consiste quant à elle à faire glisser une endoprothèse en nitinol par voie fémorale jusqu'au niveau de l'anévrisme afin de re-canaliser le flux sanguin en excluant l'athérome. Malgré tous les avantages que présente cette technique, tels qu'une durée d'hospitalisation plus courte et des pertes sanguines réduites, celle-ci n'est

pas encore totalement validée. En effet, l'évolution à long terme des endoprothèses et les complications engendrées par leurs mises en place ne sont pas encore parfaitement maîtrisées.
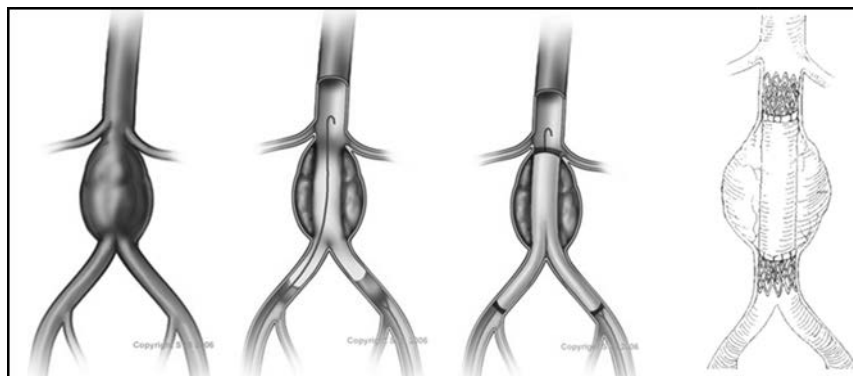
Procédure endovasculaire pour le traitement d'AAA (EVAR)

Les principales complications qui peuvent survenir après une procédure endovasculaire sont les phénomènes de migration et d'endofuites. Les phénomènes de migration se traduisent dès lors que l'endoprothèse se déplace de plus de 10 mm par rapport à sa position initiale entrainant ainsi l'apparition d'endofuites de type I. Les endofuites sont définies comme étant la persistance du flux sanguin en dehors de la prothèse et au sein de la poche anévrismale. Il existe différents types d'endofuites classés selon leur moment d'apparition et leur origine anatomique. Parmi ceux-ci, les endofuites de type I sont dues à un défaut d'accolement de l'endoprothèse à la paroi aortique et sont considérées comme étant les plus dangereuses. La forme de l'endoprothèse ainsi que ses dimensions mal adaptées aux mesures initiales de l'anévrisme sont en général mises en cause.

Ces complications surviennent principalement dans la partie thoracique de l'aorte et sont souvent occasionnées par un mauvais positionnement de l'endoprothèse dans une crosse aortique tortueuse ainsi qu'une zone de contact insuffisante entre la prothèse l'aorte.

Déployer une endoprothèse dans une aorte thoracique dont la morphologie est complexe semble donc représenter un défi, les tortuosités de l'aorte étant considérées comme étant une cause importante d'apparition précoce des endofuites. Les principaux facteurs de risque d'apparition des endofuites de type I et de migration de l'endoprothèse sont les suivants : mauvais dimensionnement de la prothèse, forces de trainée élevées dues à une angulation sévère, longueur insuffisante de la fixation proximale, présence de calcification et de thrombus dans les zones de fixation. Optimiser un seul de ces facteurs ne permet pas de garantir la prévention des phénomènes de migration ou d'endofuites de type I. Il est donc nécessaire d'étudier l'influence de ces différents facteurs.

Le principal objectif de ce travail est d'étudier les principaux facteurs, liés à la morphologie de l'anévrisme et au design du stent, responsables de l'apparition des endofuites de type I, de la migration ainsi que la ruine de l'endoprothèse. Des simulations 3D de la procédure de déploiement de l'endoprothèse ont été effectuées, en utilisant la méthode des éléments finis, afin de prédire la réponse biomécanique du système vasculaire et de l'endoprothèse. L'étude réalisée porte principalement sur l'évaluation de la stabilité du contact dans la zone d'interaction entre la prothèse et l'aorte, pour différents designs de stent, après déploiement complet du stent dans une morphologie patient-spécifique d'un

anévrisme de l'aorte thoracique (AAT). Les résultats obtenus lors de ces simulations pourront servir de guide pour optimiser le design du stent afin de renforcer le contact fournissant ainsi un compromis entre raideur et flexibilité du stent.

Chapitre 1

Dans le premier chapitre, le contexte médical et technique est présenté. Dans un premier temps, les différents anévrismes de l'aorte et leur évolution sont brièvement décrits. Les deux techniques de traitement des anévrismes de l'aorte - la procédure chirurgicale classique et la procédure endovasculaire - sont présentées ainsi que leurs avantages et leurs inconvénients. De par son caractère peu invasif, la procédure endovasculaire est en plein essor et sera certainement amenée, dans le futur, à remplacer une grande partie des interventions vasculaires ouvertes C'est pourquoi un intérêt particulier est porté dans ce chapitre sur les complications associées à la technique endovasculaire et plus particulièrement sur les phénomènes d'endofuites et de migration de l'endoprothèse.

D'autre part, le choix de l'endoprothèse elle-même est déterminant dans la réussite du traitement. C'est pourquoi les différentes endoprothèses commercialisées pour le traitement des anévrismes de l'aorte sont présentées. Ces endoprothèses sont composées de deux parties : une partie métallique, appelée stent, en nitinol ou en acier inoxydable 316L qui assure la rigidité de l'ensemble, formée d'éléments endoprothétiques souvent en forme de Z, et une partie étanche en tissu chirurgical (dacron ou polyester), les deux parties étant cousues l'une à l'autre. Les stents en nitinol sont autoexpansibles alors que ceux en acier sont expansibles par ballonnet. La géométrie et la forme des endoprothèses varient en fonction de la localisation de l'anévrisme dans l'aorte.

Chapitre 2

La simulation de la procédure complète du largage d'une endoprothèse dans un anévrisme de l'aorte en utilisant des méthodes numériques représente un réel challenge du fait des nombreuses non-linéarités inhérente au problème étudié et notamment le comportement mécanique de l'aorte ainsi que celui du nitinol, la gestion du contact entre les différents corps en présence et les grandes déformations. Dans ce cadre, le deuxième chapitre présente le noyau de base de la biomécanique du stent et de l'aorte ainsi qu'un état de l'art des méthodes numériques utilisées en biomécanique et dans la modélisation des stent.

Le chapitre débute par des notions générales de biomécanique et de bioingénierie incluant les méthodes numériques utilisées dans ces domaines ainsi que des notions sur les biomatériaux.

La réalisation de simulations réalistes de la procédure endovasculaire nécessite la connaissance et la compréhension du comportement mécanique de la paroi aortique. Les parois vasculaires présentent une structure stratifiée, composée de 3 couches (l'intima, la média et l'adventice), où 3 constituants fondamentaux (fibres d'élastine, fibres de collagène et fibres musculaires lisses) apparaissent en proportions et arrangements variés. Elles possèdent donc un comportement mécanique complexe et fortement non linéaire, dont un état de l'art détaillé est présenté dans ce chapitre. Il apparait que le comportement de la paroi aortique est un comportement principalement hyperélastique. Une revue des différents modèles hyperélastiques existants ainsi que les lois de comportement associées a donc été effectuée.

Le rôle de l'endoprothèse est d'exclure le flux sanguin du sac anévrismal afin que celui-ci ne soit plus un danger pour le patient. Dans ce contexte, l'endoprothèse doit répondre à de nombreux critères liés à son mécanisme d'expansion, au design du stent, au matériau constituant le stent et au comportement mécanique globale du stent aussi bien lors de la phase de largage que lorsqu'il est déployé. Une étude bibliographique détaillée des endoprothèses et des stents, qui tient compte tous ces aspects, a été réalisée et est présentée dans ce chapitre. Une attention particulière est portée sur le nitinol, un alliage à mémoire de forme biocompatible présent dans les stents de nombreuses endoprothèses. Ce comportement à mémoire de forme va conditionner le positionnement final de la prothèse. Il est généralement modélisé par des lois de comportement dites superélastiques. Ce comportement ainsi que les lois qui le gouvernent ont donc été également détaillés.

Le chapitre se termine sur les progrès réalisés dans la modélisation par éléments finis du système composé du stent et de la structure vasculaire.

Chapitre 3

Les phénomènes d'endofuites de type I et de migration de l'endoprothèse sont considérés comme étant les raisons principales d'échec de la procédure endovasculaire. Bien que les opinions divergent quant à la nature de ces complications, un consensus a été atteint établissant que ces deux problèmes sont liés à un contact inefficace ainsi qu'une perte d'étanchéité entre la paroi aortique et les extrémités de l'endoprothèse, distale ou proximale. De ce fait, les principaux critères anatomiques susceptibles d'exclure un patient du traitement endovasculaire concernent les dimensions et la morphologie des collets proximal et distal de l'anévrisme dans lesquelles le design et les dimensions du stent ne permettent pas d'assurer avec certitude l'étanchéité. Ces complications ont fait l'objet d'études cliniques et peuvent être reliées à l'un de des facteurs suivants : endoprothèse sous-dimensionnée, forces de trainée élevées due à une angulation importante, longueur de fixation de la zone proximale insuffisante ou torsion de l'endoprothèse. Les recherches numériques récentes utilisant la méthode des éléments finis qui ont étudié ces complications sont limitées et concernent principalement des géométries idéalisées de vaisseaux sanguins et des comportements de stent non associés à des géométries 3D réelles. De plus, l'influence des tortuosités de l'aorte ainsi que de l'oversizing sur le déploiement mécanique du stent n'a pas encore été examiné. En effet, ces études concernent essentiellement des stents coronaires ou pour des anévrismes intracraniaux afin d'évaluer leurs performances. Il semble donc important d'étudier les effets du design des stents en nitinol déployé dans un anévrisme de l'aorte thoracique sur l'efficacité du contact, aspect qui, à l'heure actuelle, n'a pas encore été examiné notamment dans le cadre d'un modèle patient-spécifique.

L'objectif de ce travail est dont de développer des simulations numériques d'un système complet de pose de stent en utilisant la méthode des éléments finis afin d'étudier la stabilité du contact lors du largage mécanique d'une endoprothèse autoexpansible dans une morphologie complexe d'un anévrisme réel de l'aorte thoracique dont la géométrie a été obtenue par CTA (Computed Tomography Angiography). Différentes études paramétriques ont été effectuées afin d'évaluer les facteurs de risque liés à la morphologie de l'anévrisme et au design du stent. Plus particulièrement, l'influence de la longueur de la zone de fixation proximale, de la valeur d'oversizing, de l'angulation du collet proximal et de l'état pathologique de la paroi aortique a été étudiée.

I.1. Modèle géométrique de l'anévrisme

Le modèle d'anévrisme aortique utilisé dans cette étude représente un cas réel et pathologique de l'aorte thoracique d'un patient atteint d'un anévrisme. Ce patient a été traite à Hôpital Cardio-Vasculaire et Pneumologique Louis Pradel de Bron. Les tranches planes obtenues des scanner micro CT sont importées dans Mimics (Materialise, Leuven, Belgium) afin de réaliser la segmentation et la reconstruction des images médicales en un modèle 3D très précis de l'anatomie du patient. Les images DICOM de l'anévrisme thoracique ont été traitées avec Mimics v15. La zone d'intérêt a été ensuite sélectionnée et les branches secondaires ont été supprimées.
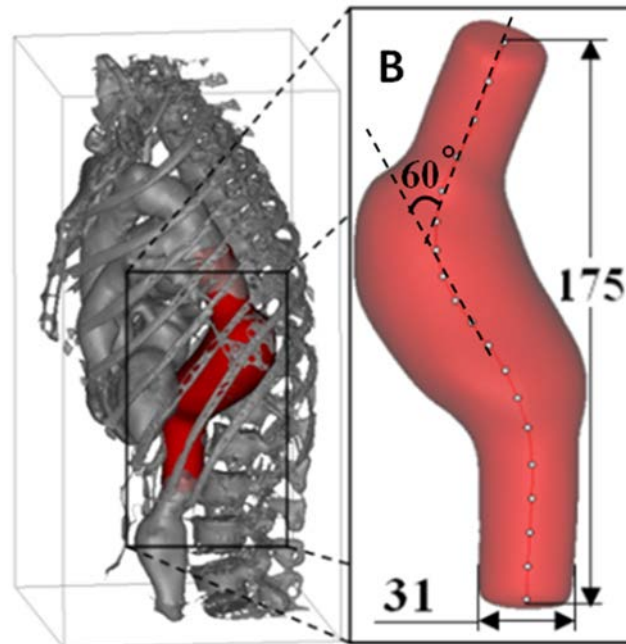
Reconstruction 3D d'un Anévrisme de l'Aorte Thoracique (AAT) avec extraction de la ligne centrale

I.2. Modèle éléments finis de l'artère

Toutes les simulations ont été effectuées avec le logiciel Abaqus/Explicit. Le modèle de comportement mécanique de l'aorte choisi est un comportement hyperélastique quasi-incompressible isotrope de type modèle de Mooney-Rivlin.

Le maillage en éléments finis de l'aorte a été effectué avec le logiciel Hypermesh afin d'être en mesure de réaliser une discrétisation en éléments héxaédriques. Plus précisément, l'élément utilisé est une brique à 8 nœuds à un point d'intégration avec contrôle des modes sabliers.

Des conditions aux limites ont été appliquées aux surfaces supérieure et inférieure de l'aorte afin de prendre en compte les effets des parties de l'aorte qui n'ont pas été modélisées et seuls les déplacements radiaux de ces surfaces sont autorisés. Une pression interne est appliquée sur la paroi vasculaire interne. En revanche l'interaction entre l'aorte et son environnement a été négligé.

I.3. Modèle de l'endoprothèses

L'endoprothèse commerciale utilisée pour ce patient était un modèle Talent Thoracic de Medtronic, stent en nitinol autoexpansible. Le flux sanguin n'étant pas modélisé, le tissu de l'endoprothèse ne le sera pas également car sa fonction n'est pas mécanique mais est d'assurer l'étanchéité de la prothèse. La géométrie du stent est générée à partir d'un algorithme de paramétrisation développé dans le cadre de ce travail, ce qui permettra d'étudier ensuite le design du stent en vue de son optimisation.

Une simulation réaliste du déploiement du stent nécessite une représentation précise de la géométrie réelle du stent. Or cette géométrie est inconnue et c'est pourquoi il est nécessaire de suivre le processus de fabrication qui permet d'obtenir le produit final expansé. Ce processus qui est modélisé inclus trois étapes : l'expansion, le formage et le recuit. Les éléments utilisés pour le maillage du stent sont également des éléments héxaédriques. Le modèle de comportement utilisé pour le nitinol est un modèle superélastique.
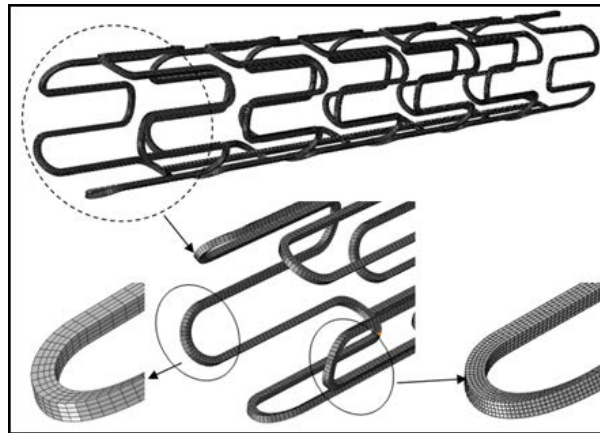
Géométrie et discrétisation par éléments finis héxaédriques du stent

1.4 Simulation numérique par la méthode des éléments finis du déploiement du stent

Du fait des nombreuses non-linéarités inhérentes au problème étudié (grandes déformations, non linéarités matérielles, problème de contact complexe…), l'utilisation d'une formulation dynamique explicite semble particulièrement adaptée à ce problème. Le logiciel commercial ABAQUS/Explicit 6.10 a donc été utilisé pour effectuer les simulations.

Les modèles de l'anévrisme et du stent présentés précédemment ont été combinés. Le cathéter a été modélisé par une surface rigide. Le cathéter impose la déformation au stent par utilisation de conditions aux limites adaptées. La ligne centrale du vaisseau est utilisée pour guider le positionnement du stent. À partir d'une configuration droite du stent, les déplacements nécessaires sont calculés à partir de la ligne centrale et de la forme de l'aorte. Un programme a été spécifiquement développé afin d'accomplir cette transformation du stent.

La méthode de gestion du contact utilisée dans ces simulations est une méthode de pénalisation et le modèle de frottement sélectionné est une loi classique de type Coulomb.
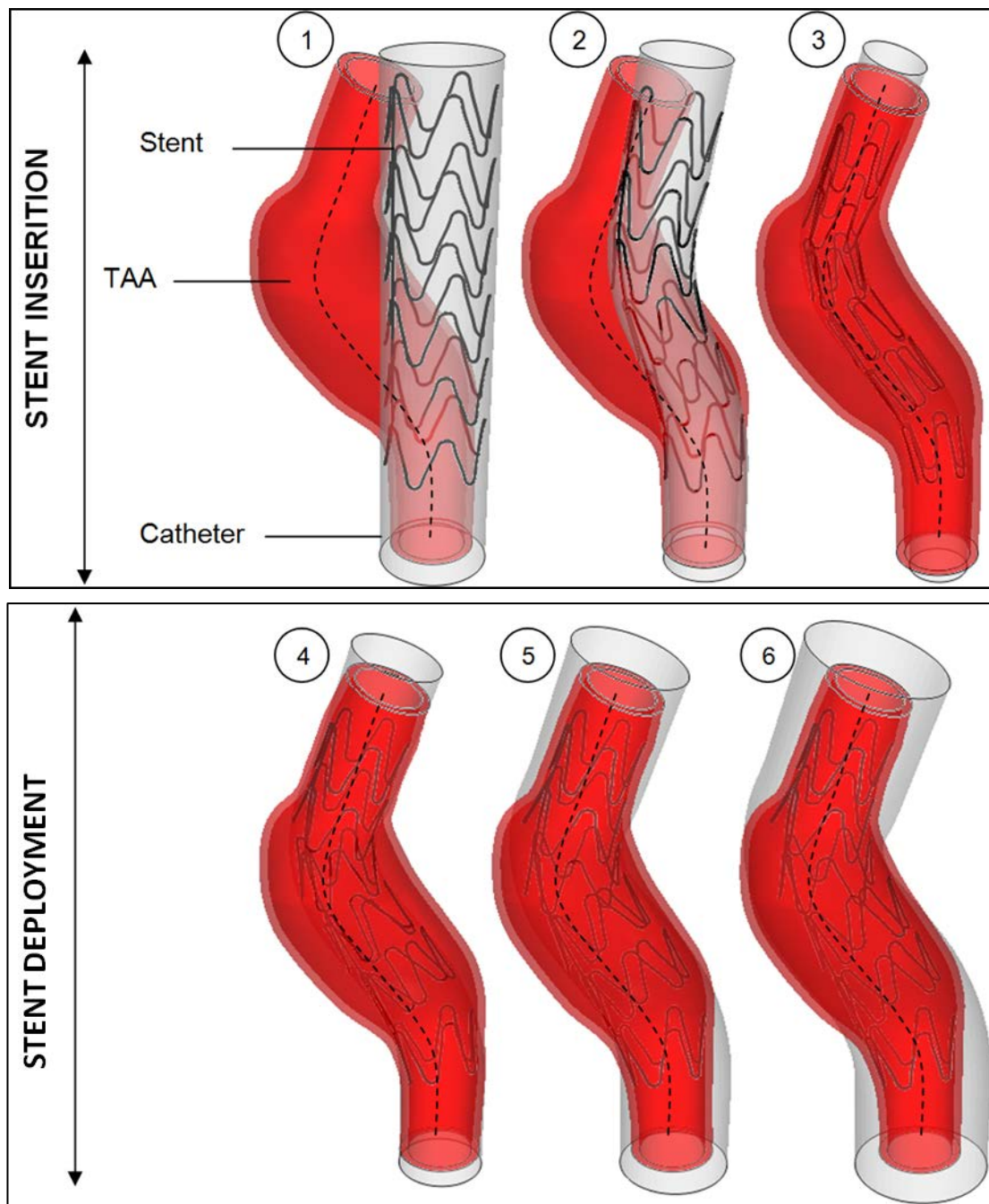
Simulation de la procédure de déploiement d'un stent dans un AAT

1. Étude de l'influence des longueurs des zones de fixations proximale et distale.

Trois simulations de déploiement de stent ont été effectuées pour trois longueurs de stent différentes et donc pour trois longueurs de zones de fixation proximale et distale différentes. Dans les trois cas, la valeur de l'oversizing était la même (15%), ainsi que la valeur du coefficient de frottement $\mu=0,05$, valeur choisie car elle représente des conditions critiques de contact. Le stent, dont la longueur de la zone de fixation est la plus faible – 18 mm – mais supérieure à la distance de sécurité critique clinique de 15 mm, subit une

migration de plus de 15 mm lors de son déploiement avec un contact hautement instable. Aucune migration n'est observé lors du largage des deux autres stents de longueur de zone de fixation respectivement de 21 mm et 23 mm, même dans des conditions critiques de contact (μ=0,05), et la stabilité du contact est nettement meilleur que dans le premier cas. D'autre part, dans le stent le plus court les contraintes présentes dans les parois artérielles sont plus élevées que dans celles des deux autres stents. Cette concentration de contraintes peut être à l'origine d'une re-sténose, particulièrement si le stent comprime une plaque d'athérome.
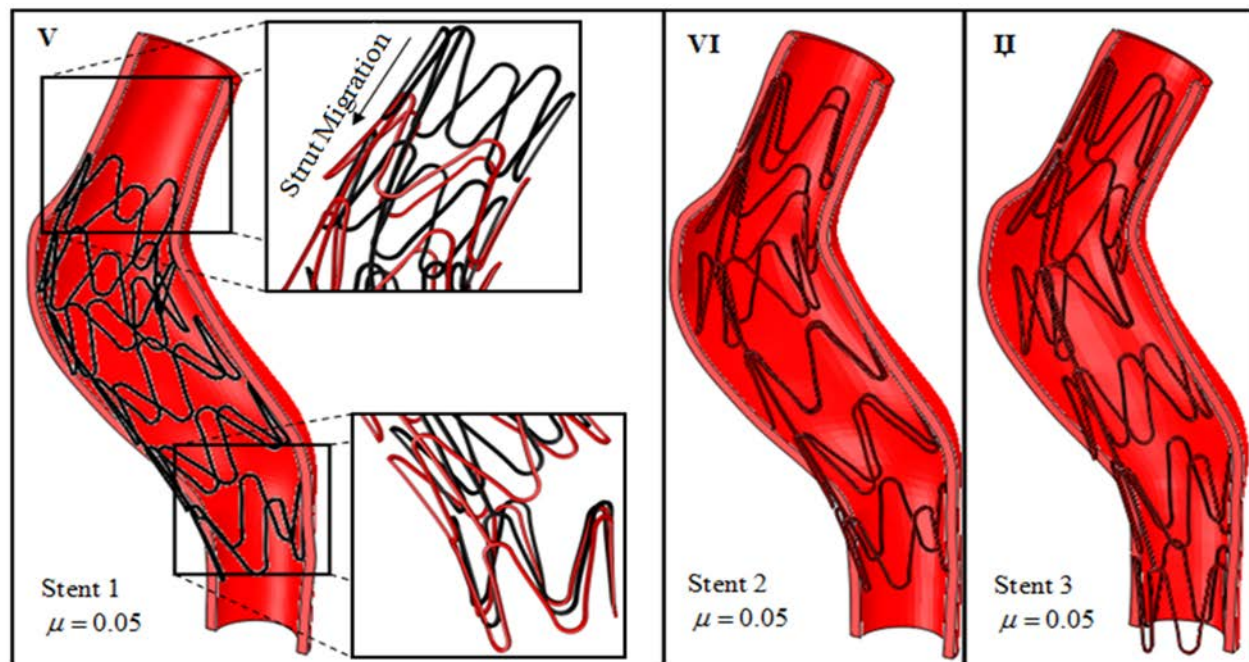
Influence des longueurs des zones de fixation proximale et distale sur la migration et sur la stabilité du déploiement

Ces résultats sont en accord avec les observations cliniques qui concluent qu'une longueur de zone de fixation proximale inférieure à 15 mm entraine un déploiement médiocre et difficile augmentant de manière drastique le risque d'apparition d'endofuites de type I et/ou de migration de l'endoprothèse. En revanche, la longueur de la zone de fixation distale possède une faible influence sur l'apparition de ces deux phénomènes, ce qui est également confirmé par les observations cliniques.

2. Influence de l'oversizing

L'oversizing est la différence entre le diamètre de l'aorte et celui du stent avant compression dans le cathéter. Différentes simulations ont été effectuées afin d'étudier l'influence de l'oversizing sur le déploiement du stent avec des valeurs variant entre 10 % et 25 %. Pour un stent court (longueur de zone de fixation distale de 15 mm) déployé dans un anévrisme avec une angulation du collet importante et des conditions critiques de contact (μ=0,05), une migration importante est observée pour un oversizing de 15 % (18 mm). Un oversizing de 20% permet alors de réduire significativement cette distance de migration (de 33 %) ainsi que les contraintes dans la paroi aortique. Dans les mêmes conditions de

déploiement mais pour un stent plus long, des valeurs d'oversizing de 10 %, 15 % et 20 % permettent d'obtenir un déploiement sans migration, le contact le plus stable étant obtenu pour une valeur de 20 %. Néanmoins l'oversizing ne peut pas être augmenté de manière inconsidérée. En effet, le déploiement d'un stent long avec un oversizing de 25 % dans une géométrie tortueuse entraine une déformation importante du stent et notamment une difformité excentrique de celui-ci dont l'extrémité proximale a tendance à se plier vers l'intérieur, ce qui diminue la surface de contact entre le stent et l'aorte. Par conséquent, une valeur excessive d'oversizing peut également être à l'origine d'apparition d'endofuites de type I et de migration, ce qui est en corrélation avec les observations cliniques.

3. Influence du coefficient de frottement

Le coefficient de frottement entre le stent et la paroi vasculaire dépend de la qualité pariétale de l'aorte, c'est-à-dire selon si le tissu est sain ou pathologique (présence de plaques d'athérome, de calcifications…). Une migration du stent lors de son déploiement avait été observée uniquement sur le stent le plus court pour un coefficient de frottement $\mu=0,05$. L'influence du coefficient de frottement a donc été étudiée uniquement pour ce stent et des simulations ont été effectuées pour trois valeurs du coefficient de frottement : $\mu=0,05$, $\mu=0,1$ et $\mu=0,5$. La distance de migration du stent lors de son déploiement diminue lorsque le coefficient de frottement augmente et devient nulle pour $\mu=0,5$. De plus, un coefficient de frottement élevé améliore considérablement la stabilité du contact proximal.

4. Influence de l'angulation du collet proximal

Les simulations précédentes ont été effectuées pour une morphologie patient-spécifique dont l'angulation du collet proximal de l'anévrisme était d'environ 60°. La gravité de l'angulation peut être classée comme étant soit légère ($< 40°$), soit modérée (comprise entre 40 et 59°), soit sévère ($> 60°$). Pour étudier l'influence de l'angulation du collet proximal, un modèle d'anévrisme de l'aorte idéalisé a été utilisé. Ce modèle possède les mêmes dimensions de longueurs et de diamètres des zones de fixation que le modèle réel. Seul le sac anévrismal a été reconstruit de manière à obtenir une angulation du collet proximal nulle. Les simulations ont été effectuées pour le stent court avec un oversizing de 15 % et un coefficient de frottement $\mu=0,05$. Pour une angulation de collet proximal nulle, aucune migration du stent a été observée lors du largage de celui-ci et la surface de contact ainsi que la stabilité du contact sont supérieures à ceux obtenus pour une angulation de 60°. Une angulation élevée augmente donc le risque d'apparition des endofuites de type I et de migration. Cependant, comme cela été montré précédemment, l'augmentation des longueurs de zones de fixation ou un oversizing adapté peuvent compenser les difficultés du déploiement du stent liées à une anatomie tortueuse, même si l'oversizing ne peut pas être augmenté de manière importante sans risque. Ainsi le niveau d'oversizing doit être choisi en fonction du niveau d'angulation du collet proximal.

5. Influence des propriétés hyperélastiques de l'aorte

Les constantes matériau utilisées dans cette étude pour le modèle hyperélastique sont issus d'essais expérimentaux uniaxial et biaxial de différents échantillons d'aorte humaine conservés dans une solution antibiotique avant les tests. Cependant ces conditions restent éloignées des conditions in-vivo et ne sont

pas patient-spécifique. Ces données ne permettent de représenter ni l'état de contrainte 3D, ni les contraintes résiduelles présentes dans la paroi aortique. C'est pourquoi des simulations ont été effectuées en modifiant les paramètres matériau, soit en les augmentant de 10 %, soit en les réduisant de 10 %. Il apparait que cette modification n'a pas d'influence significative sur la déformation de l'aorte et sur l'état de contraintes. En revanche l'augmentation des paramètres matériau de 10 % a entrainé une augmentation de la stabilité du contact.

6. Influence de la calcification de la paroi aortique

L'athérosclérose, qui est une dégénérescence de la paroi artérielle, est à l'origine de la plupart des anévrismes de l'aorte thoracique. La calcification est l'inclusion de dépôts calcaires durs dans la paroi artérielle. Les calcifications ou thrombus peuvent faire varier de manière significative le comportement biomécanique dans les zones de fixation et doivent être considérées comme un facteur important affectant la raideur de contact et la solidité à long terme de la paroi artérielle. De plus, les calcifications peuvent être une cause majeur de rupture du fait de la faible compliance et de la rigidité élevée de l'aorte calcifiée. Le risque d'apparition d'endofuites de type I proximales augmente alors si le collet contient des plaques irrégulières d'athérome. Il est donc important de prendre en compte deux aspects en cas de présence élevée de calcification : le risque de rupture du fait d'une rigidité importante et le risque d'apparition des endofuites. La qualité pariétale est obtenue à partir d'imagerie médicale, le niveau de gris pouvant être associé à un degré de calcification. Des simulations ont été effectuées en supposant soit que seul le sac anévrismal était calcifié, soit que toute l'aorte (sac anévrismal et collets) était calcifiée. Le matériau constituant les calcifications est supposé incompressible, isotrope et linéaire élastique. Les différentes simulations effectuées ne montrent pas d'influence de la présence des calcifications sur la migration lors du déploiement du stent. En revanche, une forte augmentation des contraintes dans la paroi aortique est observée et pourrait augmenter le risque de rupture de l'anévrisme. L'évaluation de ce risque nécessite une étude plus précise que le modèle présenté incluant des notions de mécanique de la rupture.

Chapitre 4

Les résultats numériques présentés dans le chapitre précédent ont montrés que, dans une morphologie de l'aorte réelle et complexe, il n'est pas toujours possible d'assurer le contact nécessaire entre le stent et la paroi aortique, c'est-à-dire d'obtenir une surface et une pression de contact suffisantes pour éviter les complications. Augmenter l'oversizing ou la longueur du stent permettent de prévenir la migration lors du déploiement mais ne permettent pas d'empêcher l'apparition des endofuites de type I. L'objectif de ce chapitre est de changer le design du stent non seulement pour éviter la migration du stent lors de son déploiement mais également pour renforcer le contact et en améliorer la stabilité.

Modifier le design du stent n'est pas une tâche aisée. En effet, alors que le stent doit être aussi flexible que possible dans une aorte très tortueuse, la raideur radiale doit être suffisamment élevée pour assurer le contact et résister aux force radiales compressives exercées par la vaisseau. D'autre part, la mesure des efforts nécessaires pour déplacer le stent après son largage est un indicateur efficace pour évaluer le risque de migration de l'endoprothèse. En effet si ces forces sont faibles, le risque est élevé. L'utilisation de crochets dans les zones de fixation conjugué à un oversizing suffisant sont les facteurs prépondérants permettant de limiter ce risque. Néanmoins, dans un collet proximal de diamètre élevé et fortement angulé, la présence des crochets n'est pas suffisante si les longueurs de fixation sont insuffisantes et l'oversizing

optimisé. En effet, un oversizing trop élevé peut également être à l'origine d'apparition de phénomènes d'endofuites et de migration.

Afin de pallier ces manques et d'augmenter la fiabilité des endoprothèses, nous proposons un nouveau type de stent pour lequel les valeurs d'oversizing sont variables sur sa longueur et plus précisément l'oversizing est plus important dans les zones de fixation. Ainsi l'anneau du stent situé à l'extrémité proximal et/ou celui situé à l'extrémité distale sont soumis à des valeurs d'oversizing de 20 % ou 25 %, le reste du stent subissant un oversizing de 15 %. Ces modifications ont été testées pour deux longueurs de stents : un stent court et un stent long.

Les résultats obtenus montrent que tous les nouveaux stents courts avec un oversizing plus élevé dans les zones proximale et distale ne subissent pas de migration lors du déploiement, bien que les conditions de contact soient critiques et l'angulation du collet élevé. Une migration inférieure à 10 mm est observée lorsque l'oversizing supplémentaire ne concerne que la zone proximale. De plus, la stabilité de contact est améliorée et les contraintes dans les parois artérielles réduites. Cette dernière observation est intéressante notamment dans le cas d'une aorte pathologique. En effet, la réduction de la pression sur des plaques d'athérome permet de limiter l'apparition de phénomènes de re-sténose. Un oversizing de 20 % dans les zones proximale et distale permet d'obtenir de résultats meilleurs que pour un oversizing de 25 % : le stent présente une bonne flexibilité et se déploie sans migration. De plus, les forces de cisaillement obtenues ne sont pas suffisamment élevées pour provoquer le déplacement du stent.

En revanche, pour le stent long, le comportement du stent optimisé ne diffère pas significativement du stent initial. D'autre part, une augmentation des contraintes dans la paroi de l'aorte est observée pour un oversizing de 25 % dans les zones proximale et distale. De plus, la raideur de contact dans la zone de fixation proximale est plus faible que pour le stent dont l'oversizing est uniforme sur la longueur et de 15 %, ce qui entraine une diminution de la surface de contact et un déploiement incomplet du second anneau dont l'oversizing est de 15 % contre 20 ou 25 % pour le premier anneau. Afin d'améliorer ces résultats, un nouveau stent est proposé possédant un oversizing plus élevé dans les deux premier anneaux de la zone proximale et dans le dernier anneau de la zone distale. Avec ce nouveau design, aucune migration n'est observée lors du déploiement du stent long. De plus, la raideur de contact est nettement améliorée.

Les résultats obtenus montrent clairement l'importance d'effectuer un oversizing supplémentaire aux extrémités du stent et notamment dans la partie proximale, notamment dans le cas d'un stent court. En effet, la flexibilité du stent est augmentée et les risques de migration à long terme sont diminués. L'oversizing de la partie distale semble également favorable car elle entraine une augmentation de la stabilité de contact et réduit le niveau de contrainte dans la partie proximale. De plus, les résultats obtenus sur le stent long ont montrés la nécessité d'appliquer l'augmentation de l'oversizing à tous les anneaux en contact avec la paroi artérielle, ce qui permet d'obtenir une meilleur raideur de contact, une meilleur flexibilité et une meilleure recouvrance superélastique.

Conclusion

Dans un contexte de vieillissement de la population, le traitement endovasculaire des anévrismes de l'aorte thoracique (AAT) a pris un essor considérable ces dernières années, constituant ainsi une alternative à la chirurgie ouverte. Il représente la seule option thérapeutique chez des patients présentant des comorbidités sévères et donc récusés pour une chirurgie traditionnelle. L'apparition des phénomènes d'endofuites de type I et de migration de l'endoprothèse peuvent conduire à une rupture de l'anévrisme due à la persistance d'un flux sanguin dans le sac anévrismal. Ces complications apparaissent plus fréquemment dans l'aorte thoracique que dans l'aorte abdominale du fait de l'angulation de la crosse aortique. Il est généralement admis que ces complications ont pour origine un contact défaillant entre le stent et la paroi artérielle dans les zones de fixation de la prothèse. Cette perte d'étanchéité peut être due à un mauvais positionnement ou un mauvais dimensionnement de l'endoprothèse, à une fatigue du matériau constituant le stent ou à une morphologie complexe de l'aorte. Les facteurs de risques généralement impliqués sont la présence d'une angulation sévère du collet de l'anévrisme et la présence de calcifications dans ce collet. L'objectif de ce travail était donc d'effectuer une étude numériques pour évaluer l'influence de ces paramètre biomécaniques sur l'apparition d'endofuites de type I et de migration de l'endoprothèse. Pour cela, un modèle 3D patient-spécifique a été construit à partir de techniques avancées d'imagerie médicale et des simulations éléments finis du déploiement de stents ont été réalisées avec le logiciel Abaqus/Explicit afin d'étudier les facteurs de risque associés aux endofuites de type I et de migration. Pour atteindre cet objectif, l'influence des longueurs des zones de fixation distale et proximale, du coefficient de frottement, de l'oversizing et de l'angulation a été étudiée. Le cas traité représentait un anévrisme de l'aorte thoracique avec une angulation sévère du collet proximale, ce type d'angulation étant connu pour jouer un rôle majeur dans la migration de l'endoprothèse. Les résultats obtenus lors des simulations sont en accord avec les observations cliniques.

Afin d'améliorer la flexibilité et la conformité du stent, la raideur et la stabilité de contact, un nouveau type de stent est proposé pour lequel l'oversizing est variable, et plus précisément l'oversizing est plus élevée dans les zones de contact avec les collets proximal et distal. L'objectif est d'améliorer la flexibilité du stent qui est un facteur déterminant pour la tenue de l'endoprothèse chez des patients présentant une aorte très tortueuse et très calcifiée. Les simulations réalisées ont permis de montrer que la stabilité et la qualité du contact étaient améliorées avec ce nouveau type de stent. Les complications de la procédure endovasculaire sont ainsi réduites de manière significative.

Perspectives

Dans ce travail, plusieurs simplifications ont été effectuées afin de réduire la complexité de la modélisation de la procédure endovasculaire complète. L'aorte a été reconstruite sans tenir compte de la présence de plaque d'athérome et de calcification alors que la présence de thrombus dans le collet proximal peut modifier la qualité de la fixation et générer des endofuites de type I. L'intégration de la qualité pariétale à partir de l'imagerie médicale est en cours de réalisation et sera pris en compte dans les simulations à venir.

D'autre part, la pré-contrainte présente dans la paroi artérielle n'a pas été prise en compte. Or elle peut modifier le comportement du vaisseau. Cette pré-contrainte devra être prise en compte si la mécanique de la rupture est intégrée dans le modèle car la contrainte est un indicateur de risque de rupture des anévrismes de l'aorte thoracique. Des modèles d'estimation de la pré-contrainte basés sur des méthodes inverses pourront être utilisés.

Le modèle isotrope hyperélastique avec épaisseur constante de la paroi utilisé pour l'aorte semble approprié à notre étude. Cependant des recherches récentes ont mis en évidence le caractère anisotrope de l'aorte et plusieurs modèles anisotropes hyperélastiques, qui ont été développés récemment, pourraient être utilisés dans notre approche. De plus le comportement mécanique réel des calcifications ou du thrombus reste, à l'heure actuelle, peu connu et demande donc à être étudié plus précisément afin d'être en mesure de l'inclure dans notre modélisation.

Une autre limitation de ce modèle est l'abstraction de l'environnement de l'aorte et de son interaction avec les tissus environnants. Cependant, dans le cadre de ce travail, cette approximation semble pertinente.

Enfin, les résultats obtenus avec les simulations éléments finis effectuées dans le cadre de ce travail peuvent être le point de départ à des calculs en dynamique des fluides. Cependant l'intégration de la modélisation du flux sanguin à ce modèle nécessite la prise en compte du tissu de l'endoprothèse. Les perturbations et turbulences de l'écoulement sanguin, les contraintes générées par le sang ainsi que la séparation de l'écoulement lors de la présence de plaque ou de thrombus ont un impact direct sur le comportement global de l'aorte et sur sa raideur. Le facteur hémodynamique peut être à l'origine d'une modification de la fixation de l'endoprothèse et peut également avoir des répercussions sur l'évolution de l'anévrisme et sur la progression de l'athérosclérose dans la paroi artérielle. Ces changements hémodynamiques peuvent compliquer la procédure endovasculaire. Dans cet optique, un projet vient de démarrer au LaMCoS dont l'objectif de modéliser la procédure endovasculaire complète en tenant compte des contraintes liées à l'écoulement sanguin en utilisant un couplage fluide-structure.

Table of Contents

TABLE OF FIGURES

LIST OF TABLES

General introduction

Aneurysm is a term used to describe a pathological condition that affects the aorta. It is considered the leading causes of death in the United States. This disease is often incidentally discovered when performing other tests. The aneurysm formation is a complex process involving many genetic variations (Upchurch & Criado, 2009). It is characterized by a weakness of the media layer resulting in destruction and weakness of all the layers of the aortic wall (Lumsden, et al., 2007) (Upchurch & Criado, 2009). This leads to reduced tensile strength resulting in mechanical dilatation followed by progressive enlargement from the pressure of blood flow and finally rupture (Lumsden, et al., 2007).

Two treatment strategies are available: classical surgery and Endovascular Aneurysm Repair (EVAR) procedures. The conventional open technique involves a major abdominal incision and replacement of the aorta with a prosthetic stent graft, i.e., large blood loss, high morbidity and mortality rates. Therefore, endovascular placement of nitinol stent grafts (EVAR) presents less invasive with many advantages, compared with conventional open surgical repair, including shorter duration in hospital and faster recovery (Lumsden, et al., 2007) (Hakaim, 2005). The ultimate objective for stent graft deployment is to exclude the aneurysmal sac from the blood circulation and prevent the growth the aneurysm.

However, the long-term durability of this new technology (EVAR) remains questionable (Veith & Baum, 2003). The main mechanical related-complications are migration, endoleak type I (Lumsden, et al., 2007) and stent folding or collapse (Wolf, et al., 2001). Migration means a separation of component parts of the device to be moved from its correct position more than (10mm). Consequently, this causes endoleak type I (Thomas & Sanchez, 2009). Endoleak type I may occur without migration or secondarily to migration. The most serious type of endoleak is proximal type Ia, which is defined by the persistent blood flow into the aneurysm sac that originates from the proximal attachment site wall. The flow leads to increased aneurysm expansion and potential rupture.

These adverse outcomes occur with high rates in thoracic stent grafts due to the stent misalignment (unconformity to tortuous aortic arch) and the inadequate area of contact between the stent graft and the aortic arch (Thompson, et al., 2007) (Hakaim, 2005) (Lumsden, et al., 2007).

Deploying the stent graft in a complex thoracic aortic morphology seems to be challenging. The tortuosity of the aorta is considered to be an important cause of early endoleak (Wolf, et al., 2001). In the aortic neck, the nitinol stent graft undergoes complex forces during and after deployment, (Albertini, et al., 2001) (Sternbergh, et al., 2004) (Fulton, et al., 2006) (Hakaim, 2005). Moreover, as the aortic neck angulation increases, the size of the endoleak increases. Therefore, clinical trial experiences have always shown the importance of the preoperative assessment of aortic morphology for success endovascular aneurysm repair (EVAR).

1

Apart from technical problems during stent graft deployment, the recent clinical investigations showed that endoleak type I and migration of nitinol stent graft are related to multiple-risk factors. These factors are represented in aortic neck morphology and stent graft design. They are: endograft under sizing (Thomas & Sanchez, 2009) (Thomas & Sanchez, 2009) (Bosman, et al., 2010), high drag forces due to severe angulation (Sternbergh, et al., 2004) (Albertini, et al., 2001) , insufficient length of proximal attachment site (Fulton, et al., 2006) (Zarins, et al., 2003), heavy or circumferential calcification and thrombus in the attachment zones (Lumsden, et al., 2007). Optimizing one factor does not guarantee the prevention of migration or endoleak type I. Thus, all of these multiple factors need to be investigated.

Computational mechanics techniques, in particular the finite element method, with merging computer-assisted tomography, technical advanced image-based techniques, can be applied to analyze the whole stenting procedure since their efficiency to solve governing differential equations and predict the overall (stent–aorta) biomechanical response.

Most of the numerical research using Computational Solid Mechanics (CSM) has focused on coronary stents deployment mechanisms (Auricchio, et al., 2011) (Conti, et al., 2011) (Beule, 2009) (Mortier, 2010) or an intracranial aneurysm (De Bock, et al., 2012). Authors (Demanget, et al., 2012) have demonstrated the efficiency of (CSM) by experimental validation of the numerical results (Demanget, et al., 2012) of two commercially stent grafts subjected to severe bending tests. More recently, investigations (Prasad, et al., 2013) have been conducted using (CSM) the previous complications, however, this work focused mainly on idealized vessel geometries and a non-real 3D geometric-connected stent behaviour without investigating the mechanism of proximal stent migration. Moreover, the stent collapse (Wolf, et al., 2001) or eccentric deformation in severe neck angulation has not yet examined. In another study by (Prasad, et al., 2011) aimed at investigating endoleak type Ⅲ, stent endograft were subjected to the displacement forces to investigate the contact stability at the intermodular junctions of a multi-component thoracic endograft in specific-patient (TAA). However, the contact stability at proximal and distal attachment sites was not evaluated as the interaction (aorta-stent graft) in these sites was considered perfect.

The main objective of this work was to investigate, based on 3D finite elements platform, the most important mentioned factors represented in morphological features and stent design which cause the migration, stent collapse and endoleak type I. Thus, approximate, three-dimensional stenting deployment simulations were performed in order to predict the mechanical response of the aorta and the deployed nitinol stent. Our interest is to evaluate the positional contact stability in the interaction area (stent-aortic wall) for different stent designs after complete device deployment. A specific- patient morphology of an aneurysmal thoracic aorta was modeled. Another idealized aorta model was reconstructed to study the effect of proximal neck angulation. Then, the numerical observations are used as a guide to optimize the stent design in order to strengthen the contact providing a compromise between flexibility and stiffness of the stent.

However, the complex stent structure, the irregular geometry of the aorta, the high nonlinearity, the complex contact problems and the many loading conditions make the modeling

2

of the complete physical problem a very challenging task. Therefore, simplification has been made with a compromise between the accuracy and objectivity of the models: the fluid is not included in this study.

The aorta tissue was reconstructed based on images of computed tomography angiography and treated as a nearly incompressible material based on a phenomenological continuum mechanics model of isotropic hyperelasticity. The nitinol stent was modeled as nonlinear superelastic in the frame of the continuum phenomenological model proposed by Ferdinand Auricchio, (Auricchio, et al., 1997). The FE simulation of stent deployment in the aorta was performed using a virtual catheter, applying appropriate boundary conditions on its nodes.

This thesis is composed of four chapters:

The chapter I provides a brief medical overview of aneurysm pathology and presents the advantages of endovascular aneurysm repair (EVAR) over open repair as a treatment option. Furthermore, it reviews the current clinical problems associated with (EVAR) technique.

The chapter Ⅱ provides the basic core of the stent and the aorta biomechanics supplying a detailed description of the equations and constitutive laws governing the description of a continuum, then a state of the art for computational approach, i.e., finite element stent modeling and stent design were supplied.

In chapter Ⅲ, we present the development procedure of the stent and specific-patient aorta geometries assigning the constitutive laws to the geometries. This chapter will identify using (FEA) the deployment quality of different parameterized stents inside the aortic wall in order to understand the most important design factors and morphological features of the aorta that may lead to stent migration, poor contact stiffness and stent collapse or folding.

Then, in chapter IV, based on the numerical results presented in chapter Ⅲ, we highlight developed new stent designs to prevent the occurred migration obtained from the previous results and improve the critical, conflicting, and required characteristics of the stent: (flexibility and stiffness). In this chapter, these characteristics were evaluated for several proposed stent designs.

From the total analysis of the obtained results, we were able to understand by numerical methods the mechanism of superelastic stent deployment in a patient-specific aneurysmal thoracic aorta and its complications represented in migration, stent folding and poor contact with the native aortic wall, the first cause of endoleak type I. This was used as starting point to optimize the stent design for a successful deployment procedure. The optimized stent results showed better contact stability to resist the migration. They also showed a considerable improvement of stent design requirements (flexibility and stiffness).

Future research perspectives and the ultimate goal will be to include the hemodynamic theory to adequately predict the effect of the physiological blood flow on the stent graft deployment in fluid structure interaction frame (FSI).

Chapter I
Medical and Technology Context

Aneurysm is the one of the most critical disease affected by a variety of pathological conditions. Ruptured Aneurysm can be fatal. Currently, 'Open-standard' repair surgery and 'endovascular-new' techniques (EVAR) are used to treat this disease. However, "Many clinical investigations have predicted that more than 80% of all vascular operation will be replaced by endovascular techniques (Hakaim, 2005), which is still in its further developments and long-term results validation.

This chapter will focus on the medical description of this pathology and present the advantage of (EVAR) compared with conventional open repair, followed by defining the most important mechanical-related complications of (EVAR).

Summery

I.1. Introduction

Vascular diseases represent a major cause of death in western countries. These diseases affect the heart and blood vessels. It includes many types of diseases. The following pathologies fall under the category of vascular diseases:

- Atherosclerosis: the build-up of fat and cholesterol deposits, called plaque, on the inside walls leading to the organ becoming clogged.
- Cardiovascular disease (CVD).
- Peripheral vascular disease (PVD): Commonly referred to as Peripheral Arterial Disease (PAD): like carotid artery disease (on either side of the neck) and renal artery disease, a result of atherosclerosis.
- Aortic Aneurysms: Thoracic Aortic Aneurysms (TAA) and Abdominal Aortic Aneurysms (AAA).

The arteries can be affected by a lot of pathological conditions. This study will focus on the aneurysm disease and more especially the Thoracic Aortic Aneurysms (TTA).

I.2. Aneurysm

I.2.1 Introduction

We all have a network of blood vessels called veins and arteries that carry blood to and from the heart to nourish every cell in the body. Healthy veins and arteries are strong and flexible and maintain their shape under the pressure of blood bombed by the heart.

The aorta is the largest blood vessel in the body. Its function is to carry blood rich in oxygen away from the heart and distribute it to the arteries supplying the entire body

Aneurysm is a term used to describe when the walls of the blood vessels become weak to balloon from the pressure of blood flow. The aneurysm can occur anywhere in the body, usually occurs in the Abdominal (AAA), Thoracic Aorta (TAA) and Iliac arteries. If left untreated, the aneurysm may rupture leading to death. The more we are getting in years and more the aortic aneurysm disease becomes expected. Unfortunately, aortic aneurysms are clinically silent. They are discovered incidentally when performing medical imaging tests for other disease processes. Improvements in detection are necessary to identify and treat aneurysms before their growth, and rupture (Upchurch & Criado, 2009).

Aneurysm is an enlargement or dilatation of the degenerated aorta. The aorta is made up of three layers, see (Ц.4.1): Intima (Endothelium layer), Media (composed of elastin and collagen) and adventitia (the external layer composed of connective tissues with elastin and collagen fibers). The elastin degradation is related to dilatation while a rupture of the wall is a result of collagen degradation (Lumsden, et al., 2007) (Upchurch & Criado, 2009) (Amplard, 2006). The aneurysmal pathology is characterized by an inveterate inflammation and destruction of the extracellular matrix which reshapes the wall layers and decrease the number of the smooth muscle cells. The smooth muscles are essential for production of extracellular matrix proteins. As the process of destruction increases, dilatation occurs. This leads to flow disturbances, changes in wall tension, and finally rupture (Lumsden, et al., 2007) (Figure I.2-1). This disease can be considered a multi-factorial disease with a significant genetic component (Upchurch & Criado, 2009).
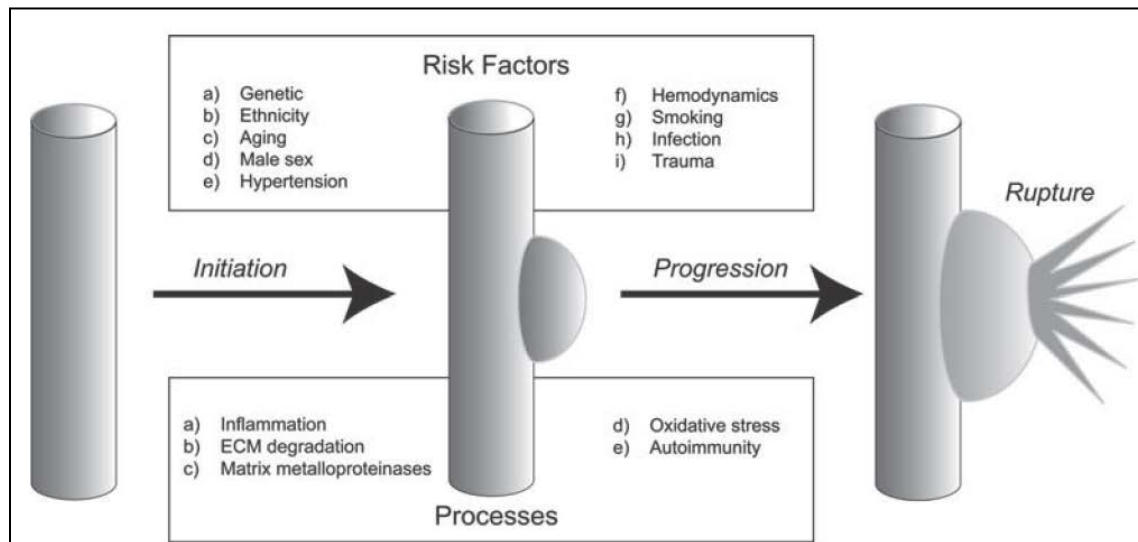
Figure I.2-1: Abdominal aortic Aneurysm (AAA), risk factors (above the arrows), biological
processes (below the arrows) observed in AAA formation, formation, growth, and rupture
are summarized (Upchurch & Criado, 2009)

Based on many research works, it is not fully understood, how (AAA) forms, grows, and ruptures. It is clear that this pathology is a complex multi-factorial disease with genetic and environmental risk factors (Upchurch & Criado, 2009). It needs many multi-factorial genetics studies to provide valuable information about the genetics of aneurysm (Upchurch & Criado, 2009). Rupture of aorta leads to death. Therefore, the detection of aortic aneurysms before the rupture is critical and a crucial issue. Typically, the critical diameter of the aneurysm is (5→5.5) cm. Beyond this value, degenerative changes predominate leading to mechanical failure and rupture. Until now, the aneurysm diameter is the best predictor of rupture. Studies have proved that the expansion rate is between 2.6 and 3.3 mm/year (Upchurch & Criado, 2009). A 3.5 cm (AAA) growing at 3.0 mm/year will exceed to 5.5 cm in less than 7 years (Figure I.2-2). This increase acceleration can be inhibited by pharmacological therapy to extend the time from detection at 3.5 cm to consideration for repair (>5.5) cm to 12 years (Upchurch & Criado, 2009).
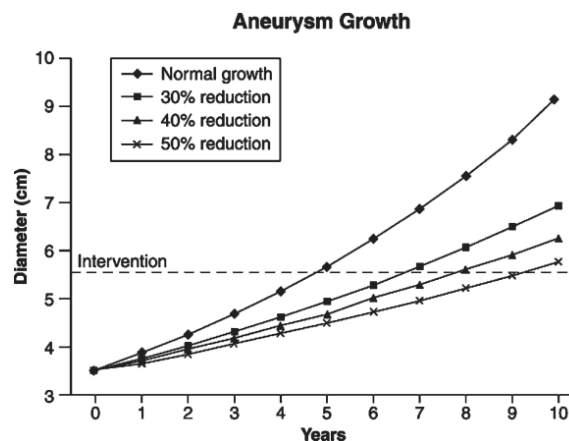
Figure I.2-2: Change in aneurysm diameter as a function of time. The other growth rates show the effects of a
medical therapy that inhibited growth by 30% (square markers), 40% (triangle markers), and 50% (x markers)
(Upchurch & Criado, 2009)

6

I.2.2 Medical Treatment
I.2.2.1 Classical surgical procedure

   Apart from the medical management of small aortic abdominal aortic aneurysms, we have two techniques of treatment: classical surgical and endovascular procedures.
The first procedure is surgical with large incisions made in front of the (Figure I.2-3). The surgeon cuts and devises the muscles and moves the internal organs out of the way to gain access to the aorta inside the abdominal cavity. The aneurysm is opened, and any damaged tissues are removed. The graft is then sewn and placed to the healthy aorta. The remaining aneurysm tissues are sewn around the graft to protect it. Once this is completed, the blood flow is restored to the aorta. The organs are moved back into place. The muscles are repaired, and the incision is closed. Most patients require about 3 months, making of all recovery. The graft can be made from a strong synthetic tube that is similar in size to the healthy aorta. This technique involves a heavy intervention, large blood loss and many preoperative complications. Moreover, not all patients can tolerate this complicated operation. This technique was the traditional, primary, effective and durable one for many patients (Amplard, 2006) (Upchurch & Criado, 2009).
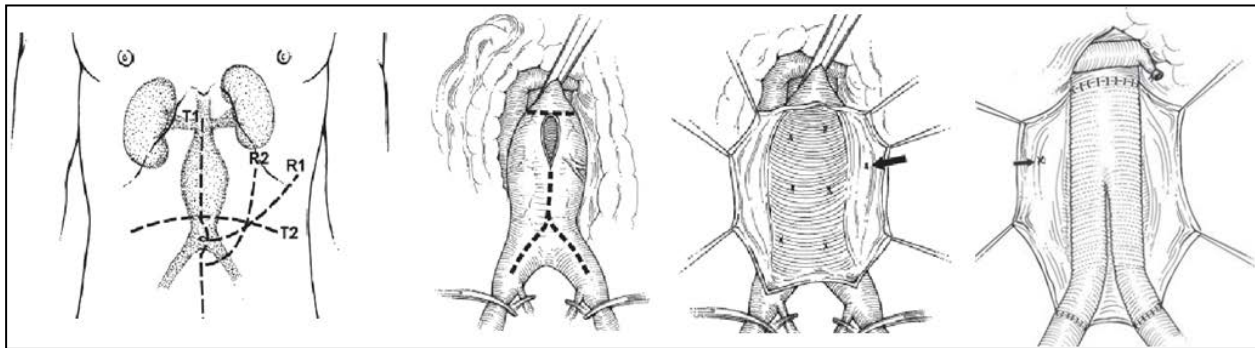
Figure I.2-3: Classical surgical procedure (Upchurch & Criado, 2009)

I.2.2.2 Endo-vascular procedure

   As an alternative to conventional open surgery, the second technique proposes a less invasive form of treatments. This procedure was initially described by Dr.Parodi and Dr.Palmaz, by introducing the concept of endovascular stent graft. This technique is called Endovascular Aneurysm Repair (EVAR) (Figure I.2-4). The endovascular stent graft is a device used to seal off the aneurysm from inside the aorta. The stent graft provides a new pathway for blood flow through the region of the aneurysm. The endovascular graft components come in different sizes to fit different anatomy.
Before endovascular repair, the surgeon will make diagnostic measurements for selecting the proper size endovascular graft to fit the anatomy. Two small incisions are made in the groin area. Using X ray guidance, the surgeon will insert the delivery catheter into the aorta and carefully position the track portions of endovascular stent graft in the health regions after the aneurysm area. When the surgeon determines that track components are in the proper positions, the compressed stent graft is released and expanded to the diameter of the aorta. The delivery catheter is then removed. This procedure is repeated for the other leg to replace contralateral leg components in the (AAA). The aneurysm will be isolated by the endovascular graft preventing rupture.

7

The aneurysm sac will be excluded decreasing the pressure stresses on the wall of the aneurysmal sac. This technique introduces less surgical time, less blood loss, less need for intensive care and shorter duration stay in the hospital. According to these positive aspects, this treatment strategy has undergone a dramatic technological evolution, which increased the public acceptance of this therapy, beside that the availability of multiple devices approved in the USA by the Food and Drug Administration (FDA) (Lumsden, et al., 2007) (Hakaim, 2005).
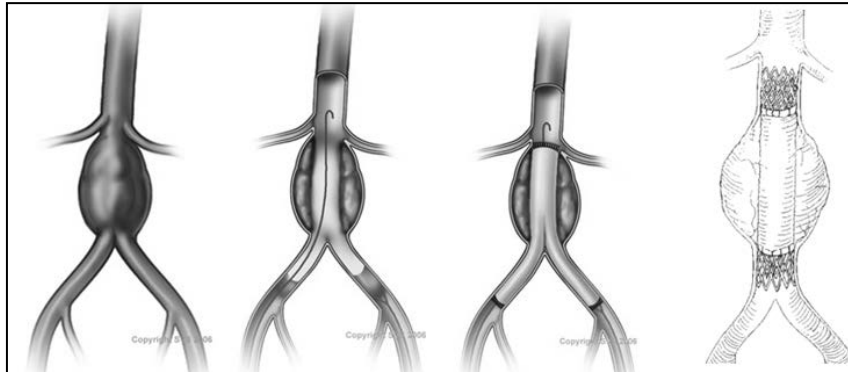
Figure I.2-4: Endovascular stent graft procedure for (AAA)

I.2.3 The complications of endo-vascular procedure

Despite presenting numerous advantages, this technique is not yet fully validated. The long-term success of (EVAR) is not definitively established because data on long-term of patients undergoing EVAR are not yet available (Hakaim, 2005) (Amplard, 2006) (Upchurch & Criado, 2009)). Moreover, it highly depends on the appropriate patient selection and post-procedural device surveillance (Lumsden, et al., 2007). This treatment strategy has to undergo many criteria, including aneurysm growth rate, the risk of rupture and the patient life expectancy, besides to the anatomical criteria which can exclude some patients from EVAR. These criteria are represented by the length, the diameter and the angulation of the proximal neck
These factors are critical to define the success of (AAA) and (TAA) so that all (EVAR) patients need careful, long-term follow up surveillance and treatment to prevent the rupture and death (Upchurch & Criado, 2009) (Hakaim, 2005) (Lumsden, et al., 2007). The primary criterion after EVAR includes: prevention of rupture and death from rupture (Hakaim, 2005). The followed secondary criterion concerns the mid and long-term durability and ultimate performance of the stent graft which remains questionable (Veith & Baum, 2003). The main mechanical related-problems of endovascular aneurysm repair are migration and endoleak type Ia (Lumsden, et al., 2007).

I.2.3.1 Endoleak/Migration

The migration is defined by the movement of the endograft more than 10mm (Figure I.2-5). This may lead to endoleak type I. An endoleak is defined as the presence of blood flow outside the lumen of the endoluminal graft, but within the aneurysm sac or adjacent vascular segment being treated by the graft, which indicates incomplete exclusion of the aneurysm (Hakaim, 2005).
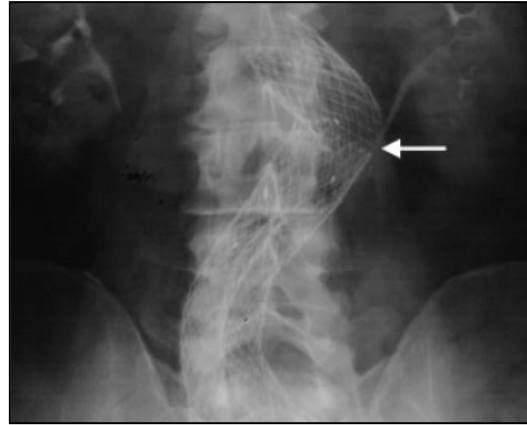
Figure I.2-5: Inferior migration of the AneuRx (Medtronic, Inc.) main body, which resulted in a delayed endoleak. Arrow indicates migration of main body from aortic cuff extension (Hakaim, 2005)

According to endoleak origin and its time detection (Figure I.2-6) Type I endoleak (graft related endoleak or attachment site endoleak): this occurs when there is no complete and effective seal between the endograft ends (proximal or distal graft aspects) and the wall of the blood vessel.

− Type Ⅱ endoleak (retrograde or non-graft related endoleak): This occurs when retrograde blood flows into the aneurysm sac from patent and lumbar arteries. In this case, there is a complete seal around the graft attachment zones and the endoleak is not related to the graft.

− Type Ⅲ (fabric defect or modular disconnection): This occurs when there is no adequate connection between the components of modular graft and the leakage occurs through a defect in the graft fabric or the segment of modular graft.

− Type IV (graft porosity): The blood leakage occurs due to the inherent porosity of the device fabric.
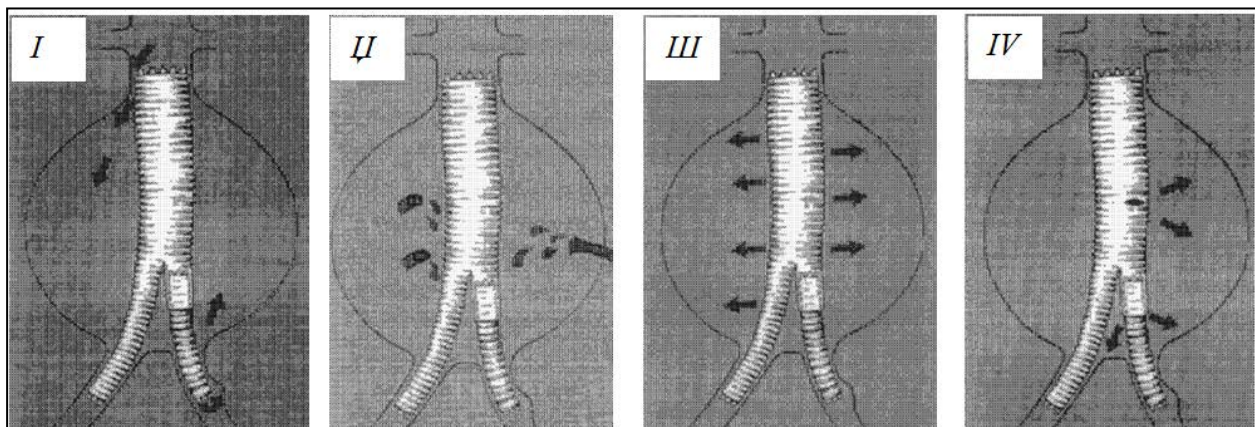
Figure I.2-6: Types of endoleak (Veith & Baum, 2003)

9

Table I.2-1 Classification for endoleaks and endotension (Veith & Baum, 2003)	
Endoleak type	*Source of blood flow*
I*	Attachment site
a	Proximal end of stent graft
b	Distal end of stent graft
c	Iliac occluder
II	Branch vessel
a	Simple or to-and-fro (from 1 patent branch)
b	Complex or flow-through (2 or more patent branches)
III*	Stent graft defect
a	Modular junctional leak
b	Fabric disruption (i.e., hole)
	Minor (<2 mm; e.g., suture hole)
	Major (≥2 mm)
IV	Stent graft fabric porosity

I.2.3.2 Endotension

The endotension or the intra sac pressure is defined as the presence of increased pressure within the aneurysm sac with no evidence of leak or blood flow outside the stent graft (Hakaim, 2005) (Veith & Baum, 2003). It should be noted that the expansion of the aneurysmal sac does not depend only on the pressure, but may be a result of continued accumulation of fluid or other materials. This term, therefore, describes the pressure within the excluded aneurysm sac (Veith & Baum, 2003).

I.2.4 Medical treatment of endovascular complications

Endoleak type I is the most dangerous and worrisome because it allows a direct blood flow into the aneurysm sac. The flow will exert a pressure force on the aortic wall. Particularly, proximal type I is directly associated with the rupture and stent migration (Hakaim, 2005). The standard medical method for treating type I is to be handled directly by securing the attachment site with angioplasty balloons, stents or stent graft extensions (Veith & Baum, 2003). Larger diameter of the stent graft at the proximal and the distal attachment site is a very effective treatment option. Type 1 primary and secondary endoleaks occurs as a result of anatomical complexity or inadequate patient selection and technical aspects errors of endograft implantation.

Primary proximal type I endoleak and migration are often a result of the following reasons (Gilbert R. Upchurch Jr et al., 2009):
1. Complex anatomy of aorta:
 − Severe neck angulations (>50) or short necks (<15mm) (Figure I.2-7)
 − Large diameters of the aortic neck (>30mm)
2. The inferior stent graft characteristic, e.g., a poor proximal fixation, material fatigue), graft limb thrombosis and the presence of calcification within the aortic neck.
3. **Kinking** stent graft migration and stent fracture.
Secondary (delayed) Type 1 endoleak is unknown, but its occurrence decreased with the newer generation of stent grafts.

10

Proximal and distal stent graft fixation is a very important criterion to get a successful treatment. This provides a hemostatic seal preventing the leakage of blood and guarantees a complete exclusion of the aneurysm (Veith & Baum, 2003) (Hakaim, 2005).

A: Proximal implantation site
B: 1 cm from proximal implantation site.
C: 2 cm from proximal implantation site.
D: Aneurysm
G: Distal implantation site.
H: Right common iliac
N: Distal neck, distance from aneurysm to celiac axis
O: Total treatment length.
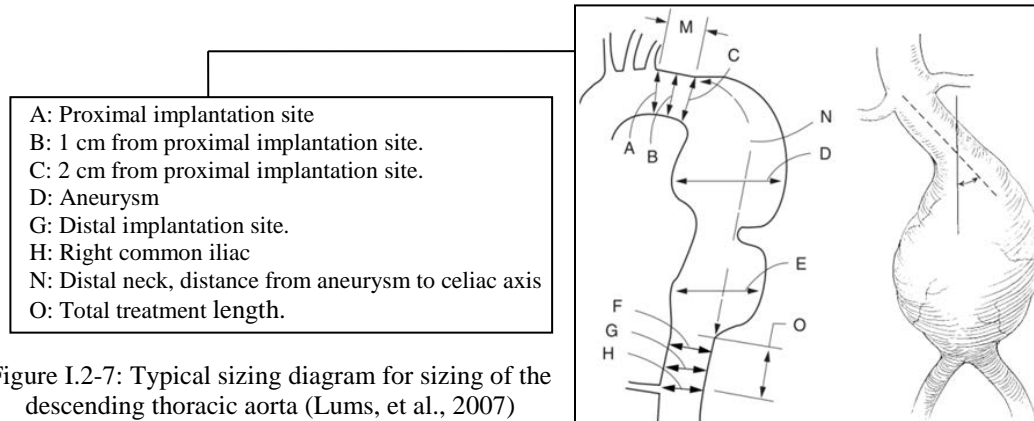
Figure I.2-7: Typical sizing diagram for sizing of the descending thoracic aorta (Lums, et al., 2007)

The (*EUROSTAR)* research showed that increasing the diameter of the stent graft (oversizing) to 20% relative to the aortic diameter will decrease the possibility of endoleak. Generally, oversizing from 10% to 15% is recommended for nitinol self-expanding stent grafts. Oversizing value can be extended until 20-25% in some cases (Lumsden, et al., 2007) (Hakaim, 2005) as the case in the vessels with diameters > 16 mm. (Thompson, et al., 2007). Stent graft oversizing will increase the radial forces of the stent graft against the wall of the aorta in order to have an optimal contact and provide a homeostatic seal between them (Veith & Baum, 2003) (Hakaim, 2005) (Lumsden, et al., 2007). However, excessive oversizing may lead to stent graft folding and followed by a proximal endoleak type I. Endoleak is often a result of failure of patient selection, device selection or technical problems (Veith & Baum, 2003) (Hakaim, 2005).

The effect of the device oversizing (<30% vs. >30%) on AAA sac behavior at 12 months has been investigated by (Sternbergh, et al., 2002). Using Zenith (AAA) endovascular graft, device migration and endoleaks were zero when the oversizing value was <30%, however, oversizing of >30% was associated with an increased rate of device migration at 12 months and with a negative effect on late (AAA) sac changes (Sternbergh, et al., 2002) (Figure I.2-8)
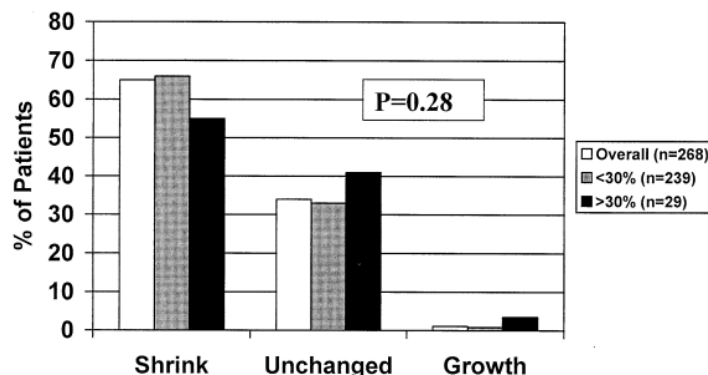
Figure I.2-8: Effect of device oversizing (<30% vs. >30%) on AAA sac behavior at 12 months. AAA shrinkage (shrink) was considered >5 mm reduction, unchanged was -5 to +5 mm change, and growth was >5 mm increase in size (Sternbergh, et al., 2004)

11

Oversizing more than 30% results in folding and poor barb penetration of the stent graft and can lead to low deployment attachment strength (Figure I.2-9). This was investigated in vitro by (Kratzberg, et al., 2009). The stent grafts were deployed into a synthetic aortic aneurysm phantom under realistic flow conditions. All the information about the attachment characteristics was documented, such as the graft apposition, the number of the penetrated barbs and the penetration depth (Kratzberg, et al., 2009).

(a) *(b)*
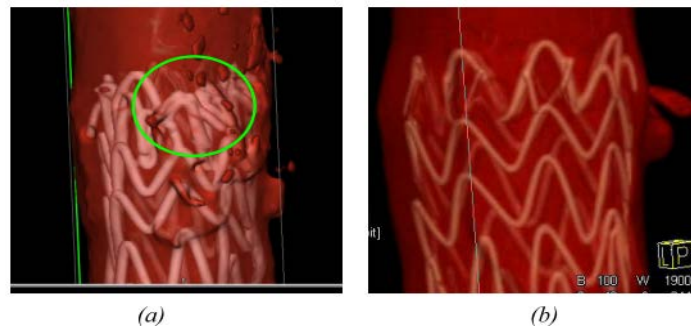
Figure I.2-9: The folding/collapsing apparent in EVGs with graft oversizing >30% (a) but not for 9% (b). The location of folding is highlighted with a green circle in the left image (Kratzberg, et al., 2009)

Migration has also been related to a short proximal fixation length (Zarins, et al., 2003). The study highlights the effect of the technical aspects of (stent-graft) deployment on migration (Figure I.2-10)
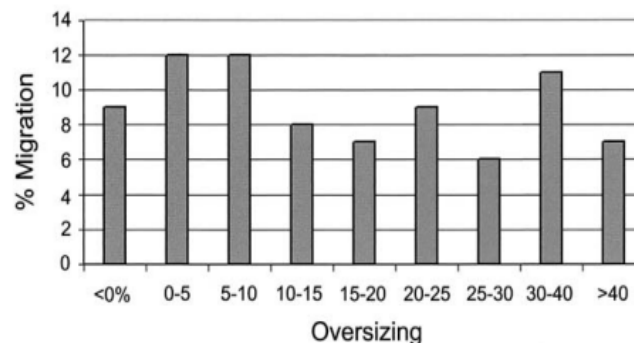
Figure I.2-10 : Migration and stent graft oversizing (Zarins, et al., 2003)

(Figure I.2-11) in reference (Hakaim, 2005) describes the detailed medical management of proximal endoleak type I. The ideal neck for EVAR should be less than 30 mm in diameter, and be at least 15 mm long as a proximal and distal part connected with the aorta. The differences in EVAR graft design (Figure I.2-11) can affect on the proximal fixation strength. (Bosman, et al., 2010) proved experimentally that the proximal binding of the Anaconda stent graft (B) was greater than Excluder (A) and the Endurant (c) at short necks of 10 and 15 mm (Figure I.2-12). Most importantly, there was a significant decrease of proximal binding for all the stent grafts, when decreasing the proximal length from (15) mm to (10) mm (Figure I.2-12) (Figure I.2-13)

12
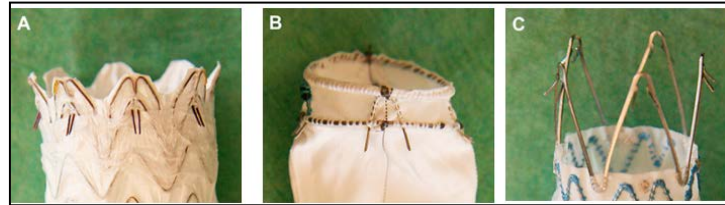
Figure I.2-11: The experimented endografts A. Gore Excluder, B. Vascutek Anaconda and C. Medtronic Endurant (Bosman, et al., 2010)
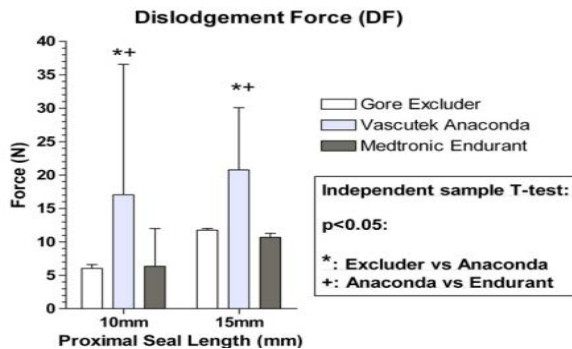
Figure I.2-12 : (design effect): forces needed to dislodge the different kinds of stent grafts from the aorta (Bosman, et al., 2010)
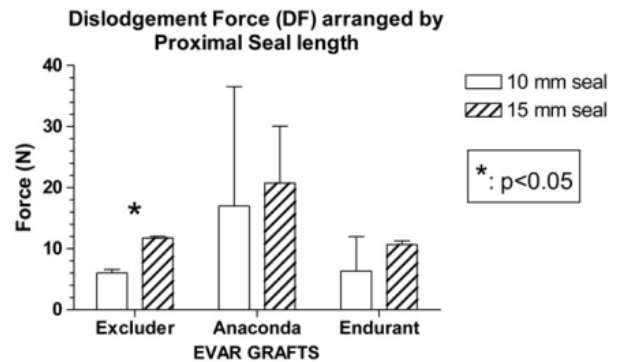
Figure I.2-13 : Influence of decreasing the proximal seal length on dislodgement force of the different grafts (Bosman, et al., 2010)

I.3. Types of aneurysms

According to the aneurysm position, it can be divided into three types: (Lumsden, et al., 2007) (Thompson, et al., 2007):

1. Thoracic Aortic Aneurysm (TAA): ascending and descending aneurysm (and their classification (Lumsden, et al., 2007) (Thompson, et al., 2007).
2. Abdominal Aortic Aneurysm (Figure I.3-1)
3. Thoroaco-Abdominal Aortic Aneurysm (TAAA) and their classification.

Thoracic aneurysm occurs in the thoracic part of the aorta and constitutes about 20% of all aortic aneurysms. It may occur in one or more segments of the thoracic aorta, including the ascending aorta, the arch, and the descending thoracic aorta (Lumsden, et al., 2007). The aneurysm can also be secular or fusiform aneurysm.
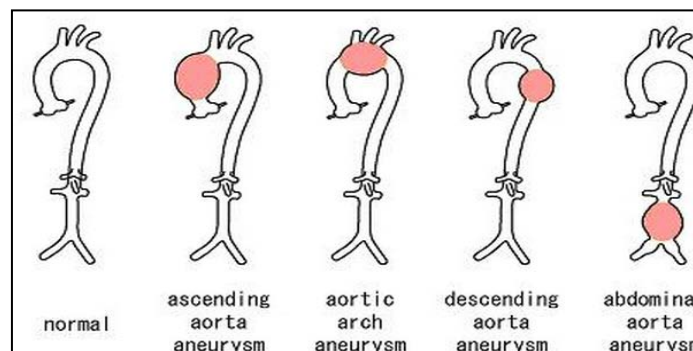
Figure I.3-1 : Various aortic aneurysms

13

I.4. Commercially available endovascular stent grafts for aneurysm treatment

Stent technologies have undergone rapid evolution. The majority of stents in use today are composed of balloon-expandable 316L stainless steel or nitinol mesh tubes. The choice of the stent is based on several factors. Medically, these factors are the characteristics of a given pathological case, such as its diameter, length, location, and the experience of the interventional cardiologist with a particular stent.

Any of approved stent graft devices has essentially three components. Everyone has a special function to get the ultimate target of the device.

These components are:

1. Support frame
  – **Support spring of stents (with or without)**: Self expanding nitinol spring or balloon expanding stainless steel part designed to provide an optimal contact and adequate radial pressure against to the wall of the aorta.
  – **Connect bar**: The primary frame parts of (SX) or (BX) stent connecting bars are integrated to provide a longitudinal support along the entire length of the stent graft. The connecting bar was designed to: (1) resist twisting or buckling of the graft, (2) eliminate foreshortening by maintaining a fixed length with proper orientation, (3) straighten anatomical curvature (4) prevent kinking in tortuous vessels. Tubes graft could have one or two connecting bars (bifurcated graft) (Hakaim, 2005).

2. Fabric covering: Often made by Polyethylene Tereph-Thalate (PET) to have a better tensile strength and wear resistance.

3. Sutures: Each stent ring is sewn individually to the graft fabric to prevent any micro movement of the stent relative to the graft material.
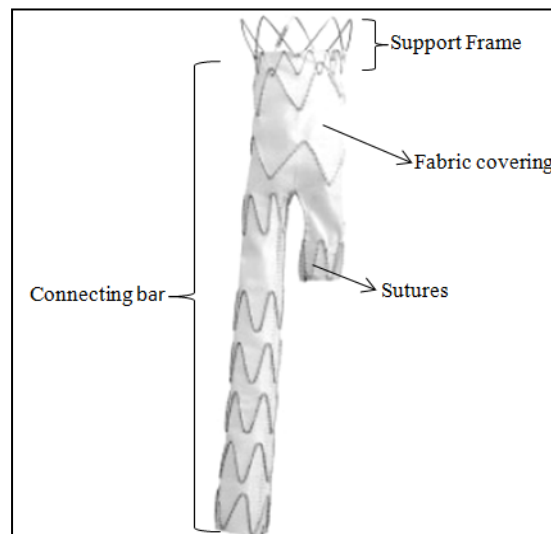
Figure I.4-1 : Main parts of stent graft (Hakaim, 2005)

I.4.1 EVAR stent grafts for (AAA)

Since the first device used in (EVAR) was in 1991, many of stent grafts had been developed, and five of them have received the US Food and drug Administration (FDA) approval. There are distinct limitations for every device, and there is no one that is totally perfect. Therefore, there are all under development and modifications. The commercial stent grafts for (AAA) are: (Hakaim, 2005) (Figure I.4-2)

− Ancure (Guidant Corp., Menlo Park, CA) (A)

− AneuRx (Medtronic, Inc., Minneapolis, MN) (B)

− Excluder (W.L. Gore and Associates, Inc, Flagstaff, AZ) (C).

− Zenith (Cook, Inc., Bloomington, IN) (D).

− PowerLink (Endologix, Inc., Irvine, CA). The Ancure device is no longer FDA approved because of commercial reasons (E).

− Lifepath AAA bifurcated graft system (F).

− Talent LPS AAA stent grafts (G).
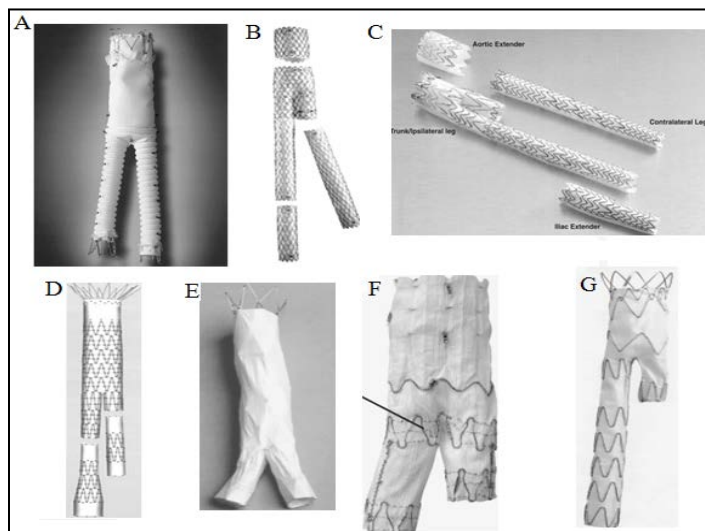
Figure I.4-2 : Commercial stent grafts for (AAA) (Hakaim, 2005)

Table I.4-1: Characteristics of commercially available bifurcated devices (Hakaim, 2005)				
Characteristic	*AneuRx**	*Excluder*[†]	*Zenith*[‡]	*PowerLink*[§]
Maximal device diameter, mm				
Proximal	28	28.5	32	28
Distal	16	14.5–20	22	20[‖]
Introducer sheath diameter, French				
Main body	21	18	18–20	21
Contralateral	16	12	14–16	12
Minimal proximal neck length, mm	15	15	15	15
Minimal iliac attachment site length, mm	10	10	14	15

Table I.4-2: Algorithm for selection of endovascular devices according to the diameter of the proximal neck of the aorta (Hakaim, 2005)

Device	Proximal neck diameter, mm		
	≤25	>25–28	>28–32
AneuRx[†]	Yes	–	–
Excluder[‡]	Yes	–	–
Talent[†]	Yes	Yes	Yes
Zenith[§]	Yes	Yes	–
PowerLink[ǁ]	Yes	–	–

I.4.2 EVAR stent grafts for (TAA)

In 1998, the core excluder was the first device used and approved by (FDA) in treatment of descending Thoracic Aortic Aneurysms (TAAs). After 2005, these devices got the (FDA) approval to treat (TAAs) (Figure I.4-3)
− The Talent thoracic and its evolution (valiant) endograft (Medtronic AVE, Santa Rosa, Calif) (A).
− Gore TAG endograft, the safe and effective of the TAG device (B).
− Cook TX2 endograft (Cook, Bloomington) (C).
− Relay TM thoracic stent graft (D).
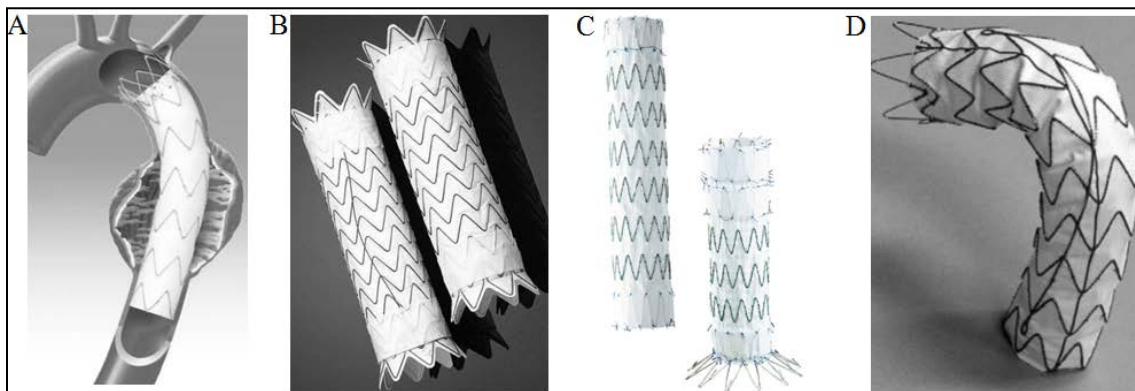
Figure I.4-3 : Stent graft devises for (TAA) (Lyden, 2010)

The devices require a proximal aortic neck length of at least 15 mm, except the Talent device, which requires at least 10 mm (Hakaim, 2005). The success of (TTA) as (AAA) is always related to patient selection criteria and governed by a number of factors like getting a detailed axial imaging with multi-planar reconstruction capabilities, planning and sizing for thoracic endovascular procedures. Some important factors (Lumsden, et al., 2007) are:
− Preoperative assessment.
− Preoperative imaging.
− Angiographic imaging.
− Evaluation of the risks of (EVAR) based on anatomical criteria explained in the top.
− Aortic neck characteristics both proximally and distally.

16

I.5. Conclusion

Biomaterials like stent grafts play a critical role to repair weakened vessels. However, many mid-long-term complications have been observed, especially in the thoracic aorta. These complications undergone a lot of research in order to improve existing devices and develop a new stent graft using engineering and medical techniques. From an engineering standpoint, this needs understanding the vessel, blood vessel, stent grafts mechanics and stent graft-vessel contact behaviour, i.e., understanding the biomechanical system behavior. Thus, we need integrative models that can explain these mechanical responses. This is the biomechanics of stent/aorta and the stent modeling.

Chapter II : Biomechanics of Stent/Aorta and Stent Modeling

It does not to be a trivial task to simulate, by numerical methods, the overall and complete stenting procedure. The complexity is represented in the high nonlinearity of the behaviour of the aorta and the nitinol super-elastic material in addition to the complex contact problems and large deformation. Therefore, several approximations of stenting procedure would be important. The present chapter serves to understand the notion of biomechanics and the macroscopic mechanical behaviour of biological tissues and stent, followed by a review of the computational methods used in biomechanics and stent modeling. Then, this introduction is applied to highlight the continuum mechanics of aorta supplying a state of the art on finite element modeling and design of nitinol stents.

Summery

II.1. Biomedical engineering approaches for treatment

Biomedical engineering (BME) applies many fields of engineering principles to understand, modify, or control biological systems, i.e., human and animal (Enderle, et al., 2005). (BME) covers many different medical applications (Figure II.1-1). It needs many different branches of education and connects engineering and physical sciences to biological science and medicine. From a medical point of view, large efforts have been made to perform the optimal treatment. However, these pure medical studies depend almost on the experience of medicine and the statistics made from experimental studies. As for the design of the stent grafts and the stent material effects, the biomechanics and its effects on the aortic wall in a long time term are challenging for medicines. The engineering aspect became very important and still necessary to support the medical studies. This cooperation between them is the essential factor of treatment success. Thus, in (BME) optimal and extensive communication is required between the potential user (the clinician) and the developer (the engineer) to build new medical devices.
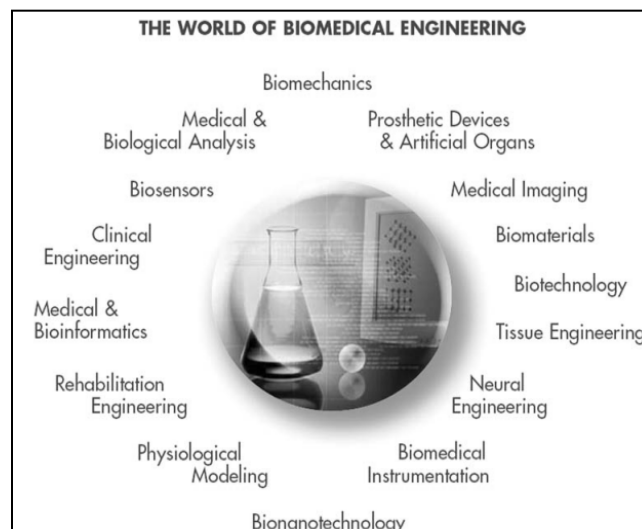
Figure II.1-1: The world of biomedical engineering (John D. Enderle et al, 2005)

In order to develop and use a medical device like stent, many different phases are necessary from 'idea' to 'clinical application' (Figure II.1-2). In the phase 'idea', and in order to build a medical device, new concepts and suggestions are developed, and an extensive communication is needed between among the engineers of different backgrounds; biomechanics, material sciences and electrical engineering. Then, new test set-ups have to be developed and built to test the functionality of these prototypes (Meyers & Chawla, 2009). Then, in the biological evaluation phase, a number of biological tests are needed to test the biological performance. In this phase communication between engineers, biologists, veterinary surgeons or clinicians is needed.

When the technical requirements of the academic university are met, a small series of a prototype is needed for animal studies to obtain more perception into the functioning of the human body. At this stage, the university must decide when they want to transfer the developed prototype to the industry. After that, the industry should develop its industrial prototypes using its own manufacturing techniques to reconstruct a safe and low-cost product (Rakhorst & Ploeg, 2007) (Ratner, et al., 2004) (Figure II.1-2) (Figure II.1-3)
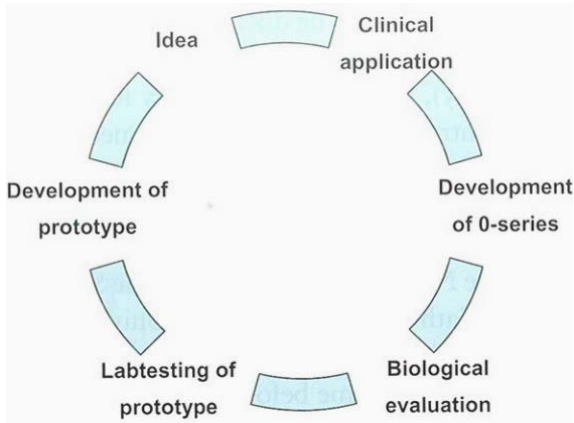
Figure II.1-2: Different phases of the development of a medical devise, from idea to clinical application. The curved blocks resemble the communication barriers that have to be overcome in order to realize the following product phase (Rakhorst & Ploeg, 2007)
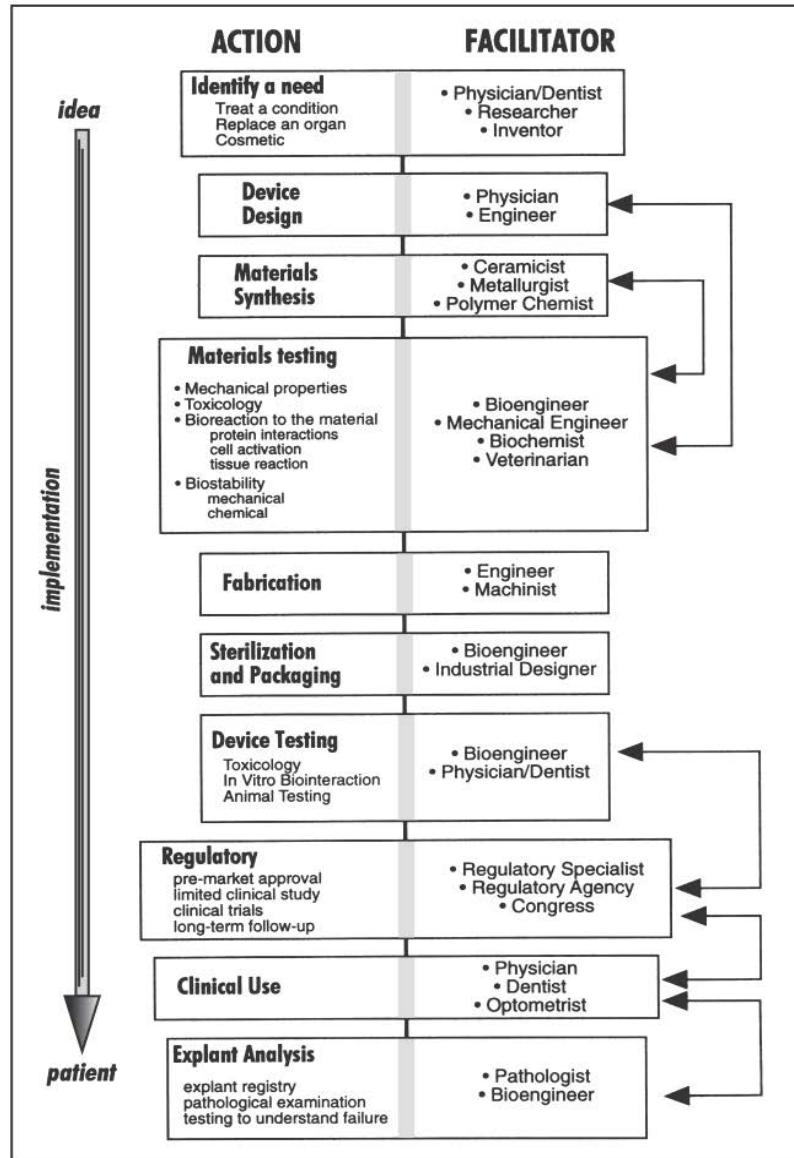
Figure II.1-3: The path from a need to a manufactured medical device encountered in the progression from identifying the need for a biomaterial or device to its manufacture, sale, and implantation (Ratner, et al., 2004)

A complex series of steps has to be performed to conceive the biomedical stent. A new method has been developed for designing consumer products, based on an iterative approach and characterized by several steps, for more information; see the reference (Ratner, et al., 2004). The roles of the engineers involve three types of individuals: the clinical engineer in health care, the biomedical engineer for industry and the research scientist. The research scientist applies the engineering concepts to study the biological processes like developing a mathematical model of a biological system. Then, in the simulation techniques, this model can be used to understand its features. For better understanding of the biological mechanism, the model can be modified depending on the experimental results of the actual biological system.

20

II.1.1 Biomaterials

Biomaterials are: **"**Any substances (synthetic and natural) that can be used as a whole or as part of a system to treat, augment, or replace any tissue, organ, or function of the body with minimal adverse or rejection by the body for an intended period of time" (Rakhorst & Ploeg, 2007). Biomaterials are in contact with biological systems.

A biomaterial is different from biological material such as the bone, which is produced by a biological system (Shi, 2004). The contact between the biomaterial and the biological system can be implemented in several ways: (1) Permanent (e.g., stents, heart valves, total joint replacement...); (2) Long-term application (e.g., fracture fixation device, contact lenses…); (3) Transient application (e.g., wound healing devices, cardiac assist systems).
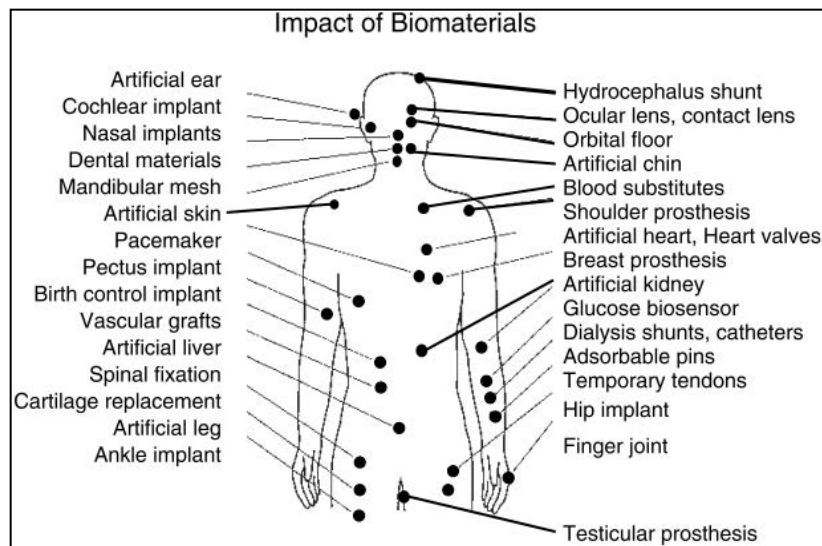
Figure II.1-4: Biomaterials have made an enormous impact on the treatment of injury and disease and are used throughout the body (Enderle, et al., 2005)

To develop any new material, the knowledge in the following three areas is fundamental: material science engineering, biology, physiology and clinical science are needed. The biomedical devices or implants are: "devices engineered from biomaterials and designed to perform specific functions in the body". The biological performance: "refers to the host and the material response, i.e., the local and systematic response of living systems to the material, and the response of the material to a living system, respectively" (Shi, 2004).

II.1.2 Biomechanics

The biomechanics understand the mechanical functioning of an organism and the behaviour of materials like kinematics, equilibrium, stresses and strains. It also focuses on large deformations and rotations and nonlinear constitutive equations, including visco-elastic behaviour and the behaviour of long, slender fibre-like structures. The biomechanics includes dynamics, vibrations and wave propagation. In other terms, it means the application of mechanics and its principles to study the properties of biological systems that can predict its normal/abnormal function. It presents at all levels of the study of living beings.

21

The biomechanics can be applied in many fields like surgery, study the mechanical properties of biological tissues like orthopedics and orthodontics, artificial organs, physical and sports activity analyses of human movement and cardiovascular system, etc. (Amplard, 2006).

Two biomechanical models are used: inverse dynamics which are commonly used (determining internal forces from measurements of external forces) and direct dynamics (calculate the resulting motions starting from known internal forces). These models require many measurements, including kinetic, kinematic and anthropometric measurements. Complex numerical optimizations are needed to solve the inverse equations as they contain more unknowns than the number of equations (Akay, et al., 2006).

II.2. Biological materials and continuum mechanics

Biomechanical study of systems requires the definition of a relevant scale of observation. It is a common practice to reduce the scale of observation at the microscopic level with a gradual change of physical properties. This means that the discontinuous heterogeneous reality is homogenized and modeled as a continuum. This phenomenon is typical for biological materials at any scale (organ level, tissue level or cellular level), where the structure on a macroscopic scale seems to be a massive structure with a filled volume in space while it is a discrete structure with open space at a smaller or a microscopic scale. This continuum will be then modeled mathematically by defining physical variables as a continuous function of the position in the space. The homogenization is necessary and depends on the objectives of the modeling where a certain level of homogenization is chosen. For biomaterials and its biomechanics, determining constitutive relations is complicated because of material nonlinearity, complex geometry, the composite nature of biological tissues and the influence of a wide range of environmental variables where thermodynamic considerations and assumptions become necessary.

The kinematic relations, the principles of conservation of mass and momenta and thermodynamic principles can then be applied to any continuum biological material. Then, constitutive equations that relate the *primary* kinematic field variables (density, temperature and deformation) to the *secondary* field kinetic variables (internal energy, heat flow, and stresses) ($e, \mathbf{q}, \mathbf{\sigma}$) are developed, complying certain rules and the entropy inequality. These mathematical models can describe and approximate the behaviour of biological materials to external stimuli, but should be validated against experimental results. The model should be modified when there is a remarkable difference between the theoretical/mathematical model and experimental observations. Experiments are necessary in the determination of various parameters and constants.

II.3. Computational methods in biomechanics and stent modeling

Since the technical research on biological soft or hard tissue are difficult in addition to the high cost involved in the experimental studies, in vitro and in vivo, beside the ethical concerns, the use of the computer model studies have been inspired. Moreover, many problems in biomechanics involve a combination of material or geometrical nonlinearity, complex geometry and mixed boundary conditions which are described by a set of differential equations. These equations are impossible to be resolved analytically, as the analytical solution is limited to linear problems and simple geometries governed by simple boundary conditions.

Thus, approximate solutions can be used. The computer-aided solutions are called a numerical solution of partial differential equations.

The continuous evolution in the powerful computer, the presence of a highly powerful package of mechanical software that model many desired problems, and the high progress in the medical image and reconstruction, these factors extremely encouraged the use of computational methods.

The computational methods (modeling software simulation) of structural mechanics can predict the mechanical behaviour of complex biological systems, including nowadays more complex prediction like 'couplings' and 'nonlinearities' and often presented in a physical phenomenon. This will finally highlight alternative solutions. Therefore, the biomechanic is constituted by models formulated in terms of partial differential equations and computer models to derive approximate solutions.

II.3.1 Biomechanics simulation

Biomechanics simulation includes the following points:

− A physical problem (structural or fluid-dynamics analysis) may contain many models (different behaviours). The physical problem is often complex and difficult to be resolved analytically. Thus, numerical approaches such as Finite Difference Method (FDM), Finite Element Method (FEM), and Boundary Element Method (BEM) have been used. (FEM) is more adapted for real and complex shapes.

− Great number of (FEM) software is commercially available to simulate and predict the behaviour of a structure subjected to mechanical or thermal loads for different material behaviours. General complex material behaviours have not yet been implemented in commercial finite element software. Thus three approaches are available (Terriault, et al., 2005):

▪ Simplifying and approximating the complex model by using a similar already implemented model in the FE software.

▪ Implementing a user-programmed constitutive material law in FE software like (ABAQUS). This approach is particularly suitable for developing a new material law and implementing it in FE software.

▪ Programming both the finite element numerical algorithms and material law behaviour, which is not a trivial task.

− Body segment is reconstructed from geometrical shape, which is similar to anthropometric characteristics.

− The geometrical body is then placed in a computer-simulated environment which can apply similar conditions and effects as those found in the real setting (Akay, et al., 2006). A constitutive mathematical complex or non-complex model is previously implanted in the software or under development.

− The simulation is run, and the model will calculate many parameters (forces, stresses, strains, etc….)

Table II.3-1: The differences between the medical and engineering approach	
Physician	**Engineer**
Reality	Numerical model
Experimental studies	Analytical approach (separating a problem into its constituent elements using the biomechanics
Calculate by measurement with a certain degree of approximation using medical, chemistry and biology aspects	Calculate by mathematical and physical equations
Results are always driven by experience	Results driven by the assumptions/approximations
Results validation needs time and experience	Results validation needs to compare the mathematical model results with the real model

II.3.2 Computational modeling in biomaterials

Computational modeling includes the following points:

− The constitutive law represents a mathematical relation which describes the study of stresses that are needed to produce certain strains or rate of strains within a given material. Rheological models include fluids and visco-elastic or viscous-plastic materials. The biological material can be modeled as a solid or fluid or a solid-fluid. The behaviour of a solid biological material can be elastic with small deformation and rotation or elastic with large deformation and rotation. The fluid biological material can be modeled as Newtonian fluid or non-Newtonian.

− The model should have underlying assumptions made previously in the development of the model, including the input data and subsequent analysis and interpretation of results. The extent of influence of these assumptions has to be known in order to have a common sense of the analyst. The model should describe the mechanical behaviour of the material.

− In terms of scale, the resulting models can be categorized as:
  - Micro scale models: they focus on fundamental phenomena, occurring at the microscopic level (phase transformation level)
  - Macroscopic phenomenological models: they model the material response at a macroscopic scale (Typically >100 microns) to describe approximately the material behaviour. These models are suitable to be used with numerical methods like (FEM) and predict the material behaviour since their simplicity and the use of parameters that are easy to measure experimentally.
  - Micro-macro models: the models combine micromechanics and macro continuum mechanics to get the constitutive laws that predict the material behaviour. These models are time-consuming and not particularly suitable for engineering applications.

For each physical reality, many models can be defined. The mathematical model is developed starting from the equations of kinematics, equilibrium and the constitutive law of the material which are the basic ingredients of continuum mechanics (The macroscopic point of view). A more complex model gives more details and accuracy, but higher complexity to solve.

− Experimental data are required to obtain the thermomechanical properties and the values needed for the material model definition used in FEA. A proper implementation of constitutive equations should be considered to increases the accuracy of model predictions (Leondes, 2001).

24

The experimental method can be noninvasive or invasive, nondestructive or destructive for the material under examination. It can be performed in vivo, ex vivo, in vitro, or in situ. Experimental tests include: compressive testing, indentation testing, tensile testing, bending tests, multiaxial and combined loading testing, torsion, pure shear testing, etc...)

− The validation of the model is made by a comparison between its results with in vivo or in vitro experimental results.

This following example shows briefly how deducing a model that describes the process and the potential mechanism of aneurysm enlargement. The model can be formulated by developing a constrained mixture model with the assumption that a stress-mediated process of growth and remodeling (G&R) is responsible for the subsequent enlargement and possible stabilization of the lesions. For numerical simulation, 2D axisymmetric cylindrical simplified geometry membrane was used for the aneurysm, assuming that the body is purely elastic and solving the inflation problem using the principle of virtual work (Mollica, et al., 2007) (Figure II.3-1).
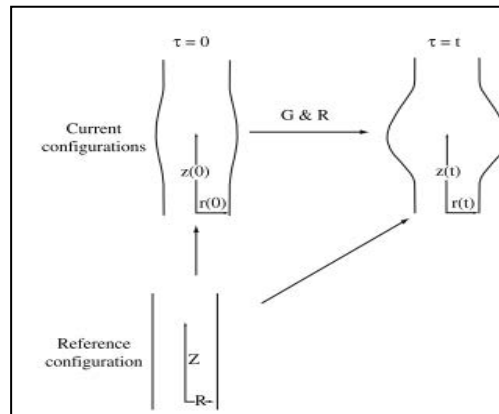
Figure II.3-1*: Axsymmetric geometries of a fusiform lesion, (i.e. Pressurized) configurations at time τ = 0 and τ as well as a convenient unpressurized reference configuration* (Mollica, et al., 2007)

Starting from the parametric relation in a fixed configuration R = R (Z), the positions of a point in the fixed and current configurations of the lesion ($\mathbf{X}, \mathbf{x}$) can be expressed by two sets of cylindrical polar coordinates (Z, θ, R) and (z, θ, r), respectively.
Using a set of two-dimensional curvilinear coordinates $\{Z, \Theta\}$, the current position can be expressed by: $x = \mathbf{x}(z(Z, \Theta), \theta(Z, \Theta), r(Z, \Theta)) = \mathbf{x}(Z, \Theta)$. The deformation due to the growth was assumed as: $z = z(Z), \theta = \Theta, r = r(Z)$. The components of the 2-D deformation gradient F(t) was deduced. In this study, the author assumed multiple hypotheses for the enlargement of the aneurysm and compared their consequences by defining a vector which relates unit vectors in the axial and circumferential directions. Then, using the principle of the virtual work, two sets of nonlinear algebraic equations can be deduced and solved using Newton–Raphson procedure to simulate the aneurysm enlargement (Mollica, et al., 2007).

II.4. Arteries and mechanics of aorta

II.4.1 Anatomy

Three types of artery can be classified according to their structure and size: (1) elastic arteries include aorta, which has a greater diameter and a greater number of elastic fibers, (2) muscular arteries, which are smaller in diameter than elastic arteries with a larger proportion of muscle compared to connective tissues, (3) arterioles which have the smallest diameter of arteries, typically (10–150 *μm*) in diameter with a few layers of smooth muscle tissues and almost no connective tissues. Blood vessels are composed of three layers (Peterson & Bronzino, 2008) (Figure II.4-1) (Figure II.4-2)

1. *Intima*: a thin layer composed primarily of endothelial cells.
2. *Media*: consists of elastin, collagen and smooth muscle cells. It determines largely the elastic properties of the vessel.
3. *Adventitia*: composed mainly of connective tissues.
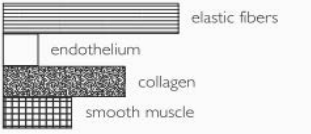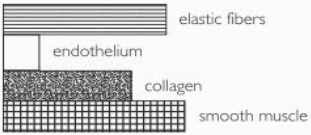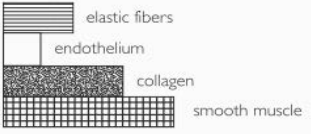
Figure II.4-2: Dimensions and composition of blood vessels (Meyers & Chawla, 2009)
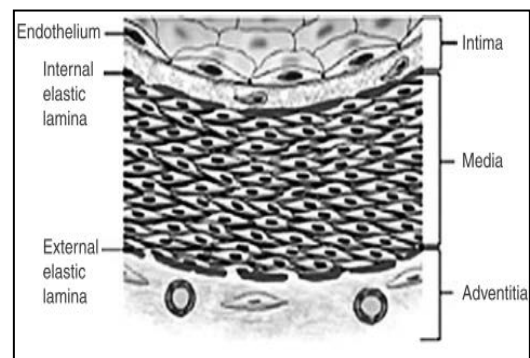
Figure II.4-1: Illustration of structure of arterial wall (Akay, et al., 2006)

II.4.2 The Mechanical behaviour of aorta

II.4.2.1 Experimental characterization

Many experimental tests are used to characterize the mechanical behaviour of aorta: pressure test, uniaxial and biaxial traction.

-Pressure Test

The test characterizes the inflation of the aorta under an internal pressure. The test can be realized *ex vivo* (Roy, 1881) (Bergel, 1961a) (Wolinsky & Glagov, 1964) *or in vivo* (Peterson, et al., 1960) (Imura, et al., 1986) (Stefanadis, et al., 1995) (Long, et al., 2005) (Wang, et al., 2006) (van't Veer, et al., 2008). These tests have been realized on a healthy animal aorta (Roy, 1881) (Bergel, 1961a) (Peterson, et al., 1960) (Wolinsky & Glagov, 1964) or a human aorta (Roy, 1881) (Imura, et al., 1986) (Länne, et al., 1992) (Wang, et al., 2006).

26

The test measures the evolution of diameter as a function of pressure. Some studies *in vivo* are affected on the aneurysmal artery (Länne, et al., 1992) (Wilson, et al., 2003) (Long, et al., 2005) (van't Veer, et al., 2008). These studies can quantify the global stiffness of the aneurysm. The stiffness is characterized by the elastic module of Peterson (E_P), which is given by:

$$E_p = \frac{\Delta p}{\varepsilon_r} \quad (ӀӀ.1)$$

Where: $(\Delta_P) = (P_{systolic} - P_{diastolic})$, $(\varepsilon_r) = (d_{systolic} - d_{diastolic})/d_{diastolic}$. The module cannot describe the real mechanical behaviour of the aorta like anisotropy, and its measurement should be followed by the standard tests of uniaxial traction (He & Roach, 1994) (Raghavan, et al., 1996) (Thubrikar, et al., 2001) (Martino, et al., 2006) and biaxial traction (Geest, et al., 2006).

-Uniaxial Traction Test

(Raghavan, et al., 1996) carried out a traction test on samples taken in orthoradial and longitudinal directions for a pathological aorta and longitudinal direction for a healthy aorta . The (Figure II.4-3) shows the results of the tests. The results showed (1) the hyperplastic nonlinear behaviour of the arterial tissue for both the healthy (AA) and the pathological (AAA) and (2) the maximal stress that corresponds to rupture. We can see that the maximal deformations until rupture are about (50%) for the healthy aorta and (25% to 35%) in the orthoradial and longitudinal directions for the pathological aorta (aneurysm). We can also see the maximal stress at which rupture occurs in both cases for the two different directions (Figure II.4-4).
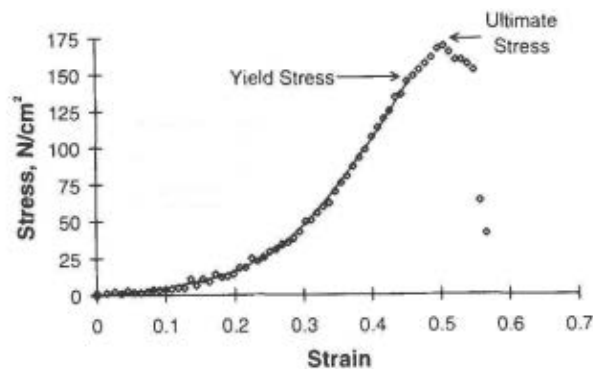
Figure II.4-3: Cauchy stress evolution as a function of Green deformation in the longitudinal direction of healthy aorta (Raghavan, et al., 1996)
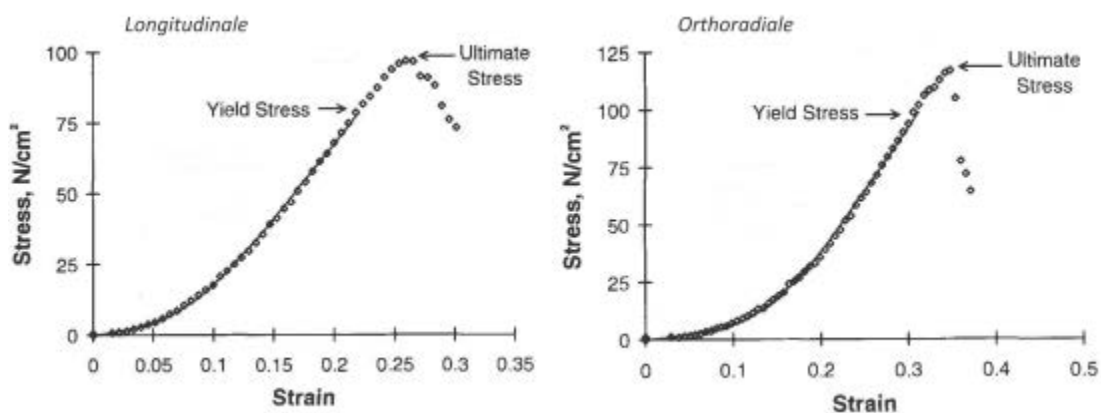
Figure II.4-4: Cauchy stress evolution as a function of Green deformation in the longitudinal and orthoradial direction of pathological aorta (Raghavan, et al., 1996)

27

(Thubrikar, et al., 2001) have also identified by the same method the elastic limit with stress and deformation $(\sigma_y, \varepsilon_y)$ to study the transition point between the elastic behaviour of the tissue and its damage before rupture.

-Biaxial traction test

The same work of (Raghavan, et al., 1996) was achieved by (Geest, et al., 2006) but in this study, the traction forces were simultaneously applied in the longitudinal and orthoradial direction for both (AA) and (AAA). They tested five relations of orthoradial traction $(T_{\theta\theta})$ and longitudinal traction (T_{LL}) . $T_{\theta\theta}: T_{LL} = \{0.5: 1, 0.75: 1, 1: 1, 1: 0.75, 1: 0.5\}$. These relations allow simulating the solicitations in vivo inside the pathologic and the healthy aorta.

(Figure II.4-5) shows the evolution of Piola-Kirchhof II (PK2) stresses as a function of Green deformations. The curves demonstrate, as before, the nonlinear anisotropic hyperelastic behaviour and the high stiffness, which is the cause of the pathology. The stiffness of the aorta is related to the macromolecular modification of the aorta tissue.
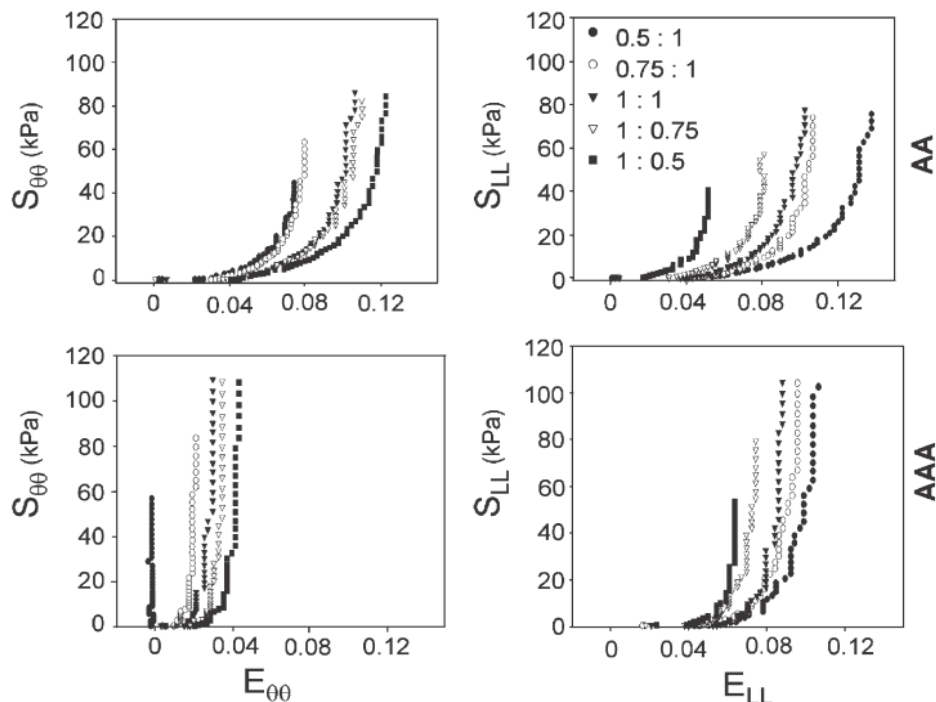
Figure II.4-5: Evolution of Piola-Kirchhoff II (PK2) stresses as a function of Green deformations in the in the longitudinal (LL) and orthoradial direction (θθ) for healthy (AA) and pathological aorta (AAA) (Geest, et al., 2006)

In the biaxial study, we can note that the values of maximal stresses were highly less than those studied by (Raghavan, et al., 1996) or (Thubrikar, et al., 2001) when only uniaxial forces were applied. More importantly, all the tests realized by (Geest, et al., 2006) have shown a large disparity of the behaviour of the healthy and the pathologic aorta according to the patient.

II.4.2.2 Basic characteristics of arterial wall

It is necessary to understand the mechanics of the aorta as it is highly concerned during the deployment of the stent. Many ideal assumptions have been considered to have a better understanding of the aorta behaviour. The following assumptions have been considered under static loading conditions:

-Homogeneity of the vessel wall

This assumption may be valid only within distinct macroscopic structures. The intima, media and adventitia are distinctly different. Although nonlinearity and anisotropy of the aortic wall properties have been well recognized (Geest, et al., 2006) (Basciano & Kleinstreuer, 2009), most studies consider the wall a homogeneous material (Leondes, 2001).

-Incompressibility of the vessel wall

Experimental measurement shows that the vessel wall is practically incompressible. The experimental results (Carew, et al., 1968) indicate that the change in volume was only 0.165% when the arterial segment was inflated in vivo by a pressure of 181 mm Hg (Leondes, 2001).

-Nonlinear large deformation

The soft biological tissues such as arteries undergo large deformations due to physiological forces. The artery can be extended up to 120-140% in the circumferential direction and up to 150% in the longitudinal direction under physiological conditions. The qualitative analysis indicates that the mechanical behaviour of the arterial tissue is essentially nonlinear in geometrical and physical aspect as shown in the (Figure II.4-6). The slope of the curve increases with strain, this increase in slope is due to the extension of collagen and elastin fibers. The nonlinear physical response is due to the mechanical properties of the basic structural components of the artery and the architecture of the arterial wall (Peterson & Bronzino, 2008) (Leondes, 2001). The mechanical response of blood vessels is nonlinear-elastic. It is elastic because it returns to its original shape on unloading. However, there is a slight hysteresis on loading and unloading due to the viscoelastic processes (Meyers & Chawla, 2009).

-Viscoelasticity

In reality, the stress state is not only determined by the current strain, but it depends also on the history of deformation. It means that the wall should be considered a viscoelastic solid since the hysteresis loop indicates that the stress state depends on the current and the history of deformation. Besides the hysteresis, the experimental results of Tanaka and Fung showed that the arterial tissue manifests stress relaxation and creep. The variation of viscoelastic properties is associated mainly with the mechanical properties of smooth muscle cells in the artery wall (Leondes, 2001). This means that the aorta exhibits solid-like and fluid-like behaviour.

-Residual stress and strain

Blood vessels are subjected to retract after longitudinal and circumferential excision. This is caused by the relief of distending forces resulting from internal pressure and longitudinal traction. The magnitude of the retractions is influenced by growth, aging and hypertension. However, it is acceptable to assume that blood vessels are in a nearly "stress-free state" when they are free of external loads, but this approach ignores the residual stress and strain effects (Peterson & Bronzino, 2008).
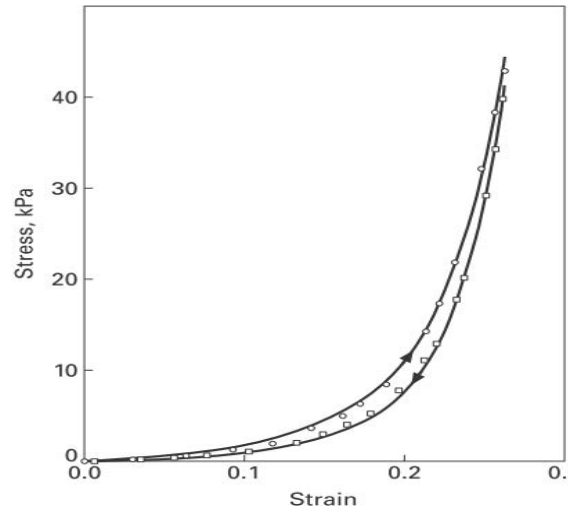
Figure II.4-6: Stress–strain response of human vena cava: circles: loading; squares: unloading
(Adapted from Y.C.Fung, Biomechanics by reference (M. A Meyers et al., 2008)

(Holzapfel & Ogden, 2010) have performed a study for a human aorta (11 corpses of 48 years). The (Figure II.4-7) shows the deformations of one of these tests in the longitudinal and the orthoradial direction. These deformations took 16h after cutting the aorta. In the orthoradial direction, the aorta was opened with an amplitude of more than 180 degrees, while a large curvature was formed in the adventitia side in the longitudinal direction (Figure II.4-7).
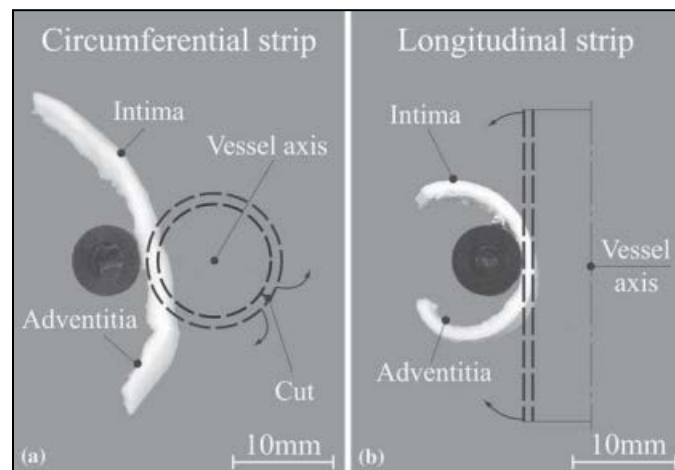
Figure II.4-7: The effects of residual strains in the in the longitudinal
and orthoradial direction for healthy aorta (Holzapfel & Ogden, 2007)

According to Holzapfel and al, these residual strains are not equal in the three layers and in the two directions, which means that the distribution of residual strains in the artery wall is not the same.

30

-Anisotropy

The arterial wall is not isotropic. When strips are subjected to an equivalent force axially and circumferentially, the mechanical response of the aorta is different. This is due to the architecture of the aortic wall. The aorta can be considered an orthotropic solid concerning the planes perpendicular to the coordinate basis. However, the blood vessel can be considered as isotropic when the degree of anisotropy is small or when the variations in internal pressure and distending force are small (Peterson & Bronzino, 2008).

II.4.2.3 Constitutive models of aorta behaviour

As explained earlier, the constitutive equation should approximate the observed physical behaviour of a realistic material. The constitutive equation is formalized using a functional relationship that specifies the stress components in term of other field function such as strain and temperature. It also determines the state of stresses at any point ($\mathbf{x}$) of a continuum body at a time (t). The main goal of the constitutive equations with thin the field of solid mechanics is that they are appropriate for approximation techniques such as (FEM). In the frame of nonlinear constitutive theory where the strain may be large, i.e., finite like aorta behaviour, the hyper elastic material is called hyperelasticity for which nonlinear continuum mechanics (Green & Adkins, 1970) is the fundamental basis for the analytical treatment and for the numerical solution techniques (Tallec, 1994).

A homogeneous material is said to be hyperelastic or (Green elastic material) if there exists a strain **Helmholtz free energy density function** $\Psi = \Psi(\mathbf{F})$, which is a scalar-valued function of one tensor variable($\mathbf{F}$). The gradient tensor of deformation ($\mathbf{F}$) is the fundamental kinematic (second-order) tensor of deformation in a nonlinear or finite deformation kinematics. ($\mathbf{F}$) characterizes the behaviour of motion or changes in the material elements during motion by the given equation:

$$d\mathbf{x} = \mathbf{F}(\mathbf{X}, t)d\mathbf{X} \quad (ĻJ.2)$$

Where $(d\mathbf{x}), (d\mathbf{X})$ denote the vector elements in current (time: t) and reference configuration (time: t_0).
If the volume changes during deformation, we write:

$$d\upsilon = J(\mathbf{X}, t)dV \quad (ĻJ.3)$$

Where $(dV), (d\upsilon)$ denote the volume elements in the reference (material or non-deformed) and the deformed (spatial) configurations respectively. (J): is the determinant of the deformation gradient($\mathbf{F}$)**.**
This will imply to introduce these changes as the (second order) strain tensors related either to reference or current configuration.
Therefore, we introduce the symmetric **right Cauchy-Green** ($\mathbf{C}$) known as **Green deformation tensor** and **Piola deformation tensors** ($\mathbf{B} = \mathbf{C}^{-1}$) **Tensor,** which are important strain measures in material coordinate:

$$\mathbf{C} = \mathbf{F}^T\mathbf{F}, \ \mathbf{B} = \mathbf{F}^{-1}\mathbf{F}^{-T} \quad (ĻJ.4)$$

Other important strain measure in terms of spatial coordinate is called **left Cauchy-Green tensor (b),** which is defined by:

31

$$\mathbf{b} = \mathbf{FF}^{T} \quad (\text{Ц.5})$$

We also introduce a strain measure in the direction of (α_0) at point $(\mathbf{X} \in \Omega_0)$, which is known as **Green-Lagrange strain tensor**:

$$\mathbf{E} = \frac{1}{2}\left(\mathbf{F}^{T}\mathbf{F} - \mathbf{I}\right) \ or \ 2\mathbf{E} = \mathbf{C} - \mathbf{I} \quad (\text{Ц.6})$$

Where $(\mathbf{I})$ is a unit tensor.

Then, the stress tensors will be used for practical nonlinear analyses. **Kirchhoff stress tensor** $(\boldsymbol{\tau})$ is introduced which differs from the symmetric Cauchy stress $(\boldsymbol{\sigma})$ by the volume ratio (or jacobiant determinant $J = \det(\mathbf{F})$), and it is defined by:

$$\boldsymbol{\tau} = J\boldsymbol{\sigma} \quad (\text{Ц.7})$$

We further introduce the **first Piola-Kirchhoff stress** $(\mathbf{P})$, which is not symmetric, and the **Second Piola-Kirchhoff stress tensor** $(\mathbf{S})$ which represents a very useful stress measure in computational mechanics and in the formulation of constitutive equations at finite strains especially for solids. They are defined by:

$$\mathbf{P} = J\boldsymbol{\sigma}\mathbf{F}^{-T}, \boldsymbol{\sigma} = J^{-1}\mathbf{PF}^{T} \quad (\text{Ц.8})$$
$$\mathbf{S} = J\mathbf{F}^{-1}\boldsymbol{\sigma}\mathbf{F}^{-T} = \mathbf{F}^{-1}\mathbf{P}, \boldsymbol{\sigma} = J^{-1}\mathbf{FSF}^{T} \quad (\text{Ц.9})$$

The hyperelastic material may be expressed by the **first Piola-Kirchhoff stress** $(\mathbf{P})$, which is not symmetric, by the following expression:

$$\mathbf{P} = \frac{\partial \Psi(\mathbf{F})}{\partial \mathbf{F}} \ and \ \boldsymbol{\sigma} = J^{-1}\frac{\partial \Psi(\mathbf{F})}{\partial \mathbf{F}}\mathbf{F}^{T} = J^{-1}\mathbf{F}\left(\frac{\partial \Psi(\mathbf{F})}{\partial \mathbf{F}}\right)^{T} \quad (\text{Ц.10})$$

Alternative expression can be deduced for $(\mathbf{P})$ and for $(\mathbf{S})$ (which is symmetric) as:

$$\mathbf{P} = 2\mathbf{F}\frac{\partial \Psi(\mathbf{C})}{\partial \mathbf{C}}, \quad \mathbf{S} = 2\frac{\partial \Psi(\mathbf{C})}{\partial \mathbf{C}} = \frac{\partial \Psi(\mathbf{E})}{\partial \mathbf{E}} \quad (\text{Ц.11})$$

Hyperelasticity is the most satisfying formulation of elasticity as it is derived from continuum thermodynamics arguments.

As the experimental works demonstrated a nonlinear, anisotropic and hyperelastic behaviour of the aorta, many different constitutive models have been proposed in the literature for numerical objectives. We present in this study the common and usual models for the aorta. Some models (viscoelastic and poro-hyperelastic models) that are used for healthy aorta are also presented.

I. Isotropic hyperelastic models

We consider an arbitrary point $(\mathbf{X})$ of an elastic-continuum solid located in (O, e_1, e_2, e_3) which occupies the volume (Ω_0) in the initial configuration at time $(t=0)$ and the volume (Ω) in the current configuration (Figure II.4-8). A motion $\varkappa$ carry this point $(\mathbf{X} \in \Omega_0)$ to a place $\mathbf{x} = \varkappa(\mathbf{X}, t)$ specifying a location in the region (Ω) (current configuration) at time (t).

In order to study the rigid body motion superimposed on the reference configuration, we assume that the body occupying the region (Ω_0) (reference configuration) is translated by the a vector $(\mathbf{c})$ and rotated by an orthogonal tensor $(\mathbf{Q})$ according to the eq. $(\mathbf{X}^* = \mathbf{c} + \mathbf{Q}\mathbf{X})$, which moves (Ω_0) to a new region $(\Omega_0{}^*)$ (new reference configuration) and the arbitrary point $(\mathbf{X})$ to a new location identified by the position vector: $\mathbf{X}^* \in (\Omega_0{}^*)$.
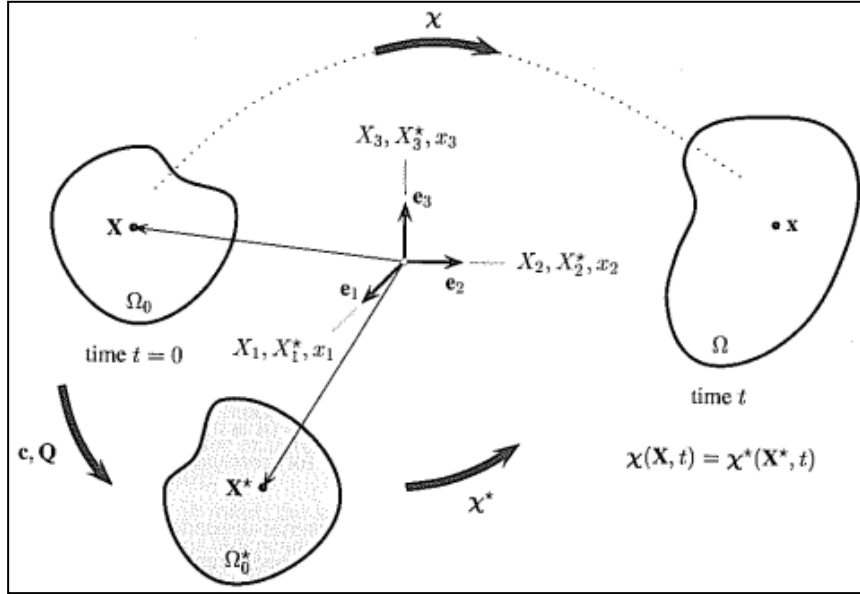
Figure II.4-8: Transformation of continuum volume

Now, a different motion $\mathbf{x} = \varkappa^*(\mathbf{X}^*, t)$ should move $(\Omega_0{}^*)$ to the current configuration (Ω), so that:

$$\mathbf{x} = \varkappa(\mathbf{X}, t) = \varkappa^*(\mathbf{X}^*, t) \quad (\text{ЏІ.12})$$

Which transforms $(\mathbf{X}^*)$ to a place $(\mathbf{x})$. Using the equation $(\mathbf{X} = \mathbf{c} + \mathbf{Q}\mathbf{X}^*)$ and the chain rule: the gradient tensor of deformation may be expressed as:

$$\mathbf{F} = \frac{\partial \mathbf{x}}{\partial \mathbf{X}} + \frac{\partial \mathbf{x}}{\partial \mathbf{X}^*}\mathbf{Q} = \mathbf{F}^*\mathbf{Q} \quad (\text{ЏІ.13})$$

Where $\dfrac{\partial \mathbf{x}}{\partial \mathbf{X}^*}$ is defined to be the deformation gradient relative to the region $(\Omega_0{}^*)$. We can also write:

$$\mathbf{F}^* = \mathbf{F}\mathbf{Q}^T \quad (\text{ЏІ.14})$$

So, the hyper-elastic material is said to be **isotropic** relative to the reference configuration (Ω_0) if the values of strain energy: $\Psi(\mathbf{F})$ and $\Psi(\mathbf{F}^*)$ are the same for all orthogonal tensors $(\mathbf{Q})$ as: $\Psi(\mathbf{F}) = \Psi(\mathbf{F}^*) = \Psi(\mathbf{F}\mathbf{Q}^T)$, and the motion of the elastic body on any particularly translated or rotated configuration always gives the same strain-energy function at time (t). However, when this relation is not satisfied the hyperelastic material is said to be anisotropic.

33

$$\Psi(\mathbf{F}) \neq \Psi(\mathbf{F}^*) \quad (\text{Ц.15})$$

-Constitutive equations in terms of invariants

The scalar valued tensor function can be expressed in terms of the principal invariants of the symmetric Cauchy-Green tensors (**C**) and (**b**): $I_\alpha = I_\alpha(\mathbf{C})$ and $I_\alpha = I_\alpha(\mathbf{b})$; ($\alpha = 1,2,3$). We may write equivalently:

$$\Psi = \Psi\left[I_1(\mathbf{C}), I_2(\mathbf{C}), I_3(\mathbf{C})\right] = \Psi = \Psi\left[I_1(\mathbf{b}), I_2(\mathbf{b}), I_3(\mathbf{b})\right] \quad (\text{Ц.16})$$

$$I_1(\mathbf{b}) = \mathbf{tr}(\mathbf{b}) = \lambda_1^2 + \lambda_2^2 + \lambda_3^2$$

With, $I_2(\mathbf{b}) = \dfrac{1}{2}\left((\mathbf{tr}\mathbf{b})^2 - \mathbf{tr}(\mathbf{b}^2)\right) = \lambda_1^2\lambda_2^2 + \lambda_1^2\lambda_3^2 + \lambda_2^2\lambda_3^2 \quad (\text{Ц.17})$

$$I_3(\mathbf{b}) = \det(\mathbf{b}) = \lambda_1^2\lambda_2^2\lambda_3^2 = J^2$$

Where (λ_α^2) are the three eigenvalues of the symmetric special tensor (**b**). The most general form of stress relation in terms of three strain invariants, which characterizes isotropic hyperelastic material at finite strains is deduced and given by:

$$\mathbf{S} = 2\frac{\partial\Psi(\mathbf{C})}{\partial\mathbf{C}} = 2\left[\left(\frac{\partial\Psi}{\partial I_1} + I_1\frac{\partial\Psi}{\partial I_2}\right)\mathbf{I} - \frac{\partial\Psi}{\partial I_2}\mathbf{C} + I_3\frac{\partial\Psi}{\partial I_3}\mathbf{C}^{-1}\right] \quad (\text{Ц.18})$$

-Constitutive equations in terms of principals stretches

The strain energy function (Ψ) can be expressed as the function of principal stretches (λ_α), ($\alpha = 1,2,3$) in the form:

$$\Psi = \Psi(\mathbf{C}) = \Psi(\lambda_1, \lambda_2, \lambda_3) \quad (\text{Ц.19})$$

In incompressible hyperelastic material, which keeps the volume constant, the volume variation is characterized by the incompressibility constraint: ($J = 1$), the aortic wall can be considered incompressible in the physiologic condition (Carew, et al., 1968), and the general constitutive equation for incompressible hyperelastic material is given by the strain energy function.

$$\Psi = \Psi(\mathbf{F}) - P(J - 1) \quad (\text{Ц.20})$$

Where ($J = 1$); the scalar (P) represents the hydrostatic pressure; **S**, **σ** are deuced with the equations:

$$\mathbf{S} = 2\frac{\partial\Psi(\mathbf{C})}{\partial C} - p\mathbf{C}^{-1} \quad (\text{Ц.21})$$

$$\boldsymbol{\sigma} = \frac{\partial\Psi(\mathbf{F})}{\partial\mathbf{F}}\mathbf{F}^T - P\mathbf{I} \quad (\text{Ц.22})$$

34

In the incompressible hyperelastic isotropic material, we consider the kinematic constraint: $I_3 = \det(\mathbf{C}) = \det(\mathbf{b}) = 1$; the invariant ($I_3$) will not be included in the (Ψ) expression. The strain energy function of this material in terms of invariants, **S**, are given by:

$$\Psi = \Psi\left[I_1(\mathbf{C}), I_2(\mathbf{C})\right] - \frac{1}{2}P(I_3 - 1) \quad (\text{Џ.23})$$

Where $P/2$ serves as *indeterminate Langrange multiplier*.

$$\mathbf{S} = 2\frac{\partial\Psi(I_1, I_2)}{\partial\mathbf{C}} - \frac{\partial\left[p(I_3 - 1)\right]}{\partial\mathbf{C}} \quad (\text{Џ.24})$$

In terms of principal stretches, $\Psi = \Psi(\mathbf{C}) = \Psi(\lambda_1, \lambda_2, \lambda_3) - P(J - 1)$. The incompressibility constrain ($J = 1$) takes on the form ($\lambda_1\lambda_2\lambda_3 = 1$).

Many models are available in the literature (table Џ.4-1). (Raghavan & Vorp, 2000) model is a quadratic model. Its parameters were identified by uniaxial traction tests. Other models are also used like: Mooney model that takes the second invariant (1940). Demiray model (1972) which uses only the first invariant and Ogden model that uses an approach based on the principal elongations (1972).

Table II.4-1: The principal isotropic incompressible models of strain energy potential
Mooney (1940) $\Psi = \Psi(I_1, I_2) = C_{10}(I_1 - 3) + C_{01}(I_2 - 3)$, Where :
(C_{10}), (C_{01}): are material constants characterizing the deviatoric deformation of the material $\mu = 2(C_{10} + C_{01})$= The initial shear modulu
Ogden (1972) $\Psi = \Psi(\lambda_1, \lambda_2, \lambda_3) = \sum_{i=1}^{N}\frac{\mu_i}{\alpha_i}(\lambda_1^{\alpha_i} + \lambda_2^{\alpha_i} + \lambda_3^{\alpha_i} - 3)$, Where:
(λ_i)($i = 1, 2, 3$) = deviatoric principal stretches of the left Cauchy-Green tensor N, α_i, μ_i, =material constants, $\mu = 1/2\sum_{i=1}^{N}(\alpha_i\mu_i)$:The initial shear modulus
Neo-Hookean (1943) $\Psi = \Psi(I_1) = C_{10}(I_1 - 3)$
Yeoh (1990) $\Psi = \Psi(I_1, I_2) = C_{10}(I_1 - 3) + C_{01}(I_1 - 3)^2 + C_{20}(I_1 - 3)^3$, Where   : C_{10}, C_{01}, C_{20}: are material constants
Raghavan and Vorp (2000) $\Psi = \alpha(I_1 - 3) + \beta(I_1 - 3)^2$ Where α, β are material parameters
Demiray (1972) $\Psi = \frac{D_1}{D_2}(\exp\{D2/2(I_1 - 3) - 1\}$ Where: D_i: are material parameters

The Neo-Hookean model can be derived from the Mooney model by taking($C_{10} = 0$). These two models are implemented in most of the commercial codes that use finite elements method.

II.Anisotropic hyperelastic models
The nonlinear anisotropic behaviour of the pathologic human aortic wall has been deduced by the uniaxial traction test (Raghavan, et al., 1996) (Thubrikar, et al., 2001). The results have been confirmed by the biaxial traction test (Matsumoto, et al., 2009). To describe these tests, different models have been proposed based on the decomposition of potential energy to isotropic and anisotropic parts as follows:

$$\Psi = \Psi_{iso} + \Psi_{aniso} \quad (Ц.25)$$

The main models that describe the hyperelastic nonlinear anisotropic behaviour are presented in (Table Ц.4-2). These models consider the experimental observations. More detailed studies are presented by (Holzapfel, et al., 2000) (Sacks, 2000) (Vito & Dixon, 2003) (Vorp, 2007) (Kalita & Schaefer, 2008) and (Holzapfel & Ogden, 2010).

Table Ц.4-2: The main hyperelastic anisotropic models of strain energy potential	
Humphrey (1995)	$\Psi = D_1 [\, exp(\, Q\,) - 1\,]$ $Q = \alpha_1 E_{\theta\theta}^2 + \alpha_2 E_{ZZ}^2 + \alpha_3 E_{rr}^2 + 2\alpha_4 E_{\theta\theta} E_{zz} + 2\alpha_5 E_{zz} E_{rr}$ $+ 2\alpha_6 E_{rr} E_{\theta\theta} + \alpha_7 E_{\theta Z}^2 + \alpha_8 E_{rZ}^2 + \alpha_9 E_{r\theta}^2$
Rodriguez et al. (2008)	$\Psi = C_1 (\bar{I}_1 - 3)$ $+ \dfrac{k_1}{2K_2} \{\, exp[\, K_2\, [(1 - \rho)(\bar{I}_1 - 3)^2 + \rho(\bar{I}_4 - \bar{I}_4^0)^2]\,]\,] - 1\, \}$ $+ \dfrac{k_3}{2K_4} \{\, exp[\, K_4\, [(1 - \rho)(\bar{I}_1 - 3)^2 + \rho(\bar{I}_6 - \bar{I}_6^0)^2]\,]\,] - 1\, \}$
Basciano and Kleinstreuer (2009)	$\Psi = C_2 (\bar{I}_1 - 3)^2 + C_{61}(\bar{I}_4 - 1)^6 + C_{62}(\bar{I}_6 - 1)^6$
Rissland e al. (2009)	$\Psi = C_1 (\bar{I}_1 - 3) + C_2 (\bar{I}_1 - 3)^2 + \dfrac{D_1}{D_2}(exp[\, D2 / 2(\bar{I}_1 - 3)\,] - 1)$ $+ \dfrac{k_1}{2K_2} \{\, exp[\, k_2(\bar{I}_4 - 1)^2\,] - 1\, \} + \dfrac{k_3}{2K_4} \{ exp[\, k_4(\bar{I}_6 - 1)^2\,] - 1\, \}$

Humphrey (1995) model is the generalization of Fung model (1967). This model is defined as a function of the Green tensor given by: $\mathbf{E} = \frac{1}{2}(\mathbf{C} - \mathbf{I})$; $(\mathbf{I})$ the unit matrix. (E_{ij}): are components of the Green tensor of deformation. (α_i): are the material constants, (D_1, C_1, C_2, C_{61}) and (C_{62}) are temperature-dependent material parameters.

Other models are based on the invariants approach (Rodríguez, et al., 2009) (Basciano & Kleinstreuer, 2009) (Rissland, et al., 2009) (Ferruzzi, et al., 2011). These models have been formalized to describe the experimental results of (Geest, et al., 2006). To consider the anisotropy that comes from the collagen fibers of the aortic wall, we introduce two anisotropic directions associated with two different families of fibers (Figure II.4-9).
Two networks of fibers are enough to capture the anisotropy and the nonlinearity of the arterial wall (Holzapfel, et al., 2000). The directions of these two networks of fibers are defined by: $(\mathbf{M} = \cos\varphi, sin\varphi, 0)$ and $(\mathbf{M}' = \cos\varphi', -sin\varphi', 0)$, $(\varphi = \varphi')$. The two vectors lead to define new invariants: $(I_4 = \mathbf{M\, C\, M})$ and $(I_6 = \mathbf{M'\, C\, M'})$ which characterize the anisotropy of the material.
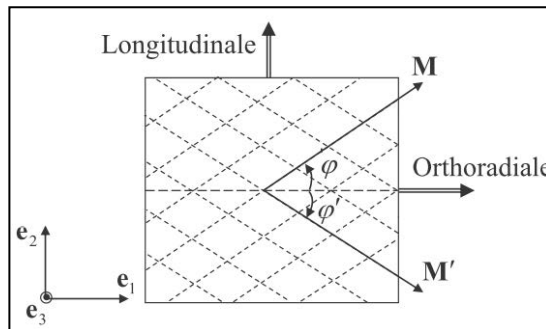
Figure II.4-9: Symmetric fibers of collagen orientation relative to orthoradiale direction

For the (Rodríguez, et al., 2009) model, the $(k_i, i = 1,2,3,4)$: are material parameters. The parameter $\rho \epsilon [0 \ 1]$ regulates the degree of material anisotropy. When $(\rho = 0)$, the material becomes isotropic. The parameters: $(\bar{I}_4^0)$ and $(\bar{I}_6^0)$ refer to the initial ripple of fibers. The anisotropy will be only taken into account if $(\bar{I}_4 \geq \bar{I}_4^0)$ or $(\bar{I}_6 \geq \bar{I}_6^0)$. (Basciano & Kleinstreuer, 2009) model is also based on the invariants approach. (Rissland, et al., 2009) model is a combination of (Raghavan & Vorp, 2000) and Demiray models. All the material parameters of the different models of anisotropic behaviour can be adjusted by the obtained experimental data of (Geest, et al., 2006).

III. Viscoelastic models

The viscoelastic behaviour of the aortic wall was observed by (Roy, 1881) during the pressure test. The demonstration of this property consists of determining the damping between the internal pressure and the dilatation of the aorta (Peterson, et al., 1960) (Bergel, 1961b) (Learoyd & Taylor, 1966) (Imura, et al., 1990). This behaviour can be modeled with the generalized Maxwell model. In the abdominal aorta, this property is neglected.

IV. Poro-hyperelastic models

The arterial wall can be considered a porous material that can be permeable to some nutritive elements of blood. There is no real data for permeability or porosity. An isotropic poro-hyperelastic model was proposed by (Simon, et al., 1998). This model describes the mechanical behaviour of rabbit aorta. Another similar model was proposed by (Koshiba, et al., 2007) that studied the lipoprotein transportation in the arterial wall. Recently, (Ayyalasomayajula, et al., 2010) have performed numerical analyses in an aneurysmal model, considering the porosity of the arterial wall.

II.5. Stenting biomechanics and modeling

II.5.1 Introduction

A stent is a cylinder metal mesh or a tubular scaffold tube that is inserted in a luminal cavity to hold a stenosed artery open, restore normal blood flow like wall stent or to exclude the blood flow from the aneurysmal sac. In this case, the stent graft is used. The metal stent framework supports the position, shape, dimensions of the stent graft and generates a seal between the ends of the stent graft and the surrounding artery. The graft transports blood from one end of the prosthesis to the other, isolating the surrounding artery from the circulation.

The deployment of the stent in the aorta can be applied either by balloon for balloon-expanding (BX) stents, or using self-expanding (SX). The difference between them is the mechanical behaviour of the stent material. General bibliographical review of stent finite element modeling and simulations will be needful. Various types of stent design are available. They are categorized, by the geometry, into: (1) coil designs, (2) modular open-cell designs, (3) multi-cell closed-cell design, (4) woven stents and more recently (5) biodegradable stents.

II.5.1.1 Balloon-expanding (BX) stents

The (BX) stent is deployed by using an inflated balloon which deforms the stent graft plastically until it obtains its final diameter larger than the diameter of the artery. The material property has the characteristics of the elasto-plastic nonlinear constitutive behaviour with large displacement. Many different types are available like wire-based stent, sheet-based stent and tube-based stent (Santillo, 2008). When the balloon deflates, the artery contracts onto the relatively unyielding stent. The stent generates high frictional forces and is incorporated into the arterial wall. The balloon-expanded stent has stable dimensions and the size of the balloon and the aorta must be precise. Too small oversizing causes insecure attachment and leakage while too large oversizing causes the aorta to damage.

The (BX) stent is mounted on a folded angioplasty balloon which expands the stent to the desired diameter by inflation of the balloon (Angioplasty). Then, the balloon is deflated and removed, leaving the stent at the targeted site. The Palmatz stent (Cordis, Johnson & Johnson, and Miami, FL) made from 316L steel was the first tubular stent (Figure II.5-1).
In (Figure II.5-2), a numerical model was developed and implemented within a finite element framework using Abaqus/Explicit to predict the behaviour of a BX stent in an arterial geometry when it was subjected to corrosion over time (Grogan, et al., 2011).

Figure II.5-1: Unconstrained expansion of the endeavor stent (Medtronic): (A) shows the stent, crimped around a folded angioplasty balloon. The deployment starts at the stent ends (B) and continues towards the stent center (panel C).
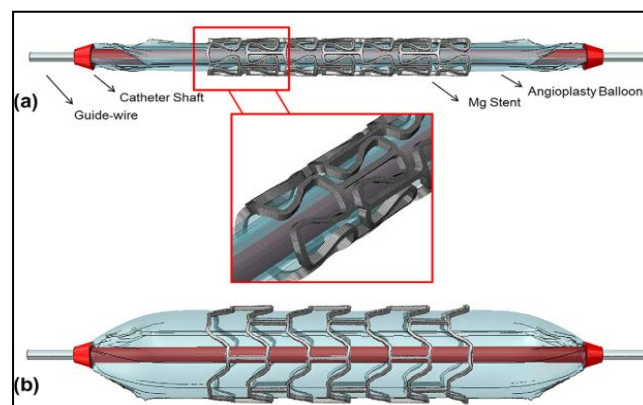
Figure II.5-2: The magnesium BX stent and delivery system FE model geometries
(a) before and (b) after deployment (Grogan, et al., 2011)

38

II.5.1.2 Self-expanding stents (SX)

Self-expanding stents do not need a balloon for expansion. Their exceptional mechanical behaviour makes these stents expand individually by a spring mechanism when the device is unloaded from a constraining delivery catheter (Figure II.5-3).

Many types are used in the market (like wire-based stent, sheet-based stent and tube-based stent) with different ability of the material to restore the elastic energy while constrained in the delivery system. Therefore, superelastic nitinol stents become a more suitable choice due to its unique and unusual properties: "the superelasticty" and "shape memory" properties.

-Wallstent (uncovered SX stent)

The wallstent is a SX metallic endoprothesis criss-cross pattern with tubular mesh configuration. The stent is compressed and constrained by a delivery system. When the delivery site is reached, the catheter is released, and the stent will expand lonely due to its superelastic behavior. The stent is pushed continually outwards against the artery. The pushing forces generated by the stent are low compared to the forces generated by arterial pressure.
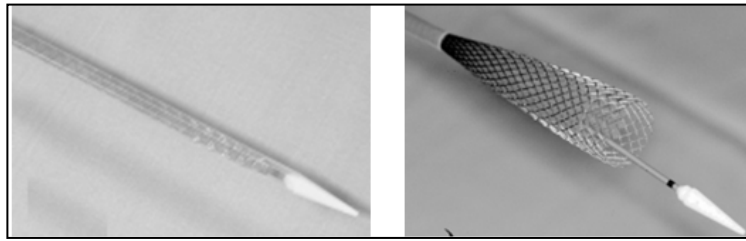
Figure II.5-3: Wallstent before deployment (left), the outer sheath is withdrawn in order to push out the stent (right)

The first application for the wall stent was treating the carotid artery stenosis, repair of traumatic pseudo aneurysm and other peripheral artery aneurysms (Assali, et al., 2001), treat obstructing (tracheo) bronchial lesions, palliation of symptoms provided by malignant lesions or (benign) stenosis in the esophagus and gastrointestinal tract and urethral strictures (Conti, 2007). More recently, a partially deployed is used as a temporary inferior vena cava filtration device during coil embolization of high-flow Arteriovenous Fstula (Conti, 2007). In (Figure II.5-4), numerical simulation of wire nitinol stent-vessel interaction has been made to evaluate the ability of the stent to hold the stenotic vessel open and to inspect the contact stresses between the two bodies.
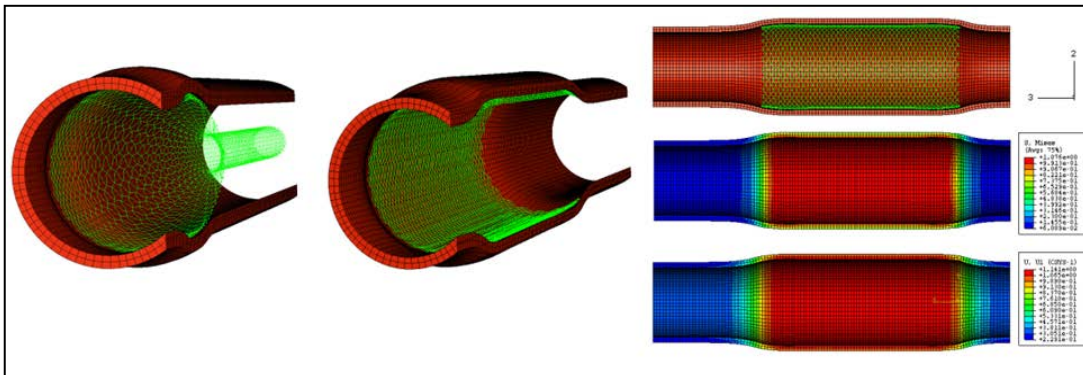
Figure II.5-4: Finite element model of self-expanding braided wire stent. Vessel and slightly deployed SX stent (left), Mises stresses and radial displacement in the vessel wall after deployment (right)

39

-Covered stents

Covered stents are composed of a fabric or graft material which covers a metal SX or EX stent. They have many applications in peripheral arterial disease, e.g., (1) rebuilt a physiological lumen in order to exclude the blood flow in diseased vessels for treatment of atherosclerotic disease, (2) sealing iatrogenic vessel perforations or ruptures, (3) exclusion of aneurysms and pseudo-aneurysms, (4) treatment of vascular fistulas, (5) management of failing dialysis grafts, (6) provides a direct barrier to tissue ingrowth from neointimal hyperplasia between the stent wire, sealing off the exposed inflammatory surface to inhibit restenosis (Conti, 2007).
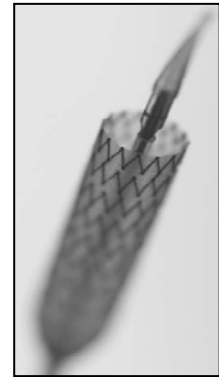
II.5.2 Stents materials and requirements:

The optimal stent material depends on the required ideal mechanical properties like biocompatibility, hemocompatibility (blood -material interaction) and non-adverse events from tissue and cell interactions with the material. This material should ensure a high degree of confidence in design and performance. The stent should be easily retrieved in case of bad deployment and the delivery system must hold the stent in place precisely without injuring the artery wall (Jr, et al., 2004). The strut stent design should not provoke the development of a new blockage (thrombosis or hyperplasia). It was shown that restenosis rates for different stent designs of balloon expanded stents vary from 20 to 50 % (Jr, et al., 2004) (Pache, et al., 2003). The optimal parameters in stent design are numerous, and in some cases inconsistent (Table Ц. 5-1) (Jr, et al., 2004).

Table II.5-1: Design considerations for vascular stents (Jr, et al., 2004)	
Characteristic	Comment
Outward radial force	Necessary to prop open artery. Excessive radial force can injure wall and promote hyperplasia over time.
Material	Must be biocompatible and non-corrosive. Typical: SS316, Co/Cr Alloys, Nitinol, Polymers.
Radiopacity	Depends on material properties and total mass present. More radiopaque markers or coatings of different material may be added to stent.
MRI artifacts	Depends on material properties.
Profile	Diameter of catheter containing crimped stent. Must be as low as possible.
Expansion ratio	The ratio of deployed to crimped diameter. Higher is better.
Expansion mode	Typically balloon or self-expanding
Foreshortening	Ratio of deployed length to crimped length. Should be 1 for accurate placement
Longitudinal flexibility	Necessary to navigate tortuous arteries. Deployment in curved arteries should not injure wall at ends of stent
Surface treatment	Highly polished and passivated to reduce thrombus and inflammation.
Surface coating	Polymers with embedded anti-inflammatory drugs show promise
Manufacturing method	Typically, laser-machined from tube stock. Also knitted mesh and coils. Thermal treatments may be necessary
Fatigue resistance	Must be able to withstand at least 10 years of cyclic fatigue

40

II.5.2.1 Stent design

The stent design strongly influences the outcome of the revascularization. It is considered the second strongest risk factor as suggested from 3370 patients inspections. The restenosis can be ranged from 20% to 50.3%, depending on the stent type (Jr, et al., 2004).

After the measurement of the artery size, the simulation shown in (Figure II.5-6) studied the impact of carotid SX stent cell design on vessel scaffolding by using patient-specific finite element analysis of Carotid Artery Stenting (CAS).

(Figure II.5-5) and (Figure II.5-6), shows the strut angle distribution for an open and a closed cell design (Conti, et al., 2011). Two different stent designs were simulated numerically and deployed in a vessel created from a micro-CT scan. The numerical simulation was validated experimentally. Then, the stent strut distribution was evaluated for the two stents in five vessel cross sections to evaluate the scaffolding results. The results suggest that a closed-cell design has a better and uniform circumferential strut distribution in the vessel compared to its open-cell stent. However, the full-strut connection design of the closed cell stent reduces the ability of a good accommodation in the irregular profile of the vessel, which leads to gaps between the stent and the aorta.
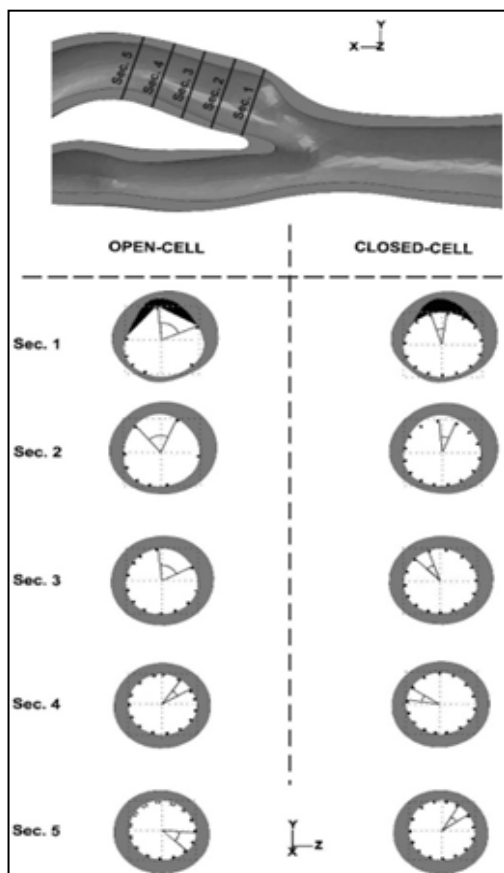
Figure II.5-6: Five ,different vessel cross sections for both stents define the inter-strut angles and show the superior scaffolding with closed-cell design and a better accommodation with open-cell stent in the eccentric profile of vessel (Conti, et al., 2011)
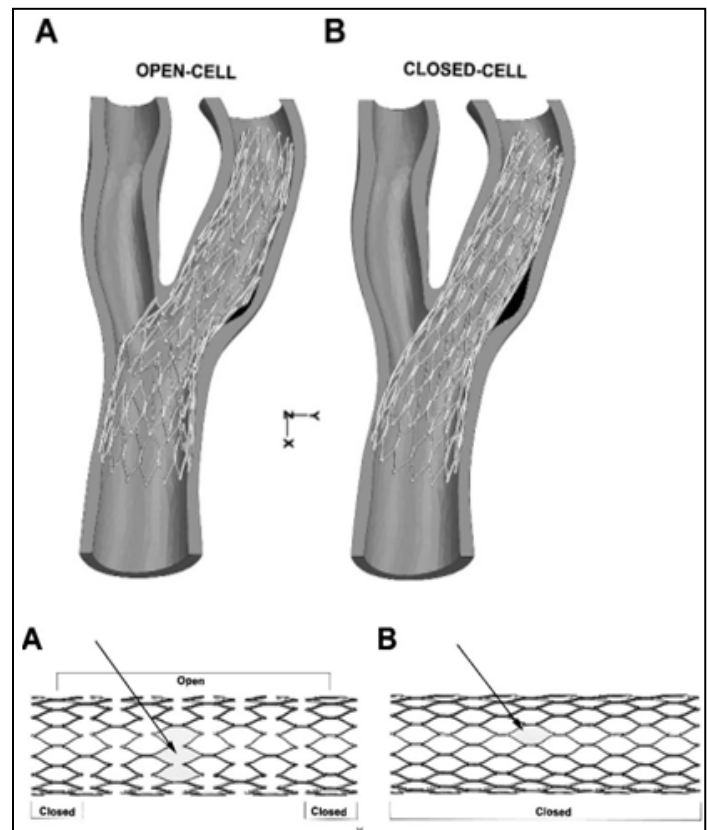
Figure II.5-5: (A) open-cell and (B) closed-cell designs. The gap between the stent and vessel is in black (Conti, et al., 2011)

41

Another study presented by (De Bock, et al., 2012) evaluates the influence of the stent design and the vessel geometry on the mechanics of intracranial aneurysm. Three stent designs were produced and deployed in three patients-specific cerebral aneurysmal vessels. To investigate the design effect, (1) percentage strut coverage (SC) of the aneurysm neck, (2) tortuosity measure (T), the relative change (%) versus the unstented condition and (3) stent apposition to the vessel wall for all cases have been evaluated. This study can predict the stent behavior for a specific patient anatomy (Figure II.5-7) (Figure II.5-8).
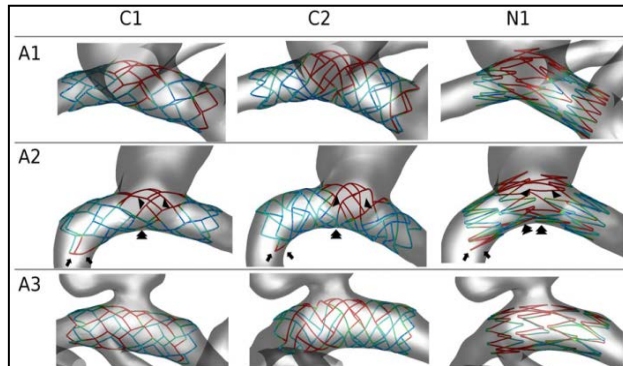
Figure II.5-8: Stent apposition to the vessel wall for all cases
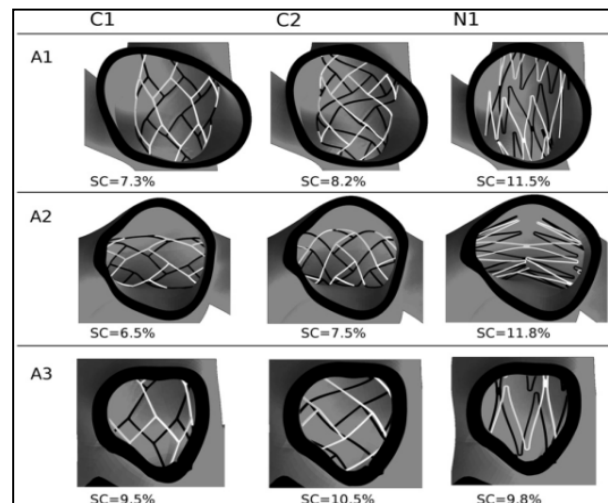
Figure II.5-7: Percentage strut coverage (SC) of the aneurysm neck, for all three designs in the three aneurysm geometries (Bock, et al., 2012)

Two different stent designs provoke two different levels of stress within an atherosclerotic artery and cause different damage values in the lumen of the artery (Figure II.5-9) (Figure II.5-10). This investigation was proved by (Lally, et al., 2005), using finite element study. The atherosclerotic coronary was modeled by a cylinder with localized stenosis. The method presented in this study can be used to develop new stent designs.
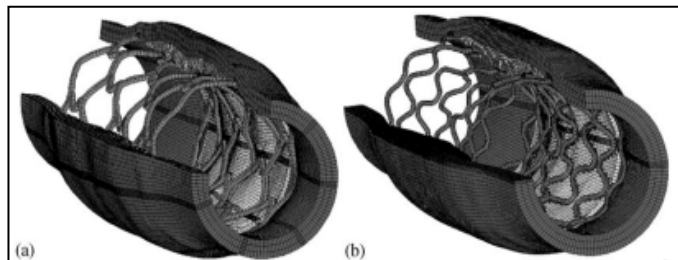
Figure II.5-9: The deformation results of the , stenotic material and stent for two stent designs (Lally, et al., 2005)
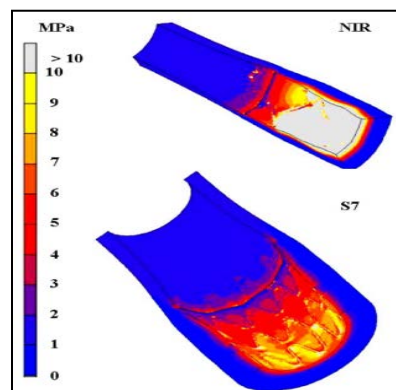
Figure II.5-10: Maximum principal stresses in atherosclerotic vessels treated by two stents (Lally, et al., 2005)

(Figure II.5-11) depicts a simulation using (FEA) of six stents to study the influence of three (SX) stent designs in a Carotid patient-specific Artery (CA). Based on DICOM images of computed tomography angiography (CTA), six stents with different designs were deployed. This study evaluates the stress induced in the vessel wall model based on (CTA) images (Auricchio, et al., 2011). The simulations give a good idea to estimate the relation between a given, real anatomy of the artery and a given stent design.
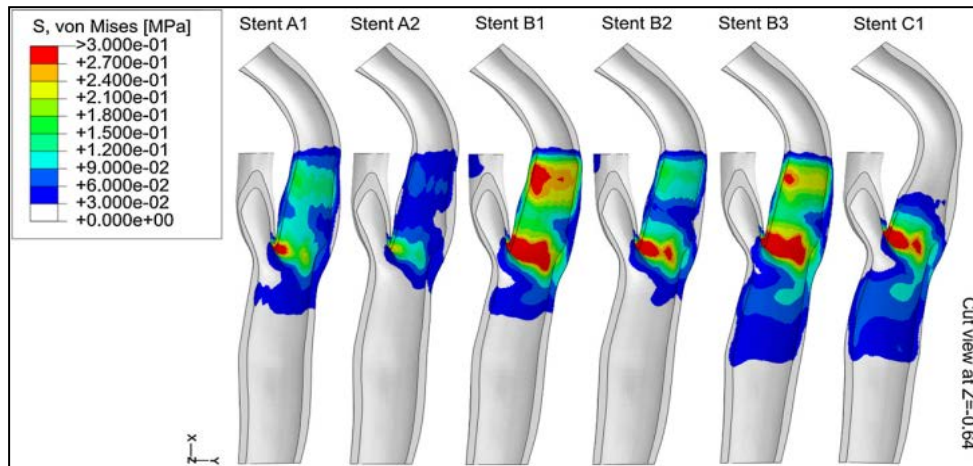
Figure II.5-11: Maximum principal stresses show the radial strength in atherosclerotic vessels stented with six nitinol stents and describe a measure of the damage induced by the stent on the vessel tissue. Auricchio, M. Conti, 2010 (Auricchio, et al., 2011)

Peter Mortier and his colleagues, 2011, (Mortier, et al., 2011) compared the strut opposition for different (BX) stent designs deployed in an idealized stenosed vessel. This study shows the effect of strut design on the stent and the vessel by evaluating the stent strut opposition (Figure II.5-12).
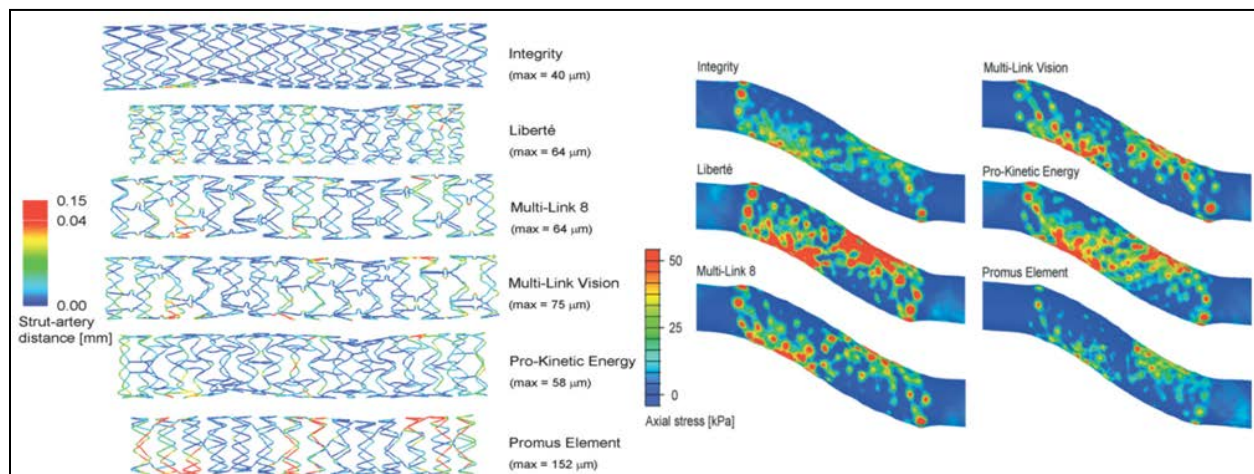
Figure II.5-12: Effect of different stent designs on the vessel and stent stresses (Mortier, et al., 2011)

(Zahedmanesh & Lally, 2009) studied, using (FEM), the influence of the same expanded stainless steel stent design with different thickness (thin and thicker strut) to determine the level of vascular injury in an idealized stenotic artery . This simulation suggests that the thicker stent induces higher stress values on loading in the lumen of the artery (Figure II.5-13). The thinner stent recoils to a greater extend and does not cause the injury to the vessel.
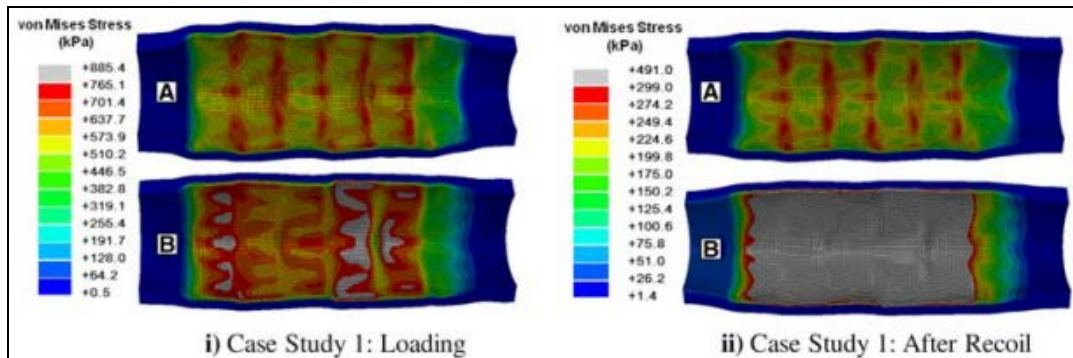
Figure II.5-13: Von Mises stresses in the intima of the stenosed vessels stented with (A) thin and (B) thick stents in loading and after recoil. Case study 1: The two stents were expanded to the same diameter (Zahedmanesh & Lally, 2009)

II.5.2.2 Mechanical and physical properties

The stent must stay in the demanded shape and withstand all the biological stresses in the stenting site. The principal mechanical characteristics or the design requirements of stent material which are necessary to minimize in-stent restenosis and achieve the optimal deployment are:

A. Expanding (Expanded) stent requirements

▪ *Radial force and strength*: The radial pressure of the stent should strong enough to provide an optimal seal and contact without damage the vessel wall. Oversizing more than (15%) can cause adverse effects and damage the vessel wall.

Covered stents consistently cause a smooth increase in radial pressure comparing with bare stents as proved by the experimental research (Marty, 2005). Stent should have enough radial strength in order to resist the compressive forces of the vessel wall (Park, et al., 2008).

(García, et al., 2012) studied the influence of the geometrical parameters on the radial forces during self-expanding stent deployment. Changing the geometrical variables (initial diameter, circumferential and radial thickness), the radial expansion force was calculated. A new stent design (variable radial force/stiffness stent (VF) design) has been used to decrease the damage in the lumen of a healthy area without decreasing the expansion pressure in an atheromatous section. Two vessels were modeled; one with an eccentric atheroma plaque and the second with a constant cross-section vessel. They demonstrated that the new stent design (decreasing the thickness of the stent sides) (Figure II.5-14), decreased the pressure in the healthy lumen zones while preserving its pressure values in the atheromatous section (Figure II.5-15).

44
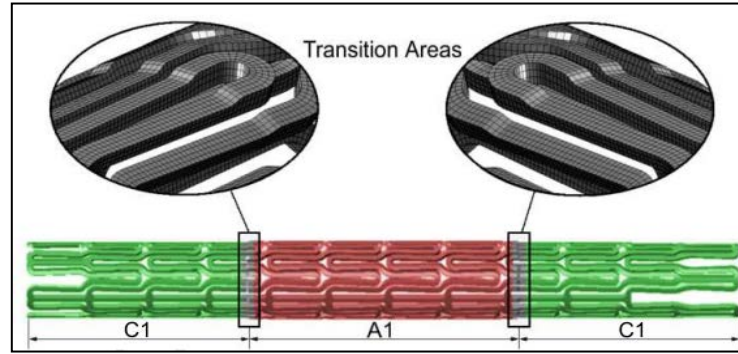
Figure II.5-14: Variable radial force/stainless stent (VF) (García, et al., 2012)
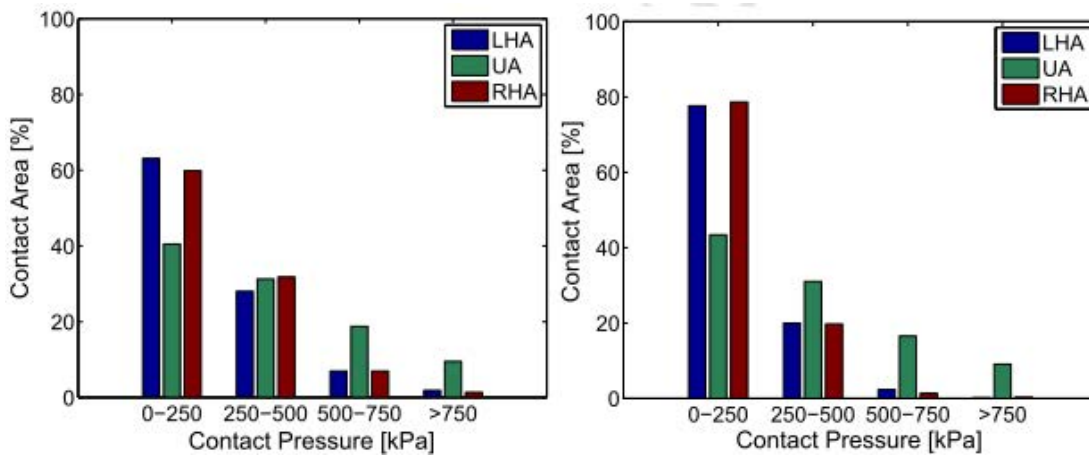
Figure II.5-15: Comparing contact pressure vs. contact areas using Variable radial Force stent (VF) (the right) and Constant radial Force stent (CF) (the left) in a vessel with calcified core Left Healthy Area (LHA), Unhealthy Area (UA) and Right Healthy Area (RHA) (García, et al., 2012)

▪ *Flexibility:* The stent should be flexible enough to allow easy placement and conformity after deployment, offering a sufficient radial strength, especially to conform better to tortuous aortic arches even in the most challenging anatomies. It is evaluated by bending equation of a simple cantilever beam such as:

$$EI = \frac{PL^3}{3\delta} \quad (ƖƖ.26)$$

Where: *EI*: Bending $_{stiffness,}$ *P*: Pressure, *L*: Length$_{stent}$. *δ* Deflection

The conformity of different types of stents is not the same because of the lack of longitudinal flexibility as the study of (Tanaka, et al., 2004) demonstrated. The experimental study compared five types of a self-expanding carotid stents deployed in silicone models of the carotid bifurcation. This method shows that some nitinol stents (such Jostent, SMART and Zliver) enhance the conformity between the stent and a vascular anatomy and have more adaptation with vascular tortuosity comparing with braided Wallstents or the Expander (Figure II.5-16). This method suggests that the segmented designs of modular nitinol stents (Jostent, SMART and Zilver) conform better than the braided Wallstents or the Expander in the tortuous . The study helps to make a good choice to use a specific stent in a given anatomic situation.

45
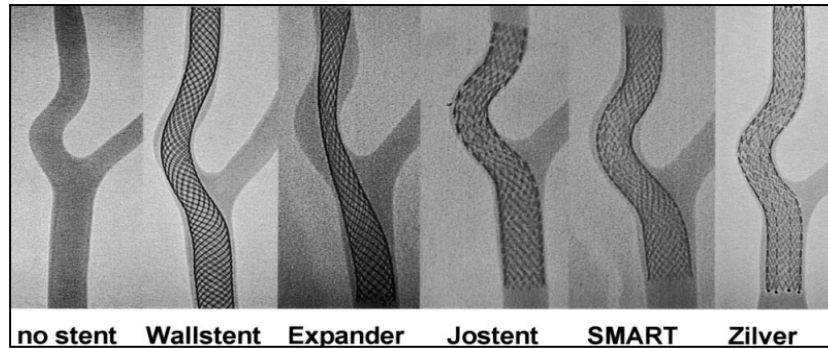
Figure II.5-16: The different conformity of five different stents in a silicon
model of carotid (Tanaka, et al., 2004)

The effect of the curvature of a real and tortuous artery on nitinol stent and mechanics has not been yet validated for (SX) stents. (Zhao, et al., 2011) compared the level of stresses induced in the lumen of an idealized artery using FEM. The simulation showed that the stresses induced by nitinol (SX) stent in a curvature artery were greater than those found in the straight artery (Figure II.5-17).
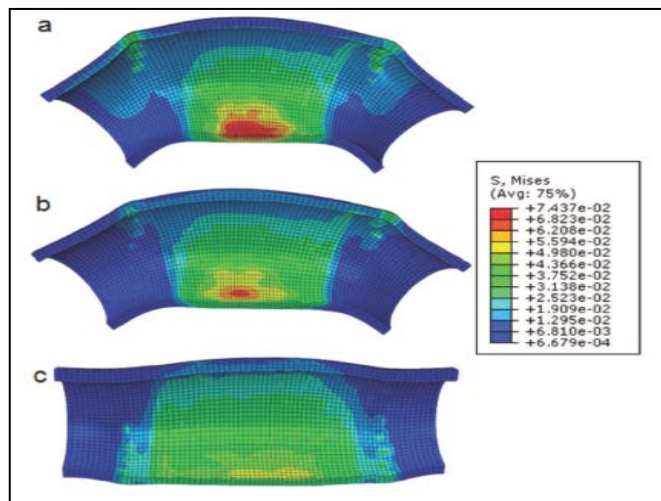
Figure II.5-17: The stress distribution on curved arteries (a) (b) and a straight (c) (Zhao, et al., 2011)

Moreover, (Demanget, et al., 2012) studied the effect of the stent graft design with two materials (Zenith composed of 316L stainless steel (Z-SG) and Aorfix composed of nitinol stent (A-SG). They compared their flexibility by evaluating four criteria, (1) maximal Luminal Reduction Rate (*LR*), (2) torque required for bending (TRB), (4) maximal membrane strains in graft and (4) maximal Von Mises stresses in stents. Using FEM for bending the two stents with angulation >60°, they concluded that A-SG was more flexible than the Z-SG as the values of these criteria were lower in the Z-stent graft (Figure II.5-18) (Figure II.5-19).

46
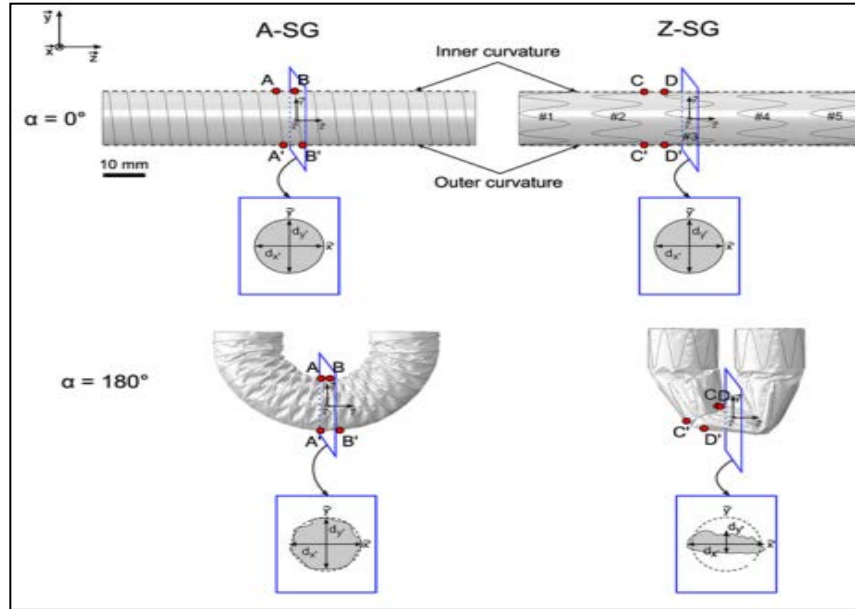
Figure II.5-18: Bending behavior of stent-grafts for A-SG and Z-SG, for α ranging from, 0° to 180°. The change of the cross-section is shown in the bottom of the panel (Demanget, et al., 2012)
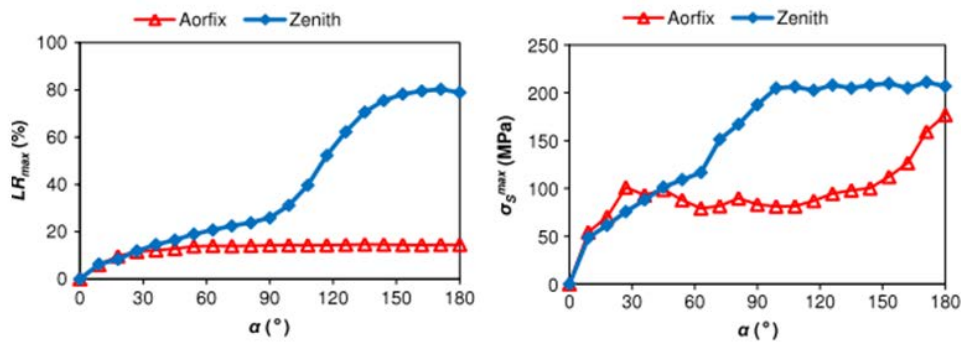
Figure II.5-19: Quantitative assessment of SGs flexibility, (a) LR vs. α, (b): σ_s^{max} vs. α. (Demanget, et al., 2012)

▪ *Low elastic recoil (for BX Stents):* To obtain the optimal contact and seal between the lumen and the stent, the amount of elastic radial recoil must be factored into the expansion of the stent (Beule, 2009). This can ensure achieving a final lumen diameter consistent with the vessel diameter. A measure of elastic recoil may be defined by:

$$\left(R_{load} - R_{unload} \right) / R_{load} \quad \text{(ІІ.27)}$$

Where (R) represents the radius of the stented vessel for full balloon expansion (load) and after deflation of the balloon (unload).

As many research showed, open cell stents have higher flexibility than closed-cell ones, but open cell confers a risk of in-stent stenosis (exaggerated tissue proliferation). Therefore, a flexible stent with a closed-cell structure is required.

47

 Different mesh patterns in the closed-cell stent have different bending stiffness. Varying the geometric configuration of the stent cell, it is possible to get a mechanical flexibility equal to an open-cell structure (Shobayashi, et al., 2010).

▪ *Minimal elastic longitudinal recoil (for BX stents):* After deflation of the balloon, the stent may recoil and a measure of longitudinal recoil may be defined by:

$$\frac{L_{load} - L_{unload}}{L_{load}} \quad (Ц.28)$$

− *Compressibility* for (**SX**): The ability to be compressed easily with large deformation inside the delivery system.

− *Foreshortening*: The decreasing amount of length, which may occur during expansion. Foreshortening should be as small as possible. This is important to minimize the shearing on the endothelial layer, which may harmful the endothelial layer of the artery, (Park, et al., 2008), and to predict the final position of the stent. Foreshortening is calculated as:

$$\text{Foreshortening} = \frac{L_{initial} - L_{final}}{L_{initial}} \quad (Ц.29)$$

Where $L_{initial}$: Original length of stent

▪ *Optimal scaffolding:* This allows the stent struts not to prolapse in the vessel tissue so that the stent should provide uniform and optimal coverage and avoid the struts to be concentrated in specific areas of the vessel (Beule, 2009).

B. Material stent requirements

▪ *Durability and Fatigue:*

Product life is estimated by fatigue durability. FDA and European standard prEN recommend product life of ten years corresponding to 420 500 000 loading cycles (Park, et al., 2008). Many studies tested the fatigue life of nitinol stent under physical loads (Pelton, et al., 2008); (Grujicic, et al., 2011) (Harvey, 2011).
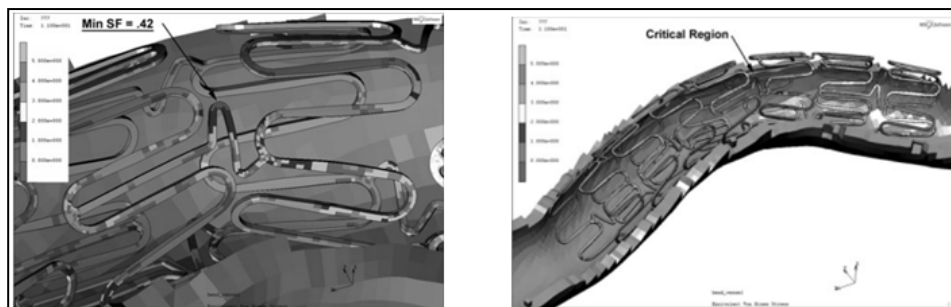
Figure II.5-20: Close-up /of nonhelical stent with safety factors contoured from bending fatigue loading. Minimum safety factor, SF = 0.42 (Harvey, 2011)

48

In the simulation (Figure II.5-20), a fatigue performance was analyzed for two types of stents in two realistic vessel models. This study gives insight into the non-uniform strain distributions of the stent due to the difference in diameter along the artery and complex tortuous nature of the artery. It also evaluates the influence of the stent design on fatigue life, especially in articulation loading conditions.

In peripheral arteries, many challenges are presented as the stents are always subject to be bent and compressed with high rates of restenosis and fracture. (Early & Kelly, 2011) studied the influence of the mechanical environment (bending and compression) on the rate of stent stresses and risks of fatigue fracture. This has been investigated by comparing two models of nitinol and stainless steel stents (Palmaz slotted tube) after deployment in peripheral arteries. The artery was modeled ideally. It was compressed and bent to simulate the physiological loading (Figure II.5-21).

The results suggest that stainless steel stent subjected to bending presents an increase in stresses in all three layers of the artery, which can lead to tissue damage while the shape memory stent presents higher flexibility and smaller stresses, which reduce the damage of the artery (Figure II.5-21). Besides, small amount of compression can generate high strain amplitude values in the nitinol stent. The study also demonstrated that compression can be the essential factor of stent fatigue in femoral arteries, whereas bending is the most significant factor in the popliteal arteries. An appropriate stent should be used according to location.
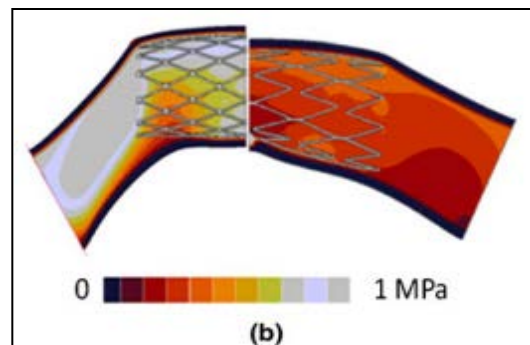
Figure II.5-21: Contour plots of BX (left) and SX (right) following (30°) of bending (Early & Kelly, 2011)

▪ ***Radiopacity:*** To enable precise positioning and evaluation of stents at follow-up under guidance of fluoroscopic imaging (Wnek & BoWlin, 2008).
▪ **Corrosion-resistant** (Wnek & BoWlin, 2008).
▪ ***Biocompatibility*** (Wnek & BoWlin, 2008).

II.5.2.3 Biocompatibility, heamocopatibility and tissue interactions

The bulk and surface properties of biomaterials have a strong influence. In some cases, they control the dynamic interactions that take place at the interface of tissue–implant.

Biocompatibility is the ability of a material to perform an appropriate host response (the reaction of living system to the presence of a material) and not to cause harmful systematic toxic and carcinogenic effects on the host (e.g. corrosion and degradation) or induce harmful response from the host (e.g. immune and inflammation) (Black, 2005) (Shi, 2004).

To have a biocompatible material, the interaction between the stent and biological tissues must be controlled as this device is a long-term implanted device. The stent should perform its task without any negative and secondary effects in the body, e.g. toxic or harmful immunological response. The device has to resist the aggression of biological fluids to inherit the corrosion and the toxic progress. Therefore, advanced coating and finished surfaces on the stent surface are being made to reduce the adverse events induced by blood-contacting devices. Thus, the material must be tested firstly in vitro, then in vivo.

The biocompatibility and biological performance are defined in successive steps as follows:
− Vitro tests: to test the reaction of the materials in vitro, including the investigation of (cytotoxicity, hemocompatibility and genotoxicology.)
− Vivo tests in animals: to assess the cell interaction with the surface properties of the material restenosis (Conti, 2007).
− Qualification of implant materials.
− Standardization and regulation of implant materials (Black, 2005).
− Design and selection of implant materials (Black, 2005).
− Testing the implant of the device into the human body during clinical trials (Conti, 2007).

The traditions metallic materials used in stenting are:
− Stainless steel (austenitic SSs)
− Gold
− Cobalt Chromium alloys: (ASTM F1058), Cobalt chromium L605
− Magnesium
− Nitinol (nickel-titanium)

The intermetallic compound 'nickel-titanium' is considered a toxic material. The bonding forces between their atoms are stronger than that in stainless steel. However, since the TIO2 is formed after proper surface treatment, the testing showed that the nitinol becomes chemically more stable and less corrosive than stainless steel (Chan, et al., 1990). This material showed no harmful effects to surrounding tissue and no allergic reactions. This is the 'Biocompatibility'.

Every material has its strong and weak points, so the choice has to be adapted according to the needs. Nevertheless, the unique properties of nitinol make this alloy particularly suitable for medical devices like SX stents. Nowadays, this material is extensively used and understanding its mechanical behaviour is important.

II.5.3 Nitinol shape memory alloy

In the mid-1990s, nitinol (nickel-titanium) (SX) was introduced in a widespread commercial, medical application and became the first available biomaterial, which makes this material a subject of active interest. Nitinol is known with its superelasticty and thermal shape memory behaviors. These special features can control the shape and stiffness of this material (Kujala, 2003).

II.5.3.1 Thermoelastic martensitic transformation

The mechanism that is responsible for both "superelasticty" and "shape memory" is a solid state phase transformation called "Thermoelastic martensitic transformation".

50

Any shape memory alloy can be in two phases:
- Martensite phase (MS, F) that is stable at low temperature, soft and easily deformable phase
- Austenite phase or parent phase (AS, F) that is stable at high temperature.

In the austenitic phase, the crystal structure has a Body Centered Cubic structure (BCC), (Nickel atom at the center of the crystallographic cube and a titanium atom at each of the cube eight corners). The austenitic phase is microstructurally symmetric and thus has one layout for the atoms (Falvo, 2007).

The martensite phase of nitinol is less symmetric, and its lattice structure consists of a rhombus alignment with an atom at each of the rhombus corners. The martensite can be in two alignments based on the level of an applied stress (Figure II.5-22) (Figure II.5-23).

The transformation between the two faces on an atomic scale (martensite and austenite) describes the unique behaviour of nitinol, which is called "Thermoelastic Martensitic Transformation (TMT)" (Falvo, 2007). Nitinol material can be transformed thermally or mechanically from austenite to martensite and vice versa as follows:

1. Reducing the temperature (Thermally Induced Martensite, TIM) or (shape memory property)
2. Applying a mechanical load in austenitic phase (Stress Induced Martensite, SIM). (Superelasticty).

Therefore, the transformation from austenite to martensite, or vice versa, can thermally or mechanically be triggered. The mechanism by which a single martensite varies from austenite by cooling is called; 'Twinning' (multi-variant martensite). Applying a mechanical loading on the martensitic structure, martensitic variants reorient into a single variant. The reorientation mechanism is called; 'Detwinning' (single-variant martensite), which is the cause of the shape memory effect (SME) (Falvo, 2007). A pure mechanical stress in the material while it is in austenitic phase can produce the martensitic phase transformation. In this case, detwinned martensite is directly produced from austenite (the cause of superelasticty).
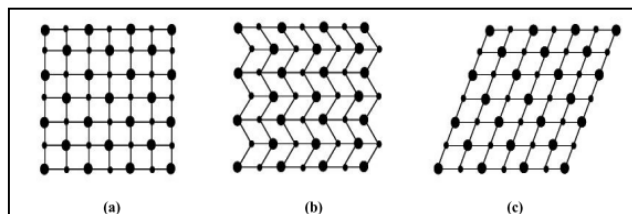
Figure II.5-23: (a) Austenite, (b) twinned Martensite, (c) detwinned martensite (Falvo, 2007)
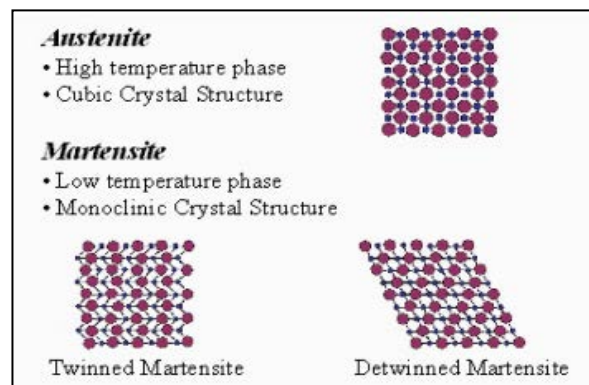
Figure II.5-22: Different phases of a shape memory alloy

II.5.3.2 Shape Memory Effect (SME) (Thermal Shape Memory)

The shape memory is a result of thermo-elastic martensitic transformation (Thermal Phase Transformation). If we cool a specimen from a fully austenite phase at a high temperature, then the martensite starts to form at a specific temperature (M_S) (Figure II.5-24). By further cooling to the temperature (M_f), the specimen will be wholly martensite (process is complete) where the metal is soft and easily deformable. If the metal is reheated, a reverse transformation process will

take place starting from the austenite start temperature (A_S) until completing the process at the austenite finish temperature (A_f). Both martensite and austenite phases coexist during the phase change from martensite to austenite and vice versa.

The shape memory effect means that when we deform the material plastically in a fully martensitic phase. This permanent macroscopic deformation will disappear by heating the specimen above (A_f). Its original shape and stiffness are restored (austenite). Strain of 6-8% can be restored, allowing full shape recovery where the maximum value of elastic strain in steel or aluminum is about l% (Wijst, 1992) (Melzer & Stoeckel, 2010) (Figure II.5-25). The difference between these transition temperatures upon heating and cooling is called hysteresis. The transformation temperature is dependent on alloy composition and processing history. Therefore, nitinol has made it possible to prepare functional implants made active at body temperature (Falvo, 2007) (Figure II.5-26) (Figure II.5-27).
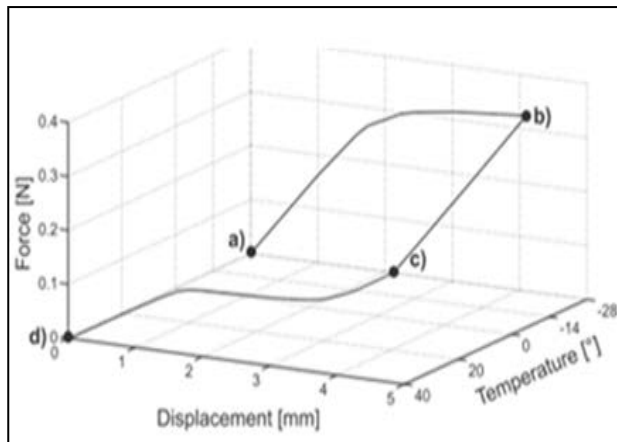
Figure II.5-25: Numerical simulation shows the reaction force and axial displacement versus temperature (Auricchio & Reali, 2008)
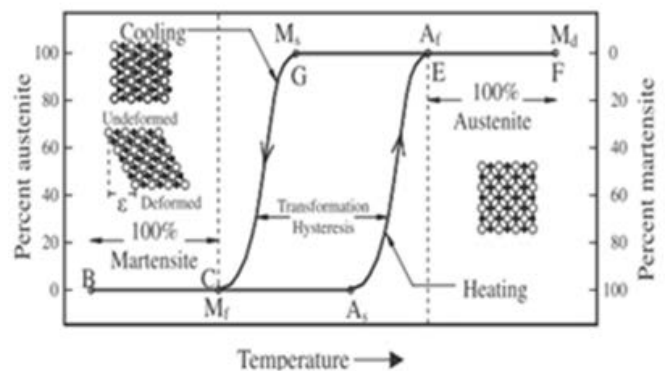
Figure II.5-24: The martensite-austenite transformation. The crystal structure and the mechanical properties of the metal are altered as a result of the temperature change, h = hysteresis. (Alam, et al., 2007)
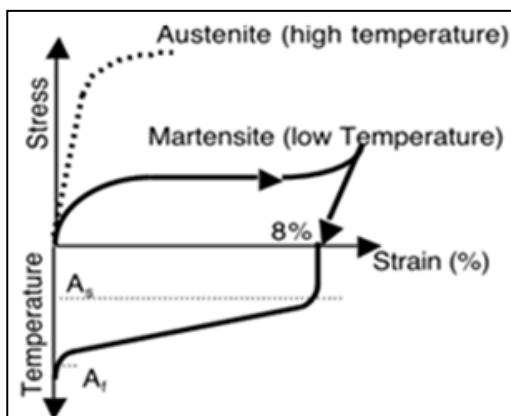
Figure II.5-26: (SME) strain stress temperature relation in shape memory
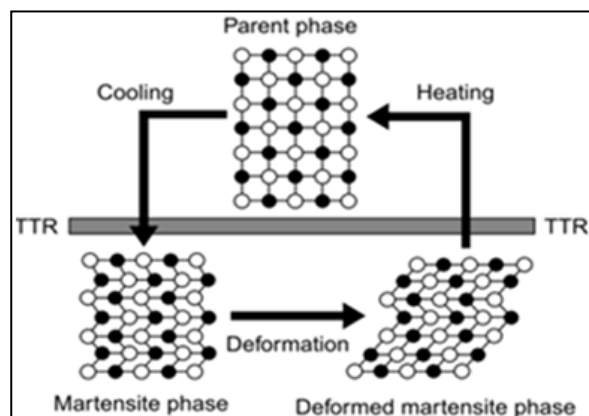
Figure II.5-27: Schematic illustration of shape memory effect, TTR: certain phase-transformation temperature range

52

− (A_S): The temperature at which the transformation from martensite to austenite begins on heating.
− (A_f): The temperature at which the transformation from martensite to austenite finishes on heating.
− (M_S): The temperature at which the transformation from austenite to martensite begins on cooling.
− (M_f): The temperature at which the transformation from austenite to martensite finishes on cooling.
− (M_d): The maximum temperature after which the superelasticty is lost.

In one-way shape memory effect (OWSME), the shape recovery is achieved only during heating (T>A_f) and it will not deform like before if it is re-cooled again. As a result, successive heating and cooling does not have any macroscopic effect, but only the first heating after loading. In one-way shape memory effect (SME): re-cooling the material, the austenite transforms into multi-variant (twinned form). Therefore, a new deformation occurs only by stressing again and not by re-cooling (Figure II.5-28) (Figure II.5-29).
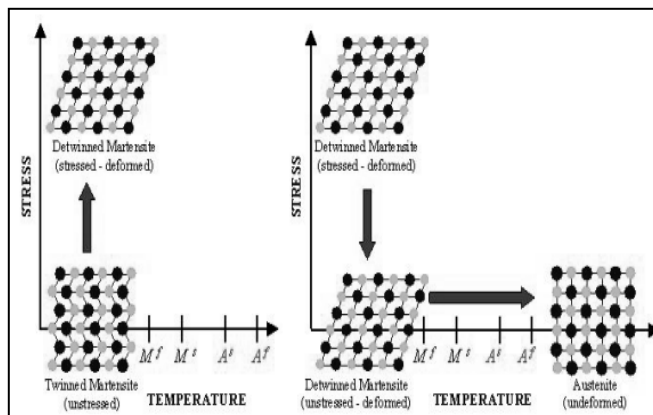
Figure II.5-28: Macroscopic range in One way shape memory effect (Darjan, 2007)
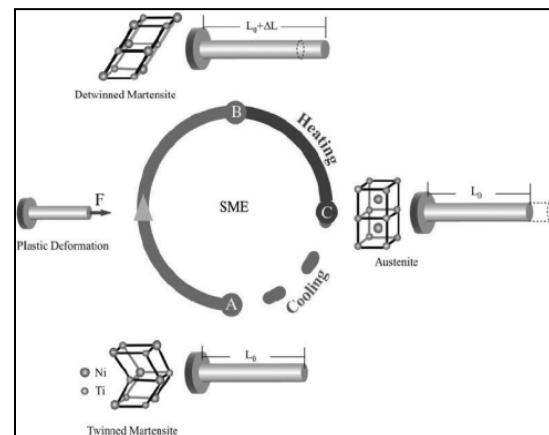
Figure II.5-29: One way shape memory effect (Falvo, 2007)

In two-ways shape memory alloy (TWME) (Figure II.5-30) (Figure II.5-31), the shape of the material change in a reversible way upon both cooling and heating (thermal cycling). It remembers its parent phase shape and its martensitic shape only by changing of temperature across (A_f) and (M_f).
(TWME) can be cycled between two shapes without the need of external stress. It differs from the One Way Memory Effect (OWME) in three aspects:
1. The shape deforms and changes during cooling.
2. Infinite repeatability of the shape memory effect by thermal cycling (heating and cooling).
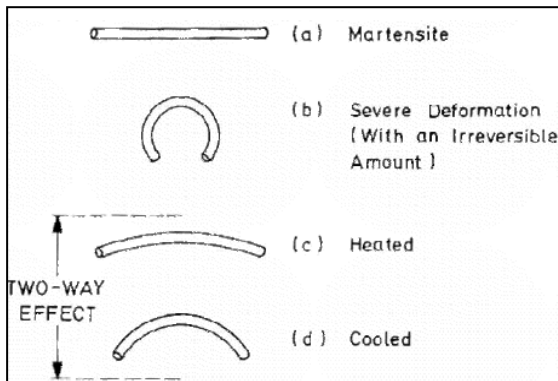
Figure II.5-30: Two way shape memory effect
(TWME) (Darjan, 2007)
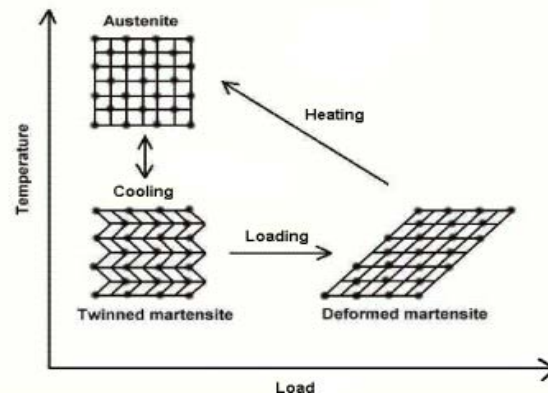
Figure II.5-31: Macroscopic range (Darjan, 2007)
In two-ways shape memory alloy

II.5.3.3 Superelasticty or pseudoelasticity or rubberlike behaviour (SE)

Superelasticty, as well as shape memory, is the result of a solid state transformation (stress induced phase transformation), which can be triggered mechanically. It can be described by the ability of the material to return to its original shape upon unloading after being restrained and deformed much greater than normal materials. Therefore, the transformation process is preceded by increasing only an applied stress at a high temperature and reversed by releasing the stress.

In the superelastic material, we start from temperature range above (A_f), i.e. at austenite phase. The martensite transformation starts and proceeds continuously increasing the applied stress until transforming into a 'Detwinned Martensite' which is not stable at high temperature (this transformation produces a substantial amount of strain). Thus, the transformation is continuously reversed back into austenite when the stress is released, and the original shape of the metal is restored (all these processes occur only in a certain temperature range, i.e. T > (A_f). The relation stress-strain exhibits a flag shape (Figure II.5-33).

Superelastic deformation up to (8%) is possible without permanent plastic deformation of the metal. It can be strained several times more than ordinary metal alloys without being plastically deformed. Alloy composition, material processing, and ambient temperature significantly affect the superelastic properties of the material (Conti, 2007). The stress-strain curve (Figure II.5-33) shows the behaviour of a sample of NiTi deformed in uniaxial compression (the initial temperature is 296 K) which is, in the room temperature, the austenitic phase.

54
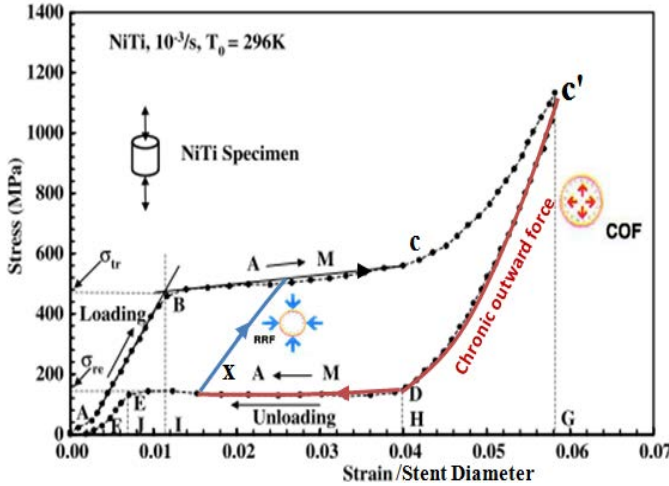
Figure II.5-33: A. stress-strain curve superelastic effect of NiTi SMA after 42% cold work followed by 30 min annealing 823 K. (Nasser & Guo, 2006)
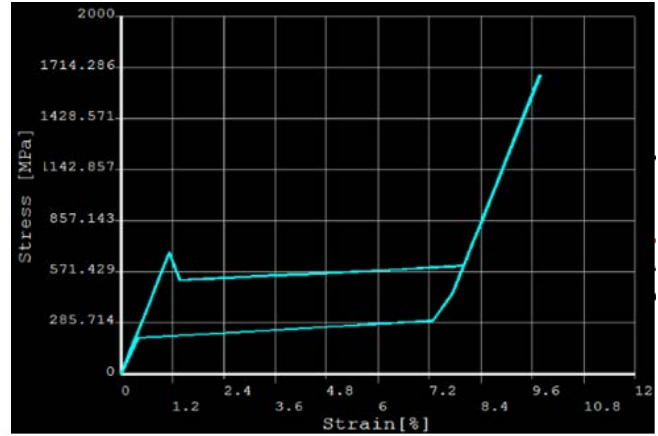
Figure II.5-32: Numerical simulation: stress-strain curve superelasticty behavior of one ring loaded and then unloaded by two rigid surfaces

Numerical simulation of superelasticty behaviour of one ring of stent (Figure II.5-34) is described by stress-strain curve (Figure II.5-32).
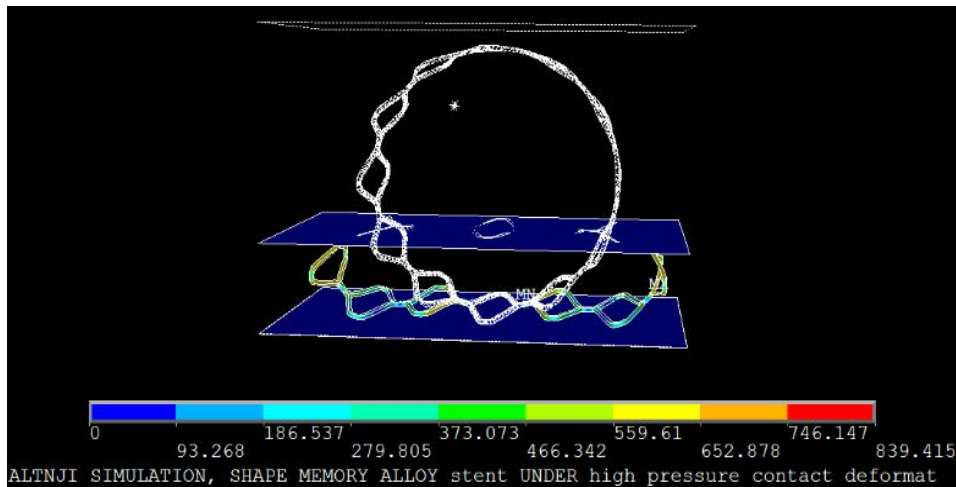
Figure II.5-34: Numerical simulation: superelasticty behavior of one ring of stent shows deformed and undeformed configuration in a prospective view at almost the end of the loading step. In the lower panel the Von Mises stresses are depicted at the end of the loading

Starting from point A in the austenite phase, the material is loaded elastically until point B. |AB| represents the elastic deformation of the austenitic phase.

At point B, microscopic martensite starts to be formed until the transformation is complete at point C. Upon point C, increasing stress deforms the material elastically until the maximum stress-induced phase-transformation is attained at point C'. After point C', the material will plasticize and fails. The stress (σ_{tr}) represents the austenite to martensite transformation stress.

At point C', if the stress is released, the strain will be completely recovered in several stages:

- ▪ |C'D| corresponds to elastic unloading of the martensite reaching at point D, at which the reverse martensite to austenite transformation starts with stress(σ_{re}).
- ▪ |DE| corresponds to the reverse martensitic transformation which starts at D until the parent phase is totally restored at point E (The reverse transformation on the |DE| segment occurs at almost a constant stress).
- ▪ |EF| corresponds to the elastic unloading of the austenite.

In the stent application, the expanded stent arrives to the artery diameter by the elastic equilibrium between the stent and the vessel wall. Further expansion of the stent is prevented and the stent, appositions itself against the vessel wall with a low outward force "Chronic Outward Force" or "COF". On the other hand, the stent will resist a recoil pressure or any external pressure with a "Radial Resistive Forces" or "RRF", which is steeper and higher than (COF) (Stoeckel, et al., 2004) (Figure II.5-33).

Superelastic material takes place over a specific range of area, and the material is superelastic at temperatures ranged from (A_f) to (M_f) (If the temperature exceeds the maximum temperature at which martensite occurs (Md), the SMA and SE properties will be lost and the material behaves like an elastio–plastic material (Figure II.5-35) (Figure II.5-36). Below (A_S), the mechanical loading in the martensitic phase induces reorientation of the variants. The material is martensitic and is not totally recovered upon unloading.
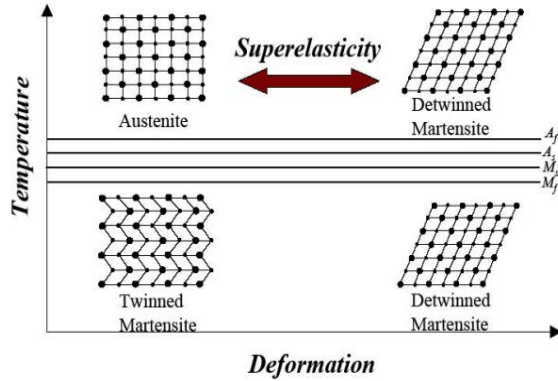
Figure II.5-35: Mechanical behavior of a NITI alloy as a function of temperature (Nasser & Guo, 2006)
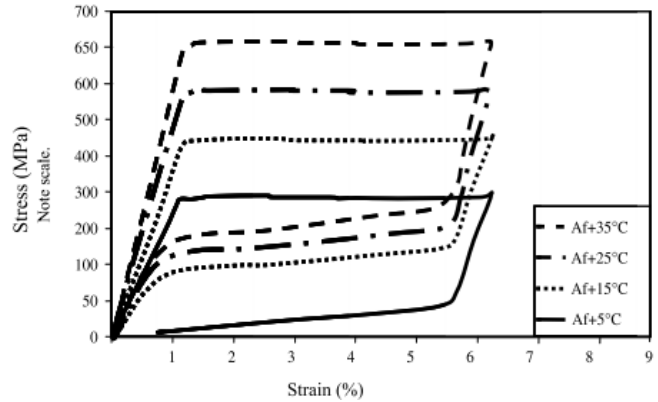
Figure II.5-36: The stress–strain response of nitinol with increasing temperature (Nasser & Guo, 2006)

II.5.3.4 Dissipated energy in superelastic loop

(Figure II.5-33) shows two different-path curves in loading and uploading with an area enclosed between them (hysteresis loop). It represents the energy dissipated during transformation from austenitic to martensitic, during loading and the reverse transformation. When the superelastic material is loaded, it dissipates a certain amount of energy without a permanent strain. The total amount of energy area during both loading and unloading is the total energy input per volume during the loading (ABCC'G) minus the energy release per unit volume during unloading (FEDC'G). Thus, the dissipated energy, per unit initial volume, is given by:

$$E_{DISP} = A_{ABCC'G} - A_{FEDC'G} = \oint_{Aloop} \sigma . d\varepsilon \quad \text{(Ц.30)}$$

Where: (σ) is the engineering stress, and (ε) is the engineering nominal strain.

56

II.5.3.5 Mechanical behaviour of a NITI alloy as a function of temperature

As mentioned before, the nitinol behaviour is strongly depending on the temperature (Figure II.5-37).

In SME: At low temperature, in the martensite phase, i.e., $(T \leq A_S)$ (point 0); if the alloy is deformed (mechanical loading), the strain will not be completely recovered, and some residual strain will take place upon unloading. That is a result of the reorientation of twin variants of atoms that results in a large inelastic strain, which is not recovered upon unloading (point 2). This is described in Curv 1 in (Figure II.5-37). However, this strain will totally be recovered if the SMA is heated above (A_f) and the atoms reassemble themselves so that the material completely recovers its original shape, points (3) (4) (5) (curve in strain-temperature plane). Only one variant of martensite will remain if enough stress is reached (curve1 point 1). Otherwise, the material will contain different variants if we released the stress in the midway.

In SE: At high temperature, i.e., $(M_d) > T > (A_f)$, starting from the point (5), the stress curve develops as a result of the transformation of austenite to detwinned martensite as follows:

- From point (5) to (6), the material is in the austenite phase. The austenite is elastically loaded (strain<1%).
- At point (6), increasing the stress will transform the austenite to martensite until the material will be wholly martensitic (detwinned) at point (7). From point (6) to (7), the material has an austenite-martensite phase with long and constant stress plateau and large strain (1%–6%).
- From point (7) to point (8), if the stress is increased, the material deforms elastically with large strains (>8%). At point (Y), a followed stress will plasticize the material until the fracture at point (F).
- From point (8) to point (9), this curve is a result of elastic recovery upon stress removal (elastic unloading of the martensite.)
- From point (9) to (10), the reverse transformation to austenite starts (at almost a constant stress) due to the instability of martensite at $T > (A_f)$ until the parent phase is completely restored at point (9).
- From point (10) to (11) (corresponding point 5) represents the elastic recovery in the austenite phase.
- The area enclosed by the loading and unloading represents the amount of dissipated energy.

At very high temperature, i.e., $T > (Md)$, the unique property of the material (SE) and (SMA) will be lost, and an applied stress does not generate the (SE). In this case, the material behaves like an elastio–plastic material as shown in curve 3 (Figure II.5-37) (Alam, et al., 2007).
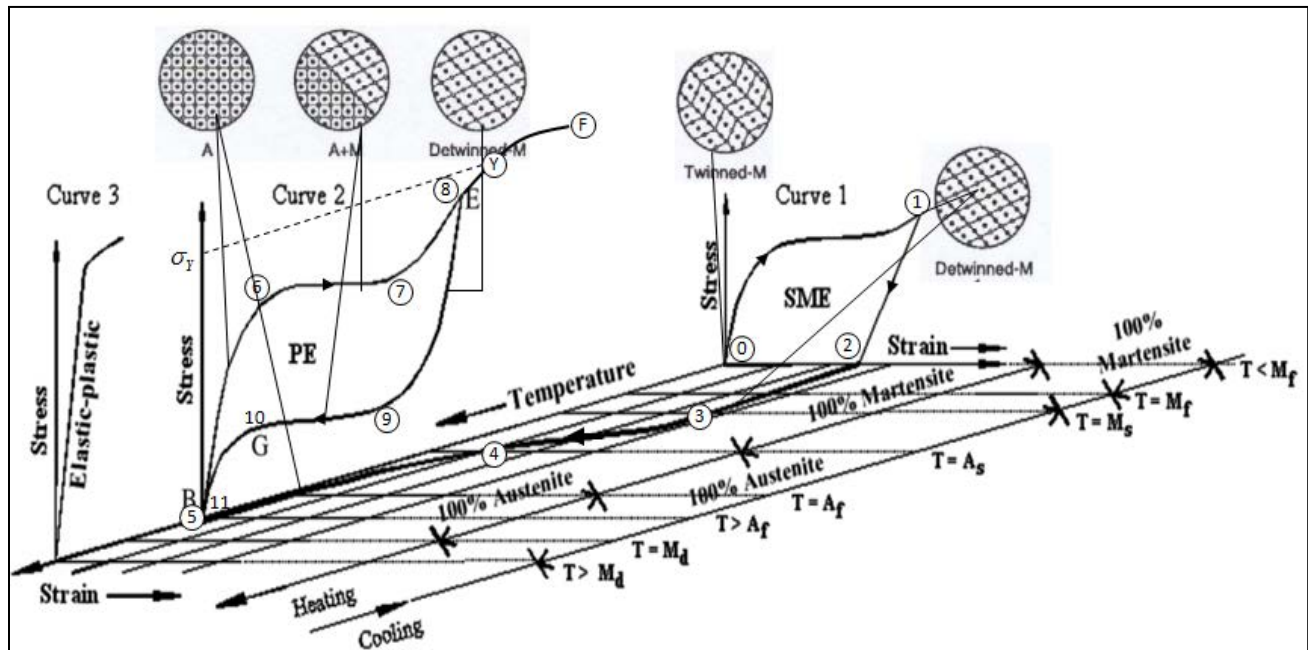
Figure II.5-37: Three-dimensional stress (Σ)-strain (δ/L)-temperature (θ) diagram of shape memory alloy showing the shape-memory effect (SME) In martensite state, superelasticty (SE) during austenite–martensite phase transformation, (Shaw, 2002), (Reprinted from Dolce Dolce and Cardone 2001, with permission from Elsevier; Vivet et al. 2001, with permission from Elsevier; and Cardone et al. 2004, with permission) from reference (Alam, et al., 2007)

The unique behaviors of nitinol make it an ideal biomedical material used as self-expanding stents and other applications. The stent with a specific transition temperature can be compressed by a catheter. It will be always deformed and compressed until we arrived at the desired location. Depending on (SME), the body temperature warms up the stent and makes the transformation to austenite; as a result, the stent will recover its original expanded shape. The stent has to be built with a specific transition temperature 40° and constrained in the delivery system until exceeds the transition temperature. This is the 'thermal deployment'.

In the elastic deployment, the stent will be constrained in a delivery system at austenite phase. The delivery system will be introduced to the desired place, and by a gradual withdraw from the delivery system, the superelastic stent expands and recovers its original shape depending on (SE) property.

Considering the amount of the elastic recoil, the stent has to be built with a diameter greater than the diameter of the artery to have a good radial force. This is called the 'elastic deployment'. Nitinol-based devices can return to its original shape if it was deformed by external forces, which is not the case for other materials. The self-expanding stents (SX) have a higher flexibility than (BX) stents. They also reduce endothelial damage and allow for more uniform radial expansion, with less longitudinal shortening.

II.5.4 Engineering model for nitinol

II.5.4.1 Conception

The published and existing models that simulate (SMA) can be classified into two types:

– Macroscopic models

– Microscopic models: simulate the macroscopic behavior from the microstructure mechanism of deformation (Lu & Weng, 1997) (Gao, et al., 2000) and (Guthikonda, et al., 2007).

As explained earlier, (see II.3.2), a macroscopic phenomenological model is used to describe the mechanical behaviour of nitinol material, which is suitable for FE simulation. Modeling such complex behaviour needs to understand the thermodynamic process involved and the macroscopic effects as well as the phase transformation (kinematics and kinetics). Any given macroscopic model is characterized by its assumptions and its approximations.

A macroscopic model can be:

1. Phenomenological (Use of the phenomenology): The model can simulate the experimentally observed behavior. Most of models use this approach because of its simplicity. Furthermore, the needed parameters are easy to measure experimentally. The phenomenological constitutive models are based on continuum thermodynamics with internal variables.

Many models have been developed like: (Brinson, 1993) (Aurrichio & Sacco., 1999) (Ikeda et al., 2004), see reference (Khandelwal & Buravalla, 2009). The numerical implementation of phenomenological models has also been developed (Auricchio, 2001) (Auricchio et al., 1997) (Govindjee and Miehe, 2001) (Qidwai and Lagoudas, 2000a) (A Khandelwal et al., 2009), see reference (Khandelwal & Buravalla, 2009). Therefore, we prefer the phenomenological models as their mathematical equations are suitable to be implemented into a finite element software. The following classification may be considered to the phenomenological theories.

Phase diagram based models

Several models for evolution kinetics in SMAs use a σ-T phase diagram to identify appropriate transformation. The models are governed by appropriate evolution functions defined to compute the extent of phase transformation.

- *Plasticity based models using phase diagram*: The models are based on plasticity achievement, i.e., the well-established principles of the theory of plasticity. (Auricchio and coworkers).

- *Phase Diagram based models for arbitrary Loading*: The models are capable of predicting SMA response under arbitrary thermomechanical loading (Bekker & Brinson, 1997).

2. Macroscopic thermodynamic based models (Free Energy Based Models): The models can simulate several macroscopic effects experimentally observed, and explain the underlying physics consistent with mathematical formulation that is based on continuum mechanics principles within a thermodynamic formulation (Leclercq & Lexcellent, 1996) (Lexcellent et al ,2000) (Kishore Kumar et al, 2007), see reference (Khandelwal & Buravalla, 2009).

The constitutive model used in this study is a phenomenological model considering the large deformation proposed by (Auricchio, et al., 1997). This model captures the three-dimensional behaviour that reproduces the 'superelastic behavior'. The model focuses on a new behaviour of inelastic, based on an internal variable formulation and known as 'generalized plasticity'.

59

The proposed model simulates the superelastic behavior, basic features of SMA, different material behaviour in tension and compression and single-variant martensite reorientation process (Auricchio, et al., 1997).

To start the modeling, the phase transformation (austenite, martensite) can be explained by the change of the atomic structures occurring during the phase transformation (kinematic). Increasing the stress above the threshold temperature (> Af) makes the active of the phase transformation from austenite to martensite.

When the martensite starts to be formed within the austenite, internal stresses are induced and partially relieved by the formation of a number of different variants of martensite. If there is no preferred direction for the occurrence of the transformation, the martensite tends to form a twinned structure, and the product phase is called 'multiple variant martensite'. If there is a preferred direction for the occurrence of the phase transformation, the martensite tends to form a de-twinned structure and is called 'single-variant martensite'. The conversion of a single-variant martensite to another single-variant martensite is possible and is called 'reorientation process' (Auricchio, et al., 1997)

In this model, the phase transformation coincides with a martensitic volume fraction where only one single phase variant is considered. The activation of the phase transformation is controlled by a 'Drucker–Prager' flow criterion, which is known for plasticity in soil and concrete materials (Reese & Christ, 2008).

II.5.4.2 The continuum mechanics superelastic constitutive model

Assuming the isotropy of the material, the phase transformation mechanisms involved in the superelastic behaviour are:
- Austenite to martensite (A→S)
- martensite to Austenite (S→A)
- martensite reorientation (S→S)

The total strain experienced by the material is given by the equation:

$$\boldsymbol{\varepsilon} = \boldsymbol{\varepsilon}^e + \boldsymbol{\varepsilon}^{tr} \quad (\text{Ц.31})$$

Where $(\boldsymbol{\varepsilon}^e)$ is the elastic strain and $(\boldsymbol{\varepsilon}^{tr})$ is the transformation strain, $(\boldsymbol{\varepsilon}^{tr})$ is given by:

$$\boldsymbol{\varepsilon}^{tr} = \varepsilon_L \boldsymbol{\varepsilon}' \quad (\text{Ц.32})$$

Where (ε_L) represents the maximum deformation obtainable by only detwinning of the single variant martensite and $(\dot{\boldsymbol{\varepsilon}})$ is the scaled transformation strain. As internal variables, we assume $(\dot{\boldsymbol{\varepsilon}})$ and the single variable martensite fraction (ξ_s). During each of the three transformation processes, these internal variables change to each process as:

$$\dot{\boldsymbol{\varepsilon}}' = \dot{\boldsymbol{\varepsilon}}'^{AS} + \dot{\boldsymbol{\varepsilon}}'^{SA} + \dot{\boldsymbol{\varepsilon}}'^{SS} \quad (\text{Ц.33})$$

$$\dot{\xi}_s = \dot{\xi}_s^{AS} + \dot{\xi}_s^{SA} \quad (\text{Ц.34})$$

60

We consider in the following two of the above phase transformations that is (A→S) and (S→A) where the material is composed of two phases; the austenite (A) and the martensite (S). Then, we introduce two internal variables; the martensite fraction (ξ_s) and the austenite fraction (ξ_A). One of them is a dependent variable. They are assumed to satisfy this relation at each time, where the independent variable chosen here is (ξ_s):

$$\zeta_s + \zeta_A = 1 \quad \text{(Ⅱ.35)}$$

Some phase transformations (A→S) and (S→A) are pressure-dependent. To model such an effect, we introduce the Ducker-Prager loading function as:

$$F(\sigma, T) = \|\mathbf{t}\| + 3\alpha p + CT \quad \text{(Ⅱ.36)}$$

Where: ($\mathbf{t}$) is the diviatoric stress tensor: ($\mathbf{t} = \sigma - \frac{tr(\sigma)}{3}\mathbf{I}$), and ($p$) is the hydrostatic pressure: $p = Tr(\sigma)$, (α), (T) are a material parameters.

The initial and final transformation functions are given by:

$$\begin{aligned}
F_s^{AS} &= F^{AS} - R_s^{AS} \\
F_F^{AS} &= F^{AS} - R_f^{AS}
\end{aligned} \quad \text{(Ⅱ.37)}$$

The following linear kinetic forms for the evolution of the martensite fraction (ξ_s) are then defined as:

$$\dot{\xi}_s = \begin{cases} -H^{AS}(1-\xi_s)\frac{\dot{F}}{F-R_f^{AS}} & (A \to S) \; (Austenite-to\;single-variant\;martensite\;transformation) \\ H^{SA}(\xi_s)\frac{\dot{F}}{F-R_f^{SA}} & (S \to A) \; (Single-variant\;martensite\;to\;austenite\;transformation) \end{cases} \quad \text{(Ⅱ.38)}$$

Where: (H^{AS}), (H^{SA}): are activation factors relative to the two evolutionary processes defined as:

$$H^{AS} = \begin{cases} 1 & if \; R_s^{AS} < F < R_f^{AS} \; A \to S \; transformation \\ \\ 0 & otherwise \end{cases} \quad \text{(Ⅱ.39)}$$

$$H^{SA} = \begin{cases} 1 & if \; R_f^{SA} < F < R_s^{SA} \; S \to A \; transformation \\ \\ 0 & otherwise \end{cases}$$

And $R_f^{AS} = \sigma_f^{AS}(\sqrt{\frac{2}{3}} + \alpha)$ where: $(\sigma_f^{AS}), (\sigma_f^{SA})$ are material parameters shown in the (Figure II.5-

$R_f^{SA} = \sigma_f^{SA}(\sqrt{\frac{2}{3}} + \alpha)$

38).
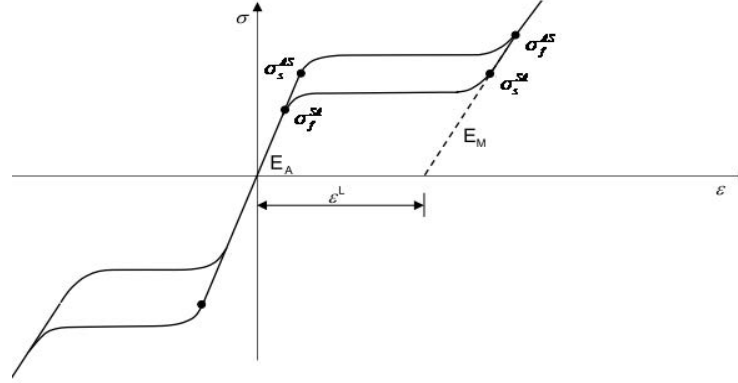
Figure II.5-38: Parameters for stress-strain behavior of the
ABAQUS UMAT for superelastic shape memory alloys

Where: $R_s^{AS} = \sigma_s^{AS}(\sqrt{\frac{2}{3}} + \alpha)$ and: $(\sigma_s^{AS}), (\sigma_s^{SA})$ are material parameters shown in (Figure II.5-38)

$R_s^{SA} = \sigma_s^{SA}(\sqrt{\frac{2}{3}} + \alpha)$

and:

$$\alpha = \begin{cases} 0 & \textit{if} \text{ tensile and compressive beavior are the the same} \\ \\ \dfrac{\sigma_c^{AS} - \sigma_t^{AS}}{\sigma_c^{AS} + \sigma_t^{AS}} & \text{otherwise, where } s_t^{AS}, s_c^{AS} \text{are initial value of austinite to martensite} \\ \text{phase transformation in tension and compression} \end{cases} \quad (Ц.40)$$

The numerical implementation of such a model in a finite element setting was developed writing a user-material subroutine (UMAT/Nitinol) following the model proposed by (Auricchio, et al., 1997). (UMAT) is considered the communication link between ABAQUS and the SMA model. Rebelo et al have developed a user-defined material subroutine UMAT (Abaqus standard) and (VUMAT) (Abaqus explicit) for nitinol (Rebelo, et al., 2001). The main computational program calls the material subroutine for each integration point of the FE model at each iteration, where the local stiffness matrix is calculated according to the constitutive model for the material.

The subroutine was developed according to the rules for user-material subroutines provided by ABAQUS using the following data:
− Material parameters required by the subroutine. The material parameters for NiTi SMA used in the analyses are taken from straightforward observations of experimental tests.

62

– Definitions of 'Input parameters' that are passed from the calling program to the subroutine and 'Output Variables' that are returned by the subroutine to the calling program (Abaqus user subroutine reference Manuel). The output of the subroutine is the updated value of the stress tensor and the tangent stiffness tensor, as well as the values of all solution-dependent (internal) variables, such as the martensitic volume fraction and the transformation strain.

The results from the constitutive model and numerical procedure were compared to representative, physical experiments and have been well tested to be used robustly for all applicable elements.

The numerical model is a mechanism based continuum mechanics and based on generalized plasticity. This theory is based on the concept of generalized plasticity and physical principles (Rebelo, et al., 2001). The algorithm provides an efficient integration scheme and is based on a discrete execution of the evolutionary equations developed in the model. The theory has strain decomposed into two parts: a purely linear elastic component ($\Delta\tilde{\varepsilon}^{el}$) and a transformation component ($\Delta\tilde{\varepsilon}^{tr}$) (Rebelo, et al., 2001).

$$\Delta\tilde{\varepsilon} = \Delta\tilde{\varepsilon}^{el} + \Delta\tilde{\varepsilon}^{tr} \quad (\text{ЏI}.41)$$

The austenite-to-martensite transformation (evolution law) is driven by the resolution of shear forces, and it takes place within a range of stress levels that are the characteristics of the material (Rebelo, et al., 2001).

$$\Delta\tilde{\varepsilon}^{tr} = \varepsilon_L \Delta\xi \frac{\partial F}{\partial\tilde{\sigma}} \quad (\text{ЏI}.42)$$

The incremental stress-strain relationship is:

$$\Delta\tilde{\sigma} = \widetilde{D}\left(\Delta\tilde{\varepsilon}^{el} - \Delta\tilde{\varepsilon}^{tr}\right) (\text{ЏI}.43)$$

Where:

$(\widetilde{D})$: Fourth-order elastic stress-strain matrix.
$(\Delta\tilde{\varepsilon}^{tr})$: Incremental transformation strain.
(ε_L): Material parameter shown in the (Figure II.5-38)
(ξ): The fraction of martensite and *(F)* is a transformation potential

$$F^s \leq F \leq F^F \quad (\text{ЏI}.44)$$

The intensity of the transformation follows a stress potential law:

$$\Delta\xi = f(\tilde{\sigma}, \xi) \quad (\text{ЏI}.45)$$

The reorientation of the martensite can be produced by changing the stress direction. Moreover, a temperature change will produce a change in the stress levels at which the transformations take place. Since the volume increase is associated with the transformation, it requires less stress to produce the transformation in tension, and more in compression (Rebelo, et al., 2001).

II.6. Advances in finite element stent/ artery modeling

The Finite Element Method, also called Finite Element Analysis (FEA) is a numerical-mathematical technique, which generally involves the use of a computer program where the simplified differential equations can be solved with computational techniques. FEM is used to virtually simulate and predict the behaviour of a complex physical problem (a boundary value problem) when the analytical solutions are not available.

This method involves:

1. The discretization of the boundary value problem (entire continuum domain) into several sub domains (elements) connected to one another at their corners or vertices (nodes) over which the interpolation functions are generated. The variables (e.g., displacement, stress, or velocity components) within each of these elements are constrained and approximated by an interpolation method (interpolating functions are traditionally piecewise polynomials and are known as 'basis' or 'shape functions'). The typical interpolating functions include linear and quadratic functions, cubic, splines.). Physical loads are applied gradually over steps after defining the boundary conditions and the state variables.

2. An approximate solution of the variables over the entire physical structure is solved from the assembly of the individual elements. The equations that define the behaviour of the unknown variable, such as the equations of motion or the relationships between stress and strain or strain and displacement, are generated for each element independently in the form of matrices. Then, the matrices are reformulated into a global system of equations for the entire discretized domain.

3. The final step in FEA involves solving the global system of equations for the unknown vectors of variables.

The output of this numerical computer technique will be a graphical representation that shows the stress (or strain) field being analyzed. Elements are color-coded to represent the magnitude of stress (or strain) in each element.

Unlike traditional analytical methods that use a higher level of mathematics, the finite element method is based on simple algebraic equations. The FE is more versatile for complex cases and better than other numerical methods like Finite Differences (FD). It becomes more common in rehabilitation and biomechanics applications to determine stress and strain on body segments, joints, devices, and a variety of arterial geometries and diseased arteries that have also been modeled to provide clinicians with useful information to guide treatment options.

The finite element method has also been employed to predict stresses in the walls of both cerebral and aortic aneurysms as well as to predict rupture of the aneurysms.

64
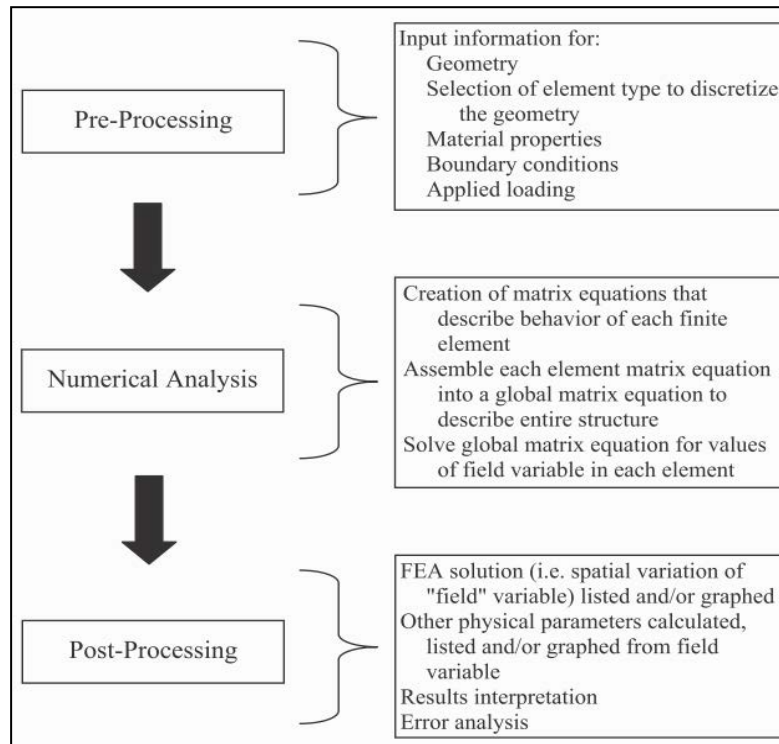
Figure II.6-1: General steps followed in finite element analysis.

FEM application in the study of aneurysms and its rupture has been improved; however, the following complications may decrease the accuracy:
− The difficulty in getting the patient-specific material properties since the tissue cannot be removed without surgery.
− The unclear material failure criteria.
− The difficulty that prevents quickly converting a patient specific geometry into FEM results.
− The difficulty of accounting for all the biological effects in one finite element model.

The finite element method (FEM) is particularly suitable for simulating complex geometry. It has been applied to numerous studies of the artery wall and other biological tissues.

The geometric models can be created by three ways:
− Only CAD software, which does not have a powerful and fast way to model the realistic complex geometries like biological tissues.

− CAD software based on medical image. This technique uses reverse engineering. This is a process of generating mathematically accurate 3-D CAD models of existing anatomical structures from measured coordinate data. For instance, a bone or artery tissue reconstruction involves these following steps:
▪ Acquisition of MRI series to collect spatial data.
▪ Export the data to CAD software. Then, it can be mathematically represented by fitting a series of closed boundary curves to be then graphically displayed and manipulated.
▪ The fitted curves will be lofted to reconstruct complete and functional surfaces.
▪ Export the final object model to FEM package.

65

– Medical imagery software: This advanced technique is particularly suitable in biomechanics modeling. It uses the segmentation of 3D medical images coming from (CT, MRI, micro CT, Ultrasound…) to create directly excellent, accurate and realistic 3D models of the anatomy. Then, export it to FEM package (ABAQUS, ANSYS, COSMOS…). Mimics software (Materialise, Leuven, Belgium) is an effective tool to make an accurate 3D reconstruction starting from DICOM images.

When we create the discretization or dividing 3D continuum domain, the polyhedral element shape can be tetrahedral (four triangular faces) or hexahedral (six quadrilateral faces). Each element is defined by nodal coordinates and a choice of interpolation basis functions (Bock, et al., 2012). A fully automatic hexahedral mesh generation algorithm for many geometries is still challenging while in tetrahedral meshes, the user can generate meshes without performing geometry decomposition. However, the hexahedral mesh is a preferred approach in many applications because of the excessive computational overhead, the oscillations and the instability of tetrahedral elements (Figure II.6-2) (Figure II.6-3).

Some advanced software can create a hexahedral mesh like PyFormex (an in-house developed open source program under developing for generating and manipulating geometrical models of 3D structures by mathematical operations (http://www.pyformex.org). It can also mesh the stent after precise geometrical transformation (Figure II.6-3).
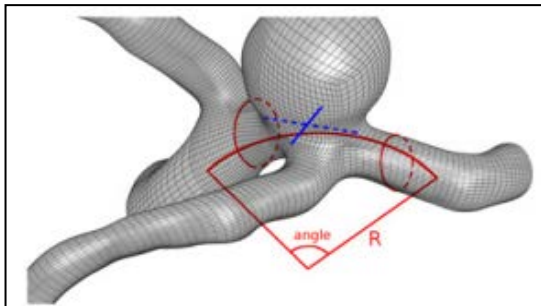
Figure II.6-3: Geometric vessel and aneurysm meshed using hexahedral element by PyFormex
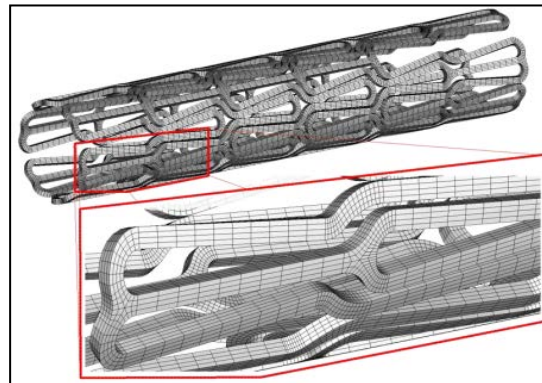
Figure II.6-2: Stent meshed using hexahedral element by PyFormex

An example is given for reconstructing 3D artery-stent using Mimics and PyFormex to export the final 3D mesh into the FEM package. Generally, the steps are as follows:

– Processing a DICOM CTA images (micro CT scans) as planar slices of the interested anatomy (-stent).
– The DICOM images are then analyzed by Mimics (http://www.materialise.com/mimics) that reconstructs a real 3D geometry. The secondary branches are removed.
– For meshing the stent with hexahedral elements, the STL stent file is virtually rolled to generate a planar mesh. The planar mesh is then converted to the final 3D mesh through appropriate geometrical transformations (Figure II.6-4).

66

– Generate an STL file that is subsequently imported into the PyFormex software to generate a parametric high-quality and full hexahedral mesh for the artery (Figure II.6-5).
– Export the final meshed geometries to FEM pancakes like ABAQUS, as PyFormex directly creates the input files for the (ABAQUS).
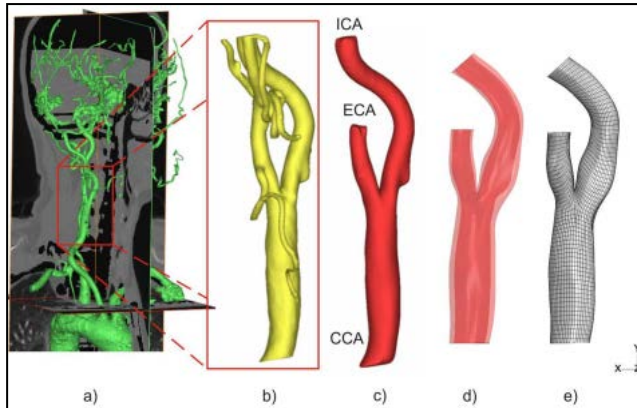
Figure II.6-5: Patient-specific Carotid (CA) model. (a): 3D reconstruction of vascular anatomy. (b), (c): lumen of CA, main and secondary branches. (d): reconstructed outer vessel wall profile. (e): The hexahedral mesh (Auricchio, et al., 2011)
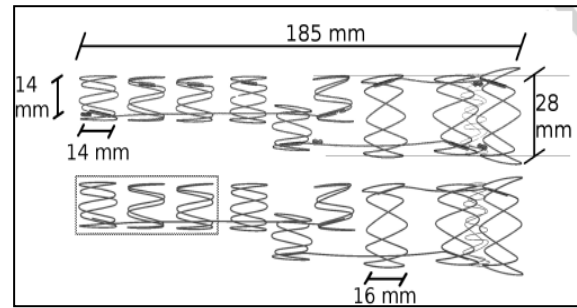
Figure II.6-4: Micro CT surface reconstruction (top) and FEA model (bottom) of the nitinol stent graft wires (Bock, et al., 2012)

The exact mechanisms can be used to create a model with fluid-structure Interactions (FSI). This FEM model performs flow and stress/strain analysis for atherosclerotic plaques and evaluates the critical flow and stress/strain conditions in the plaque (Figure II.6-6).
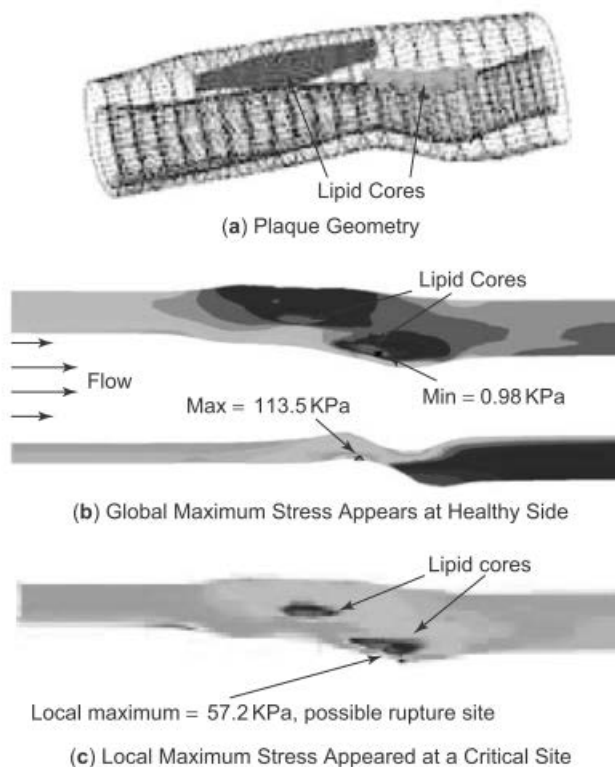
Figure II.6-6: Local stress/strain extreme values. (a): the plaque geometry, (b) sagittal slice showing maximum stresses, (c) the

67

The power of technical advanced image and finite element computer simulations can be shown in the study presented by S. De Bock and his colleagues. The work consists in simulating the deployment of a bifurcated stent graft in a patient-specific (AAA) model. This simulation evaluates the mechanics of endovascular aneurysm and can retrieve many important mechanical parameters of the stent graft.

The stent geometry was reconstructed from high resolution CT scans to be then reconstructed as a surface by Mimics software (Figure II.6-8). Using geometrical operations, the stent surface was unrolled and clipped into small wire parts to be then reconstructed as wires. The Dacron membrane was added to FEM model. Mimics were used to extract the surface of a silicon aneurysm after the image reconstruction of the silicon model to be then included in the FEM. The results of numerical simulation were validated in vitro using a mock aneurysm (Figure II.6-7); (Bock, et al., 2012).
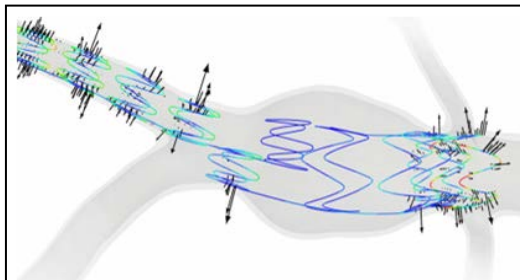
Figure II.6-8: Contour plot of the maximum principal strain in the stent wires
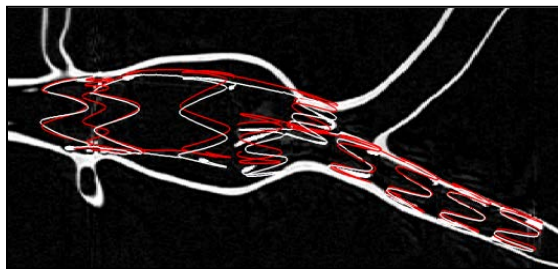
Figure II.6-7: 3D models of the experimental deployment (Bock, et al., 2012)

Mathematical and computational modeling of a stent or blood flow in the arteries should include the geometry of the artery, material properties, governing equations derived from conservation laws and proper initial and boundary conditions. Idealized and advanced geometries can be obtained by image-based techniques. Computational modeling research helps to minimize the risk associated with stent-graft and improve the surgical success rate. In the next chapters, FEM of a complete stenting system was developed to investigate the mechanical complications associated with stent deployment in a realistic thoracic aneurysm.

The objective of our research

The main and mid-long terms-mechanical related-problems of (EVAR) are migration and endoleak type Ia (Lumsden, et al., 2007). Endoleak type Ia occurs when a persistent blood flow develops due to the incomplete and ineffective seal at the attachment zone of the endograft device (Hakaim, 2005) (Veith & Baum, 2003). The flow will apply a pressure force on the lumen of the aneurysmal wall leading to rupture. The migration is defined as the movement of endograft greater than 10 mm which leads to endoleak type Ia.

The main anatomical criteria that could exclude patients from (EVAR) however concern the dimensions and morphology of the proximal and distal aneurysm neck. Stent graft dimensions and design: (proximal and distal landing zones, oversizing value) at one of the seal zones may result in endoleak type I or graft migration increasing the risk of aneurysm rupture.
These complications have been undergone to clinical investigations and can be related to one or all of these factors: endograft under sizing (Thomas & Sanchez, 2009) (Thomas & Sanchez, 2009) (Bosman, et al., 2010), high drag forces due to the severe angulation (Sternbergh, et al., 2004) (Albertini, et al., 2001), insufficient length of proximal attachment site (Fulton, et al., 2006) (Zarins, et al., 2003) or stent graft folding (Wolf, et al., 2001).

The main objective of this work is to find, based on a 3D (FE) platform, the mechanical, morphological and stent design factors which lead to stent migration and can cause a stent collapse or a poor contact between the stent and the aorta at the attachment sites. This was accomplished by evaluating the contact stiffness in the interaction area (stent-aorta) after stent deployment using a Coulomb frictional model in a short-term stent fixation frame. Therefore, seven parameteric stent models were used to evaluate the following deployment failure factors in a patient-specific (TAA): (1) the Proximal/Distal Attachment Site Length (P/D-ASL), (2) the stent Oversizing values (O %), (3) different contact friction behaviors (stent-aorta) and (4) the proximal neck angulation. The calcification impact on the biomechanical behaviour of the deployment at the attachment zone has also been investigated.

Then, based on the numerical results, new design stents were proposed and investigated. The next major goal is to evaluate the new design improvement acquired for 'contact stiffness improvement', stent flexibility and stiffness and prevention of 'migration failure' or stent collapse comparing with the old designs.

Chapter III

Virtual Stent deployment simulation in a patient-Specific Aneurysmal aorta

In this chapter, we present the numerical geometry development procedure of both specific-patient aneurysmal thoracic aorta and stent device with the mathematical formulation of their constitutive laws. The models are then combined, and computer implementation of finite element methods was performed to simulate the device deployment procedure. First, we aim to find the principal mechanical factors which lead to stent migration or poor contact between stent-aorta at the attachment sites.

Summery

III.1. Introduction

Migration and endoleak type I phenomena are considered the principal reasons for (EVAR) failure. Wide differences of opinions exist regarding the nature of these critical complications. The consensus was reached that migration and endoleak type I are related to non-complete and ineffective contact or seal between the endograft ends (proximal or distal graft aspects) and the wall of blood vessels. In this chapter, a numerical simulation of a complete, stenting system using (FEM) has been developed in order to evaluate the contact stability and the mechanical deployment of a self-expanding stent in a complex morphology of realistic human-aneurysmal thoracic aorta based on Computed Tomography Angiography (CTA). A parametric study was performed to understand the direct impact of the most related-migration or non-effective contact factors. Depending on the proximal and distal contact stability, we evaluate the impact of: (1) proximal landing zone length (PLZ), (2) oversizing value (O %), (3) proximal neck angulation (α), and the pathological state of the aorta represented by the means of different coefficients of friction *(μ)*.

The simulations will investigate the mechanisms and the self-expanding stent behaviour, including large displacements and deformations under complex mechanical loading conditions in a realistic human pathological aorta. Since the stent- mechanical interaction is considered one of the significant causes of migration and endoleak, it is necessary to understand the vessel behavior and stent performance on the biomechanical interaction with the vessel.

Furthermore, stent-graft deployment, especially in the thoracic aorta, experiences complex forces which might lead to the risk of stent-graft migration or stent collapse. This fact makes the investigation of the aorta curvature impact on stent-aorta interaction an important issue in order to evaluate the contact strength of the stent at the attachment site and its conformity with the vascular anatomy. The finite element study will consider the realistic and the complex geometry of a patient-specific aneurysm. Depending on the aim of the study, the tissues can be modeled as an isotropic-incompressible hyperelastic material or can take into account the anisotropic hyperelastic behaviour. The first approaches can capture the stent and tissue deformation while the second approach is more suitable to study: the stress distribution in the vessel wall or the mechanics of rupture.

The aneurysmal thoracic aorta model was reconstructed based on DICOM CTA images. The stent was modeled starting by a half of strut defining global variables and equations. All the analysis was performed in the frame of classical continuum (macroscopic) mechanics with a filled volume under the hypothesis of large strain conditions. The constitutive equations that describe the behaviour of the aorta and superelastic nitinol stent were assigned to the geometry models.

In general, we agree that the role of graft tissue is only to provide a passage for blood flow with negligible impact on the whole mechanical behavior of stent-graft. Thus, the fabric covering is not included in this study.

71

III.2. Aneurysm geometry model

III.2.1 Patient specific aneurysm models

The aneurysmal aorta model used in this study represents a realistic, specific and pathological case of a human aorta. This model was selected from an image database collected by the cardiological hospital in Lyon-France. The planar slices obtained from the micro-CT scans (Figure Ш.2-1) were imported into Mimics (Materialise, Leuven, Belgium) to make the segmentation and reconstruction of 3D medical images in highly accurate 3D models of the patient anatomy. The DICOM images of the thoracic aneurysm were processed using Mimics v.15. The reconstruction interval of the planar slices obtained from the micro-CT scans was 0.73 mm (38). The images were contiguous (slice thickness equal to reconstruction interval). The region of interest was then selected and the secondary branches were removed (Figure Ш.2-2).

In our case, the pre-stenting vessel centerline should be calculated to guide stent positioning as we will see later. Mimics (medCAD module) also offer interactive centerline measurements, due to the implementation of advanced algorithms. Centerline measurement tool in mimics is powerful and time-saving. The centerline of the vessel can also be extracted from the vessel geometry using 'vmtk' (the vascular modeling toolkit) (Bock, et al., 2012).
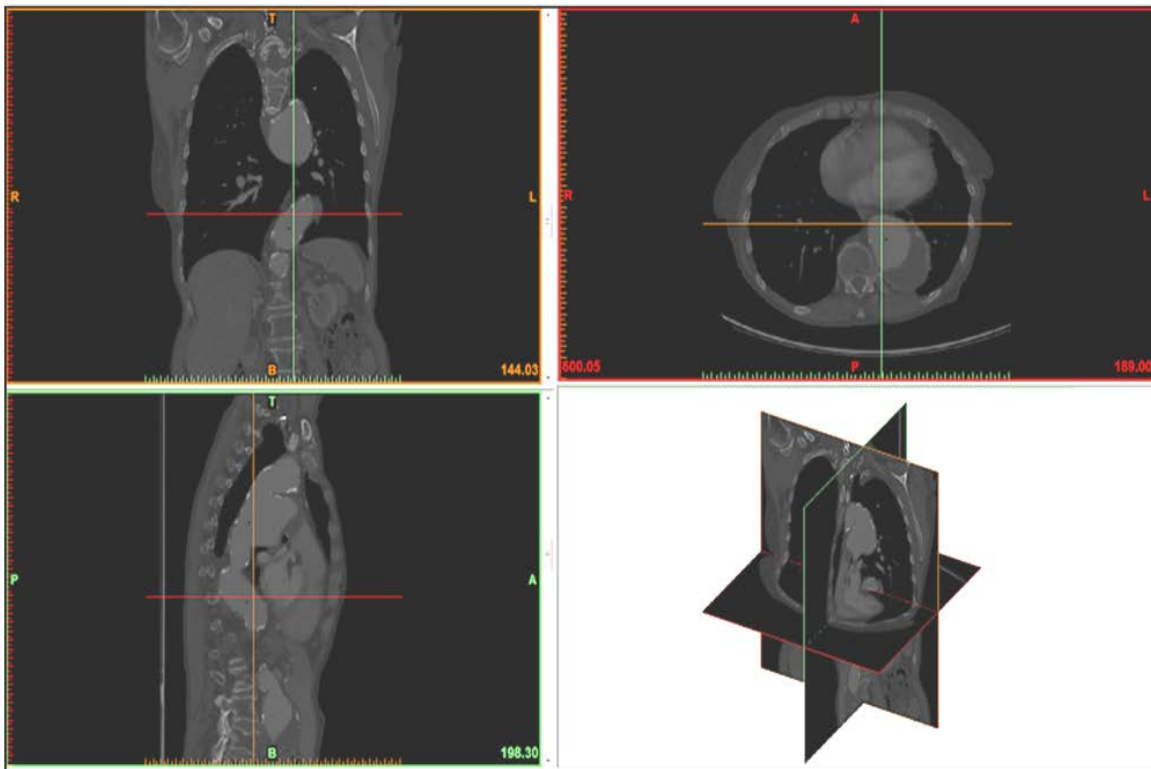
Figure III.2-1: Micro-CT scans images; the reconstruction interval of the planar slices obtained from the micro-CT scans was 0.73 mm (38). The images were contiguous (slice thickness equal to reconstruction interval).

(Figure Ш.2-2) shows the numerical morphological criteria model for thoracic aneurysm with the main definitions.

72
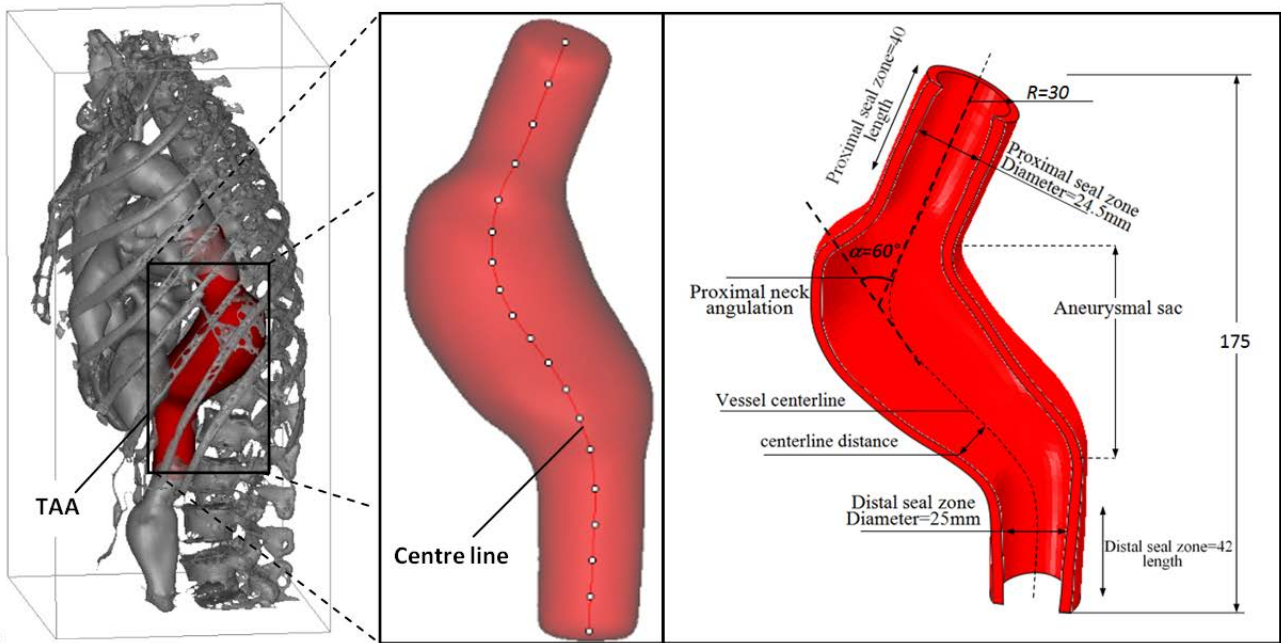
Figure Ⅲ.2-2: reconstruction of the aorta with centerline extraction and the main definitions regarding the morphological criteria for (TAA). Dimension in (mm)

The STL file can be processed within Matlab (Natick, MA, USA) to define a set of splines identifying the cross sectional contours of the aneurysmal aorta. The CAD model is then obtained by means of lofting procedure from the spline curves imported in Abaqus. This CAD model can be useful only if it was discretized by tetrahedral elements, which are not always preferable.

III.2.2 Finite element model

III.2.2.1 Introduction

In the physiological condition, the aorta can be considered as incompressible material (Carew, et al., 1968). Therefore, the mechanical behaviour that describes the isotropic or anisotropic behaviour of the aorta can be modeled under this assumption. In addition, Abaqus/Standard assumes that the hyperelastic material is incompressible by default. Abaqus/Explicit assumes that the material is nearly incompressible (Poisson's ratio is 0.475 by default). For the algorithms to work efficiently, Abaqus/Explicit cannot assume that the material is fully-incompressible. Thus, we must provide enough compressibility for the code to work and the material will be considered a quasi-nearly incompressible. It was defined as $(K_0/\mu_0=20)$ where (K_0) is the initial bulk modulus and (μ_0) is the initial shear modulus.

Relative compressibility of a material is defined by the ratio of its initial bulk modulus (k_0) to its initial shear modulus (μ_0). Poisson's ratio (υ) also provides a measure of compressibility since it is defined as:

$$\upsilon = \frac{3(k_0 / \mu_0) - 2}{6(k_0 / \mu_0) + 2} \quad \text{(Ⅲ.1)}$$

73

III.2.2.2 Formulation of quasi incompressible isotropic hyperelastic material

As mentioned earlier, in the field of computational mechanics, it is often advantageous to give a slight behaviour of compressibility (change of volume) to the material in order to avoid numerical complications in the finite element analysis. The Hyperelastic compressible material is able to sustain finite strains with volume changes. This material has different behaviour in bulk and shear. Thus, in *compressible hyperelasticity*, we often split the local deformation into a so-called: *volumetric part* and: *isochoric part* (Flory, 1961). The decoupled representation of strain-energy function $\Psi = \Psi(\mathbf{C})$ is given by the function:

$$\Psi(\mathbf{C}) = \Psi_{vol}(J) + \Psi_{iso}(\bar{\mathbf{C}}) \quad \text{(Ш.2)}$$

Where $\Psi_{vol}(J)$ and $\Psi_{iso}(\bar{\mathbf{C}})$ describe the so called volumetric or (volume changing) or (dilational) elastic response and the isochoric or (volume-preserving) or (distortional) elastic response of the material respectively.

We also perform a multiplicative decomposition of ($\mathbf{F}$) and ($\mathbf{C}$) as:

$$\mathbf{F} = (J^{1/3}\mathbf{I})\bar{\mathbf{F}} = J^{1/3}\bar{\mathbf{F}} \quad \text{(Ш.3)}$$
$$\mathbf{C} = (J^{2/3}\mathbf{I})\bar{\mathbf{C}} = J^{2/3}\bar{\mathbf{C}} \quad \text{(Ш.4)}$$

($J^{1/3}\mathbf{I}$) and ($J^{2/3}\mathbf{I}$) are associated with (*volume changing deformation)*, while ($\bar{\mathbf{F}}$) and ($\bar{\mathbf{C}}$) are associated with (*volume-preserving deformation)* of the material with: $\det(\bar{\mathbf{F}}) = \bar{\lambda}_1\bar{\lambda}_2\bar{\lambda}_3 = 1$ and $\det(\bar{\mathbf{C}}) = (\det(\bar{\mathbf{F}}))^2 = 1$, where $(\bar{\lambda}_\alpha = J^{-1/3}\lambda_\alpha)$; $\alpha = 1,2,3$.

The Second Piola-Kirchhoff stress tensor ($\mathbf{S}$) and the Cauchy stress tensor ($\boldsymbol{\sigma}$) are given by:

$$\mathbf{S} = \mathbf{S}_{vol} + \mathbf{S}_{iso} = \left(2\frac{\partial \Psi_{vol}(J)}{\partial \mathbf{C}} \right) + \left(2\frac{\partial \Psi_{iso}(\bar{\mathbf{C}})}{\partial \mathbf{C}} \right) \quad \text{(Ш.5)}$$

$$\boldsymbol{\sigma} = \boldsymbol{\sigma}_{vol} + \boldsymbol{\sigma}_{iso} = \left(2J^{-1}\mathbf{F}\frac{\partial \Psi_{vol}(J)}{\partial \mathbf{C}}\mathbf{F}^T \right) + \left(2J^{-1}\mathbf{F}\frac{\partial \Psi_{iso}(\bar{\mathbf{C}})}{\partial \mathbf{C}}\mathbf{F}^T \right) \quad \text{(Ш.6)}$$

The strain energy function for compressible isotropic hyperelastic material in terms of strain invariants is given with the decoupled representation with the first two strain invariants as:

$$\Psi(\mathbf{C}) = \Psi_{vol}(J) + \Psi_{iso}\left[\bar{I}_1(\bar{\mathbf{C}}), \bar{I}_2(\bar{\mathbf{C}}) \right] \quad \text{(Ш.7)}$$

The strains invariants $(\bar{I}_\alpha), \alpha = 1,2,3$: are the modified invariants and are defined by:

$$\bar{I}_1(\bar{\mathbf{C}}) = \mathbf{tr}(\bar{\mathbf{C}})$$
$$\bar{I}_2(\bar{\mathbf{C}}) = \frac{1}{2}\left[(\mathbf{tr}\bar{\mathbf{C}})^2 - \mathbf{tr}(\bar{\mathbf{C}}^2) \right] \quad \text{(Ш.8)}$$
$$\bar{I}_3(\bar{\mathbf{C}}) = \det(\bar{\mathbf{C}})$$

$(\bar{I}_1, \bar{I}_2, \bar{I}_3)$: are also deduced as: $(\bar{I}_1 = J^{-2/3}I_1), (\bar{I}_2 = J^{-4/3}I_2), (\bar{I}_3 = 1)$. **The associative** ($\mathbf{S}$) and ($\boldsymbol{\sigma}$) are given by:

74

$$\mathbf{S} = \mathbf{S}_{vol} + \mathbf{S}_{iso} = \left(2\frac{\partial \Psi_{vol}(J)}{\partial \mathbf{C}} \right) + \left(2\frac{\partial \Psi_{iso}(\overline{I}_1, \overline{I}_2)}{\partial \mathbf{C}} \right) \quad \text{(Ⅲ.9)}$$

$$\boldsymbol{\sigma} = \boldsymbol{\sigma}_{vol} + \boldsymbol{\sigma}_{iso} = \left(2J^{-1}\mathbf{F}\frac{\partial \Psi_{vol}(J)}{\partial \mathbf{C}} \mathbf{F}^T \right) + \left(2J^{-1}\mathbf{F}\frac{\partial \Psi_{iso}(\overline{I}_1, \overline{I}_2)}{\partial \mathbf{C}} \mathbf{F}^T \right) \quad \text{(Ⅲ.10)}$$

For example, the very useful Mooney-Revilin model can be used. Concerning numerical complications in FEA Abaqus explicit code, an isotropic compressible hyprelastic model was formulated by adding the strain energy $\Psi_{vol}(J)$ which describes the (*purely volumetric*) elastic response. The decoupled strain energy function for the Mooney-Revilin model for compressible material has the form:

$$\Psi(J, \overline{I}_1, \overline{I}_2) = \Psi_{vol}(J) + C_{10}(\overline{I}_1 - 3) + C_{01}(\overline{I}_2 - 3) \quad \text{(Ⅲ.11)}$$

III.2.2.3 Implementation of mechanical behaviour models

In Abaqus, there are many forms that capture the incompressible or quasi-incompressible isotropic hyperelastic behaviour of materials. These forms are: the polynomial form and its particular cases (*the reduced polynomial form, the neo-Hookean form, the Mooney-Rivlin form, and the Yeoh form*), Ogden form, the Arruda-Boyce form and the Van der Waals form. Assuming the isotropy, in the polynomial forms and its particular cases, the decoupled strain energy function (deviatoric and volumetric strain energy contributions) is given in Abaqus by:

$$\Psi = f(\overline{I}_1 - 3, \overline{I}_2 - 3) + g(J - 1) \quad \text{(Ⅲ.12)}$$

Setting $g = \sum_{i=1}^{N} \frac{1}{D_i}(J-1)^{2i}$ and expanding $f(\overline{I}_1 - 3, \overline{I}_2 - 3)$ in a Taylor series, we obtain the following equation:

$$\Psi = \sum_{i+j=1}^{N} C_{ij}(\overline{I}_1 - 3)^i (\overline{I}_2 - 3)^j + \sum_{i=1}^{N} \frac{1}{D_i}(J - 1)^{2i} \quad \text{(Ⅲ.13)}$$

This form is called polynomial representation of the strain energy in Abaqus. (N, C_{ij}) and (D_i) are temperature-dependent material parameters. The parameter (N) can take values up to six; values of (N) greater than 2 are rarely used.(J): the volume ratio or (the elastic volume strain). The (D_i) values determine the compressibility of the material: if all the (D_i) are zero (not allowed in Abaqus explicit), the material is taken as fully incompressible.
If the number of terms ($N = 1$) the initial shear modulus (μ_0), and bulk modulus, (K_0) are given by:

$$\mu_0 = 2(C_{01} + C_{10}), \quad K_0 = \frac{2}{D_1} \quad \text{(Ⅲ.14)}$$

$$\Psi = C_{10}(\overline{I}_1 - 3) + C_{01}(\overline{I}_2 - 3) + \frac{1}{D_1}(J - 1)^2 \quad \text{(Ⅲ.15)}$$

75

In order to define the hyperelastic material constants (coefficients of strain energy potential), we often rely on standard experimental tests (uniaxial tension and compression, equi-biaxial tension and compression, planar tension and compression and volumetric tension and compression). Abaqus uses the experimental data to calculate the necessary coefficients for specific strain energy potential (C_{10}, C_{01}). However, it is necessary to have a good correlation between the behavior predicted by the material definition and the experimental data, i.e., fit correlation.

The data used in this study were obtained from the work of C. Lally (Prendergast, et al., 2003) (Table III.2-1). In this work, uniaxial and biaxial experiments on a human femoral artery are used to obtain the necessary input data in finite element analysis. Defining the material properties of the reduced form of the generalized Mooney-Rivlin model needs only one biaxial stress-stretch curve since the Mooney-Rivlin model assumes the material to be isotropic (Prendergast, et al., 2003). This model also gives a good match of the experimental data. Using the stress-strain data for human femoral arterial tissue (Figure III.2-3); the hyperelastic constants for the Mooney-Rivlin hyperelastic constitutive equation could be defined.
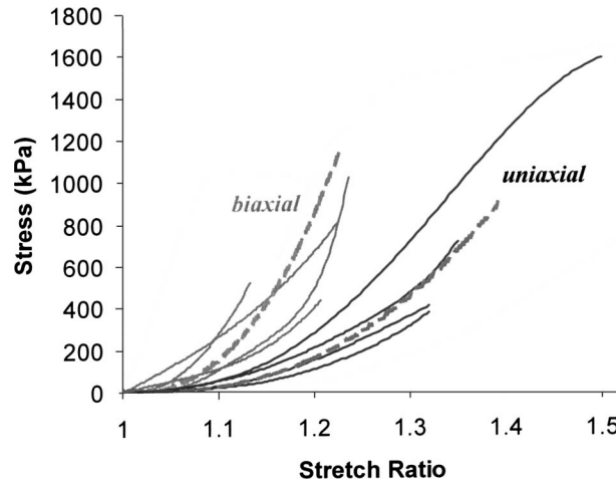
Figure III.2-3: Uniaxial and biaxial data for the human femoral artery; comparison of experimental data (dashed line) and the proposed martial behavior (Prendergast, et al., 2003)

In this study, the proposed polynomial model is appropriate for the aorta behaviour, eq. (III.15). It is also based on the accuracy of the uni/bi-axial tests on several tissue samples. There are two-three-five, and nine terms in the Mooney-Rivlin model, these can also thought as particular cases of the polynomial form (also called 'reduced form of the generalized Mooney-Rivlin model'. Thus, the five-term Mooney-Rivlin is similar to the polynomial form when ($N = 2$), and the hyperelastic constants were determined for a reduced form of the generalized Mooney-Rivlin model (Prendergast, et al., 2003), eq. (III.16).

$$\Psi = C_{10}(\bar{I}_1 - 3) + C_{01}(\bar{I}_2 - 3) + C_{20}(\bar{I}_1 - 3)^2 + C_{11}(\bar{I}_1 - 3)(\bar{I}_2 - 3) + C_{30}(\bar{I}_1 - 3)^3 + \frac{1}{D_1}(J - 1)^2 \quad \text{(III.16)}$$

76

Table III.2-1: Hyperelastic constants to describe the hyperelastic behaviorr of the aortic wall.
The constants describe a Mooney- Rivlin model of the form (P. J. Prendergast et al, 2003)

The material coefficients	Human femoral parameters best-fit values (kPa)
C_{10}	18.90
C_{01}	2.75
C_{20}	590.42
C_{11}	857.18
C_{30}	0

III.2.2.4 Discretization of finite elements

In the case of realistic aneurysmal models, hexahedral-mesh generation algorithm is still challenging. However, some software has been developed to support the hexahedral discretization for complex geometries.

In this study, meshing finite elements was developed using Hypermesh software. Hypermesh is a high-performance finite element preprocessor that provides a highly interactive and visual environment to analyze the product design performance. Hypermesh is a user-preferred environment for meshing complex solid geometries and has a direct interface with commercial CAD and CAE systems and finite element software.

The general steps of creating a hexahedral mesh starting from STL file generated by Mimics are:
- Create the surface of the aneurysmal aorta.
- Create two lines: one for the part and another for the mesh, create opposite points on the two lines and create the centerline points with a vector for each centerline point.
- Create lines and circles around the centerline and transform these circles to surfaces.
- Create the intersection surface between the circular surfaces created in step (4) and the geometry of the aneurysmal aorta.
- Mesh the first aortic surface and create the 3d mesh reconstruction with the desired thickness (Figure III.2-4).

.
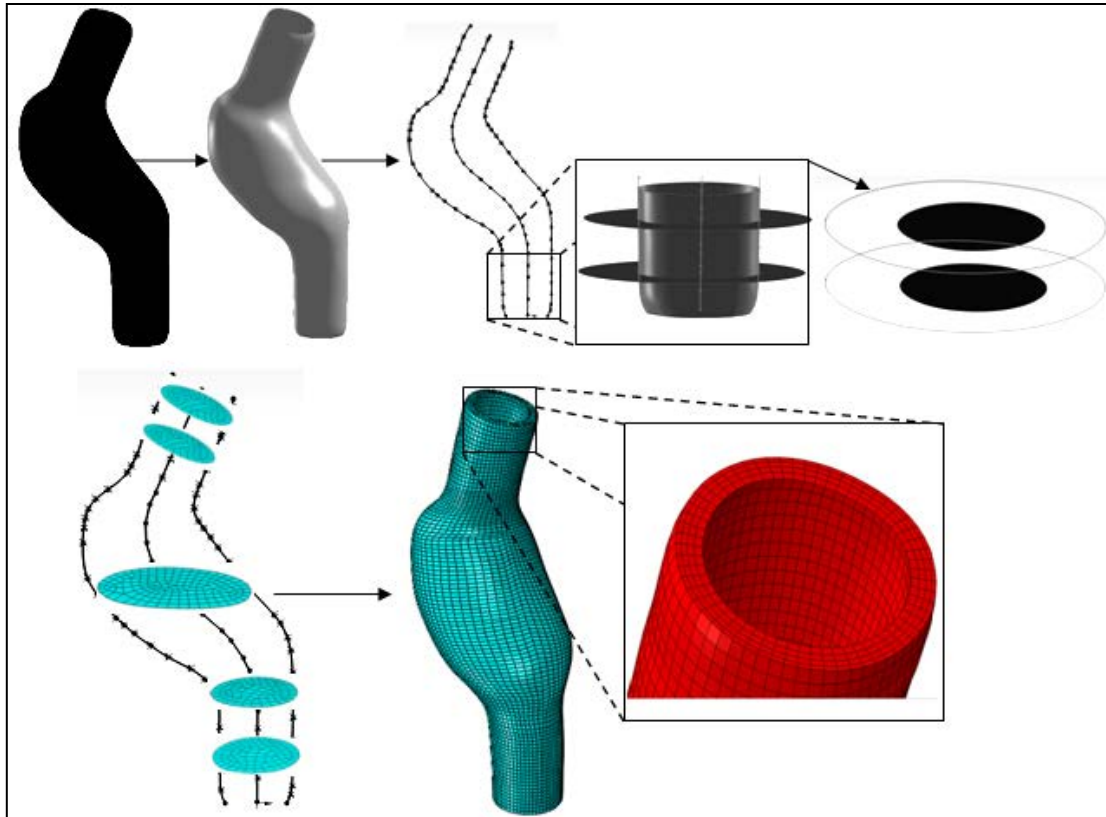
Figure Ш.2-4: Hexahedral finite elements discretization procedure by Hypermesh software

The element type used is C3D8R: an 8-node linear brick, reduced integration with hourglass control. The number of elements used in thickness was changed to evaluate the mesh dependence on the numerical results. The number of elements was precisely controlled until getting stable results decreasing the time of calculation, see Appendix. We considered a nominal uniform thickness of 3 mm (Price, et al., 1971).

III.2.2.5 Boundary conditions

The boundary conditions imposed on the aorta (A) were only on the upper (Γ_{Au}) and bottom surface (Γ_{Ab}) of the aorta. These boundary conditions represent the effect of the removed sectioned parts of the aorta.
Local cylindrical coordinate systems were defined at these surfaces in order to fix the corresponding nodes in the longitudinal and in the circumferential direction. Only radial displacements of these nodes are allowed. Moreover, we assumed no internal pressure on the vessel wall (Γ_{int}) under the hypothesis that the geometry is based on measurements achieved at 80 mmHg.

On the external face of the aneurysm (Γ_{Aex}), we assumed that there is no pressure, which means that we neglect the interaction with all tissues and organs adjacent to the aneurysm. These effects were considered in other studies by imposing external pressure of 12 mm Hg on the external face of the aneurysm. The effects of residual stresses (Holzapfel, et al., 2007) were also neglected (Figure Ш.2-5).

The applied boundary conditions are:

$$\left.\begin{array}{l} u_z = 0 \\ u_\tau = 0 \end{array}\right\} on\, \Gamma_{Au}, \Gamma_{Ab} \quad (\text{III}.17)$$

$$\boldsymbol{\sigma}.\mathbf{n} = p.\mathbf{n} = 0,\, on\, \Gamma_{Aint} \\ \boldsymbol{\sigma}.\mathbf{n} = 0\,, on\, \Gamma_{Aex} \quad (\text{III}.18)$$
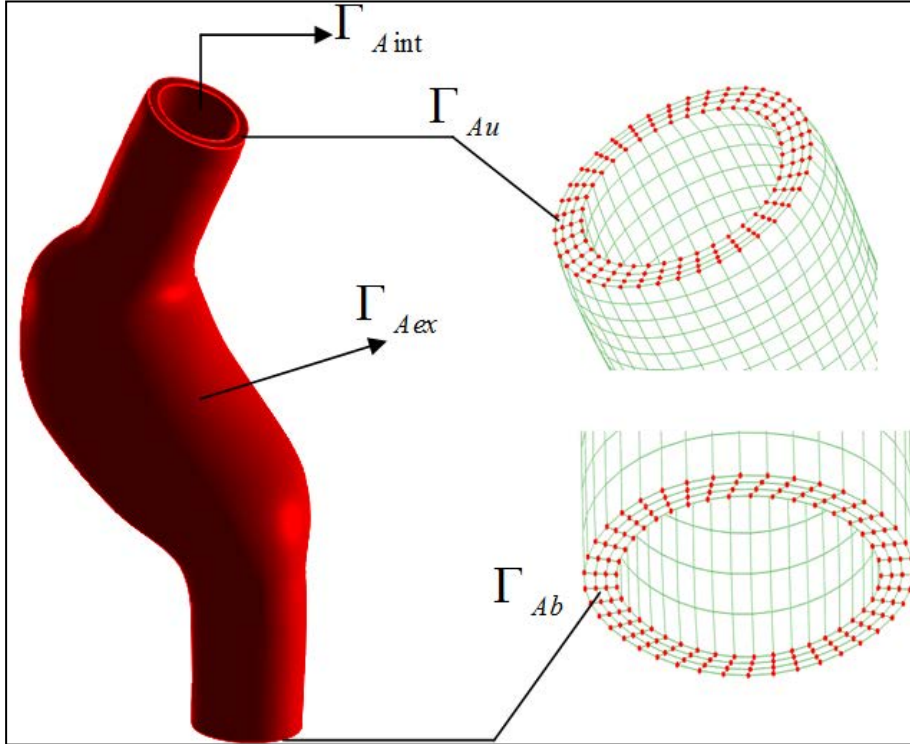
Figure III.2-5: Boundary condition designation for the aorta

III.3. Stent models: geometries and shape setting simulation

The geometry of stent based on CT-images is not always available and needs a higher resolution to obtain an accurate estimate for the strut cross-section. This method shows a real representation of the stent, but does not provide the possibility for the parametric modeling, which is important in the design phase and optimization.

As an alternative approach, the three dimensional solid models were developed using Computer Aided Design (CAD) with parametric solid modeling. This approach customizes the stent design to be suitable for various applications.

The stent design is laser-cut from a nitinol tube. In reality the expanded stent strut bends with a curvature, which is too complex to represent by CAD. Therefore, we assumed that the strut is perfectly straight in the modeling stage.

79

III.3.1 Parametric solid model

The stent geometric model was generated by means of a developed parameterization algorithm using global variables (ST_{OD}, S_{TH},S_L,B_W,S_{VW},G) illustrated in the (Figure III.3-1). Other variables (Y_{strut} ,S_{LS},R_1,R_2,S_W) were linked to previous ones by equations (Figure III.3-1), where (R_1,R_2) are the inner and outer radius of strut vertex respectively, (Y_{strut}) is a circumferential distance of a single strut at the given diameter. The stent was modeled starting from the master sketch with ten struts around its circumference ($N_{Struts}=10$) and six struts columns along the stent ($N_{CS}=6$). The 3D parametric stent model was then performed with suitable operations in CATIA V5R20.

Table III.3-1: Global variables used in the equations	
Global variables	Comment
N_{CS}	Number of columns of struts along the length of the stent
N_{Struts}	Number of struts around its circumference
ST_{OD}	Outer diameter of the tubing form
S_{TH}	Wall thickness of strut
S_L	Length of strut
S_{VW}	Strut vertex width
G_{SC}	Axial gap between adjacent columns of struts
B_W	Width of bar (bridge)
N_B	Number of bridges around around the circumference
G	Circumferential gap between two adjacent struts

Table III.3-2: Equations to define global variables linked to feature dimensions	
Equations	Comment
$Y_{strut} = (D_{stent} \times \pi)/N_{struts}$	Circumferential distance occupied by single strut at the analysis diameter
$S_W = ((D_{stent} \times \pi)/N_{struts}) - G$	Width of a strut
$R_1 = G/2$	Inner radius of an apex
$R_2 = R_1 + S_W$	Outer radius of an apex
$S_{LS} = S_L - (R_1 \times 2)$	Length of the perfectly rectangular section of a strut
$ST_{ID} = ST_{OD} - (S_{TH} \times 2)$	Inner diameter of the stent

80
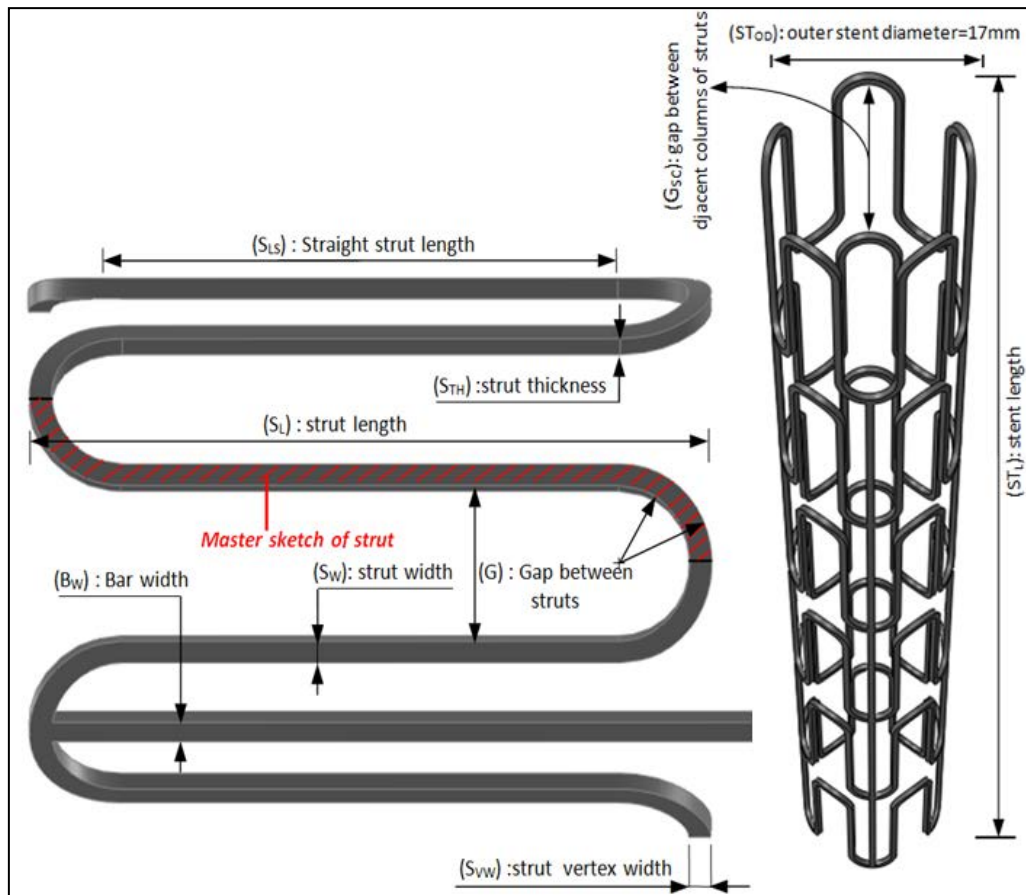
Figure III.3-1: The 3D solid stent with the global variables and equations

In our case, the algorithm enables a powerful variation of the stent configurations and the generation of new stent designs.

III.3.2 Shape setting simulation

Realistic simulation of the stent deployment requires an accurate representation of the actual stent geometry. The geometries of the stent are not known; the final 3D solid geometrical model created by CAD does not represent the realistic complex form of self-expanding stent. Therefore, in order to reproduce the actual geometric-connected behavior, it is necessary to trace the manufacturing process that produces the final expanded product. The processes that can be modeled include two steps: mandrel expansion forming and annealing.

III.3.2.1 Finite element forming tool

The first step is modeled by stent radial expansion. This was achieved by creating a cylindrical rigid surface which fits into the stent insde. Then, the stent is expanded from its 'as-cut configuration' to its 'nominal diameter' by enlarging this surface in the radial direction while ensuring its contact with the internal surface of the stent. The stent diameter will be driven by the rigid cylindrical surface, accomplishing the needed oversizing value relative to the outer diameter of the aorta.

81

The forming step was accomplished by FEM simulation using ABAQUS standard package. The cylindrical surface mesh consists of 4-node surface elements with reduced integration (SFM3D4R). The surface was expanded in the radial direction by using appropriate boundary conditions on its nodes.

III.3.2.2 Finite element stent model
Mesh and discretization

In many studies, stents were modeled with shell or beam elements. However, these elements do not capture the correct stresses and strains transformed within and by the stent. Therefore, solid elements should be used. Using ABAQUS code, the liner hexahedron element is the best one to model the stent because they provide a good balance between accuracy and efficiency. As the stent is mostly subject to bend, the fully integrated liner hexahedron element (C3D8) is not suitable for stent analysis. The recommended element types used in stent modeling are (C3D8R) and (C3D8R). In our objective of the simulation, the (C3D8R) will be more effective and less time-consuming.

The stent geometry was meshed by (C3D8R): an 8-node linear brick, reduced integration, hourglass control with liner geometric order.

At least three elements through the thickness have to be used to alleviate potential problems. Reduced integration liner brick elements should be used to avoid shear locking numerical problems. Moreover, since the elements have one integration point, proper hourglass control should be used, (Anon., s.d.)'Solid (continuum) elements' for more information about shear locking and hourglass control issues. As the geometry is so complex, the stent was carefully discretized with clean, uniform mesh using the swept algorithm. The geometry was divided into shapes that are less complex. Then, we selected the algorithm that is most appropriate to discretize the partitioned geometry (Figure III.3-2)
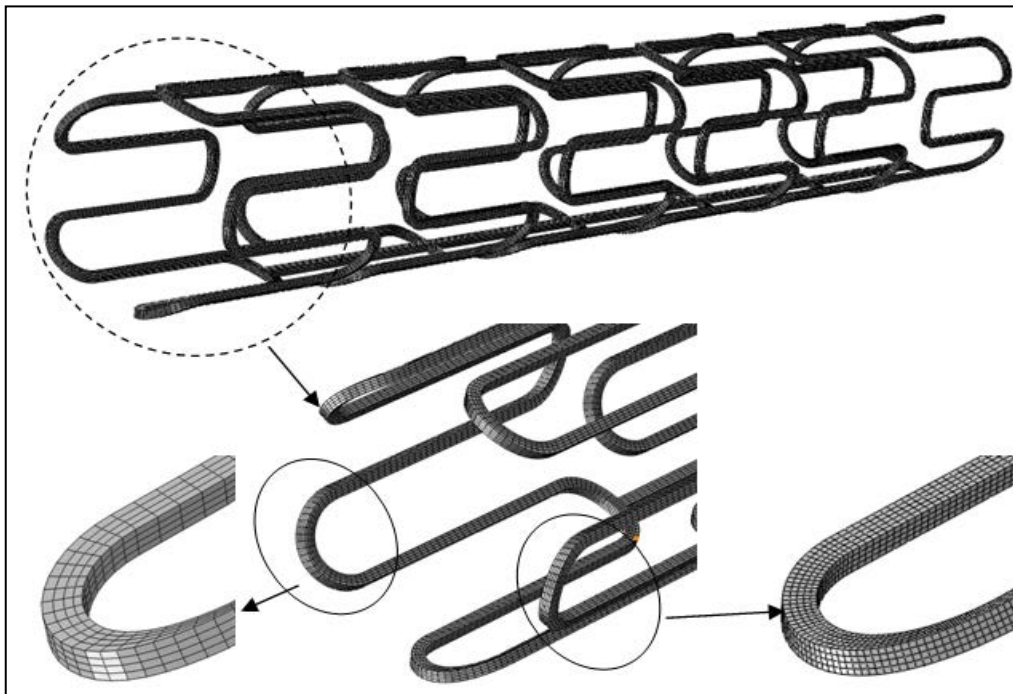
Figure III.3-2: Hexahedral stent discretization

To keep the analysis run-time reasonable, mesh convergence analysis was used (see appendix) to compare the used mesh density with the finer one until negligible divergence was obtained.

The analysis was performed in the frame of classical continuum mechanics under the hypothesis of large strain conditions.

Boundary condition and materials

In this stage (forming), Nitinol cold-worked has the same mechanical behaviour of metals such as aluminum or classic steel, consequently, in this simulation, nitinol was considered as an elastoplastic material using the material parameters based on the work of (Thériault, et al., 2006) (Figure III.3-3).
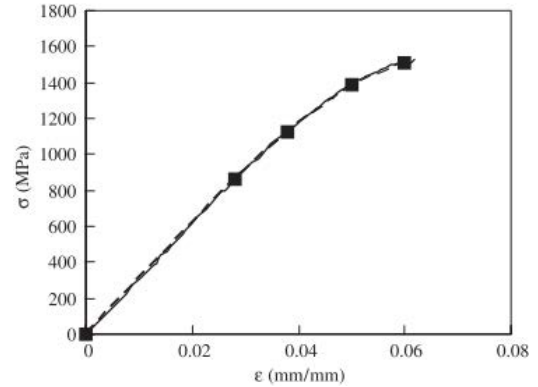
Figure III.3-3: Modeled and experimental behavior of nitinol

Regarding the stent, we apply the boundary conditions which constrain the stent only in the longitudinal direction to avoid potential rigid displacements. This boundary was applied on a node in the middle cross section of the stent indicated with (Γ_{ns}) (Figure III.3-4).
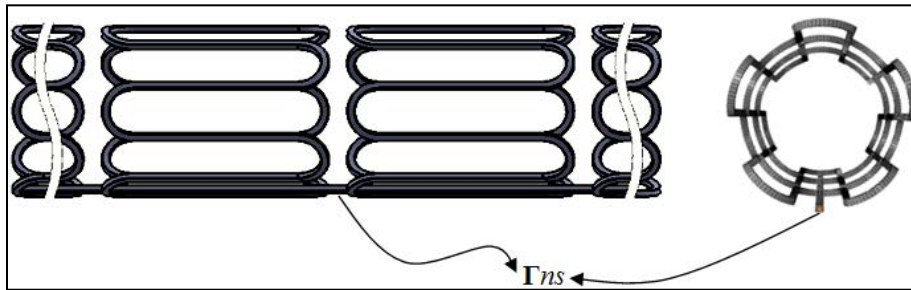
Figure III.3-4: Stent boundary condition for shape setting simulation

In the contact analysis (forming tool/stent), the contact pair surfaces were defined between the outer surface of the catheter and the inner surface of the stent. We assumed that the tangential motion between the bodies is frictionless. For the contact of pair surfaces, surface-to-surface approach was chosen as an algorithm of discretization. The finite-sliding tracking approach was applied to consider the relative motion of the surfaces where a rigid-element based surface must be chosen as the master surface. Discretization with the finite sliding tracking approach was applied. The penalty constraint enforcement method was used to approximate the hard pressure-overclosure behavior. The contact analysis in ABAQUS/standard provides many numerical problems and requires high computational efforts (Anon., s.d.).

The final deformed shape of the stent can now satisfy the actual complex geometry of real stent, (Figure III.3-5). In the second step, in order to simulate the heat setting process (annealing process), all the expansion-induced stresses were removed and the elements of the stent were added back into the model in a strain free manner, i.e., the nodal coordinates and element connectivity resulting from the shape setting simulations were re-imported, in this way modeling the annealing process.
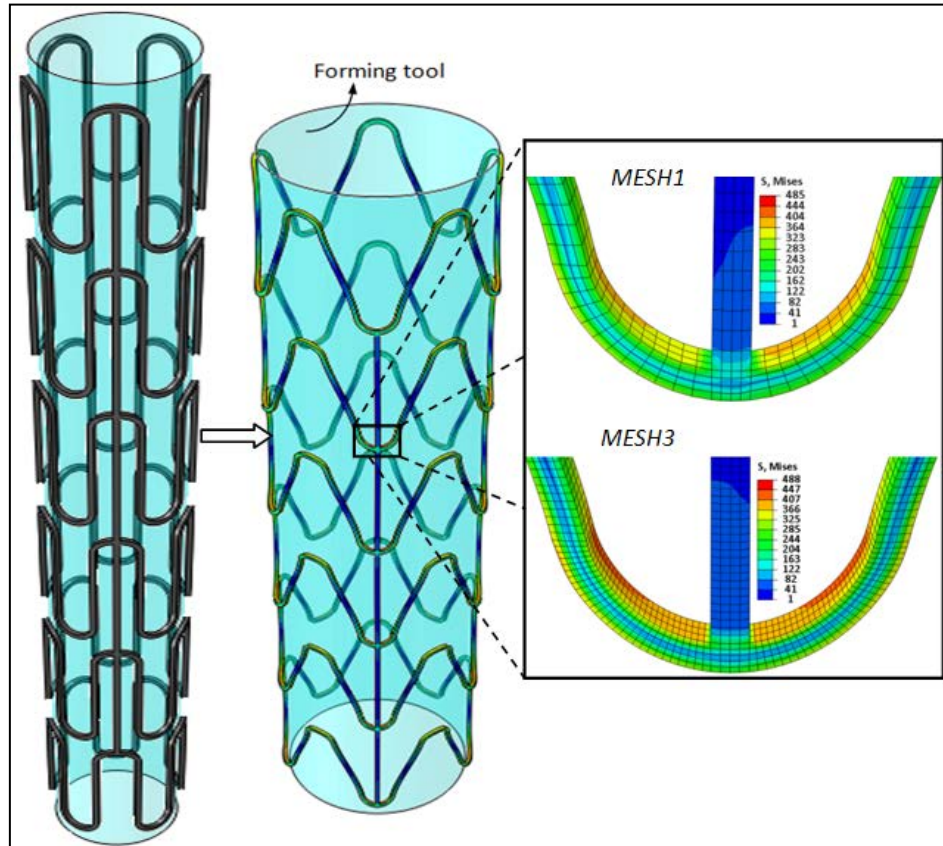
Figure III.3-5: Shape sitting simulation with mesh refinement

III.4. FEA of CAS and stent deployment: numerical simulation
III.4.1 Numerical method

Since the simulations are strongly nonlinear due to material nonlinearity, large deformations, and complex contact problems, we agree that the explicit dynamics analysis procedure is a good choice in the FEM. The commercial code ABAQUS/Explicit 6.10 was used for all the deployment simulations.

The dynamic problem is treated using the explicit central difference integration rule to integrate the equations of motion with respect to time.

Let $\mathbf{u} \epsilon R^3$ be the displacement of each element node, ($\mathbf{M}$) :diagonal element mass matrix, ($\mathbf{\ddot{u}}$): the nodal acceleration, ($\mathbf{P}, \mathbf{I}$): the external applied forces and internal element forces respectively, the dynamic equilibrium equation is given by:

84

$$\mathbf{M\ddot{u}} = \mathbf{P} - \mathbf{I} \quad (\text{III}.19)$$

In order to calculate the velocity ($\mathbf{\dot{u}}$) at the current mid-increment; $\mathbf{\dot{u}}|_{(t+\frac{\Delta t}{2})}$ and displacement at current increment: $\mathbf{u}|_{(t+\Delta t)}$, the change in velocity through time is calculated to be then added to the velocity from the middle of the previous increment $\mathbf{\dot{u}}|_{(t-\frac{\Delta t}{2})}$. Then, the integrated velocities are added to the displacements at the beginning of the increment to calculate the displacement at the current increment.

These may be expressed by the equations:

$$\mathbf{\dot{u}}|_{\left(t+\frac{\Delta t}{2}\right)} = \mathbf{\dot{u}}|_{\left(t-\frac{\Delta t}{2}\right)} + \frac{(\Delta t|_{(t+\Delta t)} + \Delta t|_{(t)})}{2} \mathbf{\ddot{u}}|_{(t)}$$

$$\mathbf{u}|_{(t+\Delta t)} = \mathbf{u}|_{(t)} + \Delta t|_{(t+\Delta t)} \mathbf{\dot{u}}|_{\left(t+\frac{\Delta t}{2}\right)} \quad (\text{III}.20)$$

The acceleration at the beginning of the increment can be calculated by inverting the dynamic equilibrium equation:

$$\mathbf{\ddot{u}}|_{(t)} = (\mathbf{M})^{-1} \cdot (\mathbf{P} - \mathbf{I})|_{(t)} \quad (\text{III}.21)$$

The element strain increment ($d\varepsilon$) is computed from the strain rate ($\dot{\varepsilon}$). Finally, the stress (σ) is calculated using the explained constitutive equations for the aorta and the stent.

$$\sigma(t + \Delta t) = f\left(\sigma_{(t)}, d\varepsilon\right) \quad (\text{III}.22)$$

Particular attention should be paid to the amount of incremented time that must not exceed the *stability limit*; which is given by the following equation for the global model:

$$\Delta t_{stable} = \frac{2}{\omega_{max}} \quad (\text{III}.23)$$

Where (ω_{max}) is the highest (eigenvalues) frequency in the system.

Considering the *element-by-element* estimate and not the *global model* (Anon., s.d.), the stability limit can be calculated using the element length (L_e) and the wave speed of the material (C_d):

$$\Delta t_{stable} = \frac{L_e}{c_d} \quad (\text{III}.24)$$

III.4.2 Stent deployment procedure

The annealed expanded stent and the aneurysm finite element models were combined. A virtual deformable surface was modeled as a rigid body, named catheter. The catheter was discretized by using three-dimensional, 4-node surface elements with reduced integration (SFM3D4R): (3456) elements and (3504) nodes. Only this special purpose element type can achieve the complex stent deformation. The catheter will impose the stent deformation by applying adapted displacement boundary conditions (BCs) on its nodes, realizing the pre-stenting centerline. The centerline of the aorta was used to guide stent positioning.

Starting from the straight configuration of the catheter, we can calculate the needed displacements based on the centerline and the shape of the aorta. To enable analytical computations, the centerline was approximated using circular arcs and lines. To achieve our simulation in the ideal way, the catheter should be gradually bent and compressed accomplishing the vessel centerline and leading to the superelastic stent deformation.

We have used Java based programming language called 'Processing' developed at MIT. The object oriented programming was chosen in order to make the program more flexible and easier to use and modify.

The program input is the set of (N) points, rotation angles (θ) and transformation parameters. The output of our program is the sets of catheter nodes in Abaqus format, in addition to the required boundary conditions of the catheter's nodes displacement, also in Abaqus format.

Firstly, we assumed that the cylindrical catheter is composed of (M) sections; each of those is a circle of (N/M) nodes and a radius of (R). Initially, all circles are aligned in a vertical line with a horizontal inclination of $(0°)$ (angle with z axis). Thus, the objective is to find the transformation (T) of each point (P), where: $P' = T(P)$.

The program functionality can be resumed in the following steps:

Step1– Read input files:

The tube (catheter) was modeled by an array of node objects. Each node represents the corresponding point coordination (x, y, z), as well as of its set id. The set id was attributed in the same order of the points in the input file, i.e. the first point was the first set, and the ith point was the ith set. An array of sections' rotation angles was then filled from the second input file containing (M) angles.

Finally, the global parameters (N, M), in addition to group section's displacement parameters were read from a separate file. This file contains the beginning and the end of each section group (sections that have the same displacement transformation). Each group was associated with one of three possible types of parameters according to the form of the target inner curve. It could be in a linear, arc or spherical form.

Step 2 – Compression/Expansion:

This function allows expanding or compressing the tube from its original diameter (R) into a new one (R'). The new coordination of each point is calculated by:

$$\begin{bmatrix} x' \\ y' \\ z' \end{bmatrix} = \begin{bmatrix} \frac{R'}{R} & 0 & 0 \\ 0 & 1 & 0 \\ 0 & 0 & \frac{R'}{R} \end{bmatrix} \cdot \begin{bmatrix} x \\ y \\ z \end{bmatrix} \qquad \text{(III.25)}$$

Where (x, y, z) are the current positions of the point.

Step 3 – Displacement:

Each group of sections was displaced starting from its current position (x, y, z) into a new one $(\dot{x}, \dot{y}, \dot{z})$ according to the type of estimated target curve (equations of line arc or sphere).

Step 4– Rotation:

Each section is rotated by the corresponding rotation angle (θ_s) read from the angles input file. The new position of each point is calculated using:

$$\begin{bmatrix} x' \\ y' \\ z' \end{bmatrix} = \begin{bmatrix} \cos\theta_s & -\sin\theta_s & 0 \\ \sin\theta_s & \cos\theta_s & 0 \\ 0 & 0 & 1 \end{bmatrix} \cdot \begin{bmatrix} x \\ y \\ z \end{bmatrix} \qquad \text{(III.26)}$$

Once all steps were applied, we calculated the displacement between the two configurations for each node, and we exported them as boundary conditions in a format suitable for Abaqus (typically an '.inp' file). All these different steps can be achieved in the simulation during the step-1. In this step, only the contact between the catheter and stent is activated. A frictionless, general contact algorithm was employed between the catheter and the stent.

Then, in step 2; to reproduce the superelastic material response, the catheter was re-expanded starting from the bent and crimped configuration so that the stent expanded and returned to its original shape. In this step, the stent was re-enlarged against the vessel and the contact between the catheter and vessel was deactivated (Figure III.4-1).

87
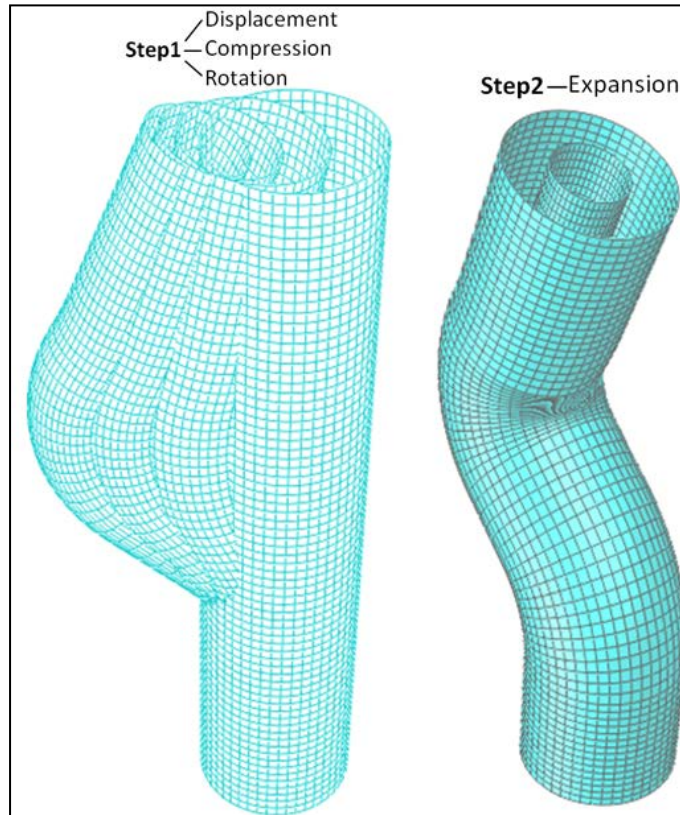
Figure III.4-1: Catheter deformation starting from the initial straight cylinder accomplishing the vessel centerline (step1) until stent deployment (step2)

III.4.3 Contact model

ABAQUS/Explicit is ideally suited for the solution of the nonlinear, dynamic, and quasi-static problems, especially those involving extremely complex contact conditions.

Abaqus/Explicit provides two distinct algorithms for modeling the contact: general contact and contact pairs contact. We used the general contact, which allows defining the contact between many or all regions of a model with very few restrictions on the types of surfaces involved.

The contact formulation in Abaqus/Explicit includes the constraint enforcement method, the contact surface weighting, the tracking approach, and the sliding formulation. The general contact formulation uses a penalty method to enforce contact constraints between surfaces. This method does not propose problems with other types of constraints. The Penalty stiffness that relates the contact force to the penetration distance is chosen automatically by Abaqus/Explicit. The effect on the time increment is less than (4%) as the penetration is not significant.
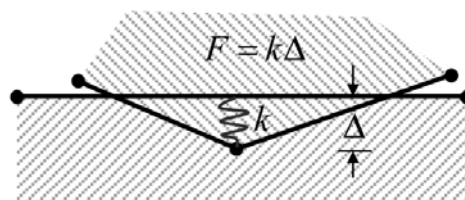
Figure III.4-2: Penalty enforcement of contact

88

The interaction between contacting surfaces is controlled by two components: one normal and the second tangential to the surfaces. The tangential behavior defines the relative motion (sliding) between contacting surfaces. The hard contact model behavior (Wriggers, 1995) was used as a normal behavior to the surfaces (catheter-stent) (stent-vessel). In the hard contact (the default pressure-overclosure relationship), the surfaces separate or come into contact depending on the clearance (the distance separating the two surfaces). When clearance=0, the contact constraint formulation is applied and the contact pressure is transmitted between the surfaces. When clearance > 0, the contact constraint is not applied and no contact pressure is transmitted between the surfaces (Figure III.4-3).
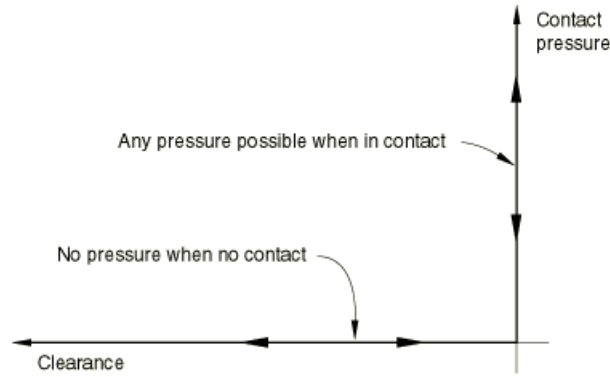
Figure III.4-3: Default pressure-overclosure relationship

The tangential behavior was described by the classical isotropic Coulomb friction model. The model relates the maximum allowable frictional (shear) stress (τ_{crit}) across an interface to the contact pressure (μ_p) between the contacting bodies. Every contacting surface can carry shear stresses up to a critical value after which the contacting surfaces start sliding relative one to another. The contact behavior can be described by 'sticking behavior' or 'slipping behavior'. The Coulomb friction model performs the stick/slip calculations to define the transitions from sticking to slipping or from slipping to sticking (Figure III.4-4).

For the stick/slip calculations, Abaqus combines the two shear stress components (τ_1, τ_1) into an 'equivalent shear stress' $(\bar{\tau}_{eq} = \sqrt{\tau_1{}^2 + \tau_2{}^2})$. Abaqus also combines two slip velocity components $(\dot{\gamma}_1, \dot{\gamma}_2)$ into an equivalent slip rate: $(\dot{\gamma}_{eq} = \sqrt{\dot{\gamma}_1^2 + \dot{\gamma}_2^2})$.
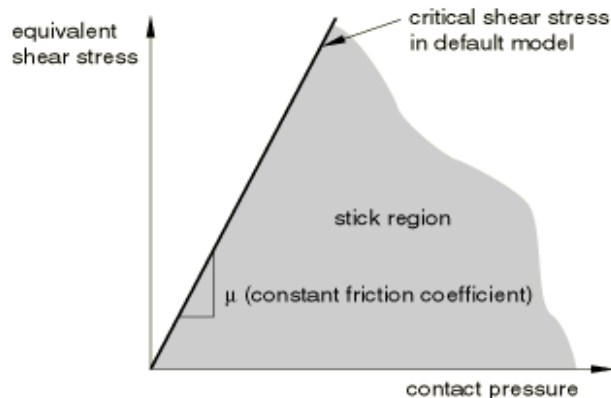
Figure III.4-4: (2D representation) in the contact pressure–shear stress space
along which a point transitions from sticking to slipping

89

The coulomb model assumes that no relative motion occurs if:

$$\left(\overline{\tau}_{eq} = \sqrt{\tau_1^2 + \tau_2^2}\right) < (\tau_{crit} = \mu p) \quad \text{(Ш.27)}$$

Where:
  – (τ_{eq}): the equivalent shear stress
  – (τ_1, τ_2): the two shear stress components that act in the slip directions for the contact surfaces.
  – (τ_{crit}) : the critical stress
  – (μ): the coefficient of friction. We consider the same value in all directions (isotropic friction)
  – (p): the contact pressure stress

During crimping and bending, the contact between (stent-catheter) was considered frictionless ($\mu = 0$). A zero coefficient of friction means that no shear forces will develop and the contact surfaces are free to slide.
The value of (μ) for (vessel-stent) contact is ranged between ($0.05 \leq \mu \leq 0.5$) (Vad, et al., 2010). The pathological state of the aorta (atherosclerotic plaques, calcifications, etc.), and the material of the endograft can change significantly (μ) value.
When:
$(\tau_{eq} < \mu p) \Leftrightarrow (\frac{\tau_{eq}}{\mu p} < 1)$: The slip between stent–aorta will not occur.
$(\tau_{eq} \geq \mu p) \Leftrightarrow (\frac{\tau_{eq}}{\mu p} \geq 1)$: The slip between stent-aorta will occur.

The equivalent shear stress (τ_{eq}) have the same notion of the so-called 'the pullout forces', which are defined as the forces needed to dislodge the stent from its first deployed position. They are inversely proportional to another, see chapter IV.
The ratio: $(\overline{F}_{CS} = \frac{\tau_{eq}}{\mu p})$; $0 \leq \overline{F}_{cs} \leq 1$ can define the friction contact stability $(\overline{F}_{cs})$ and stick/slip behavior between (stent-aorta). The high value of $(\overline{F}_{cs})$ can lead to unstable contact until the slip occurs when $(\overline{F}_{cs} \geq 1)$.

III.4.4 Numerical consideration
The numerical analysis is strongly nonlinear represented in large deformations and complex contact problems; consequently, we used Abaqus/explicit as finite element solver in quasi-static analysis with negligible kinetic energy. Abaqus/explicit also provides a very stable general contact. The general contact algorithm was used for the interactions between all model components (catheter-stent) and (stent). The nitinol superelastic behaviour was assigned to the stent. Nitinol material characterization was obtained from the PhD work of (van der Merwe, 2007). In this work, nitinol material parameters needed for the material definition were calculated from the experimental tensile test (TableШ.4-1).

Table III.4-1: Nitinol material constants obtained from the experimental tensile test (van der Merwe, et al., 2008)

Parameter	Value
Austenite elasticity (E_A)	38992 (Mpa)
Austenite poisson's ratio (v_A)	0.46
Martensite Elasticity (E_M)	21910 (Mpa)
Martensite poisson's ratio (v_M)	0.46
Transformation Strain (ε_L)	0.042
Loading Temperature Derivative of Stress ($\frac{d\sigma}{dT}$)$_L$	$0(Mpa/C^{\circ})$
Loading Start of Transformation Stress (σ_L^S)	483(Mpa)
Loading End of Transformation Stress (σ_L^E)	610(Mpa)
Reference Temperature (T_0)	-
Unloading Temperature Derivative of Stress ($\frac{d\sigma}{dT}$)$_U$	$0(Mpa/C^{\circ})$
Unloading Start of Transformation Stress (σ_U^S)	388 (Mpa)
Unloading End of Transformation Stress (σ_U^E)	256 (Mpa)
Loading Start of Transformation Stress (Compression) (σ_{CL}^S)	610 (Mpa)
Volumetric Transformation Strain (ε_V^L)	0.04
Number of Annealing to be Performed During Analysis (N_A)	0

The explicit technique is very suitable for quasi-static problems as our case. However, the quasi-static analysis requires special considerations. One important consideration is increasing the speed of the process to obtain an economical solution. This can be achieved by increasing load rates or using mass scaling (Hughes, 2000) (Prior, 1994), see Abaqus Analysis User's Manual for more information. However, by increasing the speed of the process, the state of static equilibrium evolves into a state of dynamic equilibrium where the inertia forces can become more dominant. Thus, optimization should be obtained by decreasing the calculation time without significant inertia forces (see appendix).

(Table III.4-2) resumes all the parameterized-deployment simulations to investigate the impact of several factors on migration and endoleak type I.

Table III.4-2: Parameterized-deployment simulations to evaluate the impact of several factors on migration and endoleak type 1a							
Deployment Simulation	I	II	III	IV	V		VI
(Angulated proximal neck)	*(Stent3)*	*(Stent3)*	*(Stent3)*	*(Stent3)*	*(Stent1)*		*(Stent2)*
Proximal Attachment Site Length(mm)(PASL=D)	D_{3P}=23	D_{3P}=23	D_{3P}=23	D_{3P}=23	D_{1P}=18		D_{2P}=21
Distal Attachment Site Length(mm)(DASL= D)	D_{3D}=23	D_{3D}=23	D_{3D}=23	D_{3D}=23	D_{1D}=15		D_{2D}=18
Oversizing value (O %)	10%	15%	20%	25%	15%	20%	15%
Tangential contact behavior (Coefficient of friction)	$\mu = 0.05$	$\mu = 0.05$	$\mu = 0.05$	$\mu = 0.05$	$\mu = \infty$ $\mu = 0.05$ $\mu = 0.1$ $\mu = 0.5$	$\mu = 0.05$	$\mu = 0.05$
(non-Angulated proximal neck)	*(Stent1)*						
Proximal attachment site length(mm) *Distal attachment site length(mm)*	D_{1P}=18 D_{1D}=15						
Oversizing value (O %)	15%						
Tangential contact behavior (coefficient of friction)	*($\mu = 0.05$)*						

III.4.5 Results and discussion

III.4.5.1 Post processing

The following paragraph outlines the results obtained after several deployments (Table III.4-2) of a specific geometry of the stent. (Figure III.4-5) illustrates the "reference deployment simulation" process for the stent1 with (*PASL*=18mm) and (O%=15%) using perfect contact: $(\mu = \infty) \Leftrightarrow (\bar{F}_{cs} = 0)$ so that no-slip is expected once contact (stent-aorta) occurs.
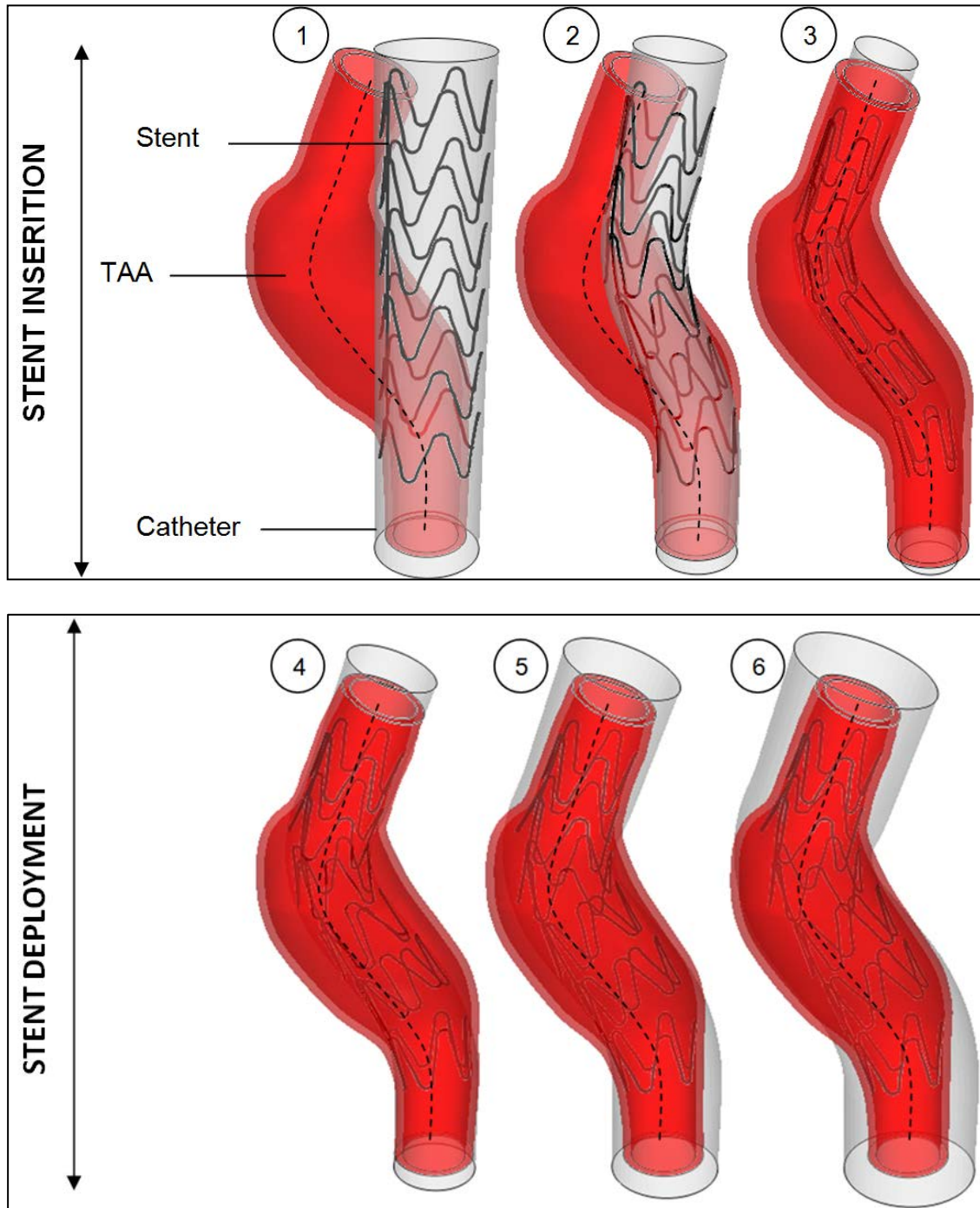
Figure III.4-5: Deployment procedure-simulation:V

93

The simulation was performed using the deployment procedure. The simulation showed large deformations and concentrations of stresses due to the high gradient of radial deformation during crimping and bending (step1). As expected, we can note that the highest values of Von Mises stresses and strains at the end of crimping-bending phase are concentrated at the arcs of the struts (Figure Ш.4-6).

The (Figure Ш.4-7) shows the reference deployment procedure for the stent1 with 18 mm of proximal length and (15%) oversizing value (O%=15%). The roughest frictional model in the tangential direction was used with $(\mu = \infty) \Leftrightarrow (\bar{F}_{cs} = 0)$, so that no tangential slip is expected once contact (stent-aorta) occurs. This behavior represents the best, ideal and stable contact.
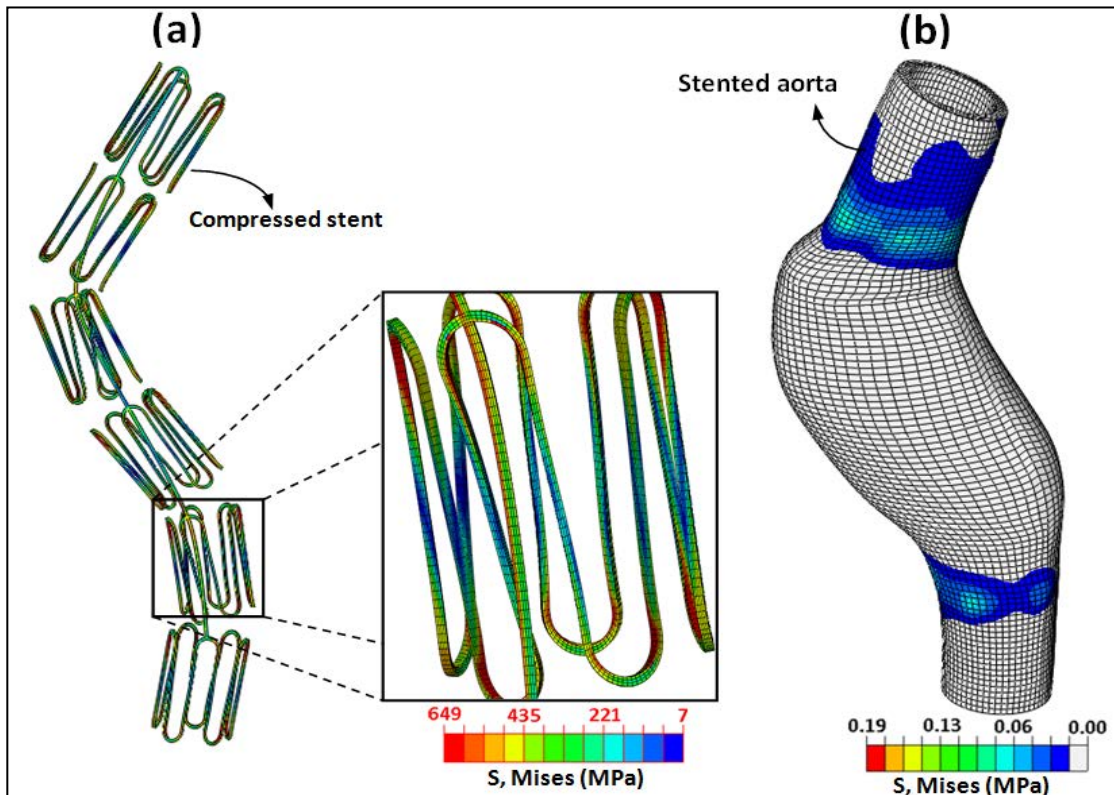
Figure Ш.4-6: (a) Von Mises stresses (MPa) in the compressed stent. (b) Von Mises stresses in the aorta after stent deployment, simulation:V (reference model)

In the deployment phase, the stent was expanding with the superelastic effect until it contacted the aorta applying the Radial Forces (RF). At the proximal and distal attachment sites, a radial decrease was observed in the deployed stent due to the Radial Compressive Forces (RCF) applied by the aorta. When the stent was fully deployed, (RF) and (RCF) forces were in equilibrium (Stoeckel, et al., 2004). The previous history of deployment behavior can be described only when no migration or folding takes place. (Figure Ш.4-7) shows the fully deployed stent and stress distribution within the aorta at the attachment sites.

94
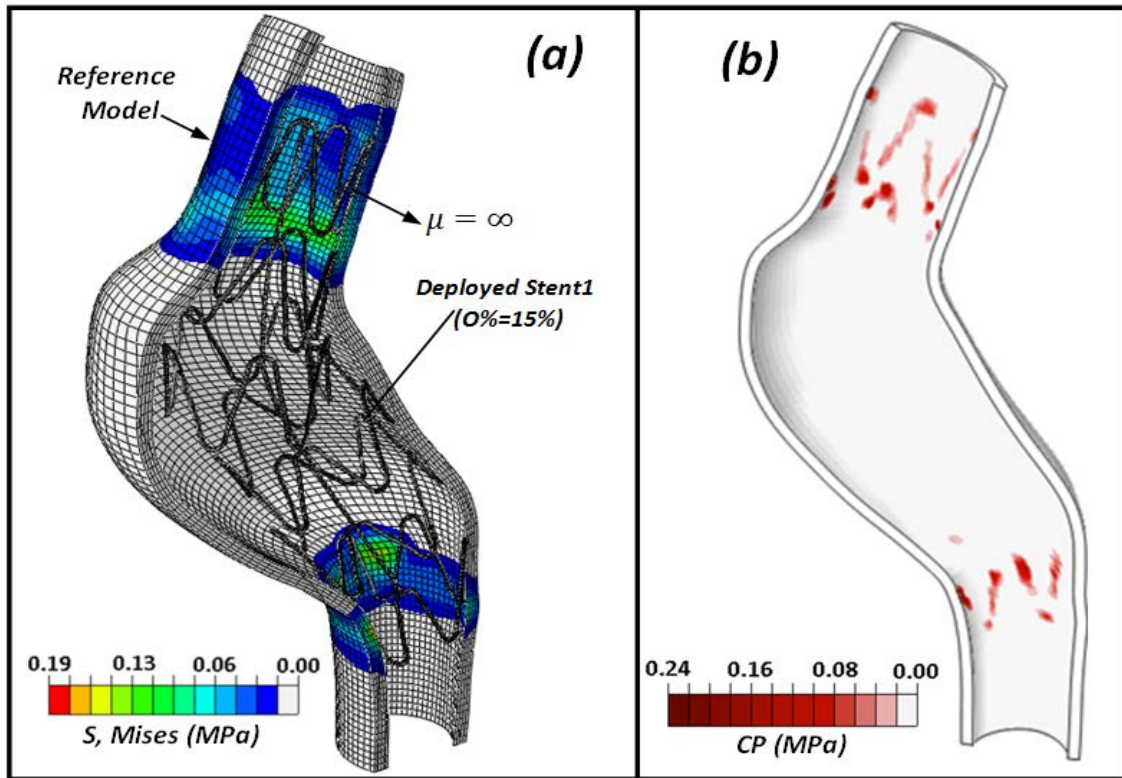
Figure Ⅲ.4-7: (Reference simulation): (a) The aneurysmal aorta and the deployed stent, contour plot of the Von Mises stresses (MPa), (b) contact pressure, simulation:Ⅴ (reference model)

During the simulation of the reference model, we can see the superelastic effect of nitinol stent (Figure Ⅲ.4-8): Von-Mises-diameter curve (Figure Ⅲ.4-9), stress-diameter nonlinear behaviour (Figure Ⅲ.4-10) and wholly recovered strain evolution-time during the whole deployment procedure (Figure Ⅲ.4-11).
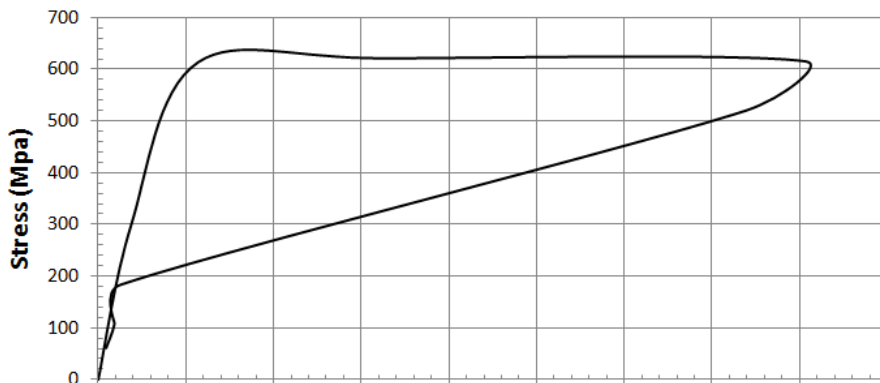
Figure Ⅲ.4-8: Non-linear stress–strain behavior of nitinol stent (element totally resorted its original shape) , simulation:Ⅴ

95
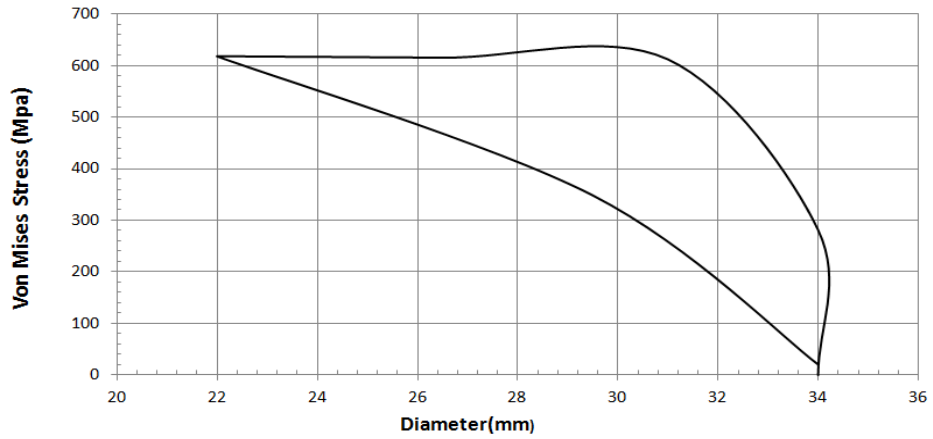
Figure III.4-9: Stress–Diameter non-linear behaviours of sitinol stent, simulation:V
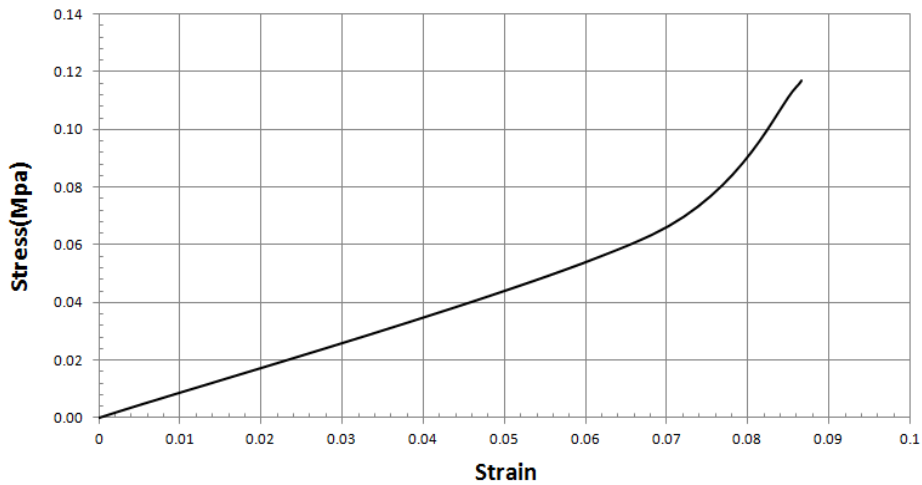
Figure III.4-10: Stress–strain non-linear behaviours of vessel, simulation:V
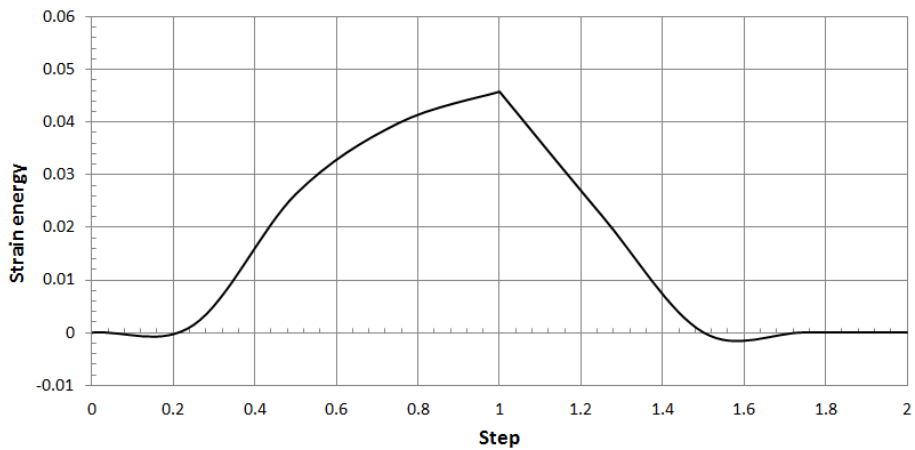
Figure III.4-11: Strain-time for the stent strut, simulation:V

96

III.4.5.2 Stent radial strength

The radial stent strength reflects the ability of a stent to resist the diameter loss. When the stent is forced to crimp down radially by cylindrical catheter, it will react by radial or circumferential reaction forces, also named (Hoop forces). These reaction forces (*N*) were induced on the surface nodes and were calculated at time intervals in every step. The hoop radial force was defined as the maximum value of the total reaction forces during crimping.
(Figure III.4-12) shows the hoop, radial strength-diameter curve during the crimping and expanding process of the simulation for the stent. The stent radial strength can be calculated by dividing the hoop strength by the total stent length *(N/mm)*.

In the beginning, the stent did not exercise any radial reaction forces. During crimping and bending process, the radial forces started to increase and reached its maximal forces of 2.64 *N* for the simulation V at the final phase of crimping. Then, in the expansion process, the radial forces suddenly dropped as the catheter surface expanded and relaxed the stent. The stent started to recover its original shape re-increasing the reaction forces against the catheter surface. At the final stage, the stent interacted with the vessel in the attachment sites and the reaction forces were applied by the vessel. The radial strength decreased and the un-contacted struts of the stent area recovered totally its energy at diameter (*D=37* mm) of the expanded surface. At this stage the

radial strength force value equals zero at stent diameter (*D=34* mm⇔15% of oversizing value).
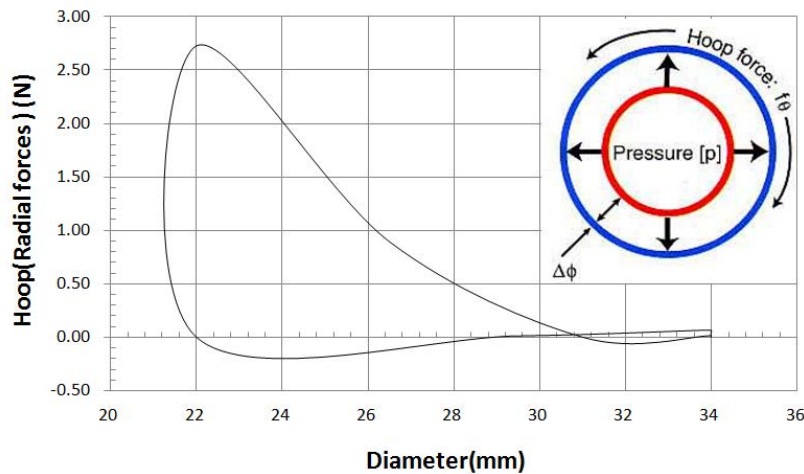
Figure III.4-12: Radial strength force-diameter curve, simulation:V

III.4.5.3 The impact of Proximal-Distal Attachment Site Length (*PASL-DASL*)

Three simulations of deployments have been performed for three stent lengths (V, VI, Ц); (stent1=144mm), (stent2=160mm), (stent3=185mm) respectively, with the attachment zone lengths indicated (Figure III.4-13) & (Table III.4-3) and an oversizing value of (O%=15%). The smoothest contact condition between the stent and the aorta was considered to be ($\mu = 0.05$). This value represents the critical value of tangential contact behaviour (stent-aorta) and can guarantee better and stable deployment for higher coefficients of friction: ($\mu = 0.1$),($\mu = 0.5$) (Vad, et al., 2010).

<center>97</center>

Deployment simulation	IJ	V	VI
	Stent3(185mm)	*Stent1(144mm)*	*Stent2(160mm)*
(PASL) (DASL)	D_{3P}=23 D_{3D} =23	D_{1P}=18 D_{1D} =15	D_{2P}=21 D_{2D} =18
Oversizing value (O %)	15%	15%	15%
Tangential contact behavior	($\mu = 0.05$)	($\mu = 0.05$)	($\mu = 0.05$)

Table Ш.4-3: Proximal-Distal Length-parameterizatic simulations
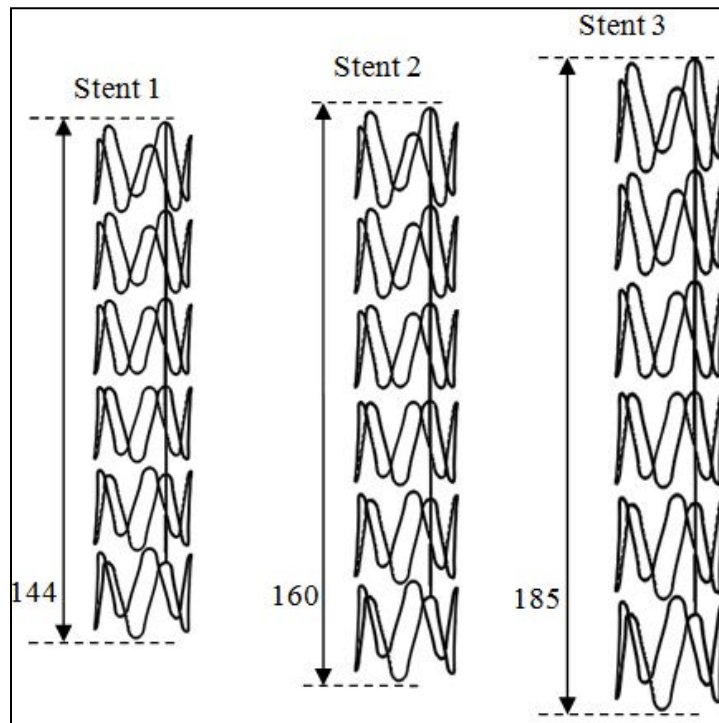
Figure Ш.4-13: Stent length dimensions (mm) with (O %) value 15%

An accurate positioning at the proximal landing zone was performed at the end of the catheter crimping and bending before the superelastic recovery took place. (Figure Ш.4-14) shows the complete-contact proximal-distal distance (stent strut-vessel). The Figure was taken just after the first interaction moment (stent-aorta), i.e., (partial deployment) so that the stent was not completely deployed and the tangential behavior cannot be seen yet. Thus, this Figure can only show the attachment sites' length just at the first moment of interaction.

The average contact stability was calculated in every simulation integrating the normal and shear contact forces in areas with positive contact pressure values. The same method was used to calculate the average normal contact pressure in the attachment sites. In the simulation ($V_{\mu=0.05}$), the contact stability values for stent1 were calculated before migration failure, i.e. when the first contact (stent-aorta) arisen.

98

One important issue is that contact stability values or the migration risk index ($\bar{F}_{cs}$) for all the simulations were calculated just after the first interaction moment for the stents undergone the migration (>10mm), and when fully stent deployment for non-migrated stents (<10mm). For comparison purposes, the ($\bar{F}_{cs}$) values were also evaluated for non migrated stents (<10mm) at partial stent deployment.
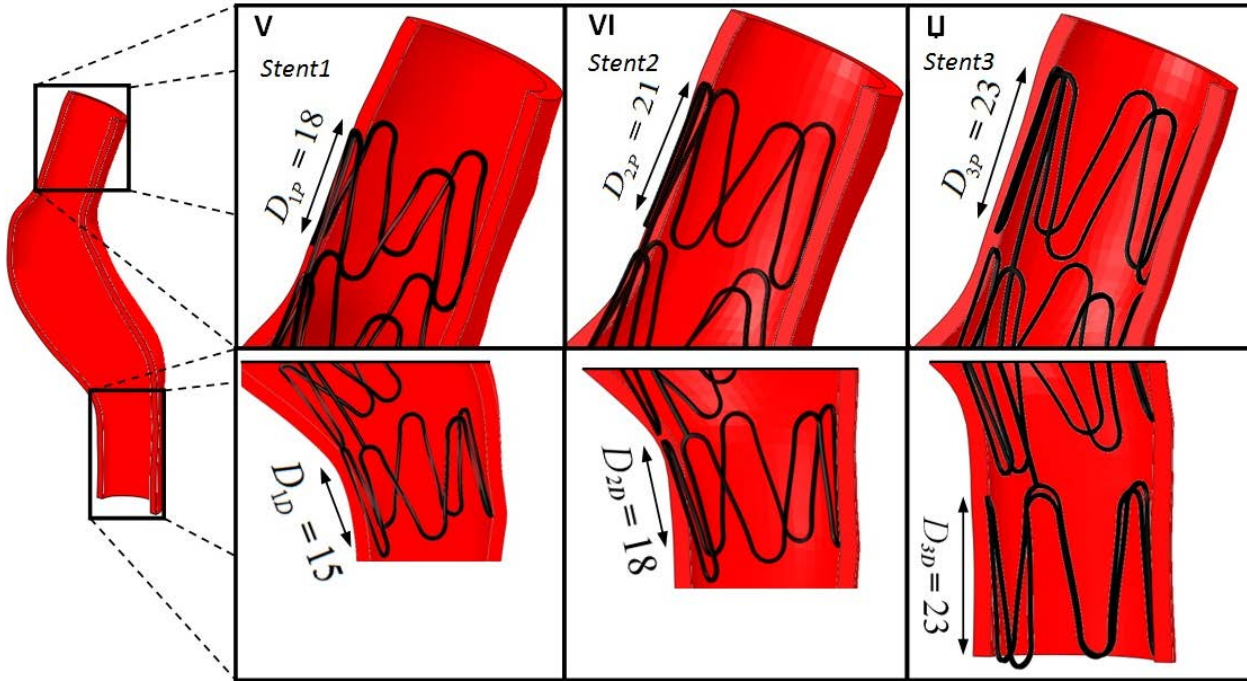
Figure Ⅲ.4-14: Proximal and distal attachment site lengths (D) (mm) just after the first interaction moment (stent-aorta), (O %) =15%. We consider (*D=P/DASL*); *D* represent the complete contact distance (stent-aorta)

In simulation V$_{O=15\%}$ (Figure Ⅲ.4-15), the stent1 was deployed with (*PASL*=18mm), which is longer than the critical clinic safety distance (15mm) (Lumsden, et al., 2007) (Hakaim, 2005) (Upchurch & Criado, 2009), however, in critical contact condition ($\mu = 0.05$) and high proximal neck angulation (α=60°) with (O%=15%), the stent1 migrated at the proximal site by more than 15mm, resulting in a higher stress concentration against the aorta (Altnji, et al., 2013) with high unstable contact ($\bar{F}_{cs} = 1$) proximally and ($\bar{F}_{cs} = 0.99$) distally (Figure Ⅲ.4-18). No remarkable migration has been reported at the distal attachment site.

99
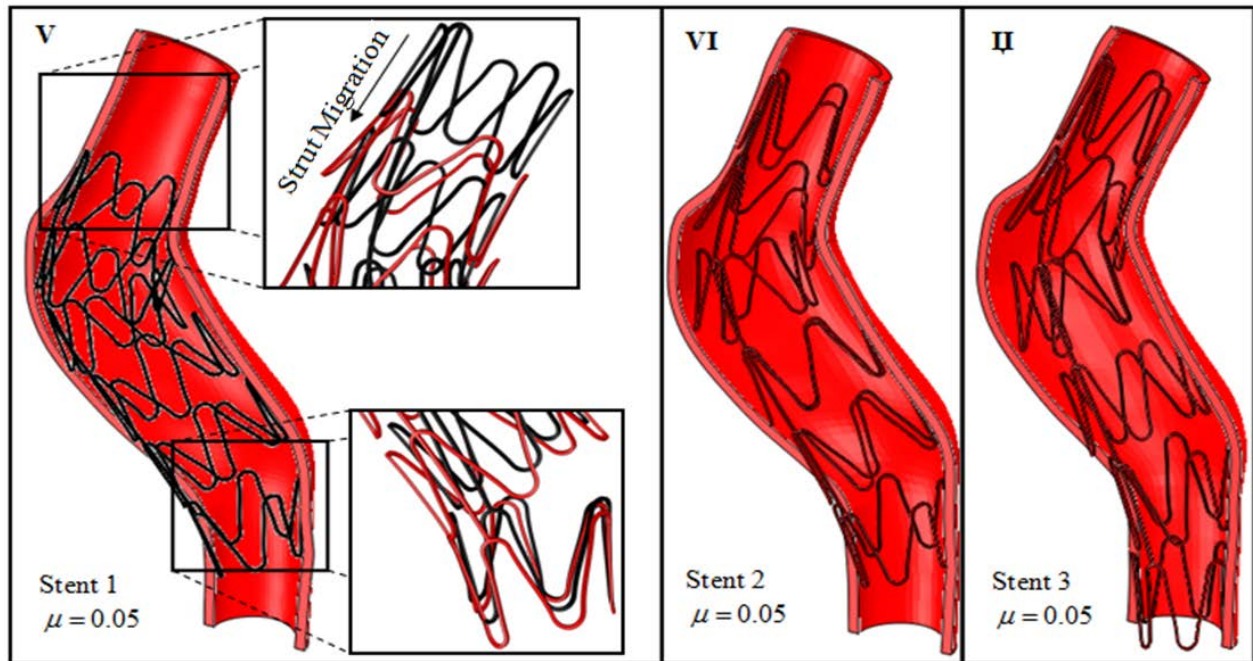
Figure Ш.4-15: Impact of proximal-distal attachment length on migration and stability of deployment- (O % =15%)

On the contrary, (stent2 and stent3) in simulations VI, Ц were deployed without any migration failure (Figure Ш.4-15). The stent2 and stent3 resulted in better contact stability with (10%) improvement in the proximal zone compared to stent1 (0.90 vs. 1). In simulation Ц, we adopted the length of the stent to be equal to the length of the centerline length. The results of simulations VI, Ц showed that the length of stent3 (185 mm) was more enough to avoid migration failure and poor deployment. Since stent3 has the longest length at the distal site, it improved the contact stability distally with (14%) improvement comparing to the stent2 (0.98 vs. 0.84) (Figure Ш.4-18).

These results principally approve the clinical findings that associated short (*PASL*) with unstable and poor deployment (Fulton, et al., 2006) (Zarins, et al., 2003) (Hakaim, 2005) (Upchurch & Criado, 2009) (Thompson, et al., 2007). The study reported by (Upchurch & Criado, 2009) showed that the short proximal attachment length (<15 mm) may result in difficult and poor deployment. This leads to consequent increased risk of endoleak type I or stent graft migration. In clinical practice, the occurrence of proximal endoleak type Ia is highest (6.25%) with proximal length less than (15 mm) and lowest (0.46%) for neck longer than (25 mm) (Upchurch & Criado, 2009). Furthermore, the study reported by (Zarins, et al., 2003) suggests that each millimeter increase in the proximal length will decrease the risk of migration by (5.8%). These results have been also supported by (Tonnessen, et al., 2005).

On the other hand, the distal attachment site did not have a considerable effect on the risk of rupture as no remarkable migration has been reported at the distal attachment site. This result agrees with the medical finding that suggests giving more control for precise proximal placement with minimal control over the distal attachment site (Lumsden, et al., 2007) (Hakaim, 2005).

In simulation($V_{\mu=0.05}$), the proximal attachment distance for stent1 was positioned to satisfy the required distance greater than 15 mm. Yet, the migration failure was reported with more than 15 mm. It is important to say that the length of attachment site is considered one of the major factors of migration and proximal attachment failure, but it is not the only component that can lead to migration, as clinical results show, (Thomas & Sanchez, 2009) (Hakaim, 2005) (Upchurch & Criado, 2009).

Different values of stresses induced within the aorta were reported (Figure ІІІ.4-16). The maximum values of Von Mises stresses (VMmax) were observed in all cases near the proximal and distal attachment sites, where the vessel cross-section is highly changed.

The stent1 in simulation ($V_{\mu=0.05}$), bring about high concentrations of stresses at a specific area in the aorta. This is explained by the additional forces of pressure applied by the slipped stent1 against the vessel. The high pressure can contribute to the occurrence of stent re-stenosis; especially, when a plaque is present in the vessel. In such case, deployment of the stent compresses the plaque and induces high stresses in lesion area (Zhao, et al., 2011) (García, et al., 2012). Thus, the stent1 produced higher concentrations of stresses and high unstable contact.

The stent2 and stent3 in simulations (VI, Џ) induce almost the same level of stresses in the vessel. The maximum value of Von Mises stresses was found to be (50%) lower than the stresses found in the simulation ($V_{\mu=0.05}$) with the stent1 (0.05Mpa vs. 0.1Mpa).
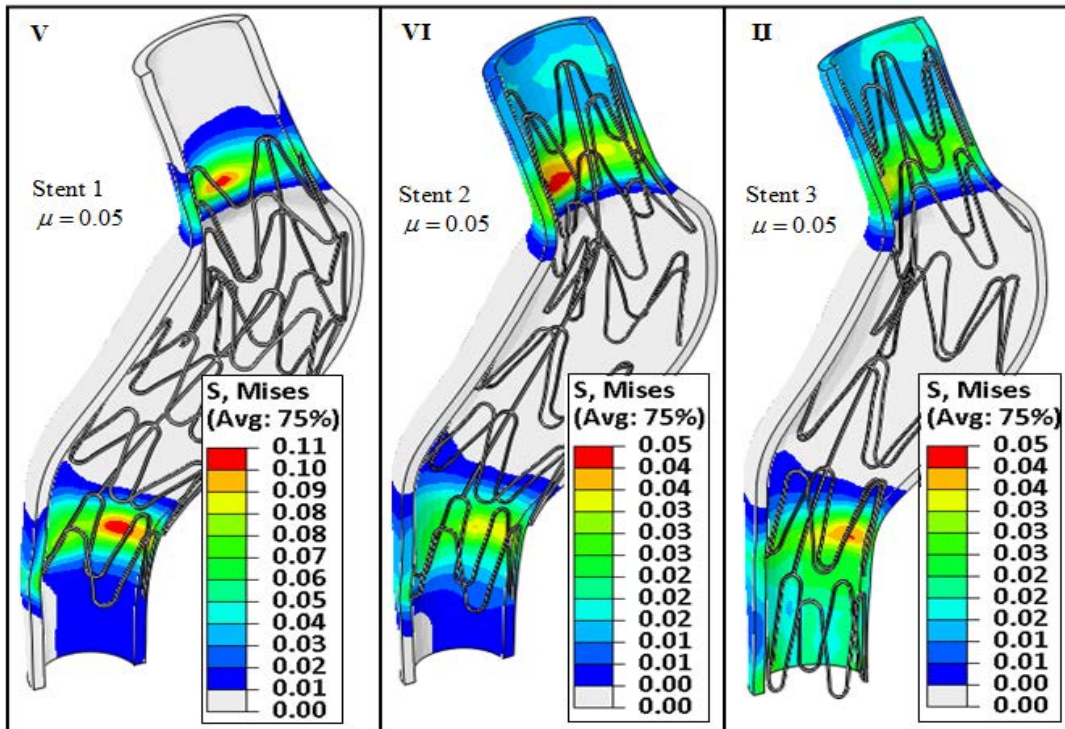
Figure ІІІ.4-16: Von-Mises stress distribution in the aorta treated by three lengths of the stent design-(O%=15%)

101

An important fact to notice is that the strain and stress relaxation induced in the stent was found to differ between the three cases. In the simulation $(V_{\mu=0.05})$, most of strut parts had undergone the elastic recovery upon stress removal until the parent phase was completely restored. Thus, the stent expanded without being pressured by chronic outward forces. This is related to the very small contact area with the proximal neck of the aorta, which makes the stent1 to restore totally its original shape after migration. The migration is attributed to the high shear stresses that dislodged the stent from the deployed position. On the other hand, in the stent2 and stent 3, only one part of struts of stent had restored its original shape and stiffness. Further expansion was prevented by the radial recoil pressure of the proximal aorta neck (Figure Ш. 4-17).
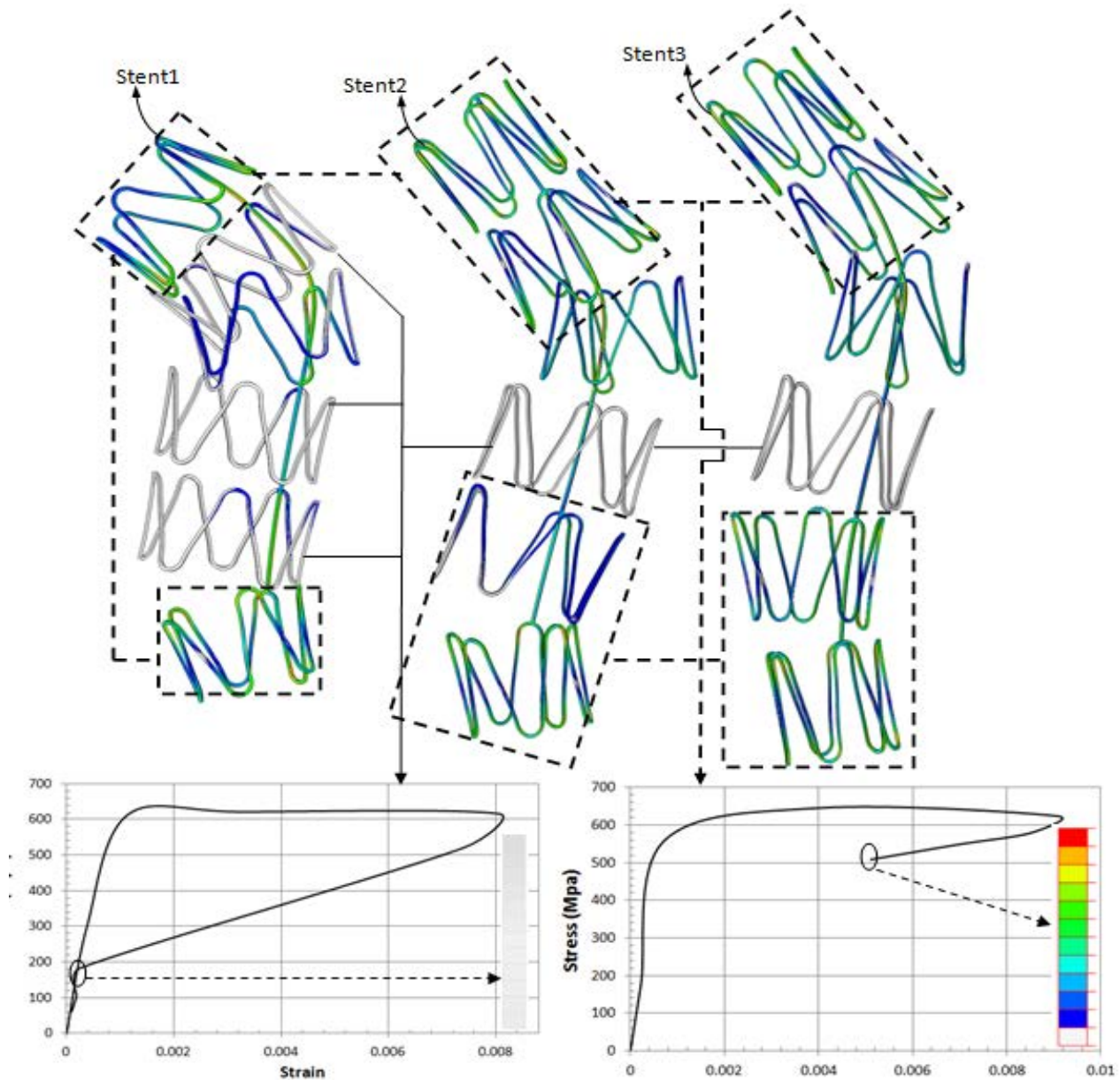
Figure Ш.4-17: Struts superelastic recovery with respect to the three stent models.

102

Simulation Stent models (PASL) (DASL)		V Stent1(144mm) D_{1P} =18 D_{1D} =15	VI Stent2(160mm) D_{2P} =21 D_{2D} =18	Ⅱ Stent3(185mm) D_{3P} =23 D_{3D} =23
Oversizing value (O %)		15%	15%	15%
Contact stability ($\overline{F}_{CS}$)	Proximal neck	1	0.89	0.90
	Distal neck	0.99	0.98	0.84
Tangential contact behavior		$\mu = 0.05$	$\mu = 0.05$	$\mu = 0.05$
Pressure contact area (mm^2) after deployment		460	1070	1133
Average normal contact forces (N)	Proximal neck	0.089	0.090	0.083
	Distal neck	0.083	0.10	0.090

Table III.4-4: Overview of the analyzed stents and their length characteristics
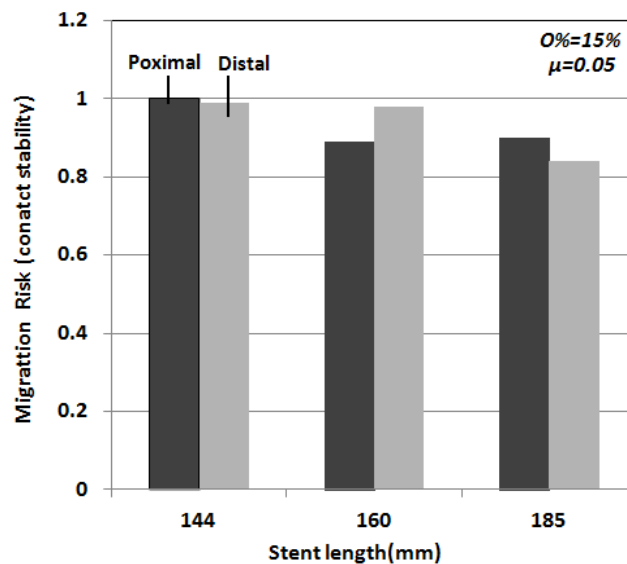
Figure Ⅲ.4-18: Contact stability values as a function of stent length

One or more of the following factors can be the cause of migration failure:

- The smoothest contact condition($\mu = 0.05$), which contributes in an unstable contact and poor, normal contact pressure as the situation for the stent1.
- The insufficient proximal attachment length of the stent which leads to decrease the pressure contact area. As a result, it increases the effect of shear stresses.
- The high neck angulation that contributes in increasing the strength of the shear forces leading to unstable contact.
- The un-sufficient oversizing value that highly contributes to fixation strength. Therefore, it is important to investigate all of these parameters for optimal stent selection.

103

III.4.5.4 The impact of oversizing on contact stability and deployment

Oversizing is calculated from the outer diameter of the stent and outer diameter of the thoracic aorta. Graft Oversizing (GO) is defined as:

$$Oversizing\,(\%) = \left(\frac{D_{EVG}}{D_{AORTA}} - 1 \right) \quad (\text{Ш}.21)$$

Where (D_{EVG}) is the outer diameter of stent; (D_{AORTA}) is the outer diameter of the aorta (Figure Ш.4-19). To investigate the impact of oversizing on the contact stability, five simulations have been performed (Table Ш-4-5). Suitable data of catheter were implemented in the code to satisfy every oversized stent diameter and deformed configuration). First, the migrated stent1 was oversized by (20%) and deployed with ($\mu = 0.05$). The result showed that the stent1 with (O%=20%) has also undergone migration failure (Figure Ш.4-21) with high unstable contact ($\bar{F}_{cs} = 1$) proximally and ($\bar{F}_{cs} = 0.99$) distally. However, the proximal slip distance was (MIG=13.5mm>10mm) (Figure Ш.4-21). The migration distance was not very important comparing to the (15%) oversized stent1 (MIG=18mm>>10mm) i.e. (25%) improvement of migration behavior.
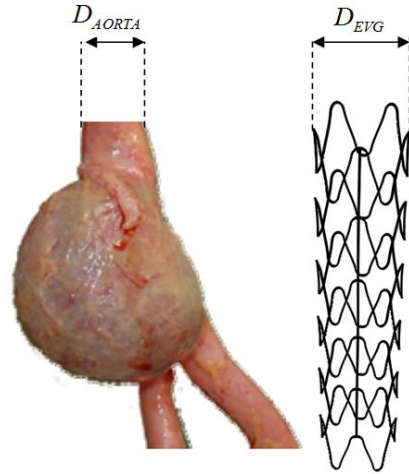
Figure Ш.4-19: Outer stent and aorta diameter

These results agree with the experimental findings which associate the valuable (Thomas & Sanchez, 2009) and insignificant impact of oversizing on contact strength at high neck angulations (Lin, 2012) (Zarins, et al., 2003).

Although migration failure has occurred, we obtained (25%) improvement of migration behavior in the smoothest contact condition and severe proximal neck angulation. A very small slip was reported in the distal neck with almost only 2 mm vs.3.7 mm reported in the (15%) oversized stent1 which means (85%) of migration improvement.

Table Ш.4-5: Oversizing (O %) parameterization, stent3				
Deployment Simulation	**I**	**Ц**	**Ш**	**IV**
	Stent3	*Stent3*	*Stent3*	*Stent3*
(PASL)	$D_{3P} = 23$	$D_{3P} = 23$	$D_{3P} = 23$	$D_{3P} = 23$
(DASL)	$D_{3D} = 23$	$D_{3D} = 23$	$D_{3D} = 23$	$D_{3D} = 23$
(O %)	10%	15%	20%	25%
Tangential contact behavior	(μ=0.05)	(μ=0.05)	(μ=0.05)	(μ=0.05)
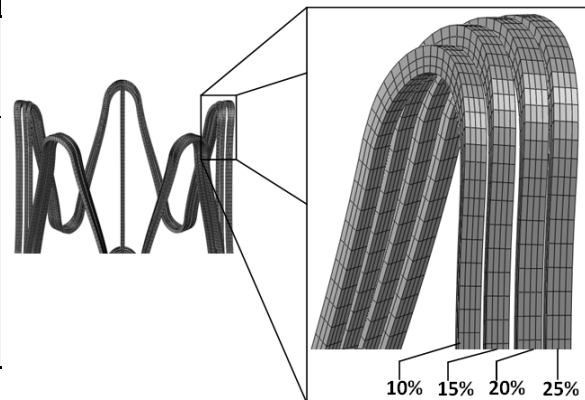
Figure Ш.4-20: Stent3 Oversizing values
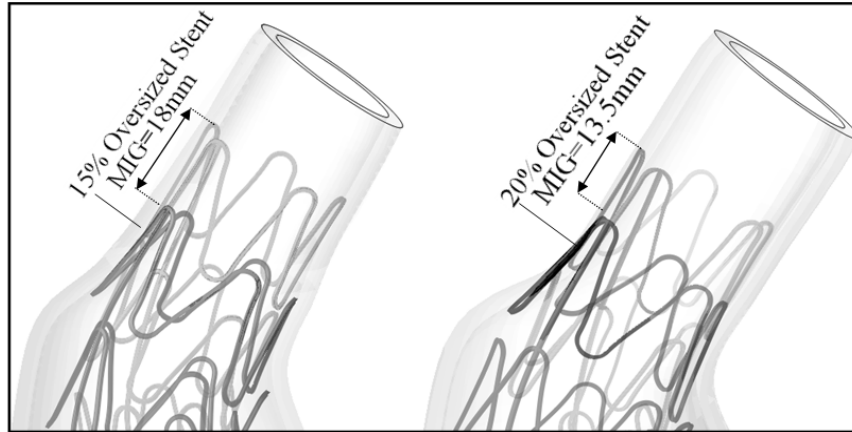
Figure Ⅲ.4-21: Stent1 migration for two oversizing values (15% and 20%) -(*μ=0.05),* simulation:Ⅴ

Since the (15%) oversized stent has the most important migration distance (Figure Ⅲ.4-21), it resulted in higher pressure and higher concentration of stresses in the distal site (0.1 Mpa) vs. (0.05 Mpa) in the (20%) oversized stnet1. The (20%) oversized stent showed more contact surface in the aneurysmal sac as more elastic energy was restored after full deployment (Figure Ⅲ.4-22).
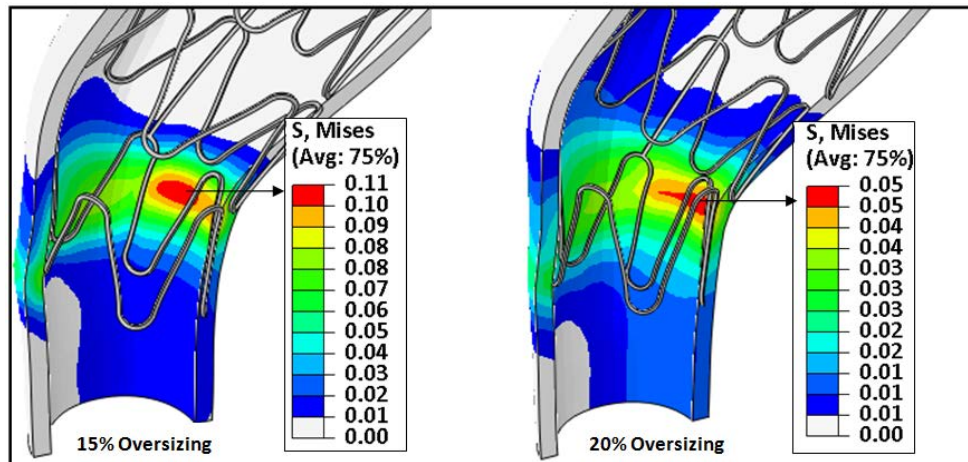
Figure Ⅲ.4-22: The maximal Von Mises stresses in the distal aorta sites treated by the 15% and 20% oversized stent, simulation:Ⅴ

Moreover, four simulations of stent3 were performed with (10% to 25%) oversizing values; we investigate the risk of neck enlargement (Matsumura & Chaikof, 1999) or stent collapse (Wolf, et al., 2001). The results showed that oversizing stent3 from (10 to 20%) resulted in an almost constant, normal and frictional force distribution, without aortic neck enlargement (Matsumura & Chaikof, 1999) or migration failure. For larger oversizing value, the radial forces were larger. Therefore, the (20%) oversized sent3 resulted in a more stable contact with ($\bar{F}_{cs} = 0.68$) proximally, i.e. a (23.6%) improvement compared with the (15%) oversized stent3 (0.68 vs. 0.89) and (28.6%) improvement in the distal site (0.60 vs. 0.84) (Figure Ⅲ.4-26).

105

Additionally, the (20%) oversized stent3 showed more connected strut points with the vessel in the attachment sites (Figure Ш.4-23) (Figure Ш.4-24).

Additionally, the (20%) oversized stent3 showed more connected strut points with the vessel in the attachment sites. Consequently, better circumferential stent strut distribution was resulted.
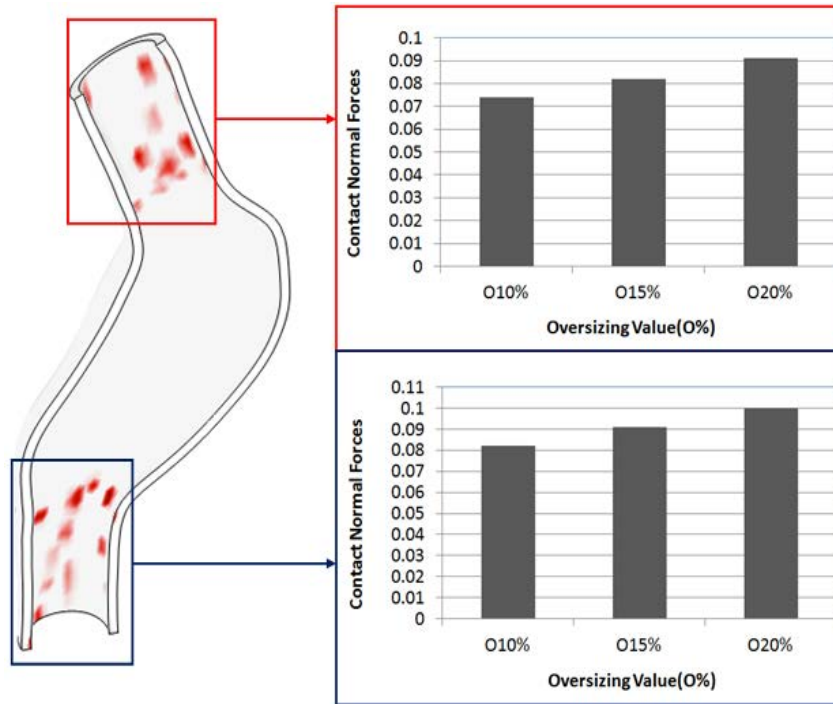
Figure Ш.4-23: Average Contact Normal Forces (CNORMF) as a function of oversizing (O%) induced in the proximal and distal attachment sites .it approximates the same contour in the one treated by (10%-20%) oversized stent with the percentile values in the right
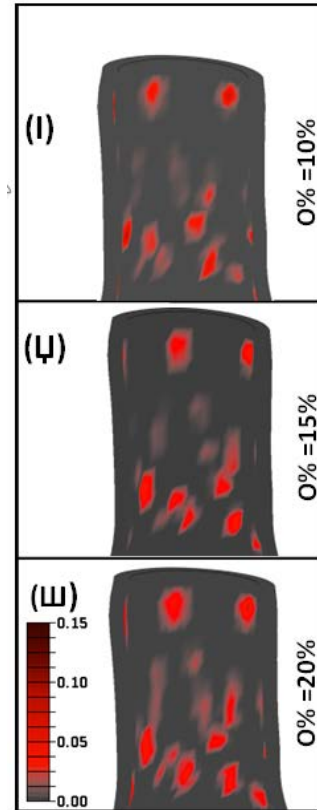
Figure Ш.4-24: Contact pressure stresses (MPa) in the aorta for different values of oversizing.

However, oversizing the stent3 by (25%) in the tortuous geometry produced a considerable amount of eccentric stent deformation and eccentric compression deformity (Wolf, et al., 2001) during the insertion phase, folding the boundary of stent3 (Figure Ш.4-25). When deployed, the eccentric stent3 expanded with unequal radial forces. This caused struts to be oriented away from the aortic wall, resulting in inconstant frictional forces. Consequently, a poor interaction on the aortic wall was resulted (Figure Ш.4-25).

Thus, the results showed that the eccentric stent caused by excessive oversizing can be a major cause of late migration and endoleak type Ia.

These results are consistent with the medical findings which associate the eccentric stent deformation with migration and endoleak type Ia (Wolf, et al., 2001) (Dias, et al., 2001) (Thompson, et al., 2007), the excessive oversizing > (25%) with increased potential of stent enfolding (Idu, et al., 2005) (Sternbergh, et al., 2002) (Hakaim, 2005) (Thomas & Sanchez, 2009) (Kratzberg, et al., 2009), and the neck dilatation with late migration (Sternbergh, et al., 2004).

106

In this morphology, the high neck angulation with excessive oversizing value can induce folding as the stent struts will experience a lot of overlapping and folding. This causes the eccentric deformation of the stent graft and prevents a good seal and contact with the aorta, specifically at the outer radius of the bend. These results prove the medical findings (Lin, 2012).

The numerical results demonstrated that the folded stent could create the eccentric pressurization which caused a single-side progressive dilation and subsequent rupture (Figure Ш.4-25). These results also correlate the medical findings that associate the eccentric stent deformation with increased risk of aneurysm rupture (Wolf, et al., 2001) (Hakaim, 2005).

The simulation also proved the experimental work of (Lin, 2012) when the folding failure was observed at (60°) of neck angles for oversizing ≥ (24%).

The (20%) oversizing showed the best fixation response that secures the best proximal fixation. Oversizing with (25%) and more in high tortuous aorta caused an eccentric stent deformation, which resulted in stent collapse. The folded stent caused eccentric-inconstant radial forces and inconstant frictional forces on the vessel.

Folding risk at the outer radius of bend has been linked with high neck angle and oversizing (Lin, 2012). The eccentric-continuous pressurization resulted in a considerable space between the aortic wall and the stent leading to problems, including stent collapse, endoleak, and migration. Folding risk may also occur if stent geometry is non-uniform or irregular.
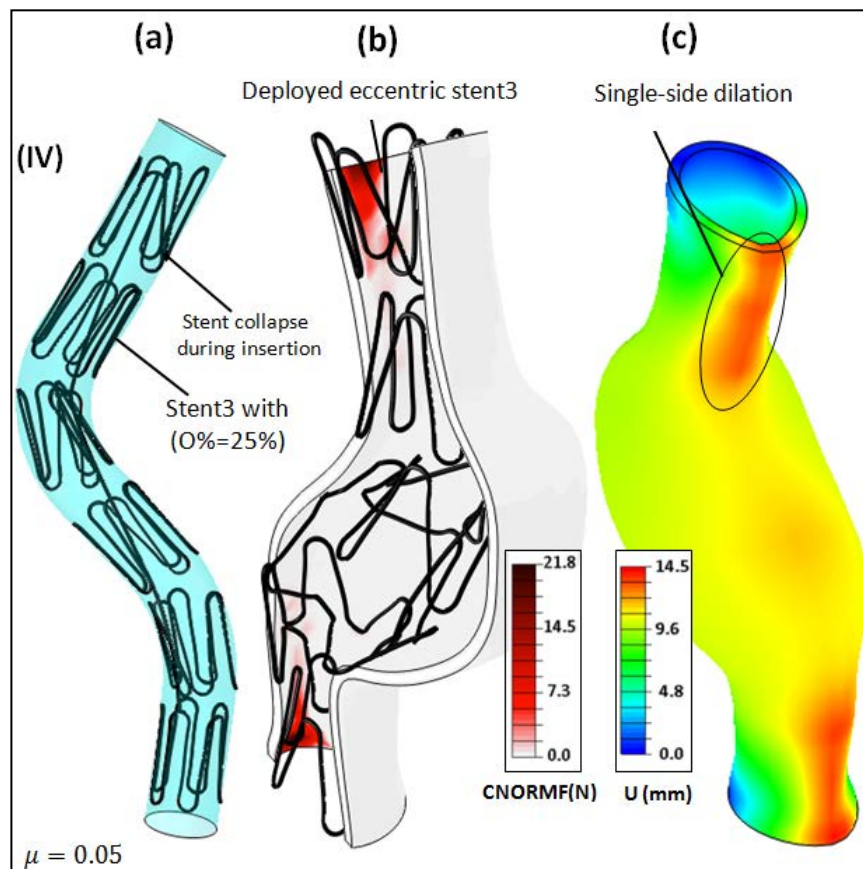
Figure Ш.4-25: (a) Numerical eccentric stent deformation as result of excessive oversizing (25%) during insertion phase; (b): The inconstant contact normal forces as result of eccentric stent deformation; (c): The high spatial displacement values results in eccentric-progressive neck dilatation leading to very poor fixation ,endoleak and migration failure

107

Oversizing from (10% to 20%) increased the hoop radial forces. The larger the oversizing is, the larger the radial forces and fixation strength are. The (20%) oversized stent resulted in a more stable contact with 0.68 proximal average contact stability, i.e., (24.4%) smaller than the (15%) oversized stent (0.68 vs. 0.9) and (28.6%) improvement in the distal site (0.60 vs. 0.84) (Figure Ш.4-26).

The (20%) oversized stent resulted in more connected strut points with the vessel in the attachment sites which means better circumferential stent strut distribution. The pressure contact area in (20%) oversized stent was increased by (24%): 1500 mm^2 vs. 1133 mm^2 in the (15%) oversized stent and (25%): 1500 mm^2 versus 1120 mm^2 in the (10%) oversized stent. The eccentric deployed deformation in the (25%) oversized stent showed a very poor contact area with only 162 mm^2 (Table Ш.4-6). The (10%) and (15%) oversized stent did not show a considerable difference in contact area, and only (1%) of larger contact area was present in the (15%) oversized stent: (1133 mm^2) vs. (1120 mm^2) in the (10%) oversized stent (Table Ш.4-7).

Consequently, when we face excessive oversizing of (25%), very high average values of normal contact forces were resulted at the proximal site (0.91 N), i.e., (90%) larger than the (20%) oversized stent (0.91 vs. 0.091) and in the distal site (0.88 N), i.e., (88.6%) larger than the (20%) oversized stent (0.88 vs. 0.1).

Table Ш.4-6: Overview of the analyzed stents and their oversizing characteristics					
Simulation		I	Ⅱ	III	
		Stent3	*Stent3*	*Stent3*	*Stent1*
(PASL)		$D_{3P} =23$	$D_{3P} =23$	$D_{3P} =23$	$D_{IP} =18$
(DASL)		$D_{3D} =23$	$D_{3D} =23$	$D_{3D} =23$	$D_{ID} =15$
Oversizing (O %)		10%	15%	20%	20%
Contact stability ($\overline{F}_{CS}$)	Proximal neck	0.80	0.89	0.68	1
	Distal neck	0.81	0.84	0.60	0.99
Tangential vontact behavior	*(μ=0.05)*	*(μ=0.05)*	*(μ=0.05)*	*(μ=0.05)*	
Pressure contact area (mm^2)		1120	1133	1500	
Average normal contact	Proximal neck	0.075	0.083	0.091	
forces (N)	Distal neck	0.088	0.090	0.10	
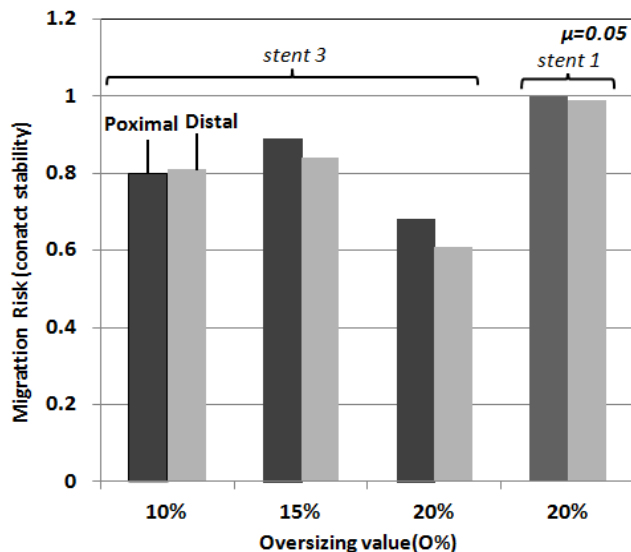
Figure Ш.4-26: Contact stability values as a function of stent oversizing (O %)

III.4.5.5 The impact of tangential contact behavior on contact stability and deployment

As mentioned before, it is not a trivial task to extract the reliable coefficient of friction (stent-aorta). The value of (μ) for (vessel-stent) contact is ranged between ($0.05 \leq \mu \leq 0.5$) (Vad, et al., 2010). The pathological state of the aorta (atherosclerotic plaques, calcifications, etc.) can significantly change (μ) value. In the smoothest contact condition ($\mu = 0.05$), the previous simulations showed that only short (stent1) slipped and resulted in migration failure. The (stent2) and (stent3) had been deployed without any migration failure Thus, it seems necessary to investigate the effect of the coefficient of friction (μ) on the contact stability for the migrated stent1 only. Three extracted experimental coefficients of friction (Vad, et al., 2010) were used for the simulation ($V_{15\%}$,): $\mu = (0.05, 0.1, 0.5)$.(Table Ш.4-7).

As seen earlier, the stent1 migrated under the smoothest contact condition ($\mu = 0.05$). Thus, smaller values of downward forces will be enough to dislodge the stent. Consequently, the smoothest contact behavior can be considered as a major cause of migration. On the other hand,

Table Ш.4-7: Overview of the analyzed stents and their tangential contact characteristics				
Simulation V :*Stent1* (144mm)- PASL=18- DASL=15				
Simulation		$V_{\mu=0.05}$	$V_{\mu=0.1}$	$V_{\mu=0.5}$
Oversizing (O %)		15%	15%	15%
Tangential contact behavior		$\mu = 0.05$ (migration failure)	$\mu = 0.1$ (small slip –no migration)	$\mu = 0.5$ (no migration)
Contact stability ($\overline{F}_{CS}$)	Proximal neck	1	0.97(first contact) 0.83(fully deployed)	0.80
	Distal neck	0.99	0.96(first contact) 0.89(fully deployed)	0.84
Pressure contact area(mm²) after deployment		460	747	1030
Average normal contact forces (N) after deployment	Proximal neck	0.097	0.088	0.11
	Distal neck	0.083	0.099	0.12

− When ($\mu = 0.1$), the results showed that stent1 has also slipped, but by a negligible proximal migration distance which was (MIG=3.5mm<10mm), i.e., no migration failure (Figure Ш.4-27). No distal migration was reported. Thus, this distance of the stent movement did not cause the migration failure since it was smaller than the critical distance (10mm). The shear forces applied in this contact condition were smaller than the hoop or radial forces applied at the proximal attachment site of stent1 and a good deployment was resulted.

− Additionally, when ($\mu = 0.5$), the stent was deployed without almost no slip or migration. Higher coefficient of friction ($\mu = 0.5$) improved proximally the contact stability by an average (17.5%) decrease from the moderate contact condition ($\mu = 0.1$): (0.80 vs. 0.97) and (20%) decrease from the smoothest contact condition ($\mu = 0.05$): (0.80 vs. 1).

    –   It also improved the contact stability index distally by an average (12.5%) decrease from the moderate contact condition ($\mu = 0.1$):(0.84 vs. 0.96) and (15%) decrease from the smoothest contact condition ($\mu = 0.05$):(0.84 vs. 0.99) (Figure Ш.4-29).

    These results can explain the different, clinical deployment results for different pathological aorta states (Wyss, et al., 2011). (Figure Ш.4-27) shows the final deployment position of stent1 (144 mm) for the three coefficients of friction. (Figure Ш-28) also displays the stress distribution of the stent1 for the three coefficients of friction.

Thus, the contact stability was improved at both proximal and distal attachment sites when ($\mu = 0.5$) (Figure Ш.4-29). These results can explain the different clinical deployment results for different aorta states. The aortic neck disease (thrombus and calcification) contributes in unstable device deployment and can result in poor clinical outcomes and complications like endoleaks (Wyss, et al., 2011).
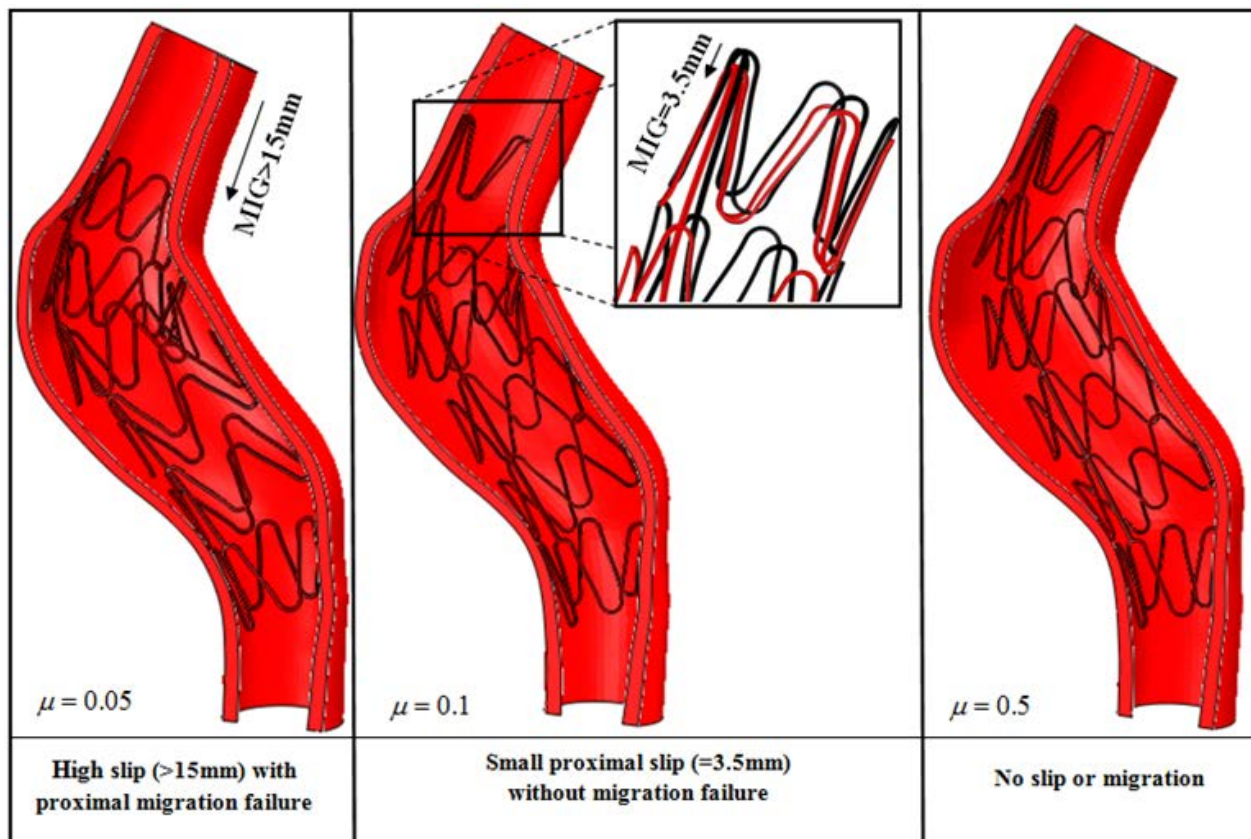
Figure Ш.4-27: Impact of coefficient of friction on migration and stability of deployment, simulation V

110
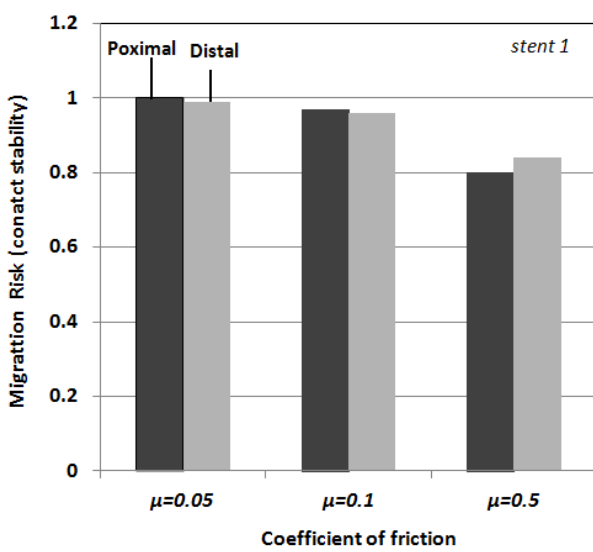
Figure III.4-29: The migration risk as a function of coefficient of friction
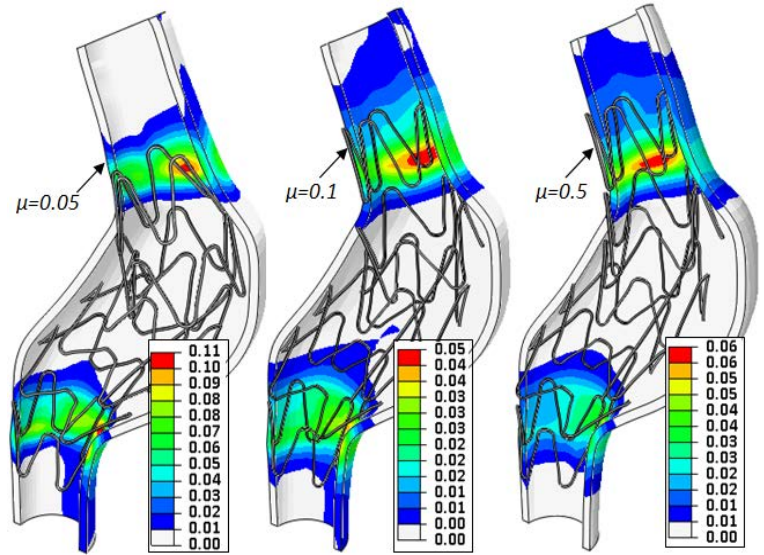
Figure III.4-28: Von Mises stress contour with respect to diffirent tangential behaviors
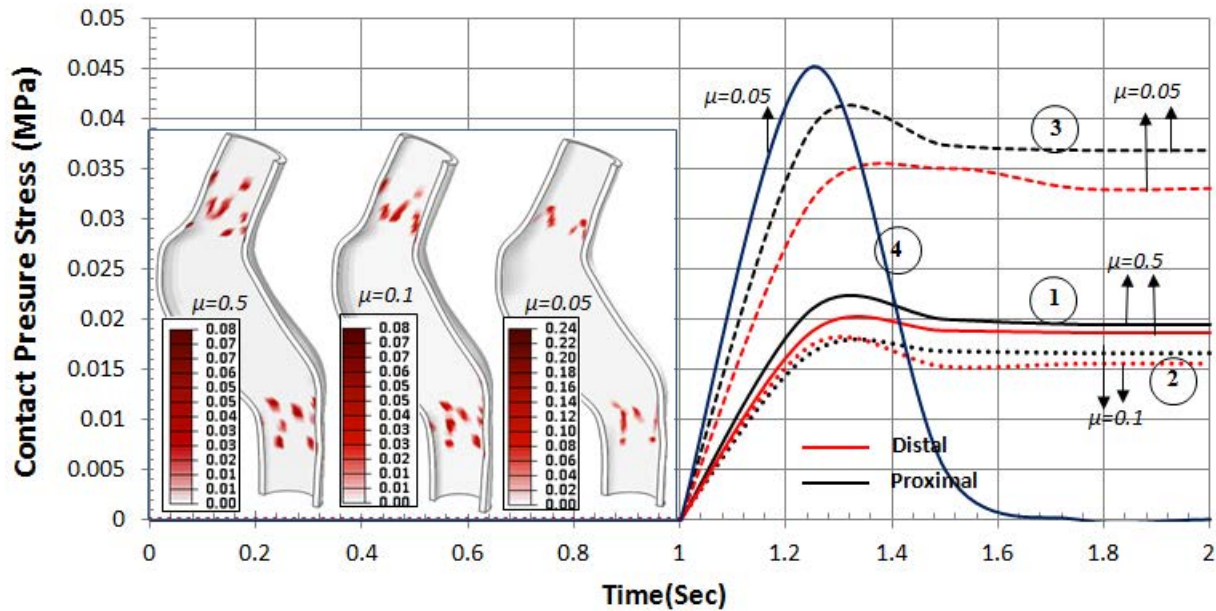
Figure III.4-30: The maximal contact pressure stresses (p) contour (MPa) induced in the aorta for three (μ) values after stent1 deployment. Curves 1, 2, and 3 represent the average (p) evolution with time simulation in both proximal and distal attachment sites. Curve4 shows the behavior of one vessel element that lost the contact after migration failure

When ($\mu = 0.05$) and ($\alpha=0°$), with (O%=15%, O%=20%) (simulation V), the stent1 started to interact with the vessel and the radial contact forces at the proximal site begun to increase. Then, when superelastic recovery took place, the shear forces which dislodge the stent increased because of the angulation that decreased the surface of interaction. These forces became higher than the radial strength stiffness of stent1 while the normal contact forces highly dropped and migration failure took place.

111

The historical behavior of the average contact pressure induced in the vessel during deployment was almost constant for every element in the proximal and distal sites when ($\mu = 0.1, \mu = 0.5$). During stent deployment, the contact pressure stresses slightly dropped because of radial compressive stresses applied by the aorta until equilibrium was reached (curve 1, 2 and 3) (Figure Ш.4-30). However; this behavior was different for many aortic elements that lost the contact with stent1 when ($\mu = 0.05$) after migration failure (curve4) (Figure Ш.4-30). This approach could introduce the effects of different tangential contact behaviors considering the overall hyperelastic aorta behavior.

III.4.5.6 Impact of proximal neck angulation on stability deployment

The previous specific-patient morphology shows high proximal angulation with ($\alpha = 60°$). According to (Sternbergh, et al., 2002), angulation severity can be classified into mild (<40 degrees), moderate (40-59°), or severe (>60°) neck angulation. Currently, US Food and Drug Administration (FDA) approved devices that require either 60° or 45° of neck angulation relative to the long axis of the aneurysm.

To investigate the effect of the challenging neck anatomy on the incidence of migration, we used an idealized aneurysmal aorta model. The model has all the same dimensions of length and diameters of attachment sites of the real model. Only the aneurysmal sac was ideally reconstructed in order to satisfy a straight proximal neck morphology with almost zero proximal angulation ($\alpha = 0°$) (Figure Ш.4-31).

In this simulation, the shortest stent1 model was used with the smoothest contact behavior ($\mu = 0.05$). Oversizing value was (O%=15%).
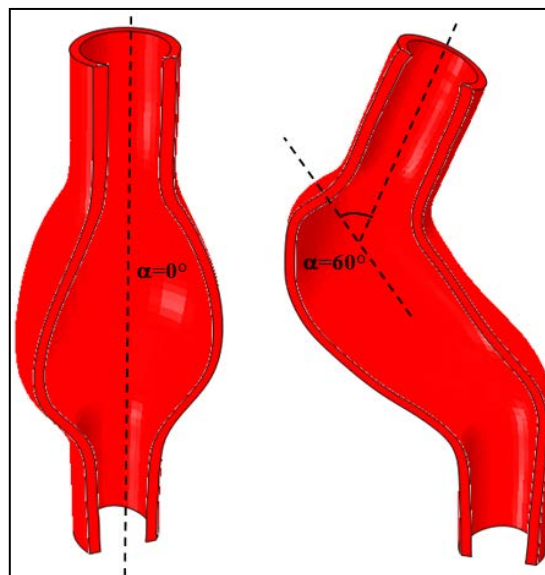
Figure Ш.4-31: The proximal neck angulation measurement of
idealized and real specific-patient aorta

Contrary to the migrated stent1 when (α=60°), the results showed that the stent1 did not migrate in the straight proximal neck even for the smoothest contact condition ($\mu = 0.05$). Slightly lower maximal Von Misses stresses (0.04Mpa) induced in the aorta were reported, versus (0.05 MPa) in simulations (Ц, VI) (Figure Ш.4-32).

112

The average contact stability decreased significantly with (20%) of contact improvement in the proximal site (0.80 vs. 1) and (23%) of contact improvement in the distal site (0.99 vs. 0.76), (Figure Ⅲ.4-33). When (α=0°), more interaction surface (stent-aorta) was reported and higher contact pressure was obtained (Figure Ⅲ.4-32).

Figure Ⅲ.4-32: Von Mises and contact pressure stress contour (MPa) induced in the straight aorta
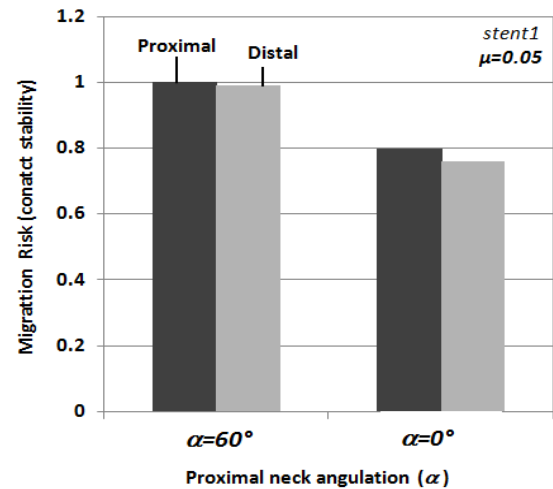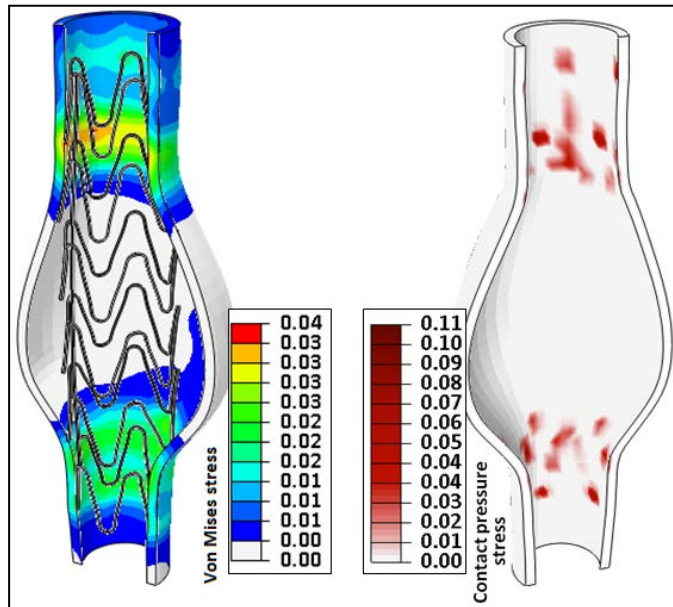
Figure Ⅲ.4-33: The migration risk as a function proxiaml neck angulation(first conatcat moment)

Table Ⅲ.4-8: Overview of the aotra tortuosity test simulation			
Tortuosity Simulation Test			
Stent model		*Stent1 (144mm); PASL=18; DASL=15;($\mu = 0.05$)*	
Oversizing (O %)		15%	15%
Tangential contact behavior		Neck angulation=60° (migration failure)	Neck angulation=0° (no migration)
Contact stability ($\overline{F}_{CS}$)	Proximal neck	1 (first contact)	0.80 (first contact) 0.85 (fully deployed)
	Distal neck	0.99 (first contact)	0.76 (first contact) 0.87 (fully deployed)
Pressure contact area (mm²) after deployment		460 (fully deployed)	1100 (deployed)
Average normal contact forces (N) after deployment	Proximal neck	0.097 (fully deployed)	0.12 (fully deployed)
	Distal neck	0.083 (fully deployed)	0.10 (fully deployed)

113

In the non-angulated aorta, as the stent1 applied higher radial strength diffusion on a larger surface on the vessel, the contact normal forces increased and became higher than the static downward forces. Therefore, a good opposition was resulting. Then, the normal forces slightly dropped because of the compressive forces applied by the vessel. Finally, the two forces will be in equilibrium at the end of deployment (Figure Ш.4-34).
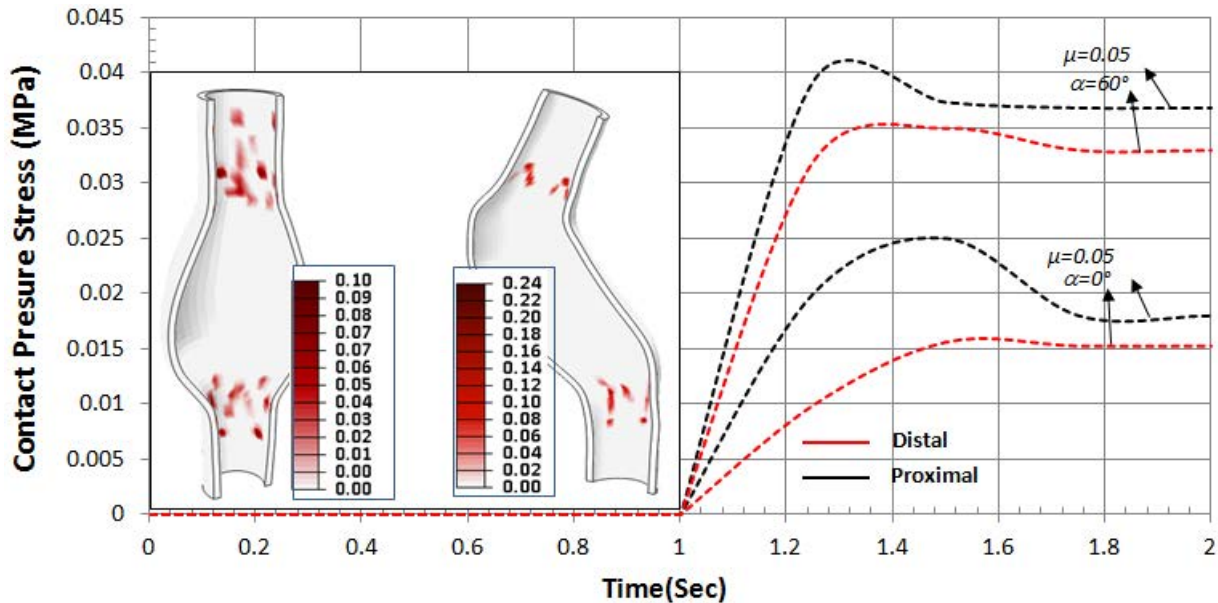
Figure Ш.4-34: The countour shows the maximaul contact pressure stresses induced in the proximal and distal attachment sites (MPa) for the straight and the angulated neck (the stent is fully deployed). The curves represnt the average contact pressure stresses evolution with time simulation in both proximal and distal attachement sites.

In a high neck angulation, the fixation length and the stent opposition were reduced. This increases the static downward forces applied to the stent, i.e., smaller values of these forces will be able to dislodge the stent. The simulation showed that a significant angulation of the aortic neck could increase the risk of stent migration due to the high shear forces applied on the device. This finding is correlated with the work of (Sternbergh, et al., 2004). High angulation can be a major factor of folding increasing the risk of migration and endoleak type I (Idu, et al., 2005).

The previous results demonstrated that increasing the length of the attachment sites and considering a suitable oversizing value could compensate the high values of tangential forces applying sufficient-normal contact forces and prevent the migration failure.

The numerical results correlate with the medical findings which consider that the unfavorable aneurysm neck anatomy can be considered the most important cause of poor outcomes like migration and endoleak type Ia: (Albertini, et al., 2001) (Sternbergh, et al., 2004) (Thomas & Sanchez, 2009) (Hobo, et al., 2007) (Fulton, et al., 2006) (Lumsden, et al., 2007) (Hakaim, 2005) (Upchurch & Criado, 2009) (Thompson, et al., 2007).

Furthermore, it is important to say that folding becomes more critical when oversizing value, neck angulation and stent length increase. A suitable level of oversizing value should be chosen for a specific level of neck angulation. The numerical results of oversizing and angulation impact support the following medical finding: *"in the extremely tortuous aorta, EVAR should not be offered as the primary treatment option"*.

114

There is evidence that proximal type I endoleaks is more common where the neck exhibits irregular contours, especially with thrombus or atherosclerotic. In our real morphology, we can note that not every point in strut surface is in contact with the aortic wall. This fact becomes more observant in highly angular neck where the struts are not subject to be uniform circumferentially. This can explain the clinical results that correlate the adverse outcomes of (EVAR) with calcification or angulation. Conventional stent grafts do not conform easily to the angles in the arch (Thompson, et al., 2007). Extending the proximal landing zone can improve the alignment of the device and the deployment, but cannot totally prevent the risk of migration or endoleak type I.

When self-expanding devices are used, it is necessary to increase the oversizing value up to (20%) in order to obtain an adequate seal. These two procedures have been suggested depending on the numerical results. The endograft should satisfy the difficult and challenging anatomy by controlling the fixation mechanism and providing a friction seal from the radial strength of the prosthesis against the native aortic wall. Moreover, in a severe neck angulation, the more flexible stent should be used.

III.4.5.7 Impact of modifying the hyperelastic properties of aorta

The material constants of the human aorta used in this study were extracted by uniaxial and biaxial testing for several samples. The samples were put in antibiotic solution to be then prepared for testing (Prendergast, et al., 2003). However, the constitutive models and material constants can be useful if they are taken in vivo conditions and over many patients. In vitro, the data reported by uniaxial and biaxial tests cannot represent the state of 3D stresses and residual stresses induced in the aortic wall (Vorp, et al., 2003) (Okamoto, et al., 2002) (Adham, et al., 1996).

Thus, the values of constants extracted from the experimental tests were modified with (10%) decreasing and (10%) increasing (Table III.4-9). The new-considered constants can represent other experimental data (stress-strain) or residual stresses of the aortic wall. In addition, different stress behaviors of the aorta can also be attributed to the pathological case of the aortic wall (ischemia, endotoxemia, and cytokine generation) (Elmarasy, et al., 2000).

Table III.4-9: The modified hyperelastic constants. The constants describe the Mooney-Rivlin model			
Material Coefficients	Human femoral parameters best-fit modified values (MPa)		
	Original values (Prendergast, et al., 2003)	+10%	-10%
(C_{10})	0.018	0.0198	0.0162
(C_{01})	0.00275	0.003025	0.002475
(C_{20})	0.59042	0.64946	0.5313
(C_{11})	0.857	0.9427	0.7713
(C_{30})	0	0	0

In case of (10%) decrease of constants' values, the Von Mises stresses induced in the aorta were equal to those in the aortic wall with original constants (0.047Mpa). A very light increasing in Von Mises stresses and contact pressure values were observed in the aorta with (10%) increase of material constants (0.47Mpa vs. 0.46Mpa).

The pressure stresses distributions across the aortic wall for the three cases showed uniform contact pressure stresses. The highest values were reported in the aorta behavior with (+10%) of material constants: 0.120Mpa vs. (0.095 and 0.096) Mpa in (-10%) and the constants extracted by (Prendergast, et al., 2003) respectively (Figure Ш.4-36).

However, a considerable improvement of contact stability was observed in the attachment necks when considering (10%) increase of material constants compared with the two other cases. The results showed almost (14%) and (18%) of contact stability improvement in both proximal and distal attachment sites respectively, compared to the original material constants: (0.76 vs. 0.89) proximally and (0.80 vs. 0.98) distally (Figure Ш.4-35). A small change in the contact stability was reported when (10%) decrease compared to the original material constants (Table Ш.4-10).

Thus, including other state of stresses or residual stresses represented in different material constants does not have such an important influence on the aorta deformation or the state of stresses. Our results showed that different states of stresses in the aortic wall can affect the contact stiffness and the deployment quality. It also approved that including the residual stresses may result in different contact pressure stresses and consequently different contact stability (Gee, et al., 2010) without a significant change in the stresses or deformation behavior.
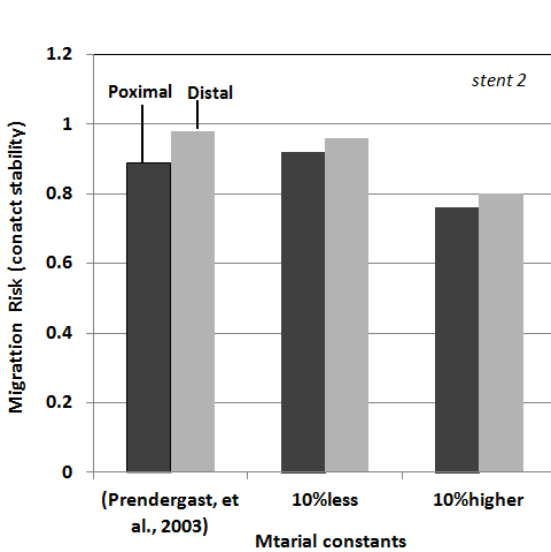
Figure Ш.4-35: The migration risk as a function of diffirent material constants
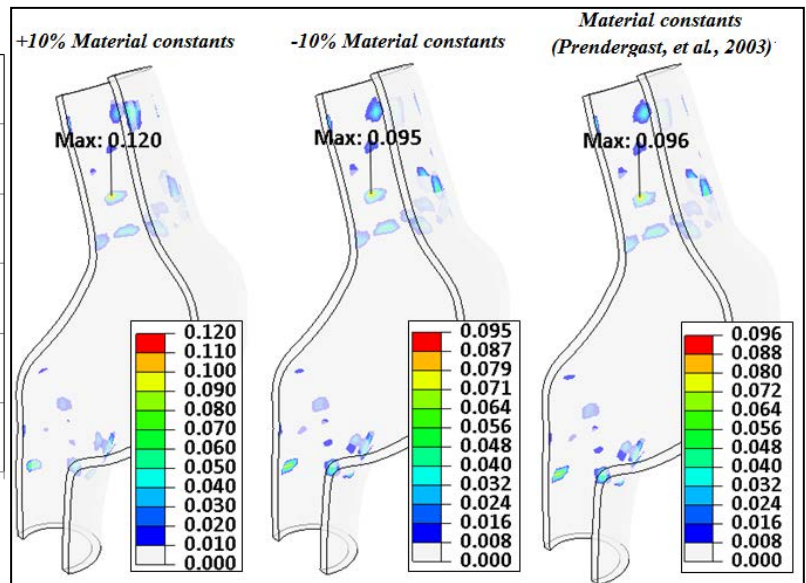
Figure Ш.4-36: Contact pressure stresses contour (MPa) with respect to diffirent material constants

116

Deployment Simulation	VI Stent2	VII Stent2	VIII Stent2
(PASL)	D_{2P} =21	D_{2P} =21	D_{2P} =21
(DASL)	D_{2D} =18	D_{2D} =18	D_{2D} =18
Oversizing (O %)	15%	15%	15%
Tangential contact behavior (coefficient of friction)	(μ = 0.05)	(μ = 0.05)	(μ = 0.05)
Material Coefficients	Original values	-10%	+10%
Contact stability ($\overline{F}_{CS}$) — Proximal neck	0.89	0.92	0.76
Contact stability ($\overline{F}_{CS}$) — distal neck	0.98	0.96	0.80

Table III.4-10: The effect of modifying the hyperelastic properties of the aorta ; (simulation results)

III.4.5.8 Impact of aorta calcification

Thoracic aortic aneurysms are characterized by the weakness or degeneration of the media layer. This degeneration can be a result of atherosclerotic degeneration or caused by non-inflammatory medial degeneration (Lumsden, et al., 2007). Calcification is the inclusion of hard, calcium based deposits within the wall of the aorta.

The circumferential calcification or the atheroma can significantly vary the biomechanical behavior in the attachment zone and must be considered as an important factor on the contact stiffness, delivery problems and long-term solidity of the aortic wall. The presence of the calcification can result in many complications to reliably measure the diameter of the aortic neck (Lumsden, et al., 2007) (Hakaim, 2005). Moreover, calcification can be a major cause of rupture because of the low compliance and high rigidity of the calcified aorta (Thompson, et al., 2007). The calcified aortic tissues have a lower tensile strength and tear resistance than healthy ones (Walraevens, et al., 2008). Thus the calcified aorta becomes stiffer and its elasticity is reduced.

The risk of a proximal endoleak type I is also increased when the neck contains non-regular forms of atheromatous plaques or ridges (Hakaim, 2005). Therefore, two aspects are important to be considered when a high calcification is presented in the lumen of the aorta; the first is the high risk of rupture caused by the high rigidity, the second is the risk of endoleak when calcified ridges are presented. Thus, the anatomical estimation of the aorta is a crucial factor in EVAR success and preoperative-high-resolution computed topographic images are needed.

To minimize the complexity, the lumen of the vessel was reconstructed regardless of the non-uniform ridges of calcification and plaques in the lumen of the aorta area (Zhao, et al., 2011), (García, et al., 2012) (Figure III.4-37). Thus, we aim only to investigate the migration behavior and stress distribution when the aorta is calcified by considering a large and uniform surface of calcification. The mechanical properties and coefficient of friction of the calcified aorta were taken from the PhD work of Mrs. G Mouktadiri.

The material behavior was considered as incompressible, isotropic, liner-elastic and dense material. The (macroscopic) assumption of the linear elastic material can be supported by the results obtained from (Wang, et al., 2001).

As an approximation, we considered the mechanical behaviour of the media layer since it plays the major role of mechanical behaviour of the entire aorta. The calcified properties were assigned one time only to the aneurysm and another time to the entire aorta for both stent1 and stent2 oversized by (O%=15%). Thus, four simulations were performed with coefficient of friction ($\mu = 0.5$) and one simulation with the stent1 with coefficient of friction ($\mu = 0.05$). The last simulation is to investigate the migration behavior and stress distribution in the aneurysmal calcified aorta with the smoothest contact condition of the healthy hyperelastic attachment sites.
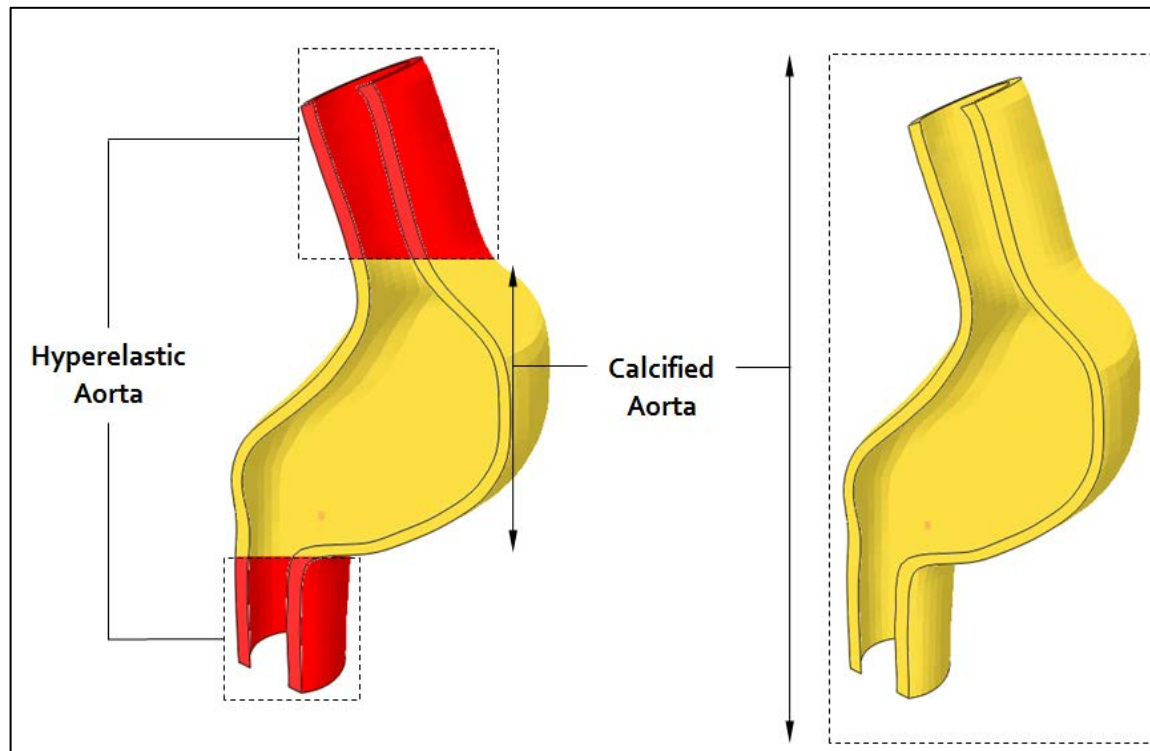
Figure Ш.4-37: The calcified aorta simulations; calcified aneurysmal sac (left) and all calcified aorta (right)

(Figure Ш.4-38) shows the deployment results of the stent1 in the aorta. The aorta was modeled as an isotopic hyperelastic material at both attachment sites and calcified elastic behaviour overall the aneurysmal sac. The coefficient of friction (aorta-stent1) is to be ($\mu = 0.05$). In this case, the stent migrated with almost (6 mm) which means no migration failure. These results are expected and explained by the high contact stiffness improvement at both attachment sites. The high rigidity or stiffer material of the calcified aneurysm will result in smaller spatial deformation of the aneurysm. Consequently, smaller enlargement of the aorta at the attachment sites are reported leading to better contact stiffness, i.e. steeper contact and higher Chronic Outward Force (COF) of the aorta were resulted compared with those when the overall of the aorta was hyperelastic.

These numerical results are in a good agreement with the experimental and clinical results: '*although the presence of thrombus and calcification in the neck does not appear to be as significant risk factor as previously thought*' (Albertini, et al., 2000) (Veith & Baum, 2003).

When the coefficient of friction (aorta-stent1) was to be ($\mu = 0.5$) with an only calcified aneurysm, smaller maximum spatial deformation was obtained compared to those when ($\mu = 0.05$) (1.85. vs. 2.31) mm, respectively (Figure ΙΙΙ.4-39). The maximal spatial deformation was reported when overall of the aorta is hyperelastic with ($\mu = 0.5$): (3.04 mm) (Figure ΙΙΙ.4-39). This is due to the high radial pressure applied by the stent against the hyperelastic aorta, where no slip was expected since the high value of ($\mu = 0.5$).

Wide differences in maximal displacement values were resulted when overall of the aorta was totally calcified compared with those when only aneurysm was calcified and non-calcified aorta: (1.85 vs. 0.66) mm. (3.04 vs. 0.66) mm, respectively, where ($\mu = 0.5$) (Figure ΙΙΙ.4-39).
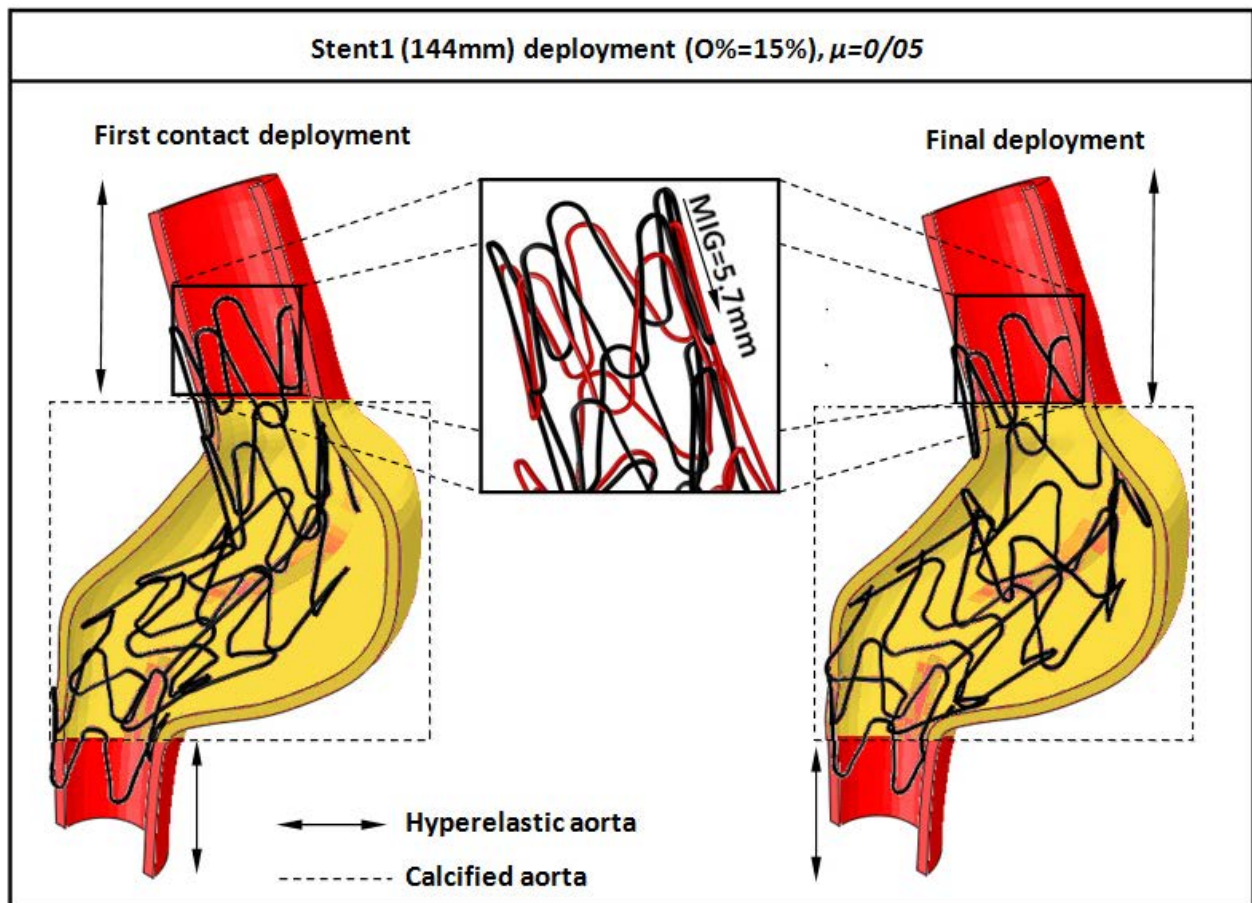
Figure ΙΙΙ.4-38: Migration behaviour when the aneurysm is calcified (stent1 deployment), ($\mu = 0.05$)
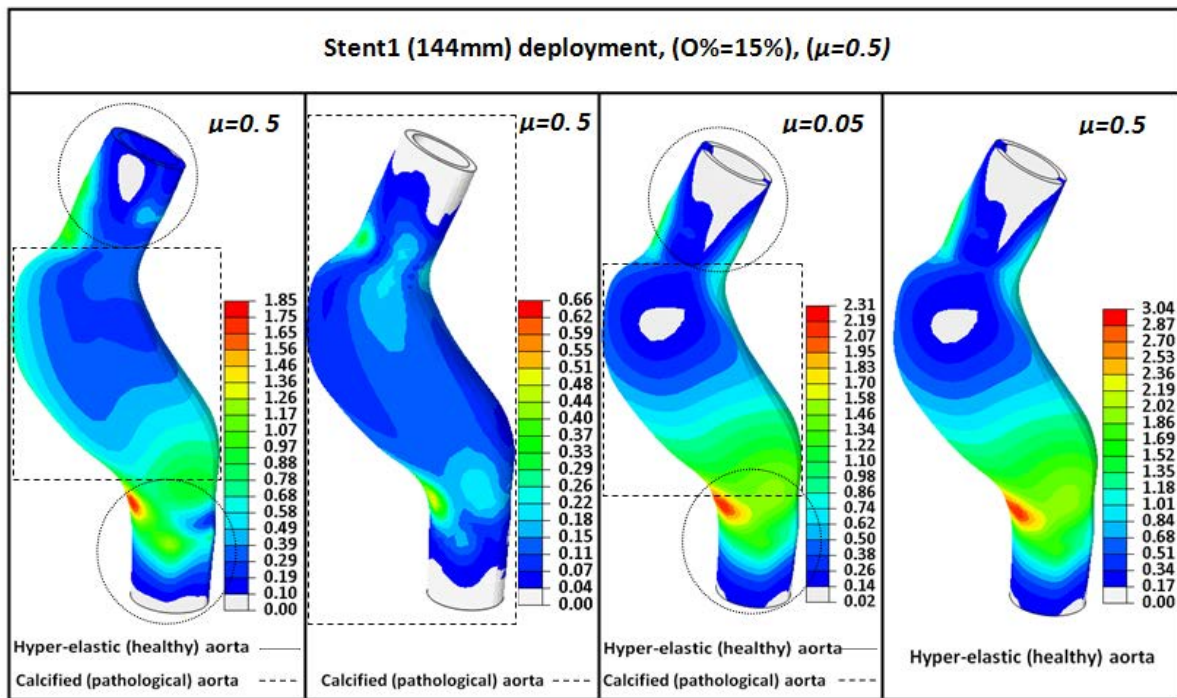
Figure Ш.4-39: Comparison of spatial displacement contour (mm) for different calcification severity
after implantation of stent1 (O%=15%) and two values of cofficient of friction

For the stent2, the results also showed that when the entire aorta was calcified, a very small spatial deformation was reported comparing with the healthy hyperelastic behaviour (0.67 vs. 3.92) mm respectively, i.e., (83%) of decrease. This is due to the high rigidity of the calcified material which is stiffer than the hyperelastic arterial wall. Higher special displacement was obtained when the overall aorta was considered hyperelastic comparing with the calcified aneurysm (3.92 vs. 2.17) mm, i.e., (44.6%) of decrease (Figure Ш.4-40).

120
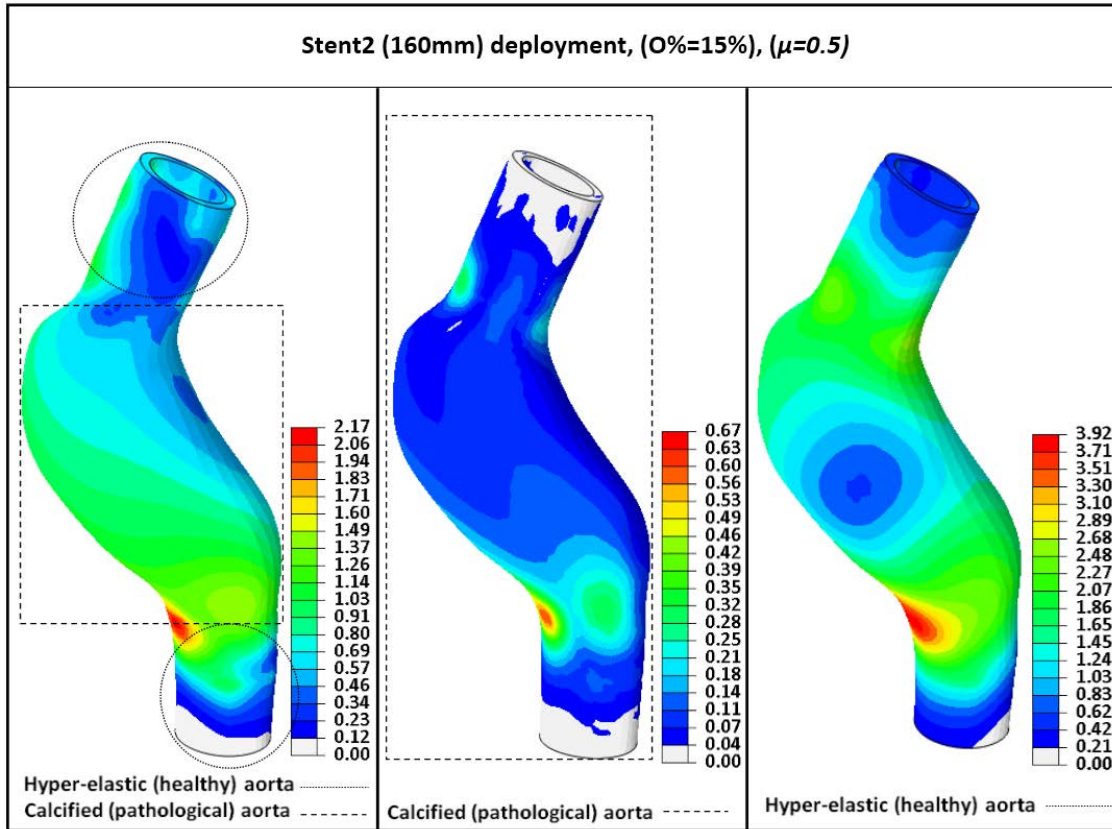
Figure ІІІ.4-40: Comparison of spatial displacement contour (mm) for different calcification severity after implantation of stent2 (O%=15%)

Thus, for both stent deployments, we expect higher values of Von Mises stresses in the calcified aorta than the healthy one. When only the aneurysm sac was calcified, the maximal Von Mises stresses were found in the section where the mechanical behaviour was changed from the hyperelastic behaviour in the attachment site to the elastic rigid behaviour in the aneurysmal sac (Figure ІІІ.4-41).

There was no reported slip or migration in all simulations with the coefficient of friction ($\mu = 0.5$). However, significantly higher values of Von Mises and contact pressure stresses were resulted in the calcified regions of the aorta.

As a result, the calcified aneurysm sac in the aorta was more sensitive to break than the hyperelastic or healthy aorta. For both stents deployments, the maximal Von Mises stresses were significantly higher comparing with the hyperelastic healthy aorta treated by (15%) oversized stent and ($\mu = 0.5$) coefficient of friction (0.06 vs. 0.29) N/mm^2 for stent1, i.e. (383%) of increase. The maximal contact pressure value was also multiplied (0.08 vs. 0.16) N/mm^2. In all cases of calcified aneurysm or calcified aorta, the highest displacement was located in the final section of the aneurysm at the distal part.

The values of Von Mises stresses observed in the calcified aorta were so high. The fracture commonly happens because of the stiff or the brittle aorta. Therefore, further improvement, including the analysis of the rupture process of the calcified material of the aorta (atherosclerotic plaques, calcification, etc.) in the model will be our future investigation.
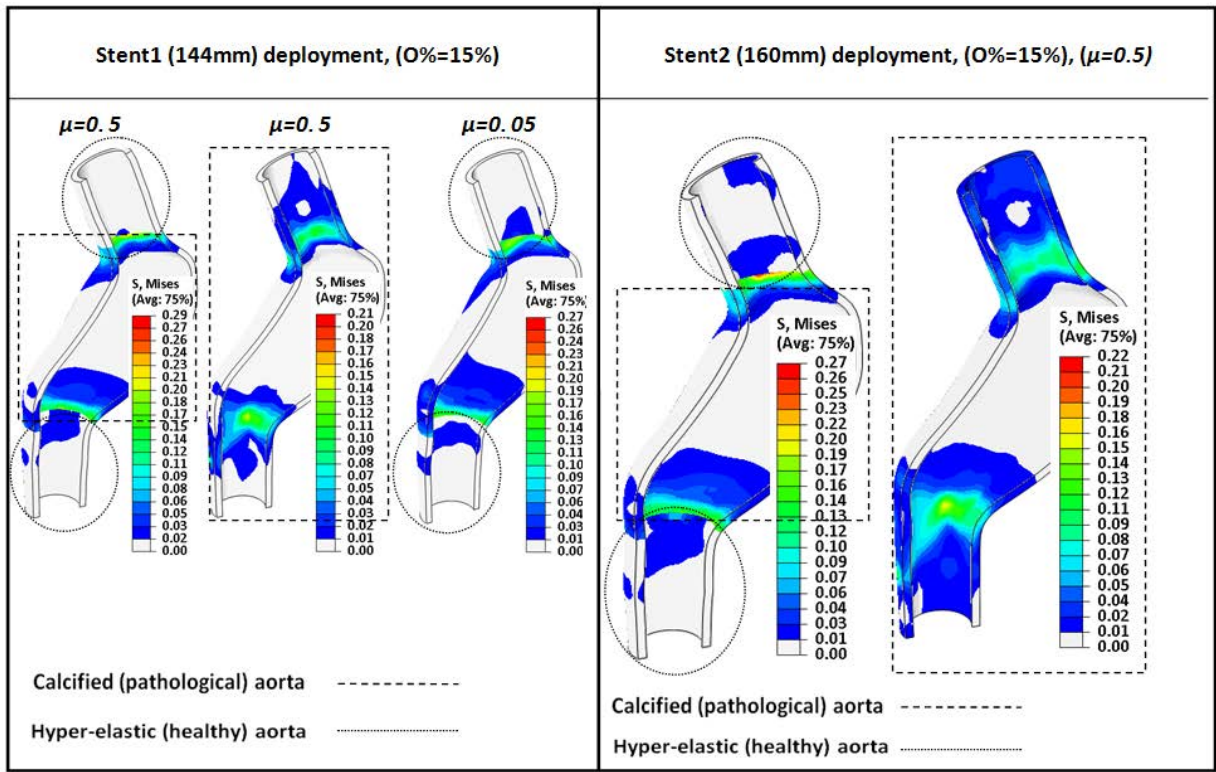
Figure Ш.4-41: Comparison of VonMises stresses contour (MPa) for different calcification severity after implantation of stent1 and stent2, (O%=15%)

Table Ш.4-11: The impact of the aorta calcification; (simulation results)					
Deployment Simulation	V *Stent1* (calcified Aneurysm)	V *Stent1* (calcified aorta)	V *Stent1* (calcified Aneurysm)	VI *Stent2* (calcified Aneurysm)	VI *Stent2* (calcified aorta)
(PASL) *(DASL)* *(angulated proximal neck)*	$D_{1P} = 18$ $D_{1D} = 15$	$D_{1P} = 18$ $D_{1D} = 15$	$D_{1P} = 18$ $D_{1D} = 15$	$D_{2P} = 21$ $D_{2D} = 18$	$D_{2P} = 21$ $D_{2D} = 18$
(O %)	15%	15%	15%	15%	15%
Tangential contact behavior (coefficient of friction)	$\mu = 0.5$	$\mu = 0.5$	$\mu = 0.05$	$\mu = 0.5$	$\mu = 0.5$
Contact stability — *Proximal neck*	0.75	0.75	0.80	0.71	0.55
distal neck	0.77	0.75	0.81	0.75	0.75

122

The results of these simulations showed smaller contact stability values than the contact stability obtained in the healthy aorta treated by the stent1 with ($\mu = 0.5$), which means better contact stiffness. When only the aneurysmal sac is calcified, the stent1 deployment resulted in a slight improvement (6.3%) of contact stability (0.80 vs. 0.75) proximally and (8.3%) in the distal part (0.84 vs. 0.77). Almost the same results were obtained for the stent1 when the entire aorta is calcified. As expected, an improvement in contact stability was reported proximally when the length of the proximal attachment zone was increased (stent2). The contact stability was significantly improved at the proximal site when the entire aorta was calcified ($\bar{F}_{cs} = 0.55$) comparing with the calcified aneurysm ($\bar{F}_{cs} = 0.71$) with ($\mu = 0.5$). When the stent1 was deployed with ($\mu = 0.05$), the calcified aneurysm resulted in a decrease in the contact stability with ($\bar{F}_{cs} = 0.80$) proximally and ($\bar{F}_{cs} = 0.81$) distally. As a result, no migration failure was reported, which was the case when the aorta was considered hyperelastic material.

These results are expected because of the high rigidity of the brittle calcified aorta. Therefore, when deployed, the reaction of compression forces applied by the aorta became so important, and the high coefficient of friction also resulted in an improved positional stability.

Our numerical approximation showed no impact on migration failure. The calcified aorta resulted in higher stresses. Consequently, the obtained results encourage the need of more accurate study of the mechanics of aorta rupture. However, we believe that the geometries of the plaque were simplified for this comparative study. More realistic models and non-homogeneous aortic wall properties and coefficients of friction may change the mechanical behaviour and the interaction between the stent and the stenosed aorta. The volume of the calcification can highly change the risk of aneurysm rupture (Fillinger, et al., 2003). Therefore, further investigation of calcification impact will be important considering more realistic mechanical behaviour of the classification material, i.e., porous-hyperelastic behaviour (Adolph, et al., 1997) and viscoelastic behaviour (Hinnen, et al., 2007) (van Dam, et al., 2008) beside anisotropic behaviour of the aorta and the inhomogeneous distribution of calcification in the aorta.

Chapter IV
Stent design evolution on the contact stability

Stent graft replacement in thoracic aortic aneurysm remains challenging due to the persistent complications rate and unstable contact at the proximal neck. Optimizing geometrical aspects of the stent design can improve the mechanical deployment performance, i.e., contact strength and flexibility. The study described in this chapter is an attempt to improve or optimize the stent geometry using computational FEA platform in order to strengthen simultaneously the radial contact and flexibility keeping in mind the non-migration failure.

Summery

IV.1. Introduction

Many stent designs have been numerically investigated to improve the stent characteristics in its crimped state and its expanded state (flexibility, conformity, uniformity, high radial strength, etc.). The open stent strut in our work was designed in order to produce a good accommodation in the aorta. However, the obtained results did not show a uniform circumferential strut distribution in the tortuous aorta (Conti, et al., 2011) (Mortier, 2010).

The previous results showed that in realistic aorta morphology, it was not possible to obtain fully adequate wall coverage, even in a good positioning of the stent struts against the aorta. Oversizing or lengthen the stent could prevent the migration failure, but could not ensure the non-occurrence of endoleak type Ia. This can be attributed to the high values of contact stability obtained in the most of deployed stents. Thus, our following interest will not be only to prevent migration, but also to strengthen the contact and decrease the contact stability values as much as possible. Our target is to find an ideal stent design for this aorta morphology.

A major goal in this chapter is to investigate numerically the effect of nitinol stent design on the overall effectiveness of the hoop radial forces (stiffness) and flexibility of the stent in both attachment sites. Furthermore, the migration behavior and stent collapse of the new designs need to be evaluated.

IV.2. Radial stiffness

Compromising stent designs is not a trivial task. The stents should be as flexible as possible in a highly tortuous aorta leading to a better conformity after deployment. However, sufficient radial strength is a crucial factor to get an effective contact and resist the compressive radial forces applied by the vessel. These two critical, stent-design requirements are often conflicting and cannot work simultaneously. In such an angulated morphology, our attempt is to search for a new flexible design, which can propose a good radial stiffness to resist aorta recoil and a good contact stability to resist to the migration.

If a stent was subjected to a radial pressure (P), it will undergo an axial elongation (δ) (Figure IV.2-1).
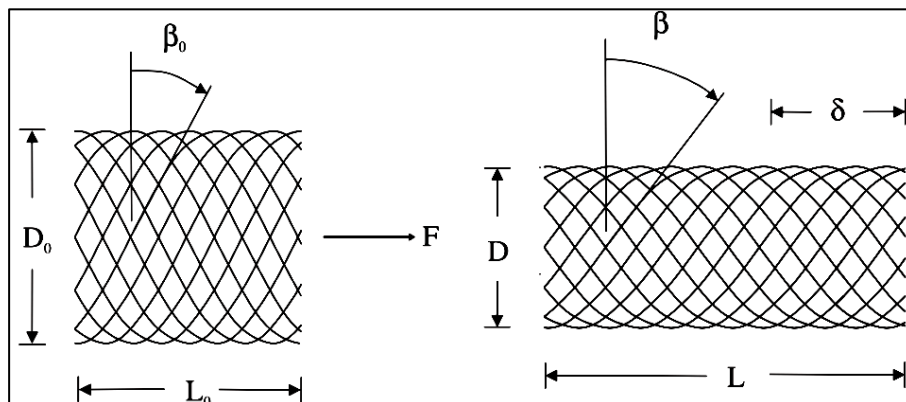
Figure IV.2-1: Stent deformation after applying an axial force

According to Wahl's theory of springs with ends fixed against rotation (Beule, 2009), it was shown that the load (F) acting on the stent can be given by:

$$F = 2n\left[\frac{GI_P}{K_3}\left(\frac{2\sin ß}{K_3} - K_1\right) - \frac{EI\tan ß}{K_3}\left(\frac{2\cos ß}{K_3} - K_2\right)\right] \quad (IV.1)$$

Where:

- $K_1 = \dfrac{\sin(2B_0)}{D_0}, K_2 = \dfrac{2\cos^2(B_0)}{\sin(B_0)}, K_3 = \dfrac{D_0}{\cos(B_0)}, I_P = \dfrac{\pi(d^4)}{32}, I = \dfrac{\pi(d^4)}{64}$; are constants
- *(F)*: the axial load subjected on the stent, see (Beule, 2009)
- (ß): new pitch angle
- (ß$_0$): initial pitch angle
- (D): stent diameter (mm)
- (δ): axial stent elongation
- (c): number of coils
- (n): total number of wires
- *(I)* and *(I$_p$)*: the moment of inertia and polar moment of inertia of a circular strut respectively
- (E): is Young's modulus of elasticity, and G is the shear modulus
- (L): the new stent length, where:

$$L = L_0 + \frac{\pi c D_0}{\cos\beta_0}(\sin\beta - \sin\beta_0) \quad (IV.2)$$

When the stent is compressed by a virtual catheter applying a radial pressure *(Pc)*, it will undergo an axial elongation and a change in strut angle and diameter.

According to (Jedwab & Clerc, 1993), the radial pressure *(P)* acting on the stent is given by:

$$Pc = \frac{-2Fc}{D\,L\,\tan ß} \quad (IV.3)$$

The radial (hoop) stent stiffness (N/mm3) measures the elastic response of the stent to an applied force, i.e., how much the stent can resist to the diameter deformation or loss (mm) as a result of vessel recoil. The radial stiffness is defined by:

$$K_p = \frac{\partial Pc}{\partial D} = \frac{2c}{K_3\sin ß\,(D\,L\,\tan ß)^2}\left[\begin{array}{l}2D\,L\,n\,\tan ß\,\left(\dfrac{GI_P}{K_3}\left(\dfrac{2\cos ß}{K_3}\right) - \dfrac{EI}{K_3}\left(\dfrac{2\cos ß}{K_3} - K_2\sec^2 ß\right)\right) \\ -F\left(\dfrac{DL}{\cos^2 ß} + K_3\sin ß\,(\pi cD - L\tan ß)\right)\end{array}\right] \quad (IV.4)$$

To compare the numerical radial stiffness and contact pressure stresses *(N/mm^2)* during the compression phase of the simulation, the previous analytical equations were implemented in Matlab software to calculate these values. Then, these values were compared to the numerical FE values. High values of contact pressure stresses mean higher stiffness and consequently lower flexibility.

The analytical results showed that the radial stiffness or contact pressure stresses induced in the stent increased with the decrease of stent length, which is physically expected.

This fact was also approved by our numerical results. The maximal average of contact pressure stresses or radial stiffness were observed in the shortest stent design (stent1) (Figure IV.2-2). The longest (stent2) have smaller values of stiffness and the stent3 resulted in the smallest values (Figure IV.2-3) (Figure IV.2-4) respectively.

126

The shorter fixation length resulted in a higher concentration of stresses and the larger contact stability (high risk of migration). Increasing the stent length can increase the flexibility; however, it reflects a small effectiveness to resist aorta recoil or other mechanical loads.
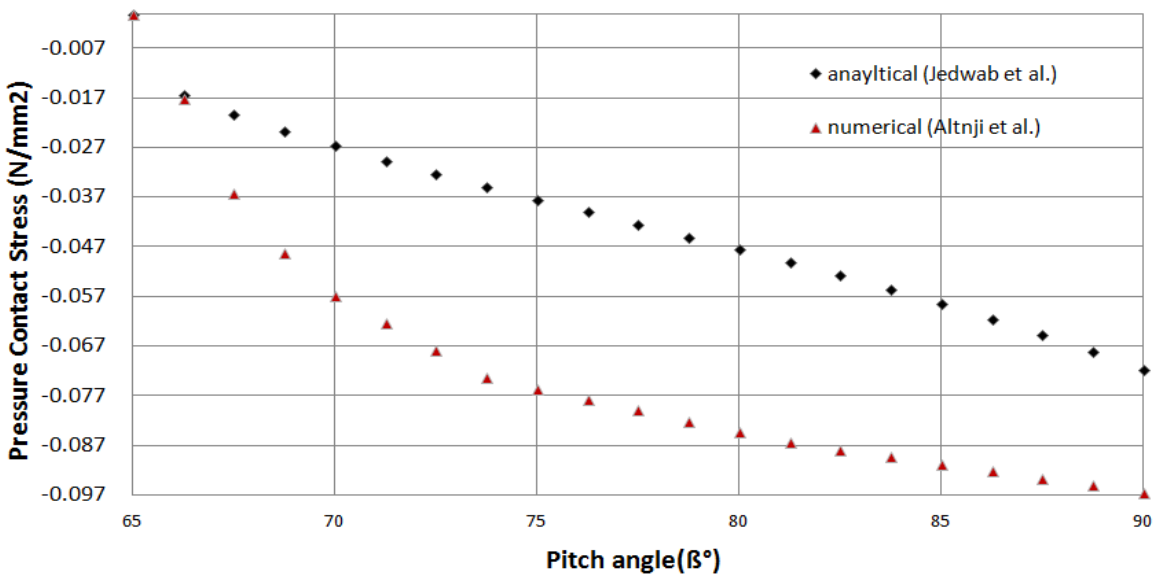
Figure IV.2-2: Radial pressure contact as a function of pitch angle (diameter loss) for numerical and analytical results (stent1, O%=15%)

(Figure IV.2-2) shows the radial contact pressure stresses applied on the shortest stent (stent1) as a function of the pitch angle (diameter decreasing). The numerical results are overestimated by those of the analytical results. We agree that this difference is due to the high concentration of stresses induced specifically in the stent1 during the compressing and bending phases. Additionally, other errors can be induced by the numerical model approximations.
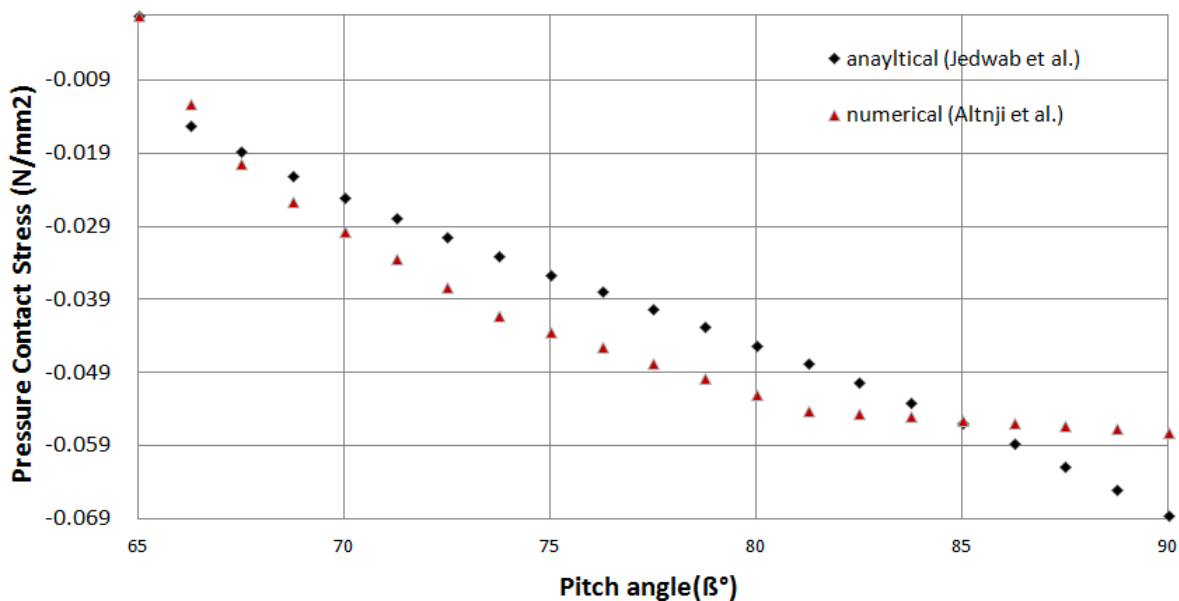
Figure IV.2-3: Radial pressure contact as a function of pitch angle (diameter loss) for numerical and analytical results (stent2, O%=15%)

127

However, for the (stent2 & stent3), the numerical results had a good agreement with the analytical representation (Figure IV.2-3) (Figure IV.2-4). We also agree that the small difference in results at the final phase of compressing is due to the high bending surface induced in the numerical simulation, which is not the case for the analytical model, where every point of the strut is in contact with the compressing surface.

The optimized length design (stent2) improved the contact stability locally 'at the proximal attachment site' and resulted in lower contact pressure stresses concentration which means better flexibility and conformity with the aorta neck angulation. Higher values of contact pressure stresses mean also high radial stiffness, but less flexibility, which is the case for (stent1). In our case, the stent2 could be a compromise between a good radial stiffness and good contact stability (stent flexibility) without migration: (38%) flexibility improvement compared to the shortest stent (stent1). Thus, the radial stiffness is an important design characteristic and an important care should be taken to maintain an optimized value.
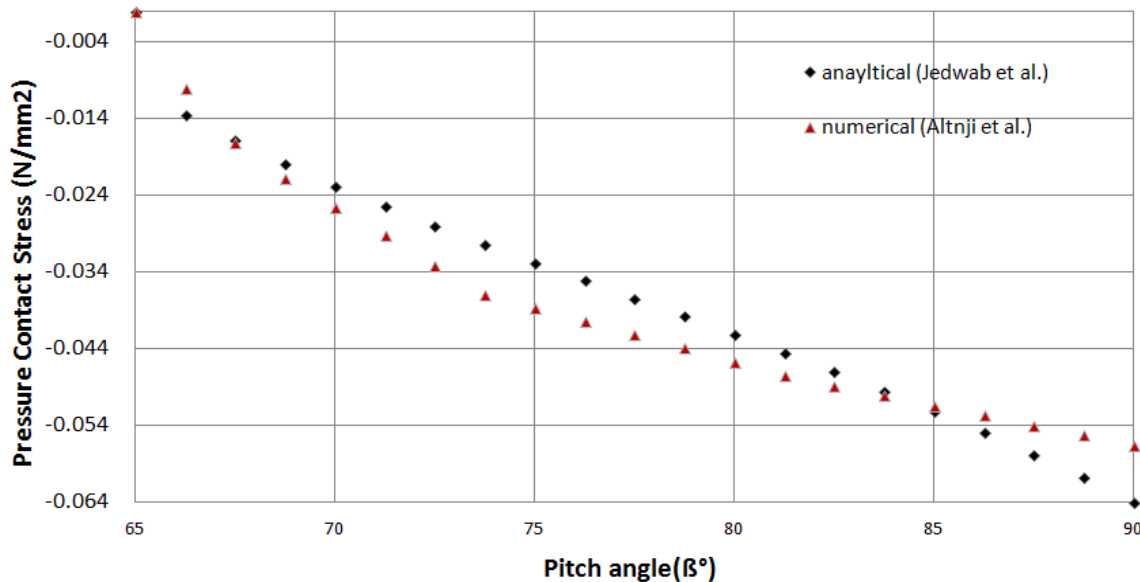
Figure IV.2-4: Radial pressure contact as a function of pitch angle (diameter loss) for numerical and analytical results (stent3, O%=15%)

Slight improvement of (1%) of flexibility was reported for the longest stent (stent3) when compared with the (stent2).

As the oversizing value was uniform along every stent, the radial stent stiffness was uniform along everyone. Oversizing the stent1 by (20%) resulted in smaller contact pressure and therefore a smaller stiffness. Considering the equation (IV.3), decreasing the diameter of the stent is associated with increasing the *'overall radial pressure contact'*, i.e., higher pressure forces are required for a smaller diameter value. However, critical length with higher oversizing could lead to adverse outcomes. If the stent is not well oversized, adverse outcomes like aorta recoil or stent collapse or migration can be resulted, and smaller values of pullout forces can withdraw the stent leading to deployment failure.

128

IV.3. Pullout forces

Pullout force is a measure of post-deployment fixation strength of stent graft to the aorta. It is the force needed to dislodge the stent graft from the aorta. This load was defined as the pullout force or static downward force or dislodgement force. Smaller values of pullout forces mean more risk of stent migration. Good frictional interactions using hook and barbs at attachment sites and stent-graft oversizing are the most important factors to resist migration. However, in a highly angulated proximal neck of the aorta, hooks do not improve the proximal fixation. Moreover, the radial forces of such stents are less important (Malina, et al., 1998). In such case, high radial forces and optimized oversizing values have considered the effective factors for migration resistance (Canaud, et al., 2008) (Vad, et al., 2010). Aortic necks with larger diameters, high angulation, insufficient fixation lengths at the proximal attachment site have also an important impact (Bosman, et al., 2010) (Li & Kleinstreuer, 2006) (Sternbergh, et al., 2004) (Thomas & Sanchez, 2009).

Based on the Coulomb friction law, the pullout force is given by:

$$F = \mu\,(P \times A) \quad \text{(IV.3)}$$

Where F (N): the pullout force, P (N/mm^2): the contact pressure stress, A (mm^2): the contact surface area, and (μ): the coefficient of friction. Principally, the equation (IV.3) has the same concept and is inversely proportional to the previously given stress equation ($\tau_{crit} = \mu p$), where (τ_{crit}), (p) are the shear and contact pressure stresses respectively.

As seen by the previous results, the severe angulation reduced the contact strength and wall opposition, i.e., smaller values of pullout forces applied on the stent may lead to an important migration. Different stent designs can propose different pullout forces ranged from (4.5N to 25N) (Kratzberg, et al., 2009). Our previous results showed that when oversizing the stent1 from (10%) to (20%), the migration was also reported. This result supports the fact that oversizing was not a significant factor in non-migration if there is not enough length of the proximal attachment site. The previous results inspire a new design as an attempt to have good contact stiffness at attachment sites and optimized oversizing values. We aim to increase the pullout forces needed to dislodge the stent after deployment.

IV.4. Stent design consideration

Based on our results, the stent1, which has (144 mm) of length with uniform (15-20%) of oversizing value along the stent, had undergone the migration failure. In this work; we propose new thoracic stent designs to improve the most important stent characteristics (stiffness and flexibility) and prevent migration, even in the most challenging conditions (tortuosity & smoothest contact behavior).

We also aim to improve the contact stability for the non-migrated stents like the case of stent2 (160mm). The proposed stents should meet a specific behavior for this morphology of the aorta and optimize the mechanical performance of stents. Moreover, the new design can help to investigate the effect of oversizing on the pullout forces or stent collapse.

We proposed variable oversizing values at one or both attachment sties of the stent. To obtain the new geometrical variables, another radial expansion was performed (Figure IV.4-1). One time for only one circle end of stent ring accomplishing (20%) and (25%) of oversizing values and another time for the two ends accomplishing the same values of oversizing. For all the new stent designs, the central part of the stent was oversized by (15%) and the end parts with (20%) and (25%) (Figure IV.4-2)

To evaluate the effect of stent-length, all these variables oversizing values were applied for both lengths of the stent; stent1 (144 mm), stent2 (160 mm) and eight simulations have been performed.
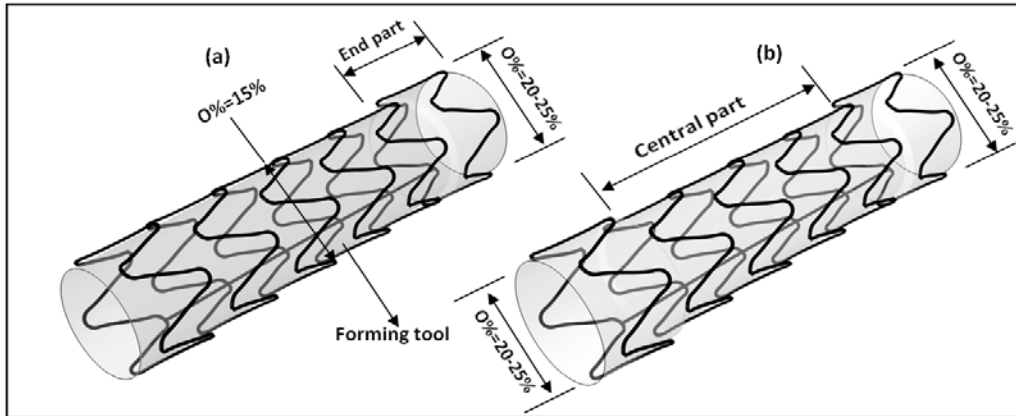
Figure IV.4-1: New design modeling for proximal (a) / (proximal–distal) (b) stent end
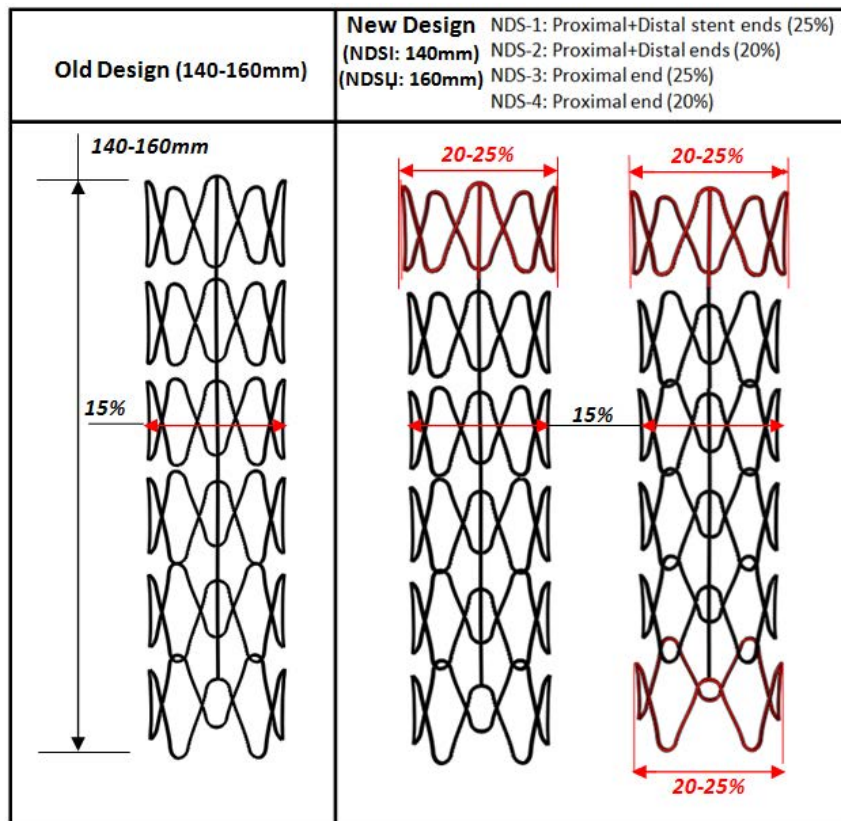
Figure IV.4-2: Optimized stent designs for both stent1 and stent2

130

IV.5. Results

IV.5.1 Migration and stiffness

The results showed that all the new designed stent1 (NDSI) with (20%-25%): (NDSI: 1-2-3-4) oversized at both proximal and distal ends did not undergo the migration failure even in the smoothest contact condition and severe angulation where the pullout forces can be high. However, (7.4 mm <10 mm) of migration distance was reported for (20%-25%) oversizing value at only proximal end (NDSI-3&NDSI-4) (Figure IV.5-1). A very slight improvement of migration (7.2 mm) was resulted when oversizing (20%-25%) at both proximal and distal ends of the stent (NDSI-1&NDSI-2) (Figure IV.5-2). The new design was able to improve the migration behavior by (59%) compared to the old stent design with (15%) uniform oversizing and (45.8%) compared to the (20%) uniform oversized one.
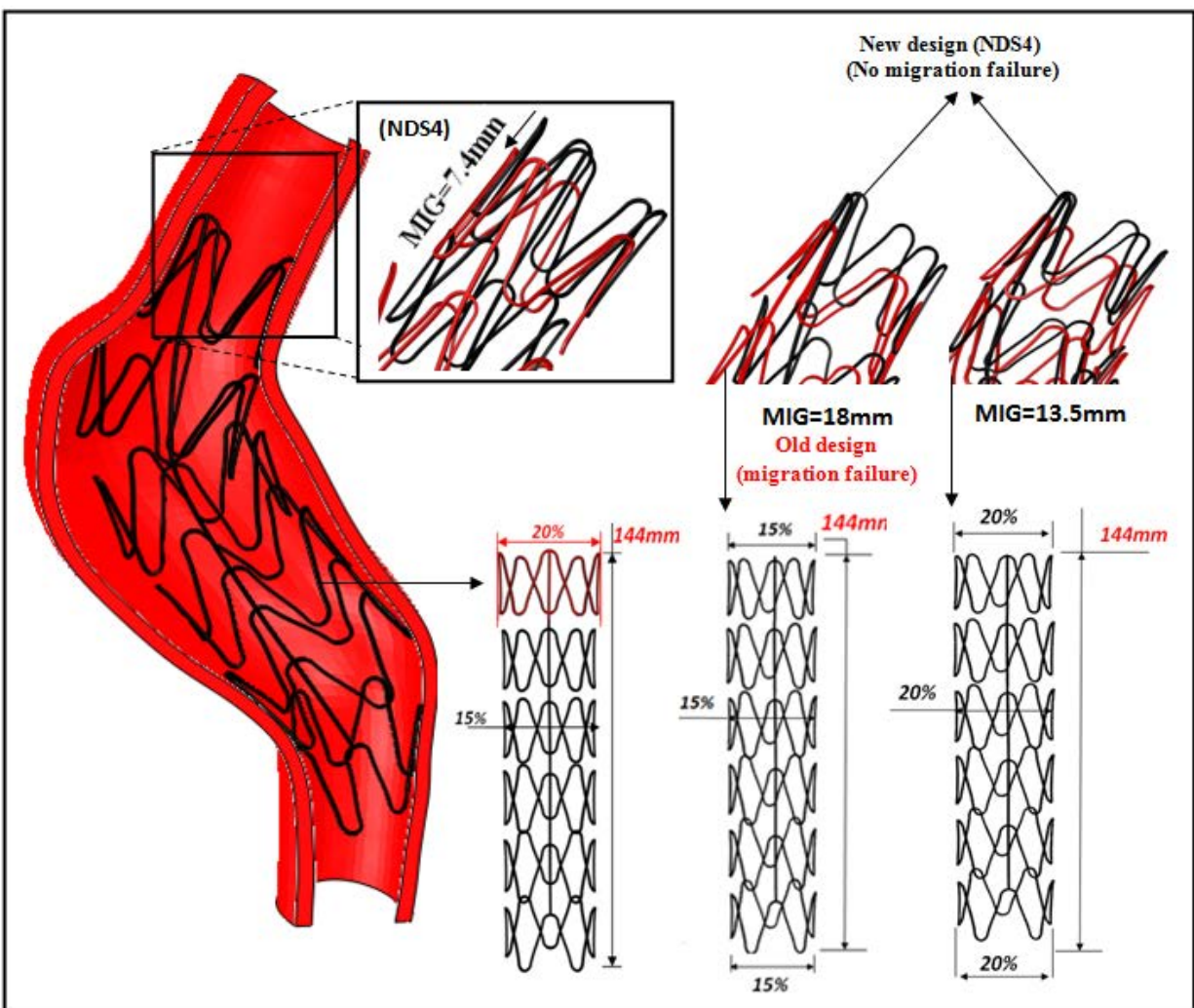
Figure IV.5-1: Migration success for the proposed new design for the stent1 (NDSI)-($\mu=0.05$)

131
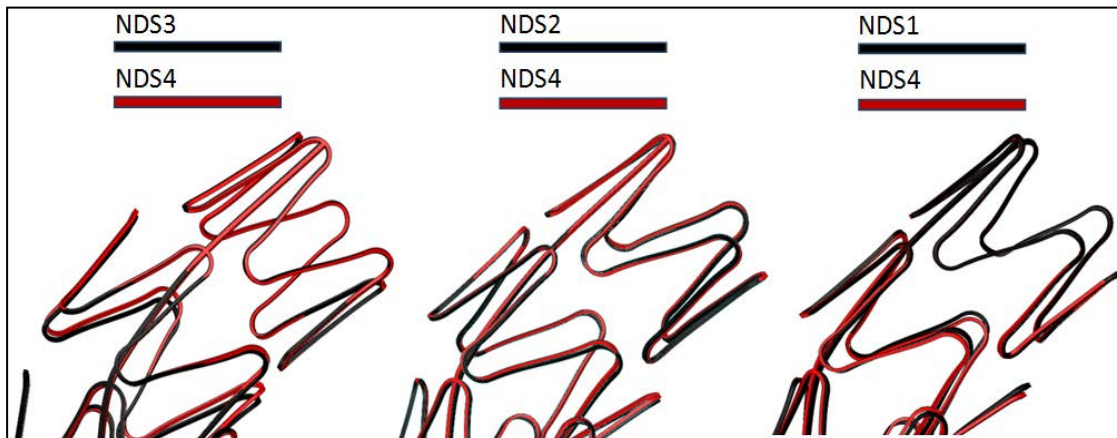
Figure IV.5-2 : Comparison of migration distance between the deployed proposed new design for the stent1 (NDSI)-(*μ=0.05)*

The new stent designs significantly reduced the stress peak, comparing to the migrated stent1, this is due to the absence of high slip, which is not the case for the old migrated design (Figure IV.5-3).
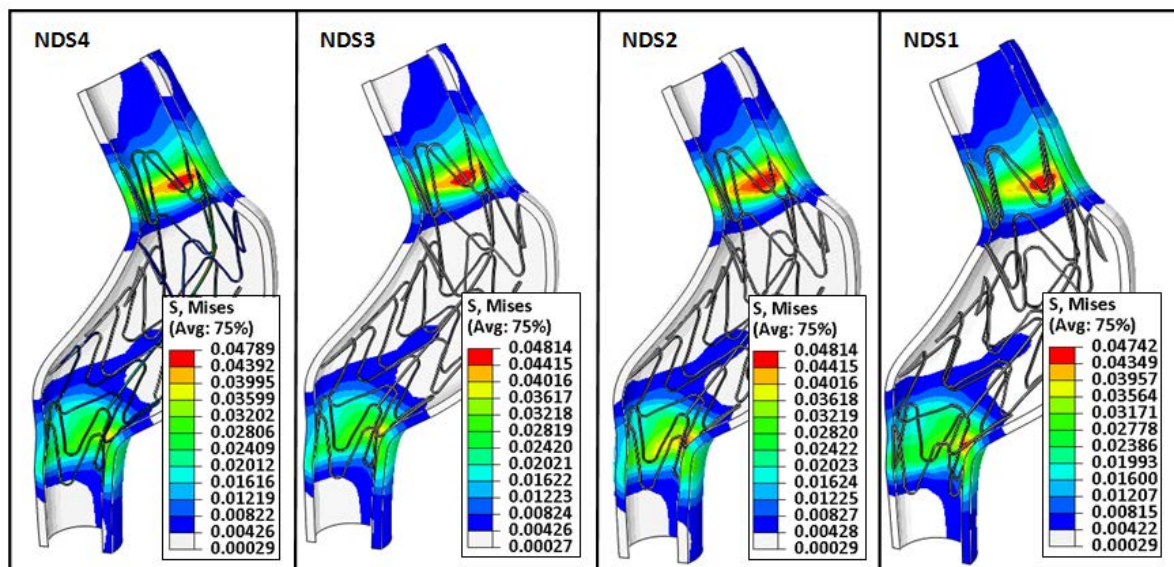
Figure IV.5-3: Von Mises stresses (MPa) in the aorta after new design stent1 (NDSI) deployment

Oversizing only one end by (25%) (NDSI-3) resulted in slightly higher stresses without a considerable improvement of migration behavior.

However, oversizing both sides (NDS1-NDS2) resulted in slightly smaller circumferential stresses comparing with (NDSI-3 & NDSI-4). (NDSI-1) resulted in smaller values of Von Misses and circumferential stresses (Figure IV.5-4). When oversizing also the distal end part of the stent as the case of (NDSI-1), the pressure stresses in the proximal aorta were mitigated by the oversized distal end, which underwent some additional stresses.

132

This observation can be very interesting; especially in a diseased state of the aorta, e.g., plaques, calcifications, etc.). Deployment of such design can moderate the pressure stresses on the plaque and induce therefore smaller stresses in the lesion area (Zhao, et al., 2011) (García, et al., 2012). The two designs (NDSI-1, NDSI-2) can contribute to the non-occurrence of stent re-stenosis. These results support the importance of stent design, especially when dealing with a rigid, calcified lesion. High stiffness design causes highest stresses, and can be more critical when dealing with high plaque stiffness, i.e., a rigid and a calcified lesion (Timmins, et al., 2008).
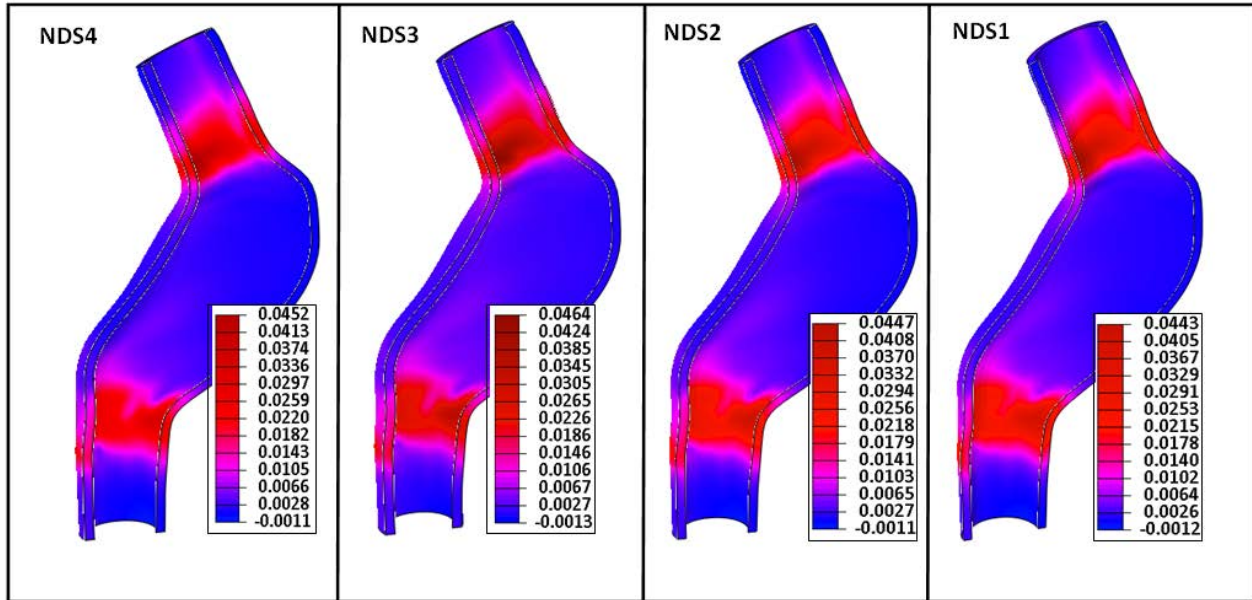
Figure IV.5-4: Circumferential stresses (MPa) in the aorta after new design stent1 (NDSI) deployment

Based on the equations (IV.3) & (IV.4), increasing stent diameter results in smaller contact pressure and stiffness. This fact was demonstrated by our numerical results. Therefore, the old design stent1 with (20%) oversizing may have a smaller stiffness and therefore better flexibility: (35%) stiffness decrease compared with the (15%) oversized stent1. However, the (20%) oversized stent1 undergone the migration failure because of the highest pullout forces caused by both oversizing and insufficient proximal attachment lengths.

Comparing with the old design stent1, the new design stents (NDSI) demonstrated smaller stiffness, i.e. better flexibility and deployment without migration failure. A very slight decrease in stiffness was reported between the new design stents (NDSI-1, NDSI-2-, NDSI-3, NDSI-4) as shown in the (Figure IV.5-5).

The proposed new design (NDSI) resulted in a better flexibility compared to the old design, allowing easy placement without migration failure. The pullout forces reported in the new designs were not enough to dislodge the stent until migration, even in such angulation and critical proximal attachment distance. Higher values of pullout forces are then needed to cause migration failure.
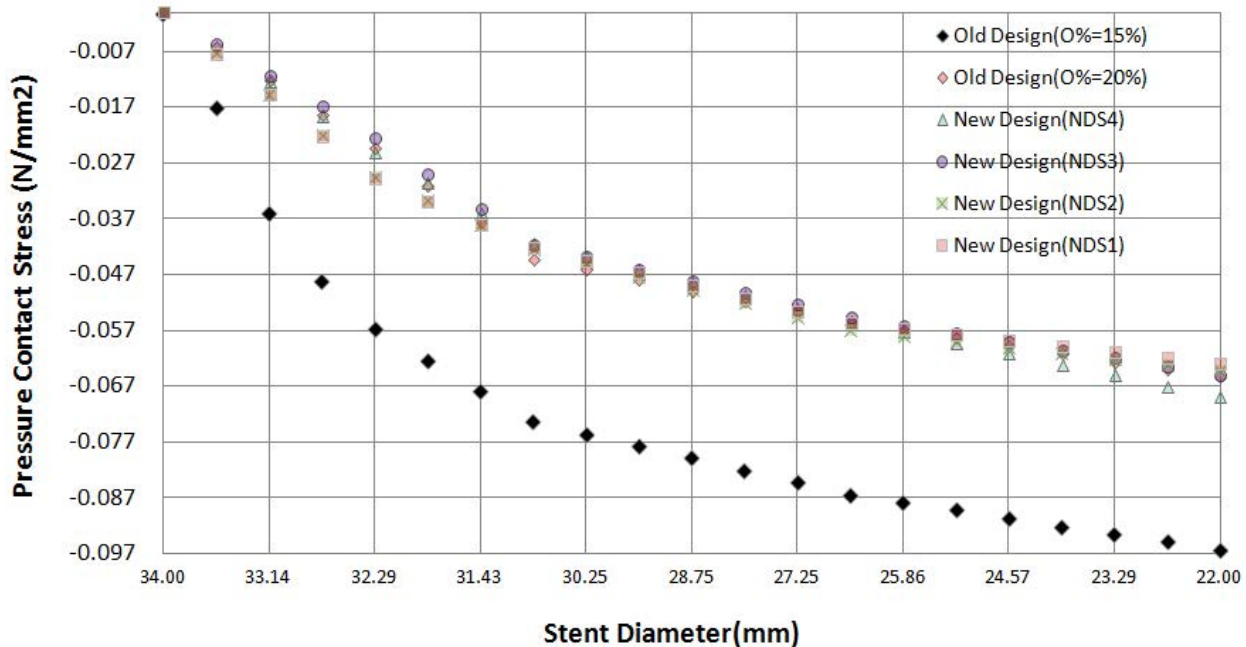
Figure IV.5-5: Radial pressure contact as a function of stent diameter for numerical results, new design stent1(NDSI) (144mm)

Concerning the vascular reaction to the new designed stent2 (NDSЦ) deployment, the equivalent Von-Mises stresses induced in the vessel wall were slightly lower than those induced in the vessel treated by the new deigned stent1 (NDSI). As seen before, the shorter stent resulted in higher stiffness and stresses, i.e., a higher capability to prevent arterial elastic recoil. However, for the new designed-longer stent2 (NDSЦ), almost similar values of stiffness and stresses were obtained comparing with the old design stent (with 15% uniform oversizing), coinciding the conformity and better flexibility between the stent and a vascular anatomy. The (NDSЦ-1) resulted in higher Von-Mises and circumferential stresses in the aortic wall caused by the (25%) oversized proximal/distal-end of the stent (Figure IV.5-6) (Figure IV.5-7). Slightly lower stresses were observed in the aorta when (NDSЦ-2) deployment. This is due to the (20%) oversized proximal/distal end. The lowest stresses were reported when using (NDSЦ-4): the (20%) oversized proximal end.
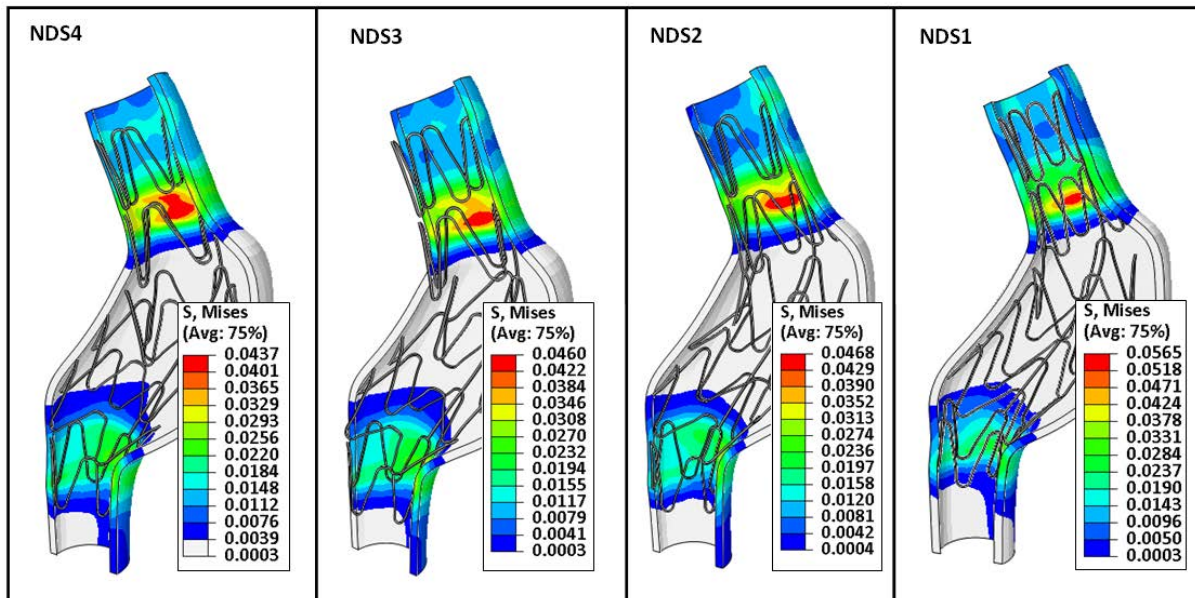
Figure IV.5-6: Von Mises stresses (MPa) in the aorta after new design stent2 (NDSЦ) deployment

All the (NDSЦ) stents demonstrated larger regions of interaction with the aorta maintaining an adequate radial displacement and causing smaller local contact stresses. A very good deployment was observed without any slip or eccentric deformation of the stent perimeter. This design showed better flexibility and contact stiffness. Furthermore, this design highly mitigated the energy of eccentric deformation caused by the severe angulation and oversizing. Therefore, (NDSЦ) have a good compromise between flexibility and stiffness (Figure IV.5-8) when reaching its nominal diameter. Implanting stents in curved aorta causes stress concentrations at both proximal and distal necks of the aorta. Therefore, the most flexible stent is the best choice in a high angulated aorta.
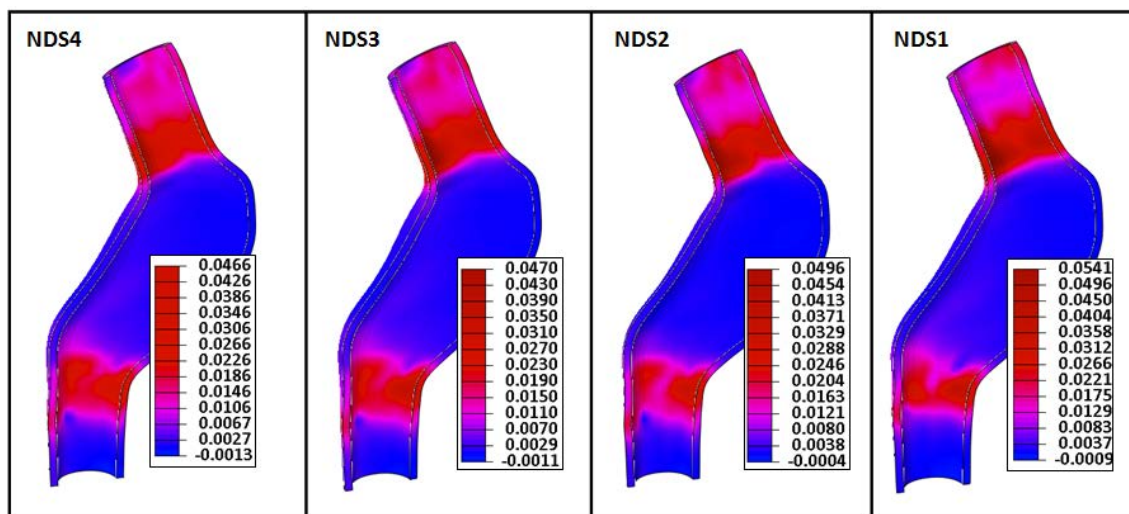
Figure IV.5-7: Circumferential stresses (MPa) in the aorta after new design stent2 (NDSЦ) deployment

135
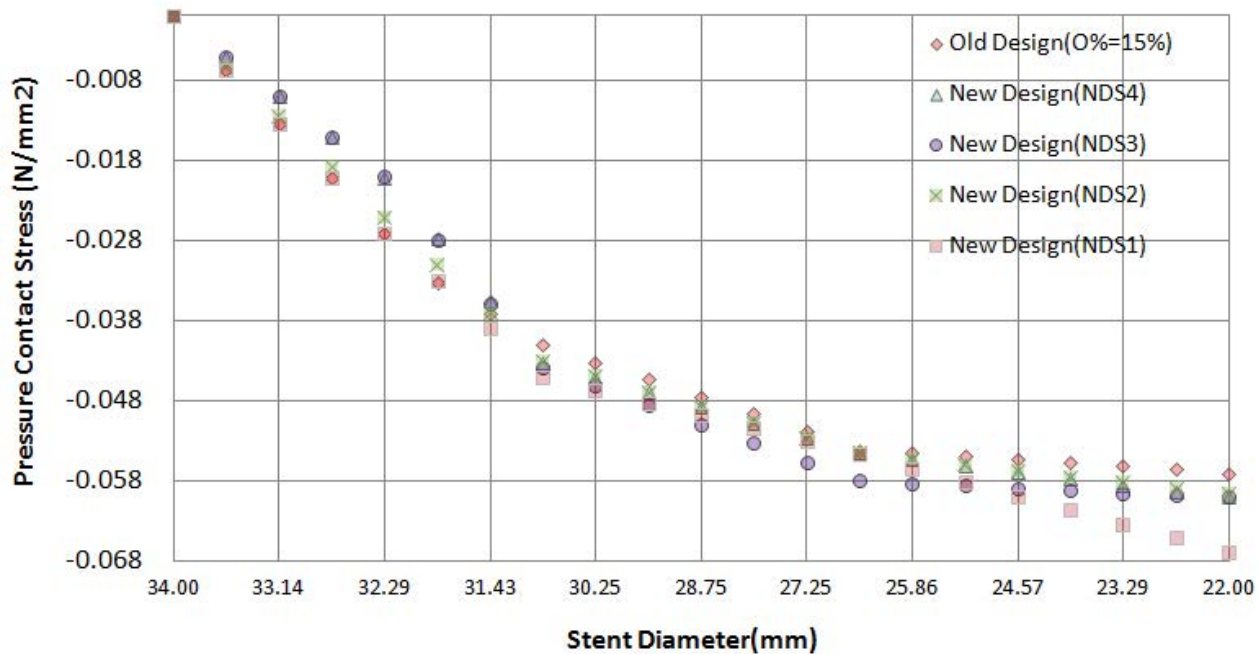
Figure IV.5-8: Radial pressure contact as a function of stent diameter for numerical results (new design stent2 (NDSЏ) (160mm))

All the new designed stents (NDSI) are more sensitive to change or decrease in stiffness value. The old designed stent1 stiffness with (O%=15%) was decreased by about (35%) compared with (NDSI-1). However, nearly the same values of stiffness were obtained for the old and new designed stent 2 (NDSЏ).

Although that both new designs significantly increased the values of the pullout forces needed to withdraw the stent and cause migration, caution should be paid to the improvement of contact stiffness acquired by both new designs (NDSI), (NDSЏ). Therefore, the contact stiffness and stability should be investigated.

IV.5.2 Contact stiffness

Ideally, all the stent ends in the proposed new designs should be in contact with the aorta at both attachment sites and especially at the proximal one. The struts not in contact with aortic wall should be avoided to prevent thrombus formation (Ormiston, et al., 1999) and floating struts. As seen earlier, the proposed design was able to improve both conflicting properties (stiffness and flexibility).

Even the new design stent1 (NDSI) did not undergo the migration failure; it seems not to be the best choice for such a curved aorta with the smoothest contact condition. However, higher oversizing only in the end parts could be one of the solutions to ensure good contact stiffness and reduce the risk of concentric deformation. In a real morphology, the results with old designed stents demonstrated that not every point in the aorta is in contact with stent struts. Our attempt in the new design also aims to increase the interaction surface and the contact stiffness.

136

Several simulations analyses were applied to understand the effects of the new design on contact behavior (metal-to- surface ratio).

The finite element results for the old and new designs stent1 deployed revealed that the pressure contact area between the stent1 and the aortic model was larger only in the new designed stent1 (NDSI). In terms of contact area ratio, the numerical results showed a progressive increase in contact when increasing the oversizing value at the stent ends in (NDSI) (Figure IV.5-9).

Comparing with the migrated stent1 with (15%) uniform oversizing, all the deployed new designed stent1 (NDSI) resulted in a significant increase in pressure contact area. The contact surface increase area was about (56%) in the (NDSI-4&3): (717 vs. 460 and 727 vs. 460) mm2 respectively. It also increased progressively by (60%) when oversizing at both ends (NDSI-2&1) :(734 vs. 460 and 742 vs. 460) mm^2 respectively (Table IV.5-1).
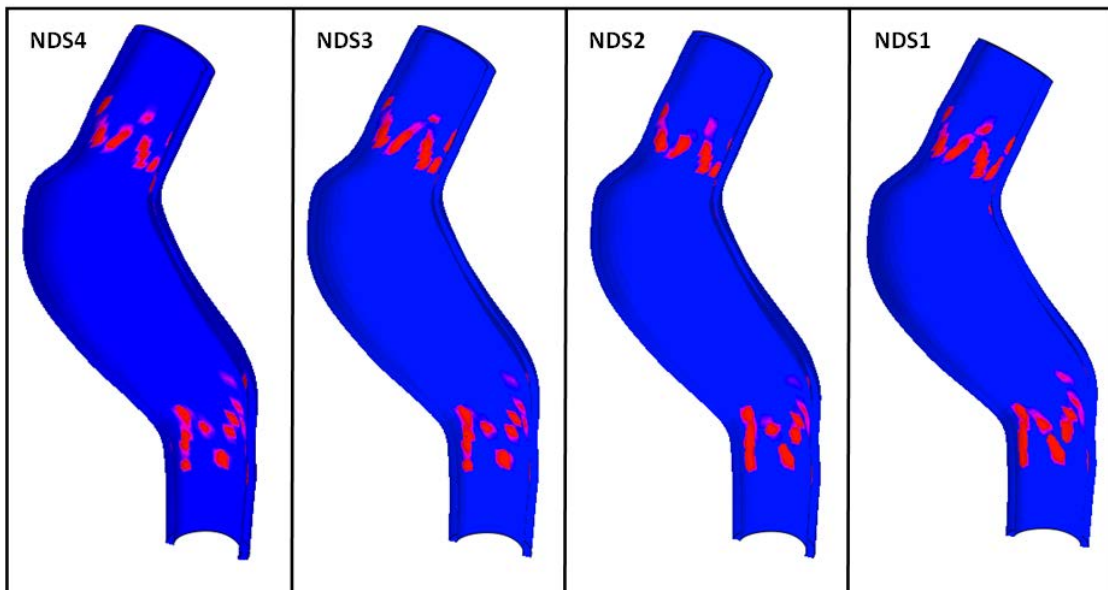
Figure IV.5-9: Pressure stress distribution after implantation of the new design stent1(NDSI) (144mm)

Giving the fact that the (NDSI) was deployed in the smoothest contact condition with a high tortuous aorta, the risk of migration and unstable contact remains potential. For (NDSI), the average contact stability in the proximal site is still high for both (NDSI-4&3) with ($\bar{F}_{cs} = 0.97\&0.98$) respectively, which means a high risk of migration under pressure of blood or other exterior loads. However, slight improvement in the proximal migration behavior was observed for both (NDSI-2&1). ($\bar{F}_{cs} = 0.95\&0.97$). Oversizing both the proximal and the distal stent ends was an important impact factor for proximal radial stiffness. For the two designs (NDSI-2&1), the pullout forces were mitigated due to both proximal and distal radial forces. The proximal radial forces applied by (NDSI-2&1) designs were greater than those (NDSI-3&4). Although the contact stability improvement was not significant, the slight improvement of contact stability in (NDSI-2&1) was able to prevent migration failure (Figure IV.5-10).

137
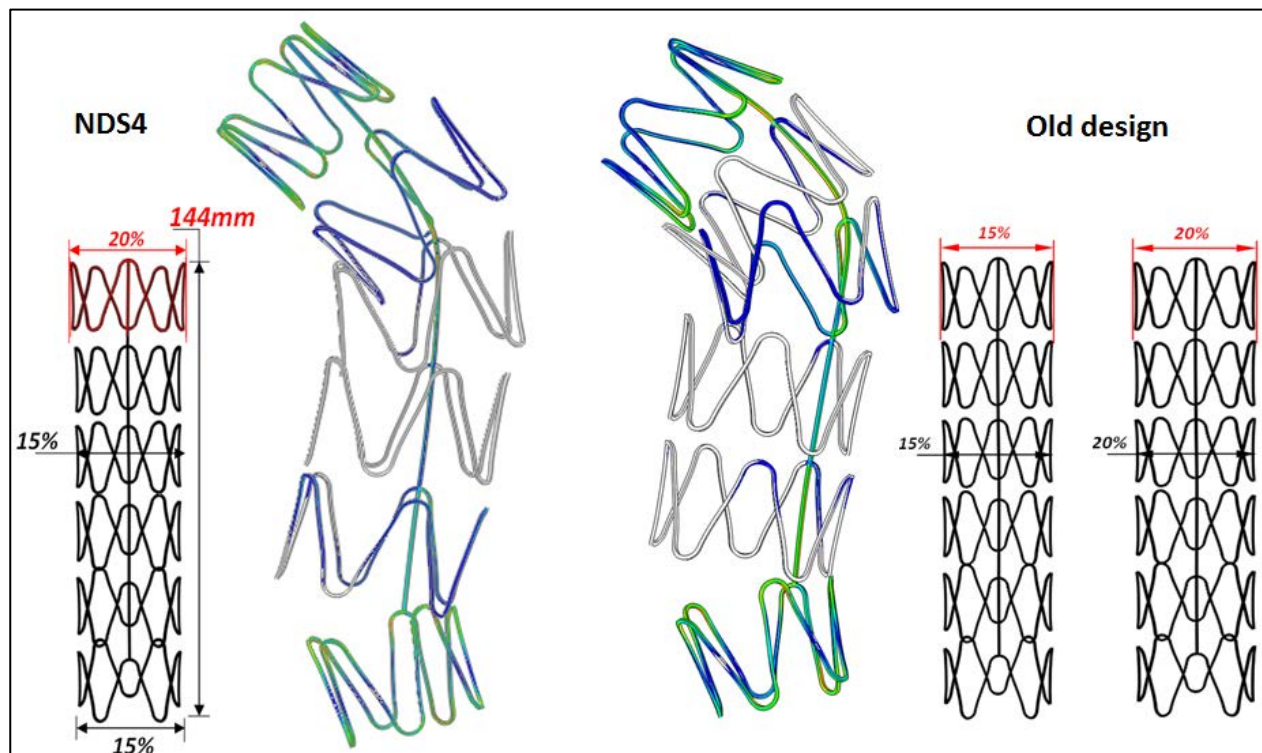
Figure IV.5-10: Comparison of struts superelastic recovery after deployment between the old (right) and new designed stent1 (NDSI) (left)

In (NDSЦ), sufficient length of the proximal site (*PASL*=21 mm) resulted in a better contact surface area, and consequently, a better radial strength comparing with NDSI. However, (NDSЦ-4) did not demonstrate any improvement of proximal contact stability ($\bar{F}_{cs}$) comparing with the old designed stent2 with (15%) uniform oversizing: (0.92 $_{NDSЦ-4}$ vs. 0.89 $_{old\ design}$). Similar values of ($\bar{F}_{cs}$) were reported distally (0.98$_{NDSЦ-4}$ vs. 0.98$_{old\ design}$). Almost the same results of ($\bar{F}_{cs}$) were observed with (NDSЦ-3): (0.91$_{NDSЦ-4}$ vs. 0.89$_{old\ design}$) proximally and (0.97$_{NDSЦ-4}$ vs. 0.98$_{old\ design}$) distally (Table IV.5-2).

NDSЦ was modeled by oversizing one circle at the proximal end of the stent. Comparing with the old designed stent2 with (O%=15%) oversizing. The decline in contact stiffness in the proximal part was due to the smaller proximal surface interaction between the new designed stent2 (NDSЦ) and the aorta: (NDSЦ-3-NDSЦ-4/aorta) comparing with the old design: (1050-1030 vs. 1070) mm^2 respectively. Slight higher values of contact pressure surfaces were obtained for (NDSЦ-1-NDSЦ-2/aorta) comparing with the old design: (1110 1090 vs. 1070) mm^2. This increase is attributed to the contact surface improvement in the distal part when (NDSЦ-1-NDSЦ-2) deployment. The proximal contact of the old design stent2 with (O%=15%) always resulted in better contact stiffness than the (NDSЦ).

The (20%) and (25%) oversized proximal end circle will result in a good contact with the aorta, however, the later circle of the struts with (15%) oversizing resulted in a smaller contact surface and lower contact stiffness comparing with the uniform, old design stent with (15%) uniform oversizing) (Figure IV.5-11).

Therefore, when also oversizing the distal stent ends (NDSЦ-2&1), a slight regression in contact stiffness was resulted for (NDSЦ-2): (0.92 vs. 0.89) proximally and significant improvement in the distal part: (0.88 vs. 0.98). The same observation was obtained for the (NDSЦ-1) with high regression in the proximal contact stiffness (0.94 vs. 0.89).

Therefore, only distal contact stability improvement was reported for the (NDSЦ-2&1), as only one (20%) or (25%) oversized circle of the struts at the distal stent end was in a good contact with the aortic wall (Figure IV.5-12). (NDSЦ-2&1) resulted in an increase of the overall contact pressure surface because of the (20&25%) oversized distal stent end, which strengthens the overall contact distally (Table IV.5-1).
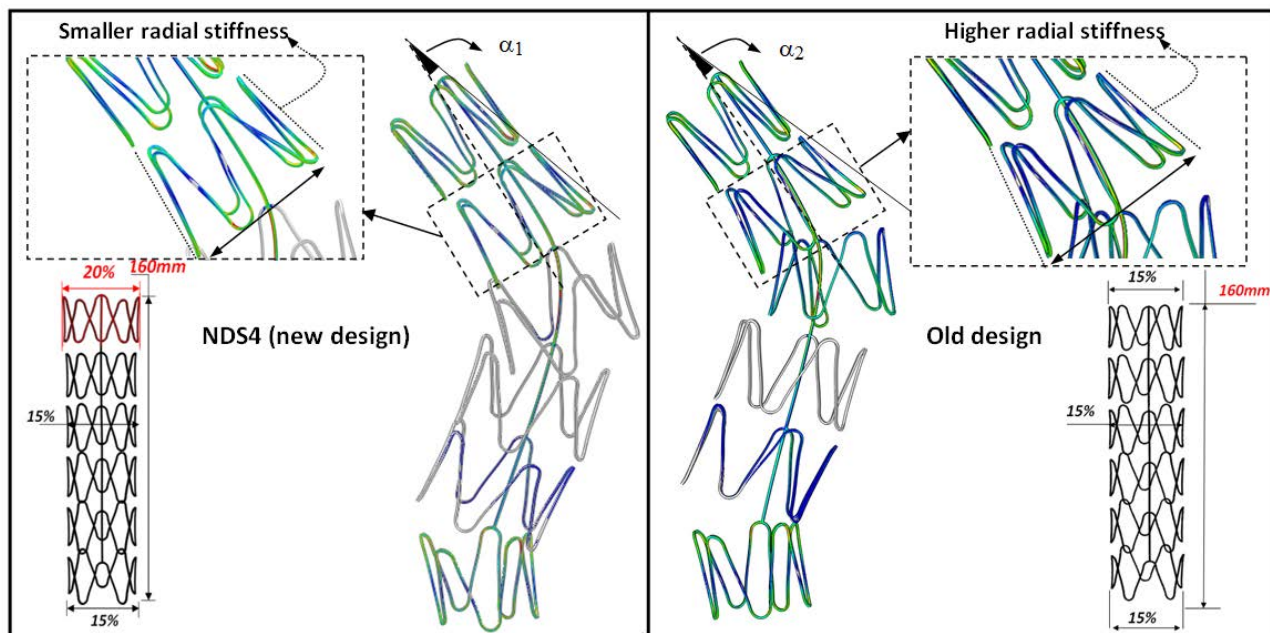
Figure IV.5-11: Comparison of struts' superelastic recovery between the old (right) and new designed stent2 (NDSЦ) (left)- best contact stiffness were produced proximally for the old design.
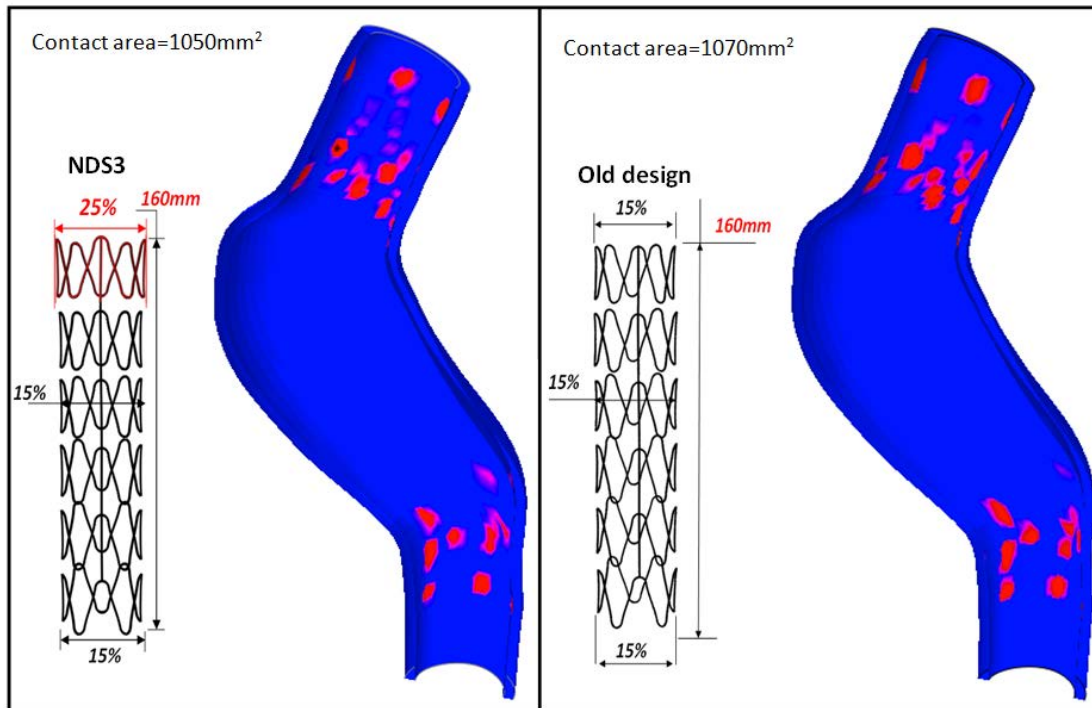
Figure IV.5-12: Pressure stress distribution after implantation of the new design stent2 (NDSЦ)

Table IV.5-1: The effect of new design stent 1 (NDSI) (144mm); (simulation results)					
Simulation *Stent models* (PASL) (DASL)		*Stent1 (144mm)* D_{IP} =18 D_{ID} =15 (NDS4)	*Stent1(144mm)* D_{IP} =18 D_{ID} =15 (NDS3)	*Stent1 (144mm)* D_{IP} =18 D_{ID} =15 (NDS2)	*Stent1 (144mm)* D_{IP} =18 D_{ID} =15 (NDS1)
Oversizing value (O %)	Stent Body	15%	15%	15%	15%
	Stent Proximal site	20%	25%	20%	25%
	Stent Distal site	15%	15%	20%	25%
Contact stability ($\overline{F}_{CS}$)	Proximal neck	0.97	0.98	0.95	0.97
	Distal neck	0.95	0.93	0.97	0.92
Tangential contact behavior		*μ=0.05*	*μ=0.05*	*μ=0.05*	*μ=0.05*
Pressure contact area (mm^2) after deployment		717	727	734	742
	Proximal neck	1.76E-02	0.0186	0.0193	0.0180
Average contact pressure stress (N/mm^2)	Distal neck	0.015	0.016	0.0174	0.0173

Simulation Stent models (PASL) (DASL)		Stent2(160mm) $D_{2P}=21$ $D_{2D}=18$ (NDS4)	Stent2(160mm) $D_{2P}=21$ $D_{2D}=18$ (NDS3)	Stent2(160mm) $D_{2P}=21$ $D_{2D}=18$ (NDS2)	Stent2(160mm) $D_{2P}=21$ $D_{2D}=18$ (NDS1)
Oversizing value (O %)	Stent Body	15%	15%	15%	15%
	Stent Proximal site	20%	25%	20%	25%
	Stent Distal site	15%	15%	20%	25%
Contact stability ($\overline{F}_{CS}$)	Proximal neck	0.92	0.91	0.92	0.94
	Distal neck	0.98	0.97	0.88	0.90
Tangential contact behavior		$(\mu = 0.05)$	$(\mu = 0.05)$	$(\mu = 0.05)$	$(\mu = 0.05)$
Pressure contact area (mm^2) after deployment		1030	1050	1090	1110
Average contact pressure stress (N/mm^2)	Proximal neck	0.0174	0.0173	0.017	0.018
	Distal neck	0.0172	0.016	0.018	0.0183

Table IV.5-1: The effect of new design stent 2 (NDSЦ) (160mm); (simulation results)

(Figure IV.5-13) & (Figure IV.5-14) show the improvement of migration behavior for the improved stent for two values of oversizing.
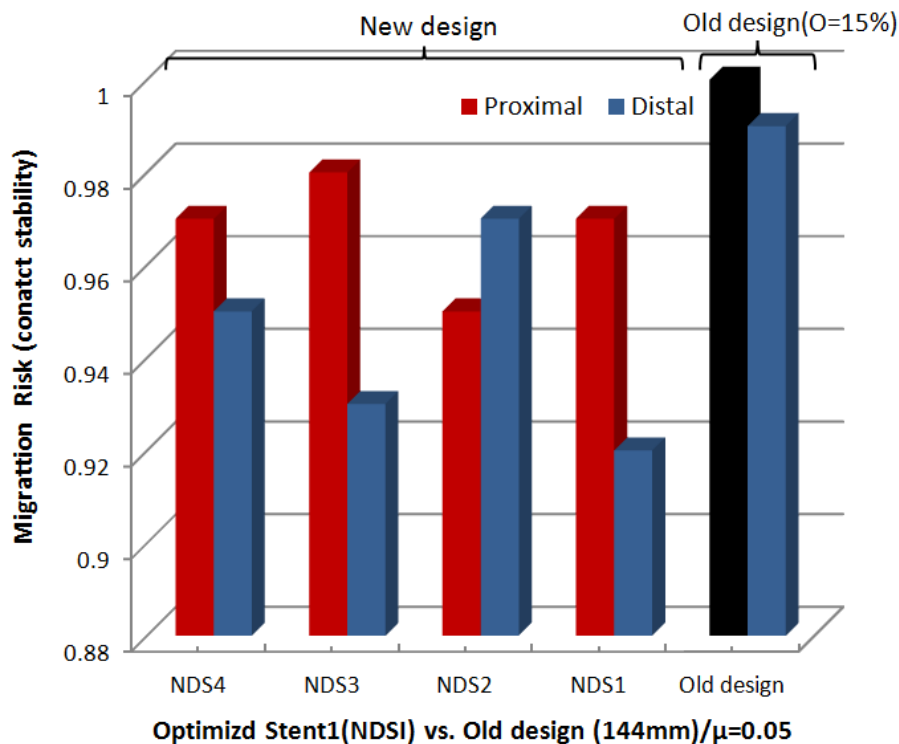
Figure IV.5-13: Migration behaviour improvement for the new stent 1(NDSI)

141
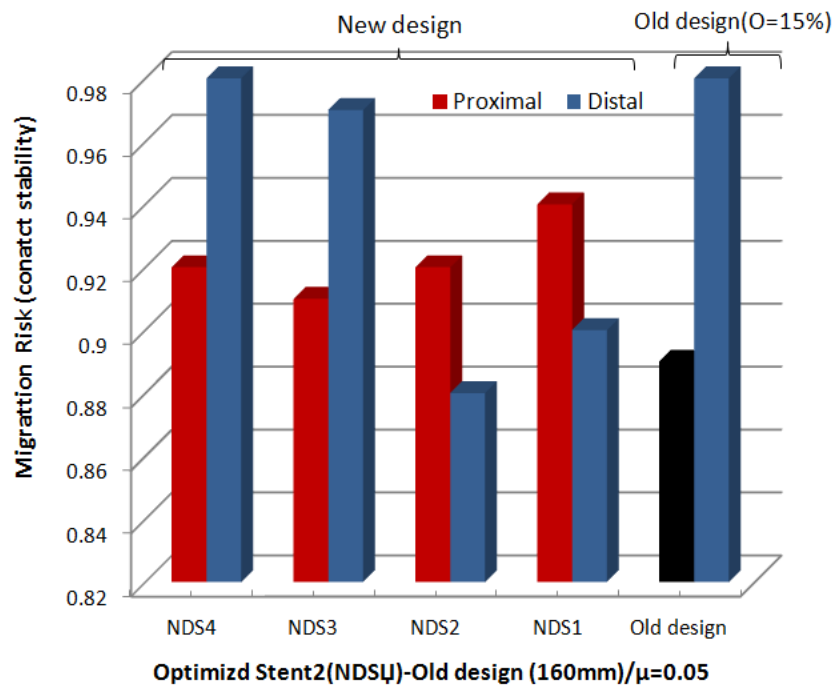
Figure IV.5-14: Migration behaviour improvement for the new stent 2 (NDSЏ)

IV.6. Improved new design for stent2

The previous results (Table IV.5-1/IV.5-2) of the proposed stent design demonstrated better wall coverage and good positioning of the stent1 struts against the vessel wall. However, when only one circle of the proximal stent end was oversized by (20%) or (25%) with (15%) oversized central part, the optimized stent2 resulted in a decrease of contact stiffness at proximal attachment zone comparing with the (15%) uniform oversizing along the stent. This is the result of the decrease of the contact surface and smaller diameter when full deployment for the second circle of struts, which was less oversized (15%) than the first circle of struts (O%=20% & 25%).

In order to improve our proposed design, we suggest oversizing the final two circle struts proximally and one circle distally for the stent2 with two oversizing values (O%=20% & 25%). The central part was oversized with (O=15%) (Figure IV.6-1). We believe that this new improved design (Imp-NDSЏ) will lead to a more uniform opposition and adequate contact at the proximal attachment zone. The improved design also aims to prevent the stent collapse.
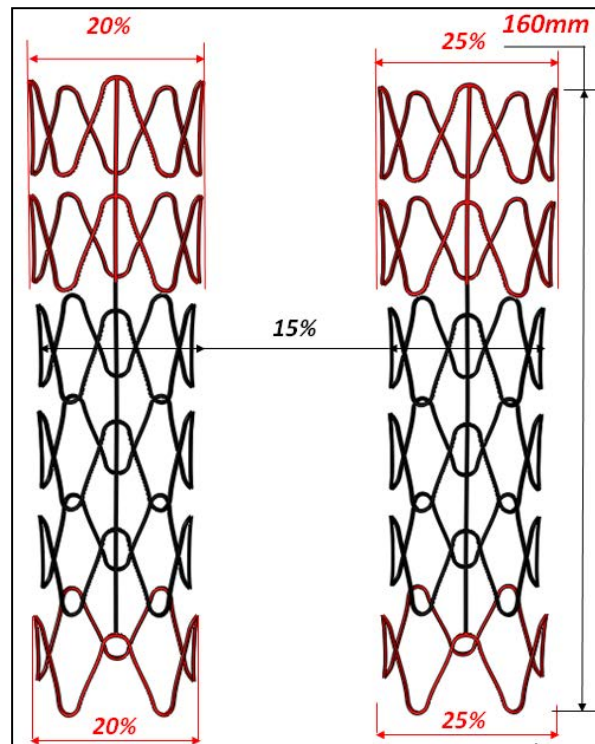
Figure IV.6-1: Improved stent2 designs modeling (Imp-NDSЩ) (Final optimization)

The obtained results from this simulation showed neither migration nor collapse. During the crimping process, the (Imp-NDSЩ)-20% demonstrated almost the same stiffness of new design NDSЩ-2 and NDSЩ-4 (Figure IV.6-2). On the other side, the (Imp-NDSЩ)-25% resulted in an observed decrease of stiffness (Figure IV.6-3). Starting from the (O%=25%) value, the (Imp-NDSЩ) stiffness was slightly decreased.

Consequently, the (Imp-NDSЩ)-25% resulted in (10%) improvement of overall flexibility behavior, comparing with the (Imp-NDSЩ)-20%. Lower stiffness means better capability to accommodate the curvature of the thoracic aorta.

143
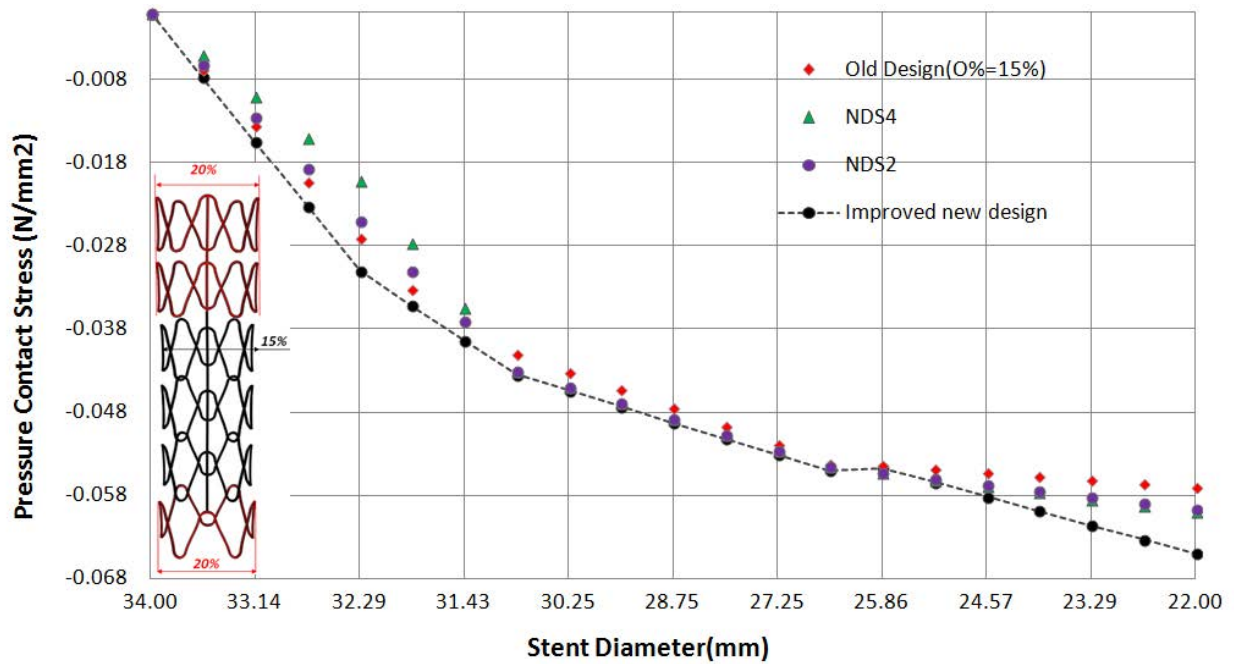
Figure IV.6-2: Radial pressure contact as a function of stent2 (160mm) diameter for numerical results for (Imp-NDSЦ)-20%
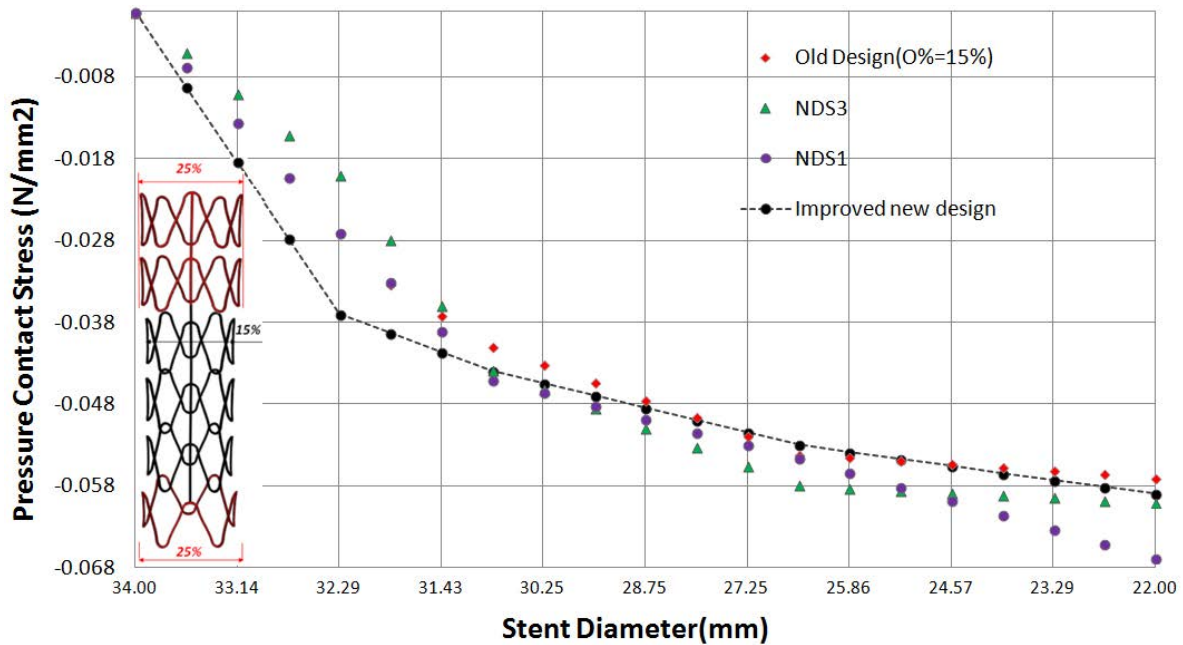
Figure IV.6-3: Radial pressure contact as a function of stent2 (160mm) diameter for numerical for (Imp-NDSЦ)-25%

144

The two improved new designs (20% & 25%): (Imp-NDSЏ)-20%&25%, demonstrated better superelastic recovery during the stent expansion, resulting in a better proximal, contact surface diffusion, comparing with those where only one circle of the strut at the proximal site was oversized with (20% or 25%).

(Figure IV.6-4) shows the struts open-angles for both designs (α_1, α_2). In the improved design, both oversized circles of struts at the proximal site had the same strain energy potential of superelastic recovery improving the expansion mechanism at the proximal attachment site. Consequently, the contact stability ($\bar{F}_{cs}$) at the proximal site was decreased for (Imp-NDSЏ)-20% and (Imp-NDSЏ)-25% as compared to (NDSЏ-20&25%): (0.89 vs. 0.92)-(0.90 vs. 0.94) respectively, i.e. the contact stiffness was improved proximally. Despite the contact improvement at the proximal site, the improved design caused an increasing of the contact stability ($\bar{F}_{cs}$) (decrease in contact stiffness) at the distal site as compared to (NDSЏ-20&25%): (0.93 vs. 0.88)-(0.95 vs. 0.90) respectively, i.e. the contact stiffness was decreased distally (Table IV.6-1) (Figure IV.6-7). This can be explained by decreasing the overall stent recovery distally when adding another oversized circle at the proximal site. As a result, the proximal part of the stent gained the important superelastic recovery comparing with the distal part.
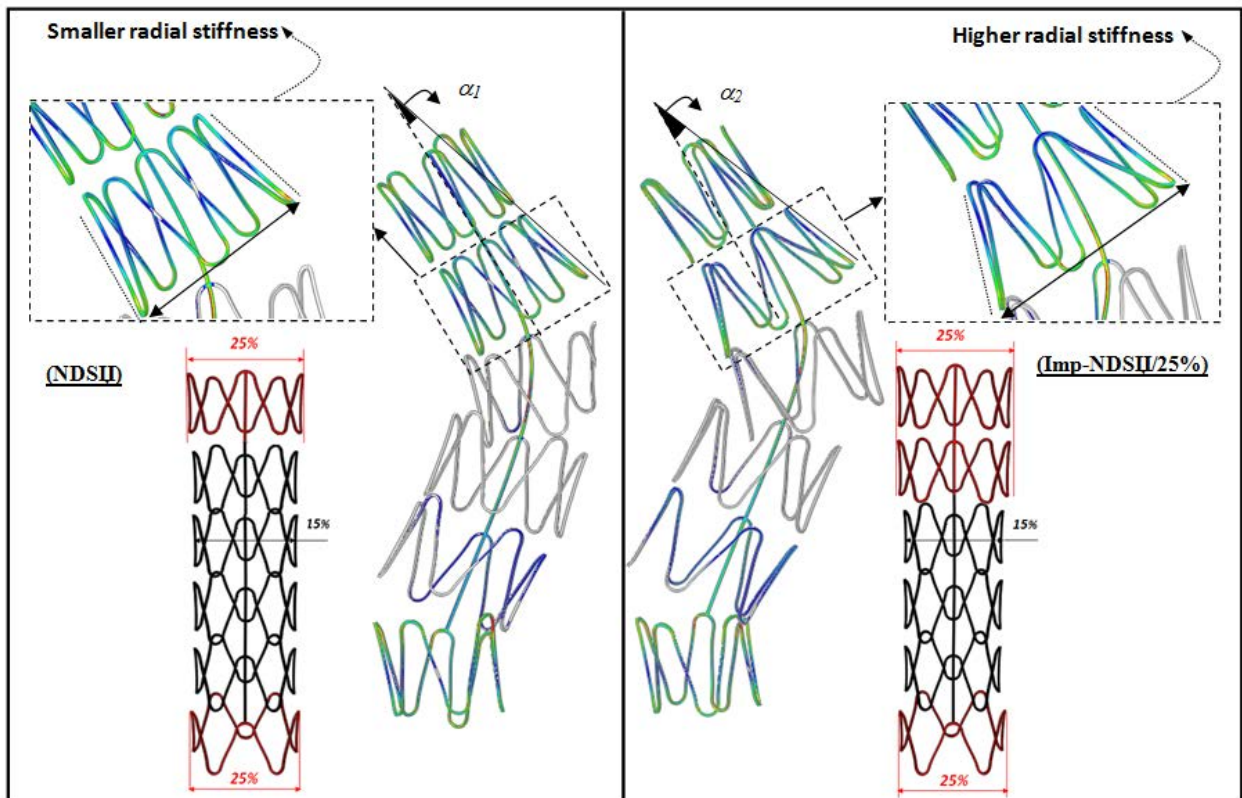
Figure IV.6-4: Comparison of struts's superelastic recovery between the NDSЏ (left) and Imp-NDSЏ of stent2 (right) after stent deployment

The variable design along the stent length with a larger diameter at the attachment sites, where the interaction is expected, could increase considerably the proximal surface of interaction compared to (NDSЦ-20&25%). It was increased by 4.6% for (Imp-NDSЦ)-20% and by 8% for (Imp-NDSЦ)-25% as: (1140 vs. 1090)mm^2- (1200 vs. 1110)mm^2 respectively (Figure IV.6-5) (Figure IV.6-6) (Table IV.6-1). The improved design can also accommodate larger aortic diameters for both proximal and distal sites.
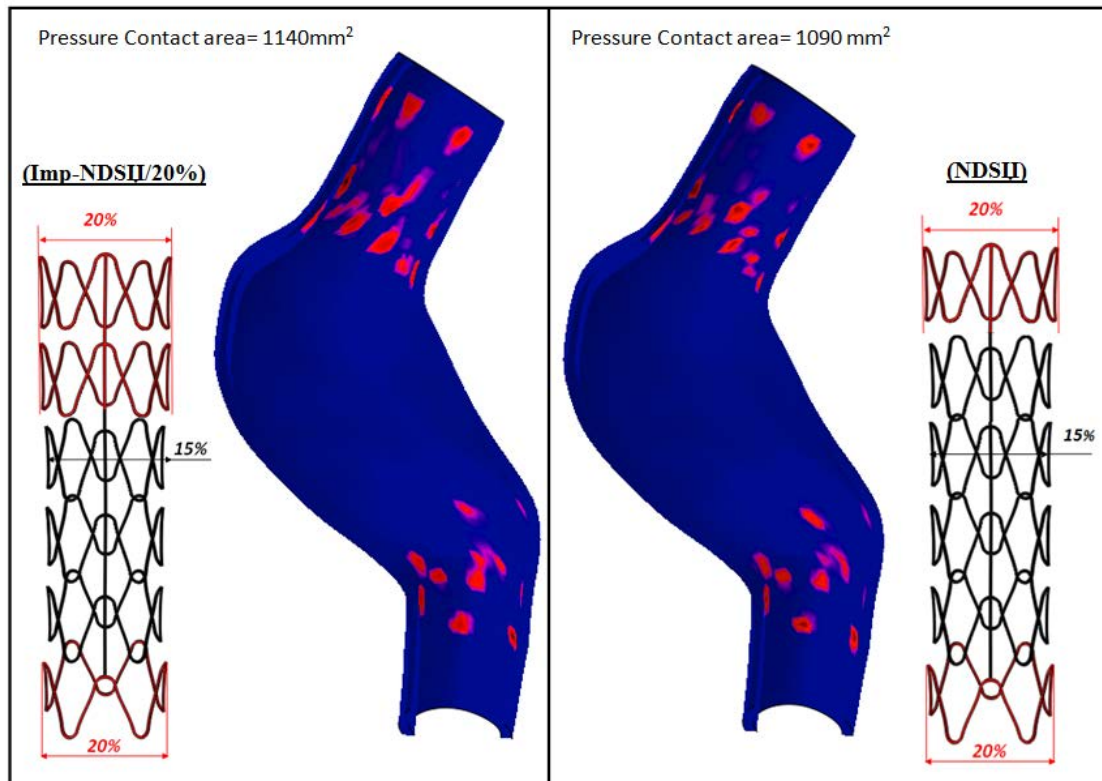
Figure IV.6-5: Pressure stress distribution after implantation of the (Imp-NDSЦ)-20% of stent2
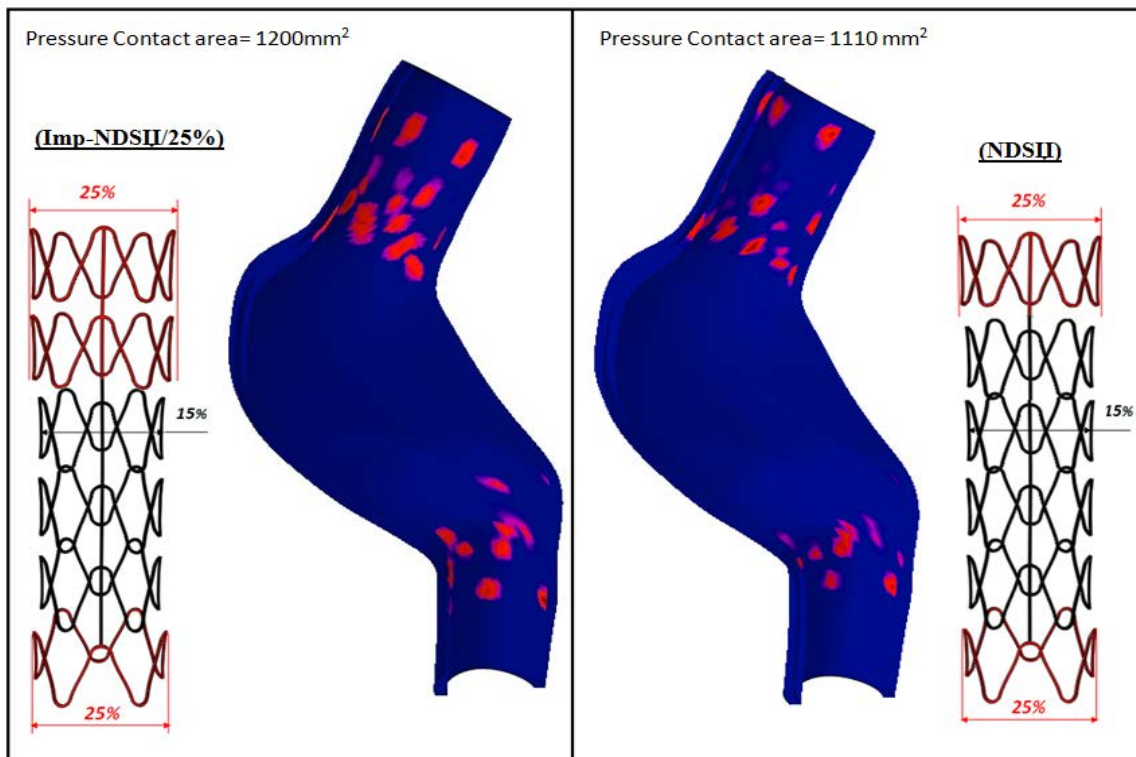
Figure IV.6-6: Pressure stress distribution after implantation of the (Imp-NDSЏ)-25% of stent2

Table IV.6-1: The effect of improved new design stent 2; (simulation results)			
Stent models *(PASL)* *(DASL)*		*Stent2(160mm)* $D_{2P}=21$ $D_{2D}=18$	*Stent2(160mm)* $D_{2P}=21$ $D_{2D}=18$
Oversizing value (O %)	Stent Body	15%	15%
	Stent Proximal site (two circles)	20%	25%
	Stent Distal site(one circle)	20%	25%
Contact stability ($\overline{F}_{CS}$)	Proximal neck	0.89	0.90
	Distal neck	0.93	0.95
Tangential contact behavior		$(\mu = 0.05)$	$(\mu = 0.05)$
Pressure contact area (mm^2) after deployment		1140	1200
Average contact pressure stress	Proximal neck	0.01196	0.021
	Distal neck	0.0187	0.0172

147

For stent2, when comparing (Imp-NDSIJ-20&25%) with the uniform oversizing, both designs demonstrated an adequate contact stiffness at the proximal site with a better advantage of contact behavior at the distal site when the uniform oversizing stent2 was used. Nonetheless, both (Imp-NDSIJ-20&25%) will decrease the dislodge forces, as the superelastic recovery is mitigated at the central part with (O%=15%). This mitigation considerably contributes to decrease the migration failure during the time (i.e. increase the forces needed to dislodge the stent). Moreover, the (Imp-NDSIJ-25%) resulted in better flexibility, comparing with the NDSIJ stent designs.
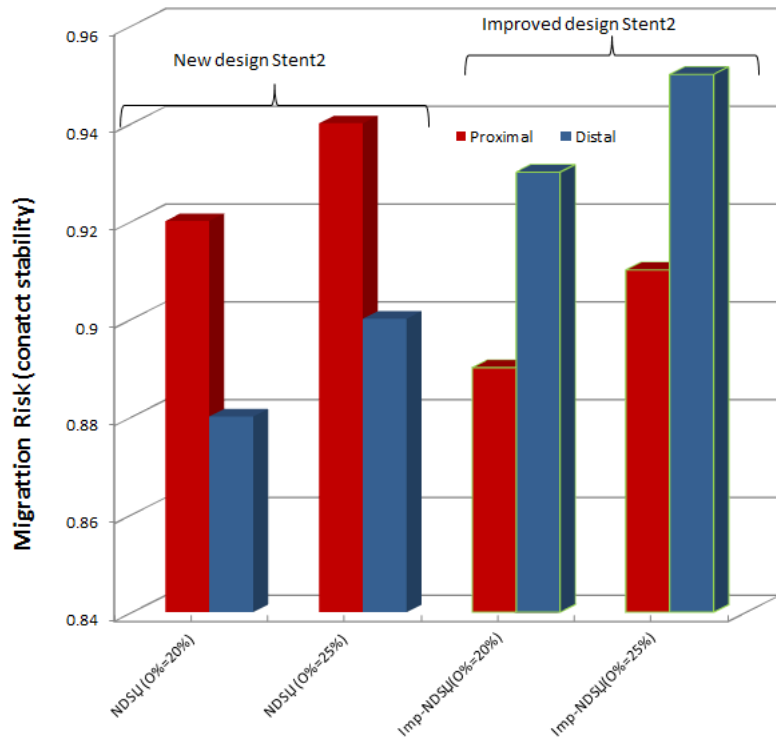
Figure IV.6-7: Migration behaviour for the new improved stent 2(NDSIJ)

IV.7. Conclusion

The obtained results clearly showed the importance of performing additional oversizing at the ends of the stent, especially the proximal one. This fact becomes more important when the length of the stent is critical as the case for the stent1. We were able to improve flexibility and prevent migration failure for the stent1. This can be explained by decreasing the potential of pullout forces when oversizing the central part with a small value (15%). This observation agrees with other experimental results (Kratzberg, et al., 2009) which associate high oversizing with greater static downward forces, i.e., more risk of stent migration.

Moreover, this design can also prevent the risk of folding or collapse of stent struts by mitigating the energy of eccentric deformation caused by high angulation and oversizing.

Oversizing the distal part of stent seems to be also beneficial. Although the lower importance of distal end oversizing, this design can increase the overall contact stability and reduce the stress

148

peak of circumferential stresses at the proximal attachment zone, especially when the stent length is critical. This idea contributed in better deployment and improved the overall behavior of deployment of this design.

Thus, this design highly mitigated the energy of eccentric deformation caused by the severe angulation and oversizing. Therefore, it is clear that better radial force and the presence of additional proximal oversizing stent segment are crucial factors to prevent proximal migration and contribute to better deployment in the severe aortic neck angulation. The results of the proposed designs support the clinical observation of the importance of additional oversizing at the aortic neck (Lambert, et al., 1999) (Canaud, et al., 2008). The proposed design contributed in more surface interaction between struts against the vessel wall. It was also necessary to improve the design of stent2 by oversizing all the struts that are expected to be in contact against the aorta. Here, better contact stiffness, flexibility and superelastic recovery were obtained. The improved design also decreased the risk of dislodging by limiting the value of oversizing at the central part of the stent. However, the realistic and the non-uniform morphology of the aortic lumen still need further improvement of interaction.

We agree that it is not a trivial task to propose an optimal stent design when the proximal neck is highly angulated. Each stent is unique and offers different behavior. However, the modular design in thoracic aneurysm requires the best radial performance, good strut coverage, flexibility to accommodate the thoracic aorta curvature, uniform radial deformation, prevent kinking and twisting and produce high contact stiffness. All of these characteristics were achieved by our numerical stent design. Despite improving the endovascular stent designs, patient cases are potentially more challenging and we are always in need of improvement in design to prevent the occurrence of material fatigue and obtain the optimal interaction against the lumen of the aorta. Finally, we agree that the better choice of graft design is governed by the proximal neck anatomy (angulation and diameter) of the aorta and all our proposed designs demonstrated the importance of finite element modeling.

Cette thèse est accessible à l'adresse : http://theses.insa-lyon.fr/publication/2014ISAL0051/these.pdf
© [S. Altnji], [2014], INSA de Lyon, tous droits réservés

Conclusions and perspectives

General Conclusion

Currently, more of aortic pathology approached with (EVAR) technique. It provides a solid alternative to open repair for many patients. Endovascular thoracic aortic repair offers decreased morbidity, shorter hospital length of stay, less invasive treatment and faster recovery. The primary criterion after EVAR includes: prevention of rupture and death from rupture (Hakaim, 2005). The followed secondary criteria concern the mid-and long-term durability and ultimate performance of the stent graft which remain questionable (Veith & Baum, 2003). The main long terms-mechanical related-problems are migration and endoleak type I (Lumsden, et al., 2007) (Veith & Baum, 2003) (Hakaim, 2005). Migration or endoleak type I can lead to aneurysm rupture due to the incomplete exclusion of the aneurysm with direct blood flow into the aneurysmal sac and outside the deployed stent graft. These complications may be a result of several factors, and wide differences of clinical opinion exist regarding the best procedure of treatment (Veith & Baum, 2003). These complications are more prevalent in the thoracic than in the abdominal aorta due to the curvature of the aortic arch.

However, it is generally agreed that all of these complications are related to unstable and poor seal or contact between stent-graft and vessel wall at the attachment landing zones (Lumsden, et al., 2007) (Veith & Baum, 2003) (Upchurch & Criado, 2009). A poor seal can be a result of misplacement or poor sizing of the endovascular stent graft. It may be a result of material fatigue or stent folding or complex aorta morphology (high angulation). Generally, a proximal type I endoleak and migration occur when a short or an angulated neck aneurysm is presented. Calcification in the neck may also have an impact on migration. We aimed in this work to investigate using the FE method the previous factors in order to understand the origin of these complications.

The power of technical advanced image-based techniques and finite element simulations using mathematical and computational modeling for a patient-specific basis can help to minimize all the risks associated with graft/stent instability and improve the surgical success rate.
To evaluate the contact strength of the stent in the attachment sites, several deployment simulations were performed to investigate the challenging morphological and stent design risk factors associated with migration and endoleak type Ia. These factors are represented as follows: the effect of Proximal-Distal attachment site length; (*PASL-DASL*) respectively, the tangential contact behavior, according to the pathological state of the aorta, the oversizing effect (O %) and the effect of severe angulation. A real, specific and aneurysmal case of specific-patient thoracic human aorta was reconstructed.

The challenging is represented in a severe angle of the descending thoracic aorta, which plays a major role in the migration of thoracic stent grafts (Sternbergh, et al., 2004) (Lumsden, et al., 2007) (Veith & Baum, 2003). Cuff extenders can be sometimes employed as a solution to compensate the adverse outcomes of high angulation. However, this technique has a high cost, is complex and can degenerate the lumen of the aorta (Hoffer, et al., 2002). Therefore, optimal radial forces and optimized oversizing values may prevent migration and improve the contact stiffness (Canaud, et al., 2008) (Vad, et al., 2010)

In this work, our focus is to investigate the impact of the previous factors which are important to optimal stent selection (the next object of this study).

An accurate representation of the strut stent geometry was performed by the manufacturing process or the shape setting simulation. The 3D thoracic aorta model was reconstructed based on DICOM CTA images of the interested anatomy. The vessel was modeled as hyperelastic isotropic nearly incompressible material. Realistic constitutive laws were attributed for the stent and aorta. The tangential behavior of interaction (stent-aorta) was described by the classical isotropic Coulomb friction model.

We found that impact of proximal length is a crucial factor of contact strength and better contact stability in order to prevent migration in the smoothest contact condition and severe angulation. In such conditions, the length of critical-clinic proximal landing zone (15-18mm: L_{stent1}=144mm) with oversizing value (O%=15%) was not enough to prevent migration failure. Lengthen the proximal attachment site to (21mm: L_{stent2}=160 mm) and more (23mm: L_{stent3}=160 mm) with (O%=15%) provided stronger proximal contact stiffness and sufficient radial strength to prevent migration.

Moreover, oversizing the stent1 (144mm) with (20%) was beneficial, but not enough to prevent migration failure. Oversizing the stent1 with (20%) can have potential results only when the proximal attachment zone is long enough, particularly with irregularly contoured necks and severe neck angulation. In such morphology, the position of the proximal implantation site of the stent should be determined. Lengthen the proximal stent site helps to have the ideal conformation and orientation with the arch of the thoracic aorta. Consequently, the positioning of the stent should be done with higher accuracy and longer stent grafts are particularly desirable when treating the aneurysmal pathology in the thoracic aorta.

We also demonstrated that the (20%) oversized stent3 resulted in the best contact stiffness outcomes compared to (10% and 15%) oversized stent3. The (10%) and (15%) oversized stent3 did not show considerable differences in results. Excessive oversizing in a severe angulation resulted in stent collapse and deployment failure. Stent folding risk increases as angulation and oversizing increase. This causes the eccentric deformation of the stent graft and prevents a good seal and contact with the aorta specifically at the outer radius of the bend. Therefore, it is important to select a suitable value of oversizing based on aortic anatomical features. High angulation (>60°) at proximal attachment increases the danger of folding and consequently migration or endoleak type I and can be considered as the most critical impact of EVAR exclusion. These results are in a good agreement with the clinical findings" *in extremely tortuous aorta, EVAR should not be offered as the primary treatment option"*. It is also important to say that the eccentric deformation or the stent collapse becomes more present if the stent is placed higher in 'both' proximal and distal attachment sites, which is the case for the stent3. To overcome stent enfolding deformity, the stent graft should be placed higher in the proximal. These numerical results are supported by the clinical studies (Lumsden, et al., 2007).

The results also showed the importance of the pathological state of aorta on migration, represented in different coefficients of friction. The high values of coefficient of friction ($\mu = 0.1 \rightarrow 0.5$) resulted in better contact stability without migration failure. When($\mu = 0.05$), the severe proximal neck angulation impact was very important on contact stability where the proximal fixation range was reduced. This would result in a small-inadequate area of contact,

reducing the friction between the aorta and stent struts. Furthermore, since the realistic morphological features of the vessel did not show uniform surface, not every point in nitinol exoskeleton was in contact with the native aortic wall. The interaction surface was also decreased in the smoothest contact condition ($\mu = 0.05$) reducing the radial force applied by the exoskeleton.

In an aneurysm that has a high angulated proximal neck, it is crucial to lengthen the proximal attachment site of the stent. Proximal aortic neck length (<20mm) increases the risk of migration and also prevents the proper alignment decreasing the contact between the stent and the vessel. However, excessive length of proximal fixation-site in a severe angulation can result in small stiffness and stent collapse, particularly if the stent is highly oversized. Oversizing of the proximal stent2 by up to (20%) resulted in adequate seal without aortic neck enlargement or stent folding. Therefore, optimizing the proximal attachment site length with suitable values of oversizing ensure an adequate seal even in challenging neck anatomy. We agree that the patient selection criterion represented in detailed imaging with multi-planar reconstruction and precise morphological dimensional measurement of the aorta and the device are governed by aortic neck characteristics and seems to be a crucial factor for endovascular success.

Furthermore, our results confirmed the important impact of the calcification on migration behavior. The high rigidity of the brittle calcified aorta changed significantly the mechanical deployment of stent when deployed. The migration behavior can be different when the mechanical behaviour of the aorta is different. The obtained results can be used as a starting point for more realistic behavior and geometry of the calcification material. These results are expected because of the high rigidity of the brittle calcified aorta. Therefore, when deployed, the reaction compression forces applied by the aorta became so important, and the high coefficient of friction also results in an improved positional stability.

However, our numerical approximation showed no impact on migration failure with a calcified aorta. The calcified aorta resulted in higher stresses and proposed consequently the need of more accurate study of the mechanic of aortic rupture. We believe that the geometries of the plaque were simplified for this comparative study. More realistic models and non-homogeneous aortic wall properties and coefficients of friction may change the mechanical behaviour and the interaction between the stent and the stenosed aorta. The volume of the calcification can highly change the risk of aneurysm rupture (Fillinger, et al., 2003). Therefore, further investigation of calcification impact will be important considering more realistic mechanical behaviour of the classification material, i.e., porous-hyperelastic behaviour (Adolph, et al., 1997) and viscoelastic behaviour (Hinnen, et al., 2007) (van Dam, et al., 2008) beside the anisotropic behaviour of the aorta and the non-uniform calcification distribution in the aorta.

In order to improve the stent flexibility, conformity, migration behavior and contact stiffness, we proposed extra oversizing at one or both end parts of the stent. This design was able to improve the flexibility, which is a crucial factor in patients with highly tortuous vessels. It also could prevent the migration when the stent was in the critical proximal length (stent1) even in the smoothest contact condition and high angulation.

The clinical results have always shown that the complex anatomy of the proximal attachment site is considered the most common reason for EVAR failure. The clinical experiments always ask for a better flexibility to accommodate the high angulation (Zannetti, et al., 2001). Therefore, the increase in flexibility for the new design stent1 (NDSI) obtained by the numerical simulations seems to be a very interesting result. A good compromise between flexibility and stiffness was obtained using the longer stent: stent2 (NDSЏ). The stiffness is also an important factor to compensate the changing in the anatomy of the aorta and prevent the high change in mechanical stresses on the stent graft.

All the suggested designs decreased the potential of downward static forces when oversizing the central part with a small value (15%), i.e., higher values are needed to dislodge the stent1 (144 mm) from its proximal site. This design resulted in an adequate area of proximal–distal interaction between the stent and the aortic neck, raising the friction and radial force applied by the proximal stent struts. These results were explained as follows: with the proposed design, the extra proximal–distal oversized stent ends expanded at the designed oversizing values (20%) or (25%), however, a continued expansion of the central part of the stent was limited at (15%) oversizing value. This decreased the potential energy which caused the stent to be dislodged, shortened or migrated by the pullout forces.

When the proximal stent length was higher for the new designed stent2 (NDSЏ), the simulations did not result in better contact stability due to the decreased interaction surfaces with the lumen of the aorta. Therefore, we suggested the extra oversizing (Imp-new design stent2) for both two circles of the stent which are expected to go into contact against the vessel wall. The improved design was able to improve the proximal contact stability compared with the (NDSЏ).

Different stent designs may lead to very different strut deformation patterns in the contact area. They may result in different outcomes of interaction surface and contact stability. Our proposed designs (NDSI) and (Imp-new design stent2) reduced significantly some complication of EVAR and leaded to uniform device delivery and conformity reducing the stent collapse or folding. Decreasing the value of oversizing in the proposed designs prevented the wrinkling of the proximal segment of the thoracic. The new designs decreased the likelihood of stent enfolding that may occur because of the high values of oversizing and severe bending angulation that creates stronger proximal and distal radial forces.

There are several commercial stent grafts, which are used in the EUROSTAR trial, however, the procedure success cannot be guaranteed or solved in the operating room. The numerical simulations, with some limitations, suggest that the stent design is the critical factor to ensure the EVAR procedure. For example, although the most of clinical studies showed direct correlation between neck angulation and endoleak type I or migration, EUROSTAR showed that the proximal neck length, diameter of the aneurysm neck and proximal attachment zone length are the most important factors which correlate with proximal type I endoleak and migration (Mohan, et al., 2001), but not the neck angulation with the endoleak. A smaller study of 33 patients (Dias, et al., 2001) also did not show any significant association between the morphological features of the aortic neck and endoleak type I.

However, further improvement should be taken to intensify the interaction contact area which could not be perfectly achieved in a non-uniform aortic neck.

Perspectives

In this work, several simplifications have been considered to minimize the complexity of the whole deployment procedure.

The present study considers that the deployment success is only associated with the mechanical fixation applied by the stent (Resch, et al., 2000). The graft effect has been neglected as it has little contribution of radial stiffness comparing with the nitinol stent when final device deployment was performed (Prasad, et al., 2011). Our study focused only on short-term stent fixation, in this case, we suspect that the wall shear stresses induced by the blood flow are negligible compared to normal forces applied by the springs when the stent was just deployed. Future work will include the graft and the residual stresses (Holzapfel & Ogden, 2010) (Speelman, et al., 2009) (Gee, et al., 2010) to evaluate long-term fixation of the stent graft under the hemodynamic factor (Zunino, et al., 2009) (Fu, et al., 2010) throughout the cardiac cycle. The hemodynamic factor may destabilize the aortic endograft fixation as shown by clinical results (Vulliémoz, et al., 2002) (Laffon, et al., 2005) and numerical results (Zunino, et al., 2009) (Fu, et al., 2010). It may affect rates of aneurysmal expansion and the progression of atherosclerosis in the aneurysm wall. This can directly increase the wall stresses in the aorta and the aneurysm expansion leading to hemodynamic changes, and consequently, complicate the stent procedure.

A mathematical analysis of geometry, using finite element analysis, can be used to estimate the wall stress and the risk of rupture. Many previous models have been suggested based on inverse design approach (Gee, et al., 2010) (Speelman, et al., 2009) (Raghavan, et al., 2006).

Additionally, the lumen of the vessel was reconstructed regardless of the calcification and plaques in the lumen of the aorta area (Zhao, et al., 2011) (García, et al., 2012). Irregular calcification or thrombus at the proximal neck can prevent a good proximal fixation and sealing of the endograft leading to migration or endoleaks. This observation is still controversial since some clinical studies did not show a direct correlation between aortic calcification at the proximal attachment aortic site and the incidence of migration or endoleak (Gitlitz, et al., 2001) (Albertini, et al., 2000) (Veith & Baum, 2003). In reality, the calcification offers discontinuity of the circumferential wall around the aorta and may affect the positional stability of the stent graft.

A clear delineation of the lumen of the thoracic aorta and classification with precise cross-sectional segmentation of the vessel can be obtained using preoperative CT image techniques.

Further improvement, including the pathological state of aorta at various locations (atherosclerotic plaques, calcification, etc.) in the model will be our future investigation.

In the objective of our study, we believe that the isotropic hyperelastic model with a constant thickness of the aorta can be appropriate. However, the recent experimental (biaxial) research showed the anisotropic behaviour of the aneurysmal wall (Geest, et al., 2006). These experiments resulted in many hyperelastic anisotropic models to be used in the numerical modeling, describing the anisotropic mechanical response of the thoracic aorta (Rodríguez, et al., 2009) (Basciano & Kleinstreuer, 2009) (Rissland, et al., 2009). The real behaviour of the calcification or thrombus is not yet completely known. Some research revealed the porous-hyperelastic behaviour (Adolph, et al., 1997) and the viscoelastic behaviour (van Dam, et al., 2008) of the thrombus. Therefore, further investigation of calcification impact is important including the realistic mechanical behaviour of the calcification material. All the material parameters of these different models can be adjusted by the experimental data.

Correspondingly, the varied thickness along the aneurysmal vessel (Thubrikar, et al., 2001) (Raghavan, et al., 2006) should be considered for more improvement of computational modeling. The varied thickness may change the stress distribution in the aortic wall as a function of the thickness. We believe that the varied thickness can be a critical factor to evaluate the evolution of martial translation from the initial configuration until the rupture.

(CSM) results can be coupled with Computational Fluid Dynamics (CFD) calculations, i.e. Fluid-Structure Interaction (FSI) (Chandra, et al., 2013) (Kelly & O'Rourke, 2012) (Wang & Li, 2011) (Wolters, 2009) (Li & Kleinstreuer, 2005) where the interaction between the fluid flow and the structural response of stent graft can be evaluated. Finally, we hope that future advances will rely more on experimental studies that are required to validate our numerical observations.

Appendix

Appendix A

Mesh convergence analysis

We have performed three different mesh resolutions of both the stent and aorta to investigate the mesh dependence on the numerical results. The element type used for both aorta and stent is C3D8R element type: An 8-node linear brick, reduced integration with hourglass control. For the stent, we evaluated different output results (Von Mises stress, logarithmic strain and contact pressure stress) at the final of the forming process simulation step. Then, we choose the mesh 1 of stent which has a low computational cost of deployment analyze procedure. Three deployments' simulations have been performed on the reference model simulation, i.e. stent 1 with ($\mu = \infty$) applying three different aorta mesh resolutions. In mesh 1, two elements were considered for the aorta thickness and 3, 4 elements for mesh2 and mesh3 respectively. The same outputs were evaluated. Consequently, the mesh 1-validated convergence analyze was used. All the simulations were run on high performance cluster calculation with 12 cpu processors.

Table: Mesh convergence study			
Mesh	**Mesh 1**	**Mesh2**	**Mesh 3**
*Element type (**C3D8R**)*			
Aorta	5680	8880	24720
Stent	58960	116070	175180
***Results**(Max)*			
Mises (MPa)			
Aorta	0.1927	0.1987	0.2121
Stent	4.8477^{e+2}	4.8677^{e+2}	4.877^{e+2}
LE (-)			
Aorta	0.1749	0.18101	0.1825
Stent	1.938^{e-1}	2.022^{e-1}	2.080^{e-1}
CPRESS (Max)			
Aorta	0.2386	0.2822	0.2939

The Measurement ratio (kinetic energy/ internal energy)

In our simulation, the mass scaling technique (Hughes, 2000) (Prior, 1994) (Anon., s.d.) was used to decrease the time process without generating high inertia forces. In order to reflect a quasi-static solution, the kinetic energy of the deforming material (ALLKE) should not exceed a small fraction of its internal energy (ALLIE), i.e. ALLKE/ALLIE $\leq 10\%$. Several simulations with different mass scaling values were performed. Finally, we chose the value which satisfies the energy measurement and validate the numerical values. Two peaks were reported (Figure), the first one was produced at the first contact (catheter-stent) in the insertion phase. The second pick was also due to the first contact (stent-vessel) in the deployment phase. However, all our results were evaluated just after the first contact and at the final phase of deployment which means that these peaks do not have an impact on our results. The same results have been obtained by (Auricchio, et al., 2011) when the deployment of the stent in the carotid was performed.
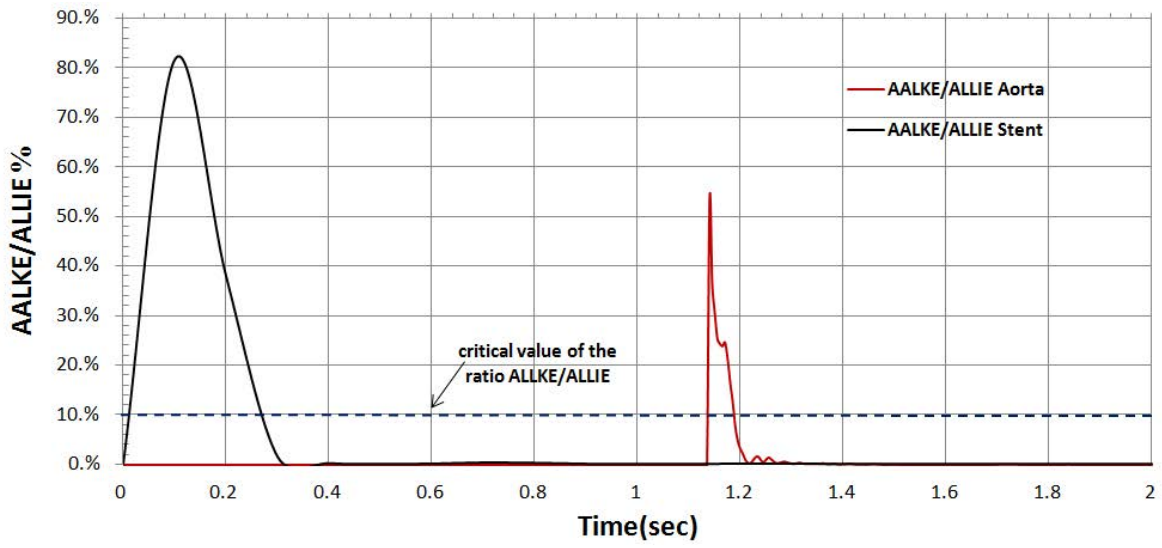
Figure: ALLKE/ALLIE ratio for stent and aorta during insertion
and deployment procedures, simulation V.

Appendix B

Catheter deformation Java Script

Principal program

```
import interact.*;
boolean Transformation = false;
boolean Bnd = false;
boolean expansion = false;
boolean scale = false;
public void fileSelected(String selection) {
  if (selection == null) {
    println("Window was closed or the user hit cancel.");
  } else {
    println("User selected " + selection);//.getAbsolutePath());
  }
}
void setup()
{
  String workSpace =  Entry.getString("Enter the experiment folder name ...") + "/" ; //Case2-19-2-2013/";
   // Select task
  int tsk = -1;
  while (tsk !=1 && tsk !=2 && tsk !=3){
   tsk = Entry.getInt("Select: \n 1) Single Transformation, 2) Double Transformation, or 3) Scaling");
  }
  // set the boolean variables according to users choice
  Transformation = (tsk == 1);
  Bnd = (tsk == 2);
  scale = (tsk == 3);

   size(500, 500);
  readNodesInfo();
   if (!scale)
   createSets();
  setSectionParts();
// selectInput("Select a file to process:", "fileSelected","","");
 //readCoordinations("Newcase_22_1_13/NODES.txt"); //XYZ_NEW.txt");
 //readCoordinations("FINAL_NODES.txt");
 readCoordinations(workSpace + "nodes.txt"); // selectInput("Select original nodes file...")
 readAngles(workSpace + "angles.txt"); //final_angles_new_2.txt");
   if (scale)
 {
   float xs = Entry.getFloat("X scaling factor");
   float ys = Entry.getFloat("Y scaling factor");
   float zs = Entry.getFloat("Z scaling factor");
   scaleNodes(xs,ys,zs);
   writeXYZtoFile(workSpace+"/nodes_scaled.txt",resNodes);
 }
  node[] Boundries1 = initBoundry();
 node[] Boundries2;
 if (Bnd) // initialize second boundires in case of double transformation
   Boundries2 = initBoundry();
    // set diameters
  R = Entry.getFloat("Input original Radius ...");
```

158

```
   R1 = Entry.getFloat("Input compression Radius ...");
   if (Bnd)
     R2 = Entry.getFloat("Input expansion Radius ...");

  if (Transformation)
  {

    calculateCompression(R, R1);
    calculateDisplacement();
    rotation(1);

    createBoundries(workSpace + "Boundries_test_" + R + "_" + R1 + ".txt");
  }

  /// ------------- TESTS, not to e used in the program ------------
  //readDisplacements("Displacement_nodes.txt");
  //readBoundries("final_Bnd_dis_compress.txt");
  if (Bnd)
  {
     Boundries2    =    readBoundries(workSpace    +    "Boundries_test_"    +    R    +    "_"    +    R2    +
".txt");//step2bnd/BoundriesTransformation_Step1_comp_dis_rot_18_12_mer1.txt");
     Boundries1    =    readBoundries(workSpace    +    "Boundries_test_"    +    R    +    "_"    +    R1    +
".txt");//step2bnd/BoundriesTransformation_Step2_comp_dis_rot_18_22_mer2.txt");

     for (int i=0; i<n ; i ++)
     {
      Boundries2[i].x = Boundries2[i].x - Boundries1[i].x;
      Boundries2[i].y = Boundries2[i].y - Boundries1[i].y;
      Boundries2[i].z = Boundries2[i].z - Boundries1[i].z;
     }
     writeBoundries(workSpace + "Boundries_test_dif_" + R1 + "_" + R2 + ".txt",Boundries2);
  }
  // FIN ------------------- TESTS -----------------

  ///  not used in the new vesions of the program,
  if (expansion)
  {
    //CalculateNEWXYZ(); // to calculate the new x y z after calculating all transformations
    // writeXYZtoFile("resultXYZ.txt",resNodes);

    // resetBoundries();
    // this loop is to be replaced by a function
    for (int i=0; i<n; i++)
    {
       nodes[i].x = resNodes[i].x;
       nodes[i].y = resNodes[i].y;
       nodes[i].z = resNodes[i].z;
    }
    expansion(12, 18);

    createBoundries("BoundriesExpansion.txt");
  }
}
```

159

```
node[] initBoundry()
{
  node[] bnd = new node[n];
  for (int i =0; i<n; i++)
  {
    bnd[i] = new node();
    bnd[i].x =0;
    bnd[i].y =0;
    bnd[i].z =0;
  }
  return bnd;
}
void writeBoundries(String fname,node[] bnd) // write the boundries in parameters into a file
{
 PrintWriter BROutput;
 BROutput = createWriter(fname);
 //** Name: BC-1 Type: Displacement/Rotation
 //*Boundary
 //Set-1, 1, 1, 10.
 for (int i=0; i<n; i++)
 {
   BROutput.println("** Name: BC-" + (i+1) + " Type: Displacement/Rotation");
   BROutput.println("*Boundary, amplitude=" + instanceName); // Amp-1");
   BROutput.println("Set-" +  bnd[i].setNum + ", 1, 1, " + bnd[i].x);
   BROutput.println("Set-" +  bnd[i].setNum + ", 2, 2, " + bnd[i].y);
   BROutput.println("Set-" +  bnd[i].setNum + ", 3, 3, " + bnd[i].z);
 }
 BROutput.close();
}
void createBoundries(String fname) //  calculate and write boundries to a file
{
 PrintWriter BROutput;
 BROutput = createWriter(fname);

 //** Name: BC-1 Type: Displacement/Rotation
 //*Boundary
 //Set-1, 1, 1, 10.
 for (int i=0; i<n; i++)
 {
   resBoundries[i].x += resNodes[i].x - nodes[i].x;
   resBoundries[i].y += resNodes[i].y - nodes[i].y;
   resBoundries[i].z += resNodes[i].z - nodes[i].z;
   BROutput.println("** Name: BC-" + (i+1) + " Type: Displacement/Rotation");
   BROutput.println("*Boundary, amplitude=" + instanceName); // Amp-1");
   BROutput.println("Set-" +  resBoundries[i].setNum + ", 1, 1, " + resBoundries[i].x);
   BROutput.println("Set-" +  resBoundries[i].setNum + ", 2, 2, " + resBoundries[i].y);
   BROutput.println("Set-" +  resBoundries[i].setNum + ", 3, 3, " + resBoundries[i].z);
 }
 BROutput.close();
}
// this function is only used in test versions of the program .... // disactivated for the moment
node[] readBoundries(String bndrFile)
{
 /// 1 ... read boundries
 node[] res = new node[n];
 BufferedReader reader;
 String ln;
 int xyzInd=0; // index to detect the current coordination (0:x , 1:y, 2:z)
 reader = createReader(bndrFile);
 int i=0; //current node(set = node) index
 res[0] = new node();
 res[0].setNum = 1;
 // boundry format - two lines text - 3 lines boundries, txt used to avoid text lines
```

160

```
try{ ln = reader.readLine(); ln = reader.readLine(); // skip two lines before each set boundries -- first two lines
}catch (IOException e) {
    e.printStackTrace();
    ln = null;
  }
/// read the rest of the file
do {
  try {
   ln = reader.readLine();
   println(ln);
  }
  catch (IOException e) {
   e.printStackTrace();
   ln = null;
  }
  if (ln != null )
  {
      String[] pieces =  splitTokens(ln, TAB+" "+",");
    //int ind = int(pieces[0]) - 1;
   //Set-1,                                    1,  1,          -6.0000 // pieces[3] being the required value
   float currVal = float(pieces[3]);
   if (xyzInd == 0)
    res[i].x += currVal;
   else if (xyzInd == 1)
    res[i].y += currVal;
   else if (xyzInd == 2)
    res[i].z += currVal;
   // set the index
   xyzInd++;
   if (xyzInd > 2)
   {
    try
    { ln = reader.readLine(); ln = reader.readLine(); // skip two lines before each set boundries -
     }catch (IOException e) {
     e.printStackTrace();
     ln = null;
    }
   // next node --> add 1 to i and reset xyzIndex
   println(xyzInd + "  , " + i + ",x : " +res[i].x +",y:"+res[i].y + ",z:"+res[i].z);
   xyzInd =0;
   i++;
   if (i <n)
   {
    res[i] = new node();
    res[i].setNum = (i+1) ;
   }
  }
 }
}
while (ln != null);
 return res;
}
```

```
void readCoordinations(String f)
{
 BufferedReader reader;
 String ln;
 reader = createReader(f);
 int ind = 0;
 println(f);
 do {
   try {
    ln = reader.readLine();
   }
   catch (IOException e) {
    e.printStackTrace();
    ln = null;
   }
   if (ln != null)
   {
    String[] pieces = splitTokens(ln, TAB+" "+",");
    //String[] pieces = split(ln, TAB);
    //int ind = int(pieces[0]) - 1;

    nodes[ind].setNum = int(pieces[0]);
    nodes[ind].x = resNodes[ind].x = float(pieces[1]);
    nodes[ind].y = resNodes[ind].y = float(pieces[2]);
    nodes[ind].z = resNodes[ind].z = float(pieces[3]);
    println(nodes[ind].setNum+",\t"+ nodes[ind].x+",\t"+nodes[ind].y+",\t"+nodes[ind].z);
    ind++;
    //point(nodes[ind].x, nodes[ind].y, nodes[ind].z);
   }
 }
 while (ln != null);
 }
void readAngles(String f)
{
 // se the angles array size
 angles = new float[n/sectionCount];
//angles = new float[75];
 BufferedReader reader;
 String ln;
 reader = createReader(f);
 int i = 0;
 do {
   println(i);
   try {

    ln = reader.readLine();
    println(ln);
   }
   catch (IOException e) {
    e.printStackTrace();
    ln = null;
   }
   if (ln != null)
   {
    String[] pieces = split(ln, TAB);
    angles[i] = float(pieces[0]);

    // println((ind+1)+",\t"+ nodes[ind].x+",\t"+nodes[ind].y+",\t"+nodes[ind].z);
    println(i + "  : " + angles[i]);
    i++;
   }
 }
 while (ln != null);
```

```
}

void CalculateNEWXYZ()
{
 for (int i=0; i<n; i++)
  {
   resNodes[i].x = nodes[i].x + resBoundries[i].x;
   resNodes[i].y = nodes[i].y + resBoundries[i].y;
   resNodes[i].z = nodes[i].z + resBoundries[i].z;
   //println(newNodes[i].x + "\t" + newNodes[i].y + "\t" + newNodes[i].z + "\t");
  }
}

void writeXYZtoFile(String fname, node[] nds)
{
 PrintWriter fOutput;
 fOutput = createWriter(fname);

 for (int i=0; i<n; i++)
  {
   println("node: " + i);
   fOutput.println(nds[i].setNum + "\t" + nf(nds[i].x,0,8) + "\t" +  nf(nds[i].y,0,8) + "\t" + nf(nds[i].z,0,8));
   println(nds[i].setNum + "\t" + nf(nds[i].x,0,8) + "\t" +  nf(nds[i].y,0,8) + "\t" + nf(nds[i].z,0,8));
  }
 fOutput.close();

}
```

Nodes Control

```
class node
{
 float x, y, z;
 int setNum;
 node()
 {
 }
}
void setSectionParts()
{
 sectionGroups = new int[8];
 sectionGroups[0] = 11;
 sectionGroups[1] = 16;
 sectionGroups[2] = 30;
 sectionGroups[3] = 36;
 sectionGroups[4] = 38;
 sectionGroups[5] = 52;
 sectionGroups[6] = 57;
 sectionGroups[7] = 73;
}
void readNodesInfo()
{
 //n = Entry.getInt("Input the total number of nodes");   // number of nodes
 nodes = new node[n];
 resNodes = new node[n];
 resBoundries = new node[n];
 displacements = new node[n];
 for (int i=0; i<n; i++)
  {
   nodes[i] = new node();
   resBoundries[i] = new node();
   resBoundries[i].x =0;
   resBoundries[i].y =0;
```

163

```
  resBoundries[i].z =0;
  displacements[i] = new node();
  resNodes[i] = new node();
 }
 //sectionCount = Entry.getInt("Input the  number of nodes per section"); // number of nodes per section
 //step =  Entry.getInt("Input the node step per section"); // node index step per section
 step = int(n/sectionCount);
 //instanceName = ", instance=" +  Entry.getString("Input the  instance name"); // current instance name
}
void createSets()
{
 PrintWriter setsOutput;
 setsOutput = createWriter("Sets.txt");
 //*Nset, nset=Set-1, instance=PART-2-1
 // 1981,
 for (int i=0; i<n; i++)
 {
   currentNode = "*Nset, nset=Set-" + (i+1)  + ", instance=" + instanceName + "\n" + (i+1);
   nodes[i].setNum = (i+1);
   resBoundries[i].setNum = (i+1);
   resNodes[i].setNum = (i+1);
   setsOutput.println(currentNode);
 }
 setsOutput.close();
}
```

Parameters

```
// Variable related to the current instance inforamtion
int n = Entry.getInt("Enter the number of nodes"); //1360; //3504;//3150;   // number of nodes
int sectionCount = Entry.getInt("Input the number of nodes per section"); //40; //48; //42; // number of nodes per section
int step; // node index step per section
String instanceName = "PART-3-1"; // current instance name
// Diameters
float R;
float R1;
float R2;

// program variables
//int nodeIndex = 0;
//int sectionIndex = 1;
String currentNode;

int[ ] sectionGroups; // to set up the number of section that have the same caracters (belong to the same line, or the same arc)

node[ ] nodes;
node[ ] resNodes; // contains the new xyz after each step // always work on those and keep the original in nodes
node[ ] resBoundries;
node[ ] displacements;

float[ ] angles;
float[ ][ ] trans = new float[3][3];
```

164

```
void expansion(float R_old, float R_new)
{
 float currAngle;
 rotation(-1);
 for (int i =0; i<n; i++)
 {
   currAngle = angles[i%(n/sectionCount)];
   println((i+1) + "OP : " + currAngle);

   float x = resNodes[i].x;
   float y = resNodes[i].y;
   float z = resNodes[i].z;
//     resNodes[i].x = -(sqrt(x*x+z*z) + (R_new-R_old)*cos(currAngle))*(x/sqrt(x*x+z*z)); // add xnew - xold to the boundry
condition
//   resNodes[i].z = (sqrt(x*x+z*z) + (R_new-R_old)*cos(currAngle))*(z/sqrt(x*x+z*z)) ;
//   resNodes[i].y = (y - (R_new - R_old)*sin(currAngle));

//    currAngle = 0;
//   resNodes[i].x = x + (R_new-R_old)*cos(currAngle)*(x/sqrt(x*x+z*z));
//   resNodes[i].z = z + (R_new-R_old)*cos(currAngle)*(z/sqrt(x*x+z*z));
//   resNodes[i].y = y - (R_new - R_old)*sin(currAngle);
//
//   currAngle = angles[i%(n/sectionCount)];
//   setRotationArray(currAngle);
//   rotation();
//   resNodes[i].x = (R_new*(x/R_old)) ; // add xnew - xold to the boundry condition
//   resNodes[i].y = resNodes[i].y;
//   resNodes[i].z = (R_new*(z/R_old));

   //println(nodes[i].x +"," + nodes[i].y +"," +nodes[i].z +",///"+resNodes[i].x +"," + resNodes[i].y +"," +resNodes[i].z );
 }
 //rotation(1);
}
void lineDisplacement(int start, int end, float a, float b)
{
 for (int i =start; i<end; i++)
 {
  for (int j =0; j <sectionCount; j++)
  {
   int currentNodeInd = j*step + i ;
   println("line: "+ currentNodeInd);
   resBoundries[currentNodeInd].x  += ((nodes[currentNodeInd].y-b)/a);// - nodes[currentNodeInd].x;
  }
 }
}
void arcDisplacement(int start, int end, float x0, float y0, float r0, int dir)
{
  for (int i =start; i<end; i++)
 {
  //println(" --- -section : " + (i+1));
  for (int j =0; j <sectionCount; j++)
  {
   int currentNodeInd = j*step + i  ;
   println("Arc: "+ currentNodeInd + "; y : " + (nodes[currentNodeInd].y - y0) +
       "; x to add: " + (dir*sqrt(r0*r0-(nodes[currentNodeInd].y-y0)*(nodes[currentNodeInd].y-y0))+x0));
   resBoundries[currentNodeInd].x  += (dir*sqrt(r0*r0-(nodes[currentNodeInd].y-y0)*(nodes[currentNodeInd].y-y0))+x0);// use
old y to refer to the section y
  }
 }
}
void calculateDisplacement()
{
 // group1 - line
```

165

```
 lineDisplacement(0,sectionGroups[0],90.1908609878164,0);
 // group2
 // arc
 arcDisplacement(sectionGroups[0], sectionGroups[1],-362.0431419,30.40632187,362.35800244,1);

 // group3 - line xx
 // arc
 arcDisplacement(sectionGroups[1], sectionGroups[2],-49.9601071,38.31261363,50.17483496,1);

 //group4
 // arc xxx
 // line
 lineDisplacement(sectionGroups[2],sectionGroups[3],-0.850795953153728,61.6841129642657);

 //group5
 // arc
arcDisplacement(sectionGroups[3],sectionGroups[4],-11.02156227,121.78681231,38.63464915,-1);

 //group6
 // arc
arcDisplacement(sectionGroups[4],sectionGroups[5],-15.46670545,118.22754189,32.94011636,-1);

 // group7
 // line xx
 // arc
 arcDisplacement(sectionGroups[5],sectionGroups[6],-142.51910153,190.90502903,113.43040147,1);

 // group 8
 // line
 lineDisplacement(sectionGroups[6],sectionGroups[7],2.43261110500766,239.261596558028);
 }
 void calculateCompression(float R_old, float R_new)
 {
  float x, y, z;
  for (int i =0; i<n; i++)
  {
   x = (R_new*(resNodes[i].x/R_old)) ; // add xnew - xold to the boundry condition
   y = resNodes[i].y;
   z = (R_new*(resNodes[i].z/R_old));
   resNodes[i].x = x;
   resNodes[i].y = y;
   resNodes[i].z = z;
  }
 }
 // this function is for a test version of the application -- disactivated in the real version
 void readDisplacements(String f)
 {
  BufferedReader reader;
  String ln;
  reader = createReader(f);
  int i = 0;
  do {
   try {
    ln = reader.readLine();
   }
   catch (IOException e) {
    e.printStackTrace();
    ln = null;
   }
   if (ln != null)
   {
    String[] pieces = split(ln, TAB);
    // pieces[0] being the node's number
    displacements[i].x =  float(pieces[1]);
    resBoundries[i].x += float(pieces[1]);
    displacements[i].y = float(pieces[2]);
```

166

```
    resBoundries[i].y += float(pieces[2]);
    displacements[i].z = float(pieces[3]);
    resBoundries[i].z += float(pieces[3]);
    // println((ind+1)+",\t"+ nodes[ind].x+",\t"+nodes[ind].y+",\t"+nodes[ind].z);
    //point(nodes[ind].x,nodes[ind0; ].y,nodes[ind].z);
    i++;
   }
  }
  while (ln != null);
}

void setRotationArray(float angle)
{
 // transformation array values
 angle = radians(angle);
 trans[0][0] = cos(angle);
 trans[0][1] = -sin(angle);
 trans[0][2] = 0;
 trans[1][0] = sin(angle);
 trans[1][1] = cos(angle);
 trans[1][2] = 0;
 trans[2][0] = 0;
 trans[2][1] = 0;
 trans[2][2] = 1;
}
void  rotation(int dir) // dir to precise in which direction to rotate /
{
 println("START ROTATION");
 float x, y, z;
 float yp ;
 for (int i =0; i<n; i++)
 {
  //print(" " + i);
  // new nodes after rotation
  setRotationArray(dir*angles[i%(n/sectionCount)]);
  //println("node "+ (i+1) + ": transfromation, section    " +       int(i%(n/sectionCount)) + " with angle : " +
angles[i%(n/sectionCount)]);
  // Calculate new x y z after rotation and save in new nodes
  yp = resNodes[i].y - nodes[i%(n/sectionCount)].y;
  x =  (trans[0][0]*resNodes[i].x + trans[0][1]*(yp) + trans[0][2]*resNodes[i].z);
  y =  (trans[1][0]*resNodes[i].x + trans[1][1]*(yp) + trans[1][2]*resNodes[i].z) + nodes[i%(n/sectionCount)].y;
  z =  (trans[2][0]*resNodes[i].x + trans[2][1]*(yp) + trans[2][2]*resNodes[i].z) ;
  resNodes[i].x = x;
  resNodes[i].y = y;
  resNodes[i].z = z;
  //println((nodes[i].x - resNodes[i].x) +"," + (nodes[i].y -resNodes[i].y)  +"," + (nodes[i].z - resNodes[i].z) );
 }
 println("END ROTATION");
}

void scaleNodes(float xScale,float yScale,float zScale)
{
 for (int i =0; i<n; i++)
 {
  println("node:" + i);
  resNodes[i].setNum = nodes[i].setNum;
  resNodes[i].x = xScale * nodes[i].x;
  resNodes[i].y = yScale * nodes[i].y;
  resNodes[i].z = zScale * nodes[i].z;
 }
}
```

167

Stent Stiffness Mtalab Script

```
%======================================================
%program to calculate the contact pressure and stiffness in the Stent
%======================================================

%Variables
%----------------------------------------------------
D=---;    % compressed Stent diameter (mm)
D0=---;   %(initial) Stent diameter (mm)
d=---;    %strut diameter (mm)
n=---;     %total number of wires
L0=---;   %(initial) Stent length (mm)
E=---;
G=---;
c=---;    % number of coils
IP=(d^4)/6;
I=(d^4)/12;
B0=---;   %(initial) pitch angle
%----------------------------------------------------

for B=73:5:93

%fprintf( 'angle(°):%2.0f', B );
L=L0+(((pi*c*D0)/(cos(B0*pi/180)))*((sin(B*pi/180)-sin(B0*pi/180))));
k1=(sin((2*B0*pi/180)))/(D0);
k2=(2*(cos(B0*pi/180)^2))/(D0);
k3=D0/(cos(B0*pi/180));
S=(((G*IP*cos(B0*pi/180))/k3)*((2*sin(B*pi/180)/k3)-k1))-(((((E*I*tan(B*pi/180)/k3)))*((2*cos(B*pi/180)/k3)-
k2)));
F=(2*n)*(S); %Axial Stent Force(N)
%fprintf('   AXForce :%3.2e', F );
Pout=-(2*F*c/(D*L*tan(B*pi/180)));  %Outer Radial Pressure Stress(N/mm2)
fprintf( ' %3.2e', Pout );
J=k3*sin(B*pi/180);
X=((D*L*tan(B*pi/180)))^2;
A=(2*c)/(J*X);
%fprintf( '  A:%3.2e', A );
T=(2*D*L*n*tan(B*pi/180));
Z=(G*IP/k3)*(2*cos(B*pi/180)/k3);
U=(((E*I)/k3)*((2*cos(B*pi/180)/k3)-(k2*((sec(B*pi/180)^2)))));
%fprintf( '  T:%3.2e', T );
O=(((D*L)/((cos(B*pi/180)^2)))+((k3*sin(B*pi/180)*(((pi*c*D)-(L*tan(B*pi/180)))))));
%fprintf( '  O:%3.2e', O );
KP=A*((T*(Z-U)-(F*O))); %  Radial Stiffness(N/mm3)
%fprintf( '  Stiff: %3.2e', KP );
hold on
plot(B,Pout,'.'),grid ;

xlabel( 'Strut angle' )
ylabel( 'pressure contact' )
fprintf( '\n' );     % new line

end
```

168

Bibliography

Adham, M. et al., 1996. Mechanical characteristics of fresh and frozen human descending thoracic aorta.. J Surg Res, Volume 64, pp. 32-36.

Adolph, R. et al., 1997. Cellular content and permeability of intraluminal thrombus in abdominal aortic aneurysm.. J Vasc Surg, Volume 25, pp. 916-926.

Akay, M., Galiana, H. & Kim, Y., 2006. BIOMEDICAL ENGINEERING. New Jersey: wiley interscience.

Alam, M., Youssef, M. & Nehdi, M., 2007. Utilizing shape memory alloys to enhance the performance and safety of civil infrastructure:a review. Can. J. Civ. Eng., Volume 34, p. 1075–1086.

Albertini, J. et al., 2000. Anatomical risk factors for proximal perigraft endoleak and graft migration following endovascular repair of abdominal aortic aneurysms. Eur J Vasc Endovasc Surg., Volume 19, pp. 308-312.

Albertini, J. et al., 2001. Pathophysiology of proximal perigraft endoleak following endovascular repair of abdominal aortic aneurysms: a study using a flow model. European Journal of Endovascular Surgery, Volume 22, p. 53–56.

Altnji, H. E., Bou-Said, B. & Walter-LE Berre, H., 2013. Numerical simulation of the migration phenomena and type 1a endoleak of thoracic aneurysm endograft. Computer Methods in Biomechanics and Biomedical Engineering, Volume 16, pp. 36-38.

Amplard, A., 2006. Contribution à l'étude du comportement d'une endoprothèse aortique abdominale: Analyse des endofuites de type I, Lyon: Institut National des Sciences Appliquées de Lyon .

Anon., s.d. Simulia abaqus theory manual, version 6.10, s.l.: s.n.

Anon., s.d. Simulia abaqus theory manual, version 6.10, s.l.: s.n.

Arati, P., 2007. A Phenomenological Model of Shape Memory Alloys Including Time-Varying Stress, Ontario: University of Waterloo Library.

Assali, A. et al., 2001. Endovascular Repair of Traumatic Pseudoaneurysm by Uncovered Self-Expandable Stenting With or Without Transstent Coiling of the Aneurysm Cavity. Catheter Cardiovasc Interv, Volume 53, pp. 253-258.

Auricchio, F. et al., 2011. Carotid artery stenting simulation: From patient-specific images to finite element analysis. Medical Engineering and Physics, Volume 33, p. 281–289.

Auricchio, F., Diloreto, M. & Sacco, E., 2000. Finite-element Analysis of a Stenotic Artery Revascularization through a Stent Insertion. Computer Methods in Biomechanics and Biomedical Engineering,, Volume 4, pp. 249-263.

Auricchio, F. & Reali, A., 2008. Shape Memory Alloys: Material Modeling and Device Finite Element Simulations. Materials Science Forum, Volume Vol. 583, pp. 257-275.

169

Auricchio, F. & RLTaylor, 1997. Shape-memory alloys: modelling and numerical simulations of the finite-strain superelastic behavior. Computer Methods in Applied Mechanics and Engineering, Volume 143, pp. 175-194.

Auricchio, F., Taylorand, R. & Lubliner, J., 1997. Shape Memory Alloy: Macromodelling and numerical simulation of the superelastic behavior. Computer Method Application,Mech, Engrg, Volume 146, pp. 281-312.

Awrejcewicz, J., Ciach, M. & Wlodarczyk, K., 2000. Finite element method analysis of non-liner behavior of implants and stents. European congress on computational method in applied sciences en engineering, Volume 1, pp. 11-14.

Ayyalasomayajula, A., Geest, J. V. & Simon, B., 2010. Porohyperelastic finite element modeling of abdominal aortic aneurysms. J. Biomech. Eng, Volume 132, p. 104502–8.

Balossino, R., Gervaso, F., Migliavacca, F. & Dubini, G., 2008. Effects of different stent designs on local hemodynamics in stented arteries. Journal of Biomechanics, Volume 41, p. 1053–1061.

Basciano, C. & Kleinstreuer, C., 2009. Invariant-based anisotropic constitutive models of thehealthy and aneurysmal abdominal aortic wall. Journal of Biomechanical Engineering, Volume 131, p. 1–11.

Bergel, D., 1961a. The dynamic elasticity properties of the arterial wall. J. Physiol, Volume 156, p. 458–469.

Bergel, D., 1961b. The static elastic properties of the arterial wall. J. Physiol, Volume 156, p. 445–457.

Besson, J., Cailletaud, G., Chaboche, J. & Forest, S., 2009. Non-Linear Mechanics of Materials. New York: SPRINGER.

Beule, M. D., 2009. Finite Element Stent Design, Ghent: Ghent University. Faculty of Engineering.

Beule, M. D. et al., 2008. Realistic finite element-based stent design: The impact of balloon folding. Journal of Biomechanics, Volume 41, p. 383–389.

Black, J., 2005. Biological performance of materials. Boca Raton: CRC Press; 4 edition.

Bock, S. D. et al., 2012. Virtual evaluation of stent graft deployment: a validated modeling and simulation study. J Mech Behav Biomed Mater., Volume 13, pp. 129-139.

Bosman, et al., 2010. The proximal fixation strength of modern EVAR grafts in a short aneurysm neck. An in vitro study. Eur J Vasc Endovasc Surg, Volume 39, pp. 187-192.

Brinson, L. & Lammering, R., 1993. Finit element analysisof the behvior of shape memory alloys and their applications. International Journal of Solids and Structures, Volume 23, pp. 3261-3280.

Canaud, L. et al., 2008. Proximal Fixation of Thoracic Stent-Grafts as a Function of Oversizing and Increasing Aortic Arch Angulation in Human Cadaveric Aortas. J Endovasc Ther, Volume 15, pp. 326-334.

Capelli, C. et al., 2009. Assessment of tissue prolapse after balloon-expandable stenting: Influence of stent cell geometry. Medical Engineering and Physics, Volume 31, p. 441–447.

170

Carew, T., Vaishnav, R. & ., D. P., 1968. Compressibility of the arterial wall.. Circ Res, Volume 23, pp. 61-68.

Chan, C., Trigwell, S. & Duerig, T., 1990. Oxidation of an NiTi alloy. Surface and Interface Analysis, Volume 15, p. 349–354.

Chandra, S. et al., 2013. Fluid-structure interaction modeling of abdominal aortic aneurysms: the impact of patient-specific inflow conditions and fluid/solid coupling.. J Biomech Eng, Volume 135(8), pp. 402-427..

Cheung, G., Zhang, E. & Zheng, Y., 2010. A numerical method for predicting the bending fatigue life if NITI and stainless steel root canal instruments. International Endodontic Journal, Volume 44, pp. 357-361.

Chua, S. D., MacDonald, B. & Hashmi, M., 2004. Effects of varying slotted tube (stent) geometry on its expansion behaviour using finite element method. Journal of Materials Processing Technology, Volume 155–156, p. 1764–1771.

Chua, S. D., MacDonald, B. & Hashmi, M., 2004. Finite element simulation of slotted tube (stent) with the presence of plaque and artery by balloon expansion. Journal of Materials Processing Technology, Volume 155–156, p. 1772–1779.

Conti, M., 2007. Finite Element Analysis of self-expanding braided wirestent, Ghent : Ghent University.

Conti, M. et al., 2009. Nitinol Embolic Protection Filters: Design Investigation by Finite Element Analysis. Journal of Materials Engineering and Performance, Volume 18, pp. 787-792.

Conti, M. et al., 2011. Impact of Carotid Stent Cell Design on Vessel Scaffolding: A Case Study Comparing Experimental Investigation and Numerical Simulations. J Endovasc Ther, Volume 18, p. 397–406.

Darjan, C., 2007. Shape memory alloys. Slovenia : University of Ljubjani.

De Bock, S. et al., 2012. Our capricious vessels: The influence of stent design and vessel geometry on the mechanics of intracranial aneurysm stent deployment.. J Biomech, Volume 45, pp. 1353-1359.

DeHerrera, M. & LLC, E. L., 2009. Numerical Study of Metal Fatigue in a Superelastic Anchoring Stent Embedded in a Hyperelastic Tube. Irvine, University of Connecticut.

Demanget, N. et al., 2012. Computational comparison of the bending behavior of aortic stent-grafts. Journal of the Mechanical Behavior of Biomedical Materials, Volume 5, pp. 272-282.

Demanget, N. et al., 2012. Severe bending of two aortic stent-grafts: an experimental and numerical mechanical analysis.. Ann Biomed Eng, Volume 40, pp. 2674-2686.

Dias, N. et al., 2001. Intraoperative proximal endoleaks during AAA stent-graft repair: evaluation of risk factors and treatment with Palmaz stents. J Endovasc Ther, Volume 8, p. 268–273.

Dumoulin, C. & Cochelin, B., 2000. Mechanical behaviour modelling of balloon-expandable stents. Biomechanics, Volume 33, pp. 1461-1470.

Early, M. & Kelly, D. J., 2011. The consequences of the mechanical environment of peripheral arteries for nitinol stenting. International Federation for Medical and Biological Engineering, Volume 49, pp. 1279-1288.

Elmarasy, N. et al., 2000. Sigmoid ischemia and the inflammatory response following endovascular abdominal aortic aneurysm repair. J Endovasc Ther, Volume 7, pp. 21-30.

Enderle, J., Blanchard, S. M. & Bronzino, J., 2005. Introduction To Biomedical Engineering. Calefornia: Elsevier Academic Press.

Etave, F. et al., 2001. Mechanical properties of coronary stents determined by using finite element analysis. Journal of Biomechanics, Volume 34, p. 1065–1075.

Falvo, A., 2007. Thermomechanical characterization of Nickel-Titanium Shape Memory Alloys, Rende Cosenza: University of Calabria.

Farnoush, A. & Li, Q., 2007. Three Dimensional Nonlinear Finite Element Analysis of the Newly Designed Cardiovascular Stent. Brisbane, Australasian Congress on Applied Mechanics.

Ferruzzi, J., Vorp, D. & Humphrey, J., 2011. On constitutive descriptors of the biaxial mechanical behaviour of human abdominal aorta and aneurysms. Journal of The Royal Society Interface, Volume 56, p. 435–450.

Figueroa, C., Taylor, C., Chiou, A. & Zarins, C., 2009b. Magnitude and direction of pulsatile displacement forces acting on thoracic aortic endografts. J Endovasc Ther, Volume 16, p. 350–358.

Fillinger, M., Marra, S., Raghavan, M. & Kennedy, F., 2003. Prediction of rupture risk in abdominal aortic aneurysm during observation: wall stress versus diameter.. J Vasc Surg, Volume 37, pp. 724-732.

Flory, P. J., 1961. Thermodynamic relations for high elastic materials. Trans. Faraday Soc, Volume 57, pp. 829-838.

Fulton, J. et al., 2006. Effect of challenging neck anatomy on mid-term migration rates in AneuRx endografts. J vasc surg, Volume 44, p. 932–937.

Fung, Y., 1967. Elasticity of soft tissues in simple elongation. American Journal of Physiology, Volume 213, p. 1532–1544.

Fu, W. et al., 2010. Numerical simulation of hemodynamics in stented internal carotid aneurysm based on patient-specific model. Journal of Biomechanics, Volume 43, p. 1337–1342.

Gao, X., Huang, M. & Brinson, L. C., 2000. A multivariant micromechanical model for SMAs: Part 1: Crystallographic issues for single crystal model. Int. J. Plasticity, Volume 16, p. 1345–1369.

García, A., Peña, E. & Martínez, M., 2012. Influence of geometrical parameters on radial force during self-expanding stent deployment. Application for a variable radial stiffness stent.. J Mech Behav Biomed Mater, Volume 10, pp. 166-175.

Gastaldi, D. et al., 2010. Modelling of the provisional side-branch stenting approach for the treatment of atherosclerotic coronary bifurcations: effects of stent positioning. Biomech Model Mechanobiol:, Volume 9, p. 551–561.

172

Gee, M., Förster, C. & Wall, W., 2010. A computational strategy for prestressing patient-specific biomechanical problems under finite deformation. Int J Numer Methods Biomed Eng, Volume 26, p. 52–72.

Geest, J. V., Sacks, M. & Vorp, D., 2006. The effects of aneurysm on the biaxial mechanical behavior of human abdominal aorta. Journal of Biomechanics, Volume 39, p. 1324–1334.

Gervaso, F. et al., 2008. On the effects of different strategies in modelling balloon-expandable stenting by means of finite element method. Journal of Biomechanics, Volume 41, p. 1206–1212.

Gijsen, F. et al., 2008. Simulation of stent deployment in a realistic human coronary artery. BioMedical Engineering OnLine, Volume 1, pp. 7-23.

Gitlitz, D. et al., 2001. Endovascular stent grafting in the presence of aortic neck filling defects: early clinical experience. J Vasc Surg. 2001, Volume 33, pp. 340-304.

Grabenwoger, M. et al., 2004. Secondary surgical interventions after endovascular stent-grafting of the thoracic aorta. Eur J Cardiothorac Surg, Volume 26, p. 608–613.

Green, A. & Adkins, J., 1970. Large Elastic deformation. Oxford : Oxford university Press.

Grogan, J., Leen, S. & McHugh, P., 2013. Comparing coronary stent material performance on a common geometric platform through simulated bench-testing. Journal of the Mechanical Behavior of Biomedical Materials, Volume 12, pp. 129-138.

Grogan, J., O'Brien, B., Leen, S. & McHugh, P., 2011. A corrosion model for bioabsorbable metallic stents. Acta Biomaterialia, Volume 7, p. 3523–3533.

Grujicic, M., Pandurangan, B., Arakere, A. & Snipes, J., 2011. Fatigue-Life Computational Analysis for the Self-Expanding Endovascular Nitinol Stents. Journal of Materials Engineering and Performance, Volume 21, pp. 2218-2230.

Gu, L., Santra, S., Mericle, R. & Kumar, A., 2005. Finite element analysis of covered microstents. Journal of Biomechanics, Volume 38, p. 1221–1227.

Gu, L., Zhao, S., Muttyam, A. & Hammel, J. M., 2010. The Relation Between the Arterial Stress and Restenosis Rate After Coronary Stenting. Journal of Medical Devices, Volume 4, pp. 41-48.

Guthikonda, V., Kiran, M., Sivakumar, M. & Srinivasa, A., 2007. On smeared and micromechanical approaches to modeling martensitic transformations in SMA, Nonlin. Anal.: Real World Applications, Volume 9, pp. 990-1011.

Hakaim, A., 2005. Current Endovascular Treatment of Abdominal Aortic Aneurysms. Oxford: Wiley-Blackwell.

Harewood, F., Geogan, J. & Hugh, P. M., 2010. A MULTISCALE APPROACH TO FAILURE ASSESSMENT IN DEPLOYMENT FOR CARDIOVASCULAR STENTS. Journal of Multiscale Modelling, Volume 10, pp. 1756-9737.

Harewood, F. & McHugh, P., 2007. Modeling of size dependent failure in cardiovascular stent struts under tension and bending.. Annals of Biomedical Engineering, Volume 35, p. 1539–1553.

Harvey, S., 2011. Nitinol Stent Fatigue in a Peripheral Human Artery Subjected to Pulsatile and Articulation Loading. JournalofBiomechanics, Volume 45, pp. 468-475.

He, C. & Roach, M., 1994. The composition and mechanical properties of abdominal aortic aneurysms. Journal of Vascular Surger, Volume 20, p. 6–13.

Hendersona, E., Nashb, D. & Dempsterb, W., Received 1 July 2010 Received in revised form 2010. On the experimental testing of fine Nitinol wires for medical devices. journal of the mechanical behavior of bio medical materials, Volume 4, pp. 261-268.

Hinnen, J. et al., 2007. Development of fibrinous thrombus analogue for in-vitro abdominal aortic aneurysm studies.. J Biomech, Volume 40, pp. 289-295.

Hobo, R., Kievit, J., Leurs, L. & Collaborators., J. B. ;. E., 2007. Influence of severe infrarenal aortic neck angulation on complications at the proximal neck following endovascular AAA repair: a EUROSTAR study.. J Endovasc Ther, Volume 14, pp. 1-11.

Hoffer, E. et al., 2002. Treatment of acute thoracic aortic injury with commercially available abdominal aortic stent-grafts.. J Vasc Interv Radiol, Volume 13, pp. 1037-1041.

Holzapfel, A. & Ogden, R., 2010. Constitutive modelling of arteries.. Proceedings of the Royal Society A : Mathematical, Physical and Engineering Science, Volume 466, p. 1551–1597.

Holzapfel, G., Gasser, T. & Ogden, R., 2000. A new constitutive framework for arterial wall mechanics and a comparative study of material models. Journal of Elasticity, Volume 61, p. 1–48.

Holzapfel, G. & Ogden, R., 2010. Constitutive modelling of arteries.. Proceedings of the Royal Society A : Mathematical, Physical and Engineering Science, Volume 466, p. 1551–1597.

Holzapfel, G. et al., 2007. Layer-specific 3d residual deformations of human aortas with non-atherosclerotic intimal thickening. Ann. Biomed. Eng, Volume 35, p. 530–545.

Hsiao, H., Chiu, Y., Lee, K. & Lin, C., 2012. Computational modeling of effects of intravascular stent design on key mechanical and hemodynamic behavior. Computer-Aided Design, Volume 44, p. 757–765.

Hughes, T., 2000. The finite element method: linear static and dynamic finite element analysis. s.l.:Dover Publications.

Humphrey, D., 1995. Mechanics of the arterial wall : review and directions. Crit Rev Biomed Eng, Volume 23, p. 1–162.

Idu, M. et al., 2005. Collapse of a stent-graft following treatment of a traumatic thoracic aortic rupture. J Endovas Ther, Volume 12, p. 503–507.

Imura, T. et al., 1986. Non-invasive ultrasonic measurement of the elastic properties of the human abdominal aorta. Cardiovasc Res, Volume 20, p. 208–214.

Imura, T. et al., 1990. In vivo viscoelastic behavior in the human aorta. Circulation Research, Volume 66, p. 1413–1419.

Jaber, M. B., Smaoui, H. & Terriault, P., 2008. Finite element analysis of a shape memory alloy three-dimensional beam based on a ?nite strain description. Smart Mater. Struct., Volume 17, pp. 1-11.

Jedwab, M. R. & Clerc, C. O., 1993. A study of the geometrical and me-. J Appl Biomater, Volume 4, p. 77–85.

Jeon, D. et al., 2009. The Verification of Computer Simulation of Nitinol wire Stent using Finite Element,Sang-Ho Kim Analysis. Korean journal of medical physics, Volume 20, pp. 139-144.

Johnson, K., 1987. Contact mechanics. Trinity Ln: Cambridge University Press Cambridge.

Jr, J., Jalisi, M. & Moreno, M., 2004. Minimally Invasive Cardiovascular Technologies. Dans: Biomedical Technology and Devices Handbook. s.l.:CRC Press LLC, p. 15.

Ju, F., Xia, Z. & Sasaki, K., 2008. On the finite element modelling of balloon-expandable stents. journal of the mechanical behavior of bio medical materials, Volume 1, pp. 86-95.

Kalita, P. & Schaefer, R., 2008. Mechanical models of artery walls. Arch. Comput. Methods. Arch. Comput.Methods. Eng., Volume 15, p. 1–36.

Kelly, S. & O'Rourke, M., 2012. Fluid, solid and fluid-structure interaction simulations on patient-based abdominal aortic aneurysm models.. Proc Inst Mech Eng H, Volume 226, pp. 288-304.

Khandelwal, A. & Buravalla, V., 2009. Models for Shape Memory Alloy Behavior: An overview of modeling approaches. international journal of structural changes in solids, Volume 1, pp. 111-148.

Kiousis, D., Wulff, R. & Holzapfel, G., 2009. Experimental Studies and Numerical Analysis of the Inflation and Interaction of Vascular Balloon Catheter-Stent Systems. Annals of Biomedical Engineering, Volume 37, pp. 315-330.

Kleinstreuer, C. et al., 2008. Computational mechanics of Nitinol stent grafts. Journal of Biomechanics, Volume 41, p. 2370–2378.

Koshiba, N., Ando, J., Chen, X. & Hisada, T., 2007. Multiphysics simulation of blood flow and ldl transport in a porohyperelastic arterial wall model. J. Biomech. Eng, Volume 129, p. 374–385.

Kratzberg, J., Golzarian, J. & Raghavan, M., 2009. Role of graft oversizing in the fixation strength of barbed endovascular grafts. J Vasc Surg, Volume 49, pp. 1543-1553.

Kujala, S., 2003. Biocompatibility and Biomechanics Aspects of Nitinol Shape Memory Metal Implants. OULU: university of Oulu.

la Flor, S. D., Urbina, C. & Ferrando, F., 2006. Constitutive model of shape memory alloys: Theoretical formulation and experimental validation. Materials Science and Engineering, Volume 427, p. 112–122.

Laffon, E. et al., 2005. Feasibility of aortic pulse pressure and pressure wave velocity MRI measurement in young adults. J Magn Reson Imaging, Volume 21, pp. 53-58.

Lagoudas, D., Bo, Z., Qidwai, M. & Entchev, P., 2003. SMA UM User Material Subroutine for Thermomechanical Constitutive Model of Shape Memory Alloys. Comput. Methods Appl. Mech. Engrg., Volume 1, pp. 281-312.

Lally, C., Dolan, F. & Prendergast, P., 2005. Cardiovascular stent design and vessel stresses:a finite element analysis. Journal of Biomechanics, Volume 38, p. 1574–1581.

Lambert, A., Williams, D., Budd, J. & Horrocks, M., 1999. Experimental assessment of proximal stent-graft (InterVascular) fixation in human cadaveric infrarenal aortas.. Eur J Vasc Endovasc Surg, Volume 17, pp. 60-65.

Länne, T. et al., 1992. Diameter and compliance in the male human abdominal aorta : Influence of age and aortic aneurysm. European Journal of Vascular Surgery, Volume 6, p. 178–184.

Learoyd, B. & Taylor, M., 1966. Alterations with age in the viscoelastic propertiesof human arterial walls. Circulation Research, Volume 18, p. 278–292.

Leondes, C., 2001. Cardiovascular Techniques. Florida: CRC Press LLC.

Leondes, C., 2001. Computer Techniques and Computational Methods in Biomechanics. Florida: CRC Press LLC.

Liang, D., Yang, D., Qi, M. & Wang, W., 2005. Finite element analysis of the implantation of a balloon-expandable stent in a stenosed artery. International Journal of Cardiology, Volume 104, p. 314– 318.

Lim, D. et al., 2008. Suggestion of Potential Stent Design Parameters to Reduce Restenosis Risk driven by Foreshortening or Dogboning due to Non-uniform Balloon-Stent Expansion. Annals of Biomedical Engineering,, Volume 36, p. 1118–1129.

Lin, K. K., 2012. ROLE OF NECK ANGULATION AND ENDOGRAFT OVERSIZING IN FOLDING AND ITS IMPACT ON DEVICE FIXATION STRENGTH, Iowa: University of Iowa.

Li, N., Zhang, H. & Ouyang, H., 2009. Shape optimization of coronary artery stent based on a parametric model. Finite ElementsinAnalysisandDesign, Volume 45, pp. 468-475.

Li, Z. & Kleinstreuer, C., 2005. Blood fow and structure interactions in a stented abdominal aortic aneurysm model. Med Eng Phys, Volume 27, p. 369–382.

Li, Z. & Kleinstreuer, C., 2006. Analysis of biomechanical factors affecting stent-graft migration in an abdominal aortic aneurysm model. Journal of Biomechanics, Volume 39, p. 2264–2273.

Long, A. et al., 2005. Compliance of abdominal aortic aneurysms evaluated by tissue doppler imaging : Correlation with aneurysm size.. J. Vasc. Surg, Volume 42, p. 18–26.

Lumsden, A., Lin, P., Ch, C. & Parodi, J., 2007. Advanced Endovascular Therapy of Aortic Disease. New Delhi: Wiley-Blackwell.

Lu, Z. & Weng, G., 1997. Martensitic transformations and stress–strain relations of shape-memory alloys.. J. Mech. Phys. Solids, Volume 45, p. 1905–1928.

Lyden, S., 2010. Description and comparison of Food and Drug Administration-approved thoracic endovascular aneurysm devices. J Vasc Surg, Volume 52, pp. 10S-4S.

Malina, M. et al., 1998. Endovascular AAA exclusion: will stents with hooks and barbs prevent stent-graft migration?. J Endovasc Surg, Volume 5, pp. 310-317.

176

Mano, J., Thubrikar, Al-Soudi, M. & Robicsek, F., 2001. Wall Stress Studies of Abdominal Aortic Aneurysm in a Clinical Model. Annals of Vascular Surgery, Volume 15, pp. 355-366.

Martin, D. & Boyle, F., 2011. Computational Structural Modelling of Coronary Stent Deployment. Comput Methods Biomech Biomed Engin., Volume 4, pp. 331-348.

Martino, E. D. et al., 2006. Biomechanical properties of ruptured versus electively repaired abdominal aortic aneurysm wall tissue. J Vasc Surg, Volume 43, pp. 570-576.

Marty, B., 2005. Andovascular Aneurysm Rebair. Lausanne: Steinkpoff Darmstadt -Springer.

Matsumoto, T. et al., 2009. Biaxial tensile properties of thoracic aorticaneurysm tissues. Journal of Biochanical Science and Engineering, Volume 4, p. 518–529.

Matsumura, J. & Chaikof, E., 1999. Anatomic changes after endovascular grafting for aneurysmal disease. Semin Vasc Surg, Volume 12, p. 192–200.

McCummiskey, E. et al., 2008. The determination and evaluation of Nitinol constitutive models for finite element analysis. Applied Mechanics and Materials, Volume 7-8, pp. 81-88.

Melzer, A. & Stoeckel, D., 2010. Function and Performance of Nitinol Vascular Implants. The Open Medical Devices Journal, Volume 2, pp. 32-41.

Meyers, M. & Chawla, K., 2009. Mechanical Behavior of Materials. New York: Cambridge University Press.

Migliavacca, F. et al., 2002. Mechanical behavior of coronary stents investigated through the finite element method. Journal of Biomechanics, Volume 35, p. 803–811.

Migliavacca, F. et al., 2004. Stainless and shape memory alloy coronary stents:a computational study on the interaction with the vascular wall. Biomech Model Mechanobiol, Volume 2, p. 205–217.

Migliavacca, F. et al., 2005. A predictive study of the mechanical behaviour of coronary stents by computer modelling. Medical Engineering and Physics, Volume 27, p. 13–18.

Mohan, I., Laheij, R. & Harris, P., 2001. Risk factors for endoleak and the evidence for stent-graft oversizing in patients undergoing endovascular aneurysm repair. Eur J Vasc Endovasc Surg, Volume 21, pp. 344-349.

Mollica, F., Preziosi, L. & Rajagopal, K., 2007. Modeling of Biological Materials. Berlin: Birkhauser Boston.

Molony, D. et al., 2010. A Computational Study of the Magnitude and Direction of Migration Forces in Patient-specsific Abdominal Aortic Aneurysm Stent-Grafts. Eur J Vasc Endovasc Surg, Volume 40, pp. 332-339.

Mortier, P., 2010. Computer Modelling of Coronary Bifurcation Stenting, Ghent: Ghent University. Faculty of Engineering.

Mortier, P. et al., 2008. Automated generation of a finite element stent model. Med Biol Eng Comput, Volume 46, p. 1169–1173.

Mortier, P. et al., 2011. Virtual bench testing of new generation coronary stents. EuroIntervention, Volume 7, pp. 369-376.

Nagl, F., Siekmeyer, G., Quellmalz, M. & Schuessler, A., 2011. A Comparison of Different Nitinol Material Data Sources for Finite Element Analysis. Journal of Materials Engineering and Performance, Volume 20, pp. 737-744.

Nasser, S. & Guo, W., 2006. Superelastic and cyclic response of NiTi SMA at various strain rates and temperatures. Mechanics of Materials, Volume 38, p. 463–474.

Okamoto, R. et al., 2002. Mechanical properties of dilated human ascending aorta.. Ann Biomed Eng, Volume 30, pp. 624-635.

Ormiston, J. et al., 1999. Stent deformation following simulated side-branch dilatation. Catheter Cardiovasc Interv, Volume 47, pp. 258-264..

Ozawa, E., Bottom, K., Xiao, X. & Kamm, R., 2001. Numerical simulation of enhanced external counterpulsation.. Ann Biomed Eng, Volume 29, pp. 284-297.

Pache, J. et al., 2003. Intracoronary stenting and angiographic results: strut thickness effect on restenosis outcome. J Am Coll Cardiol, Volume 41, pp. 1283-1288.

Paiva, A. & Savi, M., 2006. An overview of constitutive models for shape memory alloys. Mathematical Problems in Engineering, Volume 2006, p. 1–30.

Pant, S., Bressloff, N., Forrester, A. & Curzen, N., 2010. The Influence of Strut-Connectors in Stented Vessels: A Comparison of Pulsatile Flow Through Five Coronary Stents. Annals of Biomedical Engineering,, Volume 38, p. 1893–1907.

Park, W. et al., 2008. Evaluation of Stent Performances using FEA considering a Realistic Balloon Expansion. Engineering and technology, Volume 37, pp. 1-6.

Pasta S, R. A. L. A. P. M. S. C. G. T. V. D., 2013. Difference in hemodynamic and wall stress of ascending thoracic aortic aneurysms with bicuspid and tricuspid aortic valve.. J Biomech, Volume 46, pp. 1729-1738.

Pasta, S. et al., 2013. Difference in hemodynamic and wall stress of ascending thoracic aortic aneurysms with bicuspid and tricuspid aortic valve.. J Biomech, Volume 46, pp. 1729-1738.

Patel, D. & Fry, D., 1969. The elastic symmetry of arterial segments in dogs. Circ. Res, Volume 24, p. 1–8.

Pelton, A. et al., 2008. Fatigue and durability of Nitinol stents. Journal of the Mechanical Behavior of Biomedical Materials, Volume 1, pp. 153-164.

Pelton, Rebelo, Duerig & Wick, 1994. Experimental and FEM Analysis of the Bending Behaviour of Superelastic Tubing. California, Proceeding of of the First International Conference on Shape Memory alloy and Superelastic technologies.

Pericevic, I., Lally, C., DToner & Kelly, D., 2009. The influence of plaque composition on underlying arterial wall stress during stent expansion: The case for lesion-specific stents. Medical Engineering and Physics, Volume 31, p. 428–433.

178

Peterson, D. R. & Bronzino, J., 2008. Biomechanical Principales and Applications. New York: CRS Press Taylor \& Francis Group, LLC.

Peterson, L., Jenesen, R. & Parnell, J., 1960. Mechanical properties of arteries in vivo. Circulation Research, Volume 1, p. 622–639.

Petrini, L., Migliavacca, F., Auricchio, F. & Dubini, G., 2004. Numerical investigation of the intravascular coronary stent flexibility. Journal of Biomechanics, Volume 37, p. 495–501.

Petrini, L., Migliavacca, F., Dubini, G. & Auricchio, F., 2003. NUMERICAL ANALYSIS OF VASCULAR STENTS EXPLOITING SHAPE-MEMORY-ALLOY BEHAVIOR. Pavia, 16th AIMETA Congress of Theoretical and Applied Mechanics .

Petrini, L. et al., 2005. Computational Studies of ShapeMemory Alloy Behavior in Biomedical Applications. Journal of Biomechanical Engineering, Volume 127, pp. 716-725.

Prasad, A. et al., 2011. Computational analysis of stresses acting on intermodular junctions in thoracic aortic endografts.. J Endovasc Ther, Volume 18, pp. 559-568.

Prasad, A. et al., 2013. A computational framework for investigating the positional stability of aortic endografts.. Biomech Model Mechanobiol, 12(5), pp. 869-887.

Prasad, A. et al., 2013. A computational framework for investigating the positional stability of aortic endografts.. Biomech Model Mechanobiol, Volume 12, pp. 869-887.

Prendergast, P. et al., 2003. Analysis of Prolapse in Cardiovascular Stents: A Constitutive Equation for Vascular Tissue and Finite-Element Modelling. J Biomech Eng, Volume 125, pp. 692-699.

Price, J. J., Gray, R. & Grollman, J. J., 1971. Aortic wall thickness as an unreliable sign in the diagnosis of dissecting aneurysm of the thoracic aorta. Am J Roentgenol Radium Ther Nucl Med, Volume 4, pp. 710-713.

Prior, A., 1994. Applications of implicit and explicit Finite-Element techniques to metal-forming. J Mater Process Technol, Volume 45, p. 649–656.

Pujari, S. & Udupi, V., May 2009. Stent Biomechanics in Marginal coronary Stenotic Arteries. International Journal of Recent Trends in Engineering,, Volume 1, pp. 1-3.

Raghavan, M. et al., 2006. Regional distribution of wall thickness and failure properties of human abdominal aortic aneurysm. J Biomech, Volume 39, p. 3010–3016.

Raghavan, M., Ma, B. & Fillinger, M., 2006. Non-invasive determination of zero-pressure geometry of arterial aneurysms. Ann Biomed Eng, Volume 34, pp. 1414-1419.

Raghavan, M. & Vorp, D., 2000. identification of a finite strain constitutive model and evaluation of its applicability. Journal of Biomechanics, Volume 33, p. 475–482.

Raghavan, M., Webster, M. & Vorp, D., 1996. Ex vivo biomechanical behavior of abdominal aortic aneurysm : Assessment using a new mathematical model. Annals of Biomedical Engineering, Volume 24, p. 573–582.

Rakhorst, G. & Ploeg, R., 2007. Biomaterials in modern medicine. The Netherlands: world scientific publishing.

Ratner, B., Hoffman, A., Schoen, F. & Lemons, J., 2004. An Introduction to Materials in Medicine. s.l.:Elsevier Academic Press.

Rebelo, N., Fu, R. & Lawrenchuk, M., August. Study of a Nitinol Stent Deployed into Anatomically Accurate Artery Geometry and Subjected to Realistic Service Loading. Journal of Materials Engineering and Performance, Volume 18, pp. 655-663.

Rebelo, N. et al., 2004. Finite Element Analysis on the Cyclic Properties of Superelastic Nitinol. Kurhaus of Baden-Baden, Proceeding of the international conference on shape memory alloy and superelastic technologies.

Rebelo, N., Hsu, M. & Foadian, H., 2001. Simulation of Superelastic Alloys Behavior with Abaqus. s.l., Proceedings of the International Conference on Shape Memory and Superelastic Technologies.

Reese, S. & Christ, D., 2008. Finite deformation pseudo-elasticity of shape memory alloys – Constitutive modelling and finite element implementation. International Journal of Plasticity, Volume 24, p. 455–482.

Resch, T. et al., 2000. The impact of stent design on proximal stent-graft fixation in the abdominal aorta: an experimental study. Eur J Vasc Endovasc Surg, Volume 20, pp. 190-195.

Rissland, P. et al., 2009. Abdominal aortic aneurysm risk of rupture :Patient-specific fsi simulations using anisotropic model. Journal of Biomechanical Engineering, Volume 131, p. 1–10.

Rodríguez, J., Martufi, G., Doblaré, M. & Finol, E., 2009. Effect of material model formulation in the stress analysis of abdominal aortic aneurysms. Annalsof Biomedical Engineering, Volume 37, p. 2218–2221.

Roy, C., 1881. The elastic properties of the arterial wall. J. Physiol, Volume 3, p. 125–159.

Sacks, M., 2000. Biaxial mechanical evaluation of planar biological materials. Journal of Elasticity, Volume 61, p. 199–246.

Santillo, M., 2008. Fracture and crack propagation study of a Superficial Femoral Artery Nitinol stent, Pavia : Universita degli Studi di Pavia.

Schievano, S. et al., 2010. Patient specific finite element analysis results in more accurate prediction of stent fractures: Application to percutaneous pulmonary valve implantation. Journalof Biomechanics, Volume 43, p. 687–693.

Sehitoglu, H., Hamilton, R., Maier, H. & Chumlyakov, Y., 2004. Hysteresis in NiTi alloys. Journal L de physique, Volume 115, p. 3–10.

Shi, D., 2004. Biomaterials and tissu engineering. Cincinnati: springer- biological and medical physics biomedical engineering.

Shobayashi, Y., Tanoue, T., Tateshima, S. & Tanishita, K., 2010. Mechanical design of an intracranial stent for treating cerebral aneurysms. Med Eng Phys, Volume 32, pp. 1015-1024.

Silva, D., Martins, R. & Fernandes, F. B., 2010. Finite Element Modelling of Ni-Ti Shape Memory Alloys. Materials Science Forum, Volume 636-637, pp. 1112-1118.

Simon, B. et al., 1998. Identification and determination of material properties for porohyperelastic analysis of large arteries. J. Biomech. Eng, Volume 120, p. 188–194.

Speelman, L. et al., 2009. Initial stress and nonlinear material behavior in patient-specific AAA wall stress analysis.. J Biomech, Volume 42, p. 1713–1719.

Stefanadis, C. et al., 1995. Pressure-diameter relation of the human aorta, a new method of determination by the application of a special ultrasonic dimension catheter. Circulation, Volume 92, p. 2210–2219.

Sternbergh, W. et al., 2002. Aortic neck angulation predictsadverse outcome with endovascular abdominal aortic aneurysm repair. J Vasc Surg, Volume 35, p. 482–486.

Sternbergh, W., Money, S., Greenberg, R. & Chuter, T., 2004. Influence of endograft oversizing on device migration, endoleak, aneurysm shrinkage, and aortic neck dilation: results from the Zenith Multicenter Trial. J Vasc Surg, Volume 39, pp. 20-26.

Stoeckel, D., Pelton, A. & Duerig, T., 2004. Self-expanding nitinol stents: material and design considerations. Eur Radiol, Volume 14, p. 292–301.

Sweeney, D. & Moore, B., 2003. Internet Delivery of Medical Device Simulation. Dublin, International Congress on FEM Technology.

Takashima, K., Kitou, T., Mori, K. & Ikeuchi, K., 2007. Simulation and experimental observation of contact conditions between stents and artery models. Medical Engineering and Physics, Volume 29, p. 326–335.

Tallec, P. L., 1994. Numerical Methods for Nonlinear Three-dimensional Elasticity. s.l.:Handbook of Numerical Analysis, Vol. III.

Tammareddi, S. & Li, Q., 2010. Effects of Material on the Deployment of Coronary Stents. Advanced Materials Research, Volume 123-125, pp. 315-318.

Tanaka, N. et al., 2004. Conformity of carotid stents with vascular anatomy: evaluation in carotid models. AJNR Am J Neuroradiol, Volume 25, pp. 604-607.

Terriault, P., Viens, F. & Brailovski, V., 2005. Non-isothermal finite element modeling of a shape memory alloy actuator using ANSYS. Computational Materials Science, Volume 36, p. 397–410.

Thamburaja, P., 2010. A finite-deformation-based phenomenological theory for shape-memory alloys. International Journal of Plasticity, Volume 26, p. 1195–1219.

Thériault, P., Brailovski, V. & Gallo, R., 2006. Finite element modeling of a progressively expanding shape memory stent. Journal of Biomechanics, Volume 39, p. 2837–2844.

Thomas, B. & Sanchez, L., 2009. Proximal migration and endoleak: impact of endograft design and deployment techniques. Semin Vasc Surg, Volume 22, pp. 201-206.

Thompson, M. M. et al., 2007. Endovascular Intervention for Vascular Disease. New York: Informa Healthcare USA, Inc..

Thubrikar, M., Al-Soudi, M. & Robicsek, F., 2001. Wall Stress Studies of Abdominal Aortic Aneurysm in a Clinical Model. Annals of Vascular Surgery, Volume 15, pp. 355-366.

Thubrikar, M. et al., 2001. Mechanical properties of abdominal aortic aneurysm wall. Journal of Medical Engineering and Technology, Volume 25, p. 133–142.

Timmins, L., Meyer, C., Moreno, M. & Moore, J. J., 2008. Mechanical Modeling of Stents Deployed in Tapered Arteries. Annals of Biomedical Engineerin, Volume 36, p. 2042–2050.

Toner, D., 2009. An Investigation into Stent Expansion using Numerical and Experimental Techniques, Dublin : Dublin City University.

Tonnessen, B., 3rd, W. S. & Money, S., 2005. Mid- and long-term device migration after endovascular abdominal aortic aneurysm repair: a comparison of AneuRx and Zenith endografts. J Vasc Surg, Volume 42, pp. 392-400.

Upchurch, G. & Criado, J. E., 2009. Aortic Aneurysms. New York: Humana Press, a part of Springer Science+Business Media.

Vad, S. et al., 2010. Determination of coefficient of friction for self-expanding stent-grafts. J Biomech Eng-Trans Asme, Volume 132, p. 12.

Vaishnav, R., Young, J., Janicki, J. & Patel., D., 1972. Nonlinear anisotropic elastic properties of the canine aorta. Biophysical J, Volume 12, pp. 1008-1027.

van Dam, E. et al., 2008. Non-linear viscoelastic behavior of abdominal aortic aneurysm thrombus.. Biomech Model Mechanobiol, Volume 7, pp. 127-137.

van der Merwe, H., 2007. Development of a Numerical Tool for the Optimisation of Vascular Prosthesis towards Physiological Compliance, Cape Town: University of Cape Town.

van't Veer, M. et al., 2008. Biomechanical properties of abdominal aortic aneurysms assessed by simultaneously measured pressure and volume changes in humans. J. Vasc. Surg, Volume 48, p. 1401–1407.

Veith, F. & Baum, R., 2003. Endoleaks and Endotension. united states: Libraray of congress cataloging-in-Publication Data.

Vidal, N. et al., 2008. FEM simulation of the Nitinol wire. The European Physical JournalL Special Topics, Volume 158, p. 39–44.

Vito, R. & Dixon, S., 2003. Blood vessel constitutive models. Annu. Rev.Biomed. Eng, Volume 5, p. 413–439.

Vorp, D., 2007. Biomechanics of abdominal aortic aneurysm. Journal of Biomechanic., Volume 40, p. 1887–1902.

Vorp, D. et al., 2003. Effect of aneurysm on the tensile strength and biomechanical behavior of the ascending thoracic aorta.. Ann. Thorac. Surg, Volume 76, p. 1210–1214.

Vulliémoz, S., Stergiopulos, N. & Meuli, R., 2002. Estimation of local aortic elastic properties with MRI. Magn Reson Med, Volume 47, pp. 649-654.

Walke, W., Paszenda, Z. & Filipiak, J., 2005. Experimental and numerical biomechanical analysis of vascular stent. Journal of Materials Processing Technology, Volume 164–165, p. 1263–1268.

Walraevens, J. et al., 2008. Correlation between compression, tensile and tearing tests on healthy and calcified aortic tissues.. Med Eng Phys, Volume 30, pp. 1098-2104.

Wang, D., Makaroun, M., Webster, M. W. & Vorp, 2001. Mechanical Properties and Microstructure of Intraluminal Thrombus From Abdominal Aortic Aneurysm. J Biomech Eng, Volume 123, pp. 536-539.

Wang, J. et al., 2006. Noninvasive determination of arterial pressure-dependent compliance in young subjects using an arterial tonometer.. Biomed. Eng. Appl. Basis Communic, Volume 18, p. 111–118.

Wang, W., Liang, D., Yang, D. & Qi, M., 2006. Analysis of the transient expansion behavior andd esign optimization of coronary stents by finite element method. Journal of Biomechanics, Volume 39, p. 21–32.

Wang, X. & Li, X., 2011. Fluid-structure interaction based study on the physiological factors affecting the behaviors of stented and non-stented thoracic aortic aneurysms. J Biomech, Volume 44, pp. 2177-2184.

Wang, Y., Yi, H. & Ni, Z., 2002. Computational Biomechanics and Experimental Verification of Vascular Stent. Journal of Materials Processing Technology, Volume 120, pp. 335-340.

Wijst, v. d., 1992. Shape Memory Alloys featuring Nitinol. Veldhoven: TU Eindhoven-Faculteit der Werktuigbouwkunde-Vakgroep WFW.

Wilson, K. et al., 2003. The relationship between aortic wall distensibility and rupture of infrarenal abdominal aortic aneurysm. J Vasc Surg 2003, Volume 37, p. 112–117.

Wnek, G. & BoWlin, G., 2008. Encyclopedia of Biomaterials and Biomedical engineering. New York: informa health care.

Wolf, Y. et al., 2001. Eccentric stent graft compression: an indicator of insecure proximal fixation of aortic stent graft. J Vasc Surg, Volume 33, pp. 481-487.

Wolf, Y. et al., 2001. Impact of aortoiliac tortuosity on endovascular repair of abdominal aortic aneurysms: evaluation of 3D computer-based assessment.. J Vasc Surg, Volume 34, pp. 594-994..

Wolinsky, H. & Glagov, S., 1964. Structural basis for the static mechanical properties of the aortic media. Circulation Research, Volume 13, p. 400–413.

Wolters, B. J. B. M., 2009. Computational modelling of fluid-structure interaction in abdominal aortic aneurysms, Eindhoven : Eindhoven University .

Wriggers, P., 1995. Finite element algorithms for contact problems. Arch Comput Methods Eng, Volume 4, p. 1–49.

Wu, W. et al., 2011. Finite element analyses for design evaluation of biodegradable magnesium alloy stents in arterial vessels. Materials Science and Engineering, Volume 196, p. 1733–1740.

Wu, W. et al., 2007. Delivery and release of nitinol stent in carotid arery their interactions: A finite element analysis.. journal of biomechanics, Volume 40, pp. 3034-3040.

Wu, W., Wang, W., Yang, D. & Qi, M., 2007. Stent expansion in curved vessel and their interactions:A finite element analysis. Journal of Biomechanics, Volume 40, p. 2580–2585.

Wyss, T., Dick, F., Brown, L. & Greenhalgh, R., 2011. The influence of thrombus, calcification, angulation, and tortuosity of attachment sites on the time to the first graft-related complication after endovascular aneurysm repair. J Vasc Surg, Volume 54, pp. 965-971.

Xu, W., 2010. Finite Element Modelling of NITI Shape Memory Alloy Abutment for an Osseointegration Trans-femoral Implant. the open medical divices journal, Volume 2, pp. 2-10.

Zahedmanesh, H., Kelly, D. J. & Lally, C., 2010. Simulation of a balloonexpandable stent in a realistic coronary artery:Determination of the optimum modelling strategy. Journal of Biomechanics, Volume 43, p. 2126–2132.

Zahedmanesh, H. & Lally, C., 2009. Determination of the influence of stent strut thickness using the finite element method: implications for vascular injury and in-stent restenosis. Med Biol Eng Comput, Volume 47, p. 385–393.

Zannetti, S. et al., 2001. Endovascular abdominal aortic aneurysm repair in high-risk patients: a single centre experience.. Eur J Vasc Endovasc Surg, Volume 21, pp. 334-338.

Zarins, C. et al., 2003. Stent graft migration after endovascular aneurysm repair: importance of proximal fixation. J Vasc Surg, Volume 38, pp. 1264-1272.

Zhao, S., Gu, L. & Froemming, S. R., 2011. Assessment of Shape Memory Alloy Stent Deployment in a Stenosed Artery. Biomedical Engineering Letters, Volume 1, p. 226–231.

Zunino, P. et al., 2009. Numerical simulation of drug eluting coronary stents: Mechanics, fluid dynamics and drug release. Comput. Methods Appl. Mech. Engrg., Volume 198, p. 3633–3644.

FOLIO ADMINISTRATIF

THÈSE SOUTENUE DEVANT L'INSTITUT NATIONAL DES SCIENCES APPLIQUÉES DE LYON

NOM :	ALTNJI	DATE de SOUTENANCE : 2 juin
Prénoms :	Sam	
TITRE:	Morphological and Stent Design Risks Factors to prevent Migration Phenomena and Type 1a Endoleak for Thoracic Aneurysm: a numerical analysis	
NATURE :	Doctorat	Numéro d'ordre :

École doctorale : Mécanique, Énergétique, Génie Civil, Acoustique (MEGA)
Spécialité: Biomécanique

RÉSUMÉ:

The main mechanical related problems of endovascular aneurysm repair are migration and endoleak type Ia. They occur when there is no effective seal between the proximal end of stent-graft and the vessel. In this work, we have developed parameterized-deployment simulations of a complete stenting system using finite element method (FEM) to investigate the contact stiffness of a nitinol stent in a realistic Thoracic Aortic Aneurysm (TAA). Therefore, the following factors associated with these complications have evaluated: (1) Proximal Attachment Site Length (PASL), (2) stent Oversizing value (O %), (3) different contact friction situations (stent/aorta) and (4) proximal neck angulation. The calcification impact on the biomechanical behaviour of the deployment at the attachment zone has also been investigated. The simulation results showed that PASL>18mm was a crucial factor to prevent migration at a neck angle of 60^0 and smoothest contact condition ($\mu = 0.05$). The increase in (O %) ranging from 10% to 20% improved the fixation strength; however, O % $\geq$ 25% at 60° caused eccentric deformation and stent collapse. No migration was reported in an idealized aorta model with a neck angle of 0^0, PASL=18mm and $\mu = 0.05$. The numerical observations are used as a guide to optimize the stent design in such neck morphology to strengthen the contact and prevent migration or endoleak type Ia. The optimized stent results showed better contact stability to resist the migration. They also showed a good compromise of stent design requirements (flexibility and stiffness). Moreover, the new design can also prevent the risk of folding or collapse of stent struts by mitigating the energy of eccentric deformation caused by high angulation and oversizing.

MOTS-CLÉS: Aortic aneurysm, Migration, Endoleak type1, Finite element, Self-expanding stent, Stent design

Laboratoire(s) de recherche : **La**boratoire de **M**écanique des **Co**ntacts et des **S**tructures
LaMCoS - INSA de Lyon - CNRS UMR5259
20, avenue Albert Einstein
69621 Villeurbanne Cedex, France

Directeurs de thèse : BOU-SAÏD Benyebka (Maître de Conférences, HDR)

Président du jury:

Composition du jury:

Rapporteur	Valérie DEPLANO	Chargée de Recherche, HDR (IRPHE, Marseille)
Rapporteur	John TICHY	Professeur des Universités (R.P.I, Troy, USA)
Examinateur	Jérôme CHEVALIER	Professeur des Universités (INSA de Lyon)
Examinateur	Philippe VEZIN	Directeur de Recherche (IFSTTAR-Université Lyon 1)
Examinateur	Patrick LERMUSIAUX	Professeur des Universités (Hospices Civils de Lyon)
Directeur de thèse	Benyebka BOU-SAÏD	Maître de Conférences, HDR (INSA de Lyon)
Co-Directrice de thèse	Hélène WALTER-LE-BERRE	Maître de Conférences (INSA de Lyon)
Examinateur	Fouad EL-KHALDI	Ingénieur, Docteur (ESI GROUP de Paris)